# *Formation and function of lipid nano-domains investigated through model membrane systems*

NICOLO TORMENA

Durham University

# Formation and function of lipid nano-domains investigated through model membrane systems


*Author:*

Nicolò Tormena

*Primary supervisors:*

Dr. Kislon Voïtchovsky

Dr. Teuta Pilizota


A thesis presented for the degree of

*Doctor of Philosophy*



Centre for Materials Physics

Department of Physics and Astronomy

Stockton Road

Durham

DH1 3LE


May 28, 2025

# Abstract

The plasma membrane plays a fundamental role in cellular biology, separating the cell from its surroundings and regulating key processes such as macromolecular trafficking, cell-cell communication, and signalling. However, the plasma membrane is a highly complex, heterogeneous, and dynamical structure which renders its study often challenging. As a result, model membrane systems have been developed, offering simplified biomimetic platforms to study membrane phenomena under controlled conditions and with various experimental techniques. This thesis aims to provide new insights into the structure and function of the plasma membrane, with a particular focus on the formation and role of nanoscale lipid domains.

Chapter 1 introduces plasma membranes, both from a functional biological perspective and from a biophysical point of view, highlighting general features of structure, function and behaviour, including the membrane thermodynamics. The chapter concludes with a discussion outlining the gaps in understanding that the thesis proposes to answer.

Chapter 2 describes the different techniques used throughout the thesis, namely a combination of atomic force microscopy (AFM) and calorimetric analysis. AFM offers molecular-level details and localised mechanical characterisation while calorimetry provides a bulk thermodynamic quantification, making it possible to compare and contrast the behaviour of supported and unsupported membranes.

In Chapter 3, a novel model membrane systems for *Escherichia coli* inner membrane is developed, aiming to accurately replicate the compositional, thermodynamical, and mechanical properties of the native lipid membrane. Given the importance of *E. Coli* as a bacterial model, the results offer a new platform for in vitro studies, particularly where involving membrane proteins and mechanotransduction.

Chapter 4 investigate the impact of supporting the bilayer on a solid, showing

that the membrane phase behaviour is significantly altered by surface interactions over multiple timescales. At room temperature, the *E. Coli* model membrane developed in Chapter 3 undergoes multiple complex reorganisation consistent with a surface-induced bias in the lipid flip-flop, enabling local compositional fluctuations and long-term leaflet asymmetry.

Chapter 5, the last experimental chapter, explores the role of lipid phases in extracellular vesicle (EV) uptake by eukaryotic membranes, demonstrating that phase-separated domains are central to EV uptake. Even in the absence of membrane proteins, EVs primarily interact with ordered, less fluid lipid domains, highlighting the functional role of lipid rafts in native membranes. Observed variations in EV-membrane fusion mechanisms, depending on EV origin, offer additional insights into a process that has been widely debated.

Finally, Chapter 6 discusses all the results together, aiming to address some of the questions raised in the introduction and where relevant suggest future experiments and developments in the field.

# Declaration

The work presented in this thesis has been developed under the supervision of Dr. Kislon Voitchovsky of the Department of Physics and Astronomy at Durham University and of Dr. Teuta Pilizota of the Department of Engineering Biology at the University of Edinburgh. All text and Figures are the work of the author, unless otherwise stated. Any external contribution of other researchers is detailed in the specific section.

# Acknowledgements

This thesis is just a reflection of the endless support and love that I've received from multiple people throughout these years. Here, I would like to express my gratitude to all of you.

First, I would like to extend my heartfelt gratitude to my supervisors, Kislon Voitchövsky and Teuta Pilizota. You have been exceptional mentors, fostering my professional growth through your constant encouragement and invaluable wisdom. Beyond the academic guidance, you have supported me personally, offering reassurance, laughter, and understanding when I needed it most.

I would like to thank my lab colleagues in both Durham and Edinburgh. You have always been there whether I needed a professional help or a friendly chat. I wish I was able to pay you back with the same kindness, and I truly wish you the best for your future careers.

A special thanks goes to my friend, Miro. You have been an amazing colleague, a mentor, my personal counsellor, and the most loyal friend I could have asked for. Words can't express my gratitude. Grazie, amico.

I would like to express my heartfelt thanks to Carolina, Caterina, and my master's supervisor Loredana Casalis in Trieste for their unwavering kindness, friendship, and invaluable professional support throughout these last years.

My appreciation also goes to the faculty and staff in the Department of Physics at University of Durham, whose resources and assistance have been invaluable.

I would like to express my deepest gratitude to all the friends I've met during my journey in the UK. Despite occasional homesickness, you have always made me feel at home, bringing the light-heartedness I truly needed. While I wish I could name each of you, I want to extend special thanks to a few: Alberto, Darryl, Adriano, and everyone I met in Coviello - thank you for being like my second

home. To Corey and Seb — thank you for being my first true friends in this chapter of my life and for always being there for me.

Mi prendo questo momento in italiano per condividere gli ultimi ringraziamenti. Vorrei ringraziare tutti i miei amici/amiche in Italia. Sarete sempre una specie di seconda famiglia, e non potrò mai ringraziarvi abbastanza per quello che fate per me. Non avrei mai potuto desiderare degli amici migliori.
Ringrazio tutti i miei parenti per la loro gentilezza ed incondizionata stima dimostratami negli anni.
Infine, dedico questo lavoro ai miei genitori. Vi ringrazio per la fiducia, l'affetto e il supporto che mi avete dimostrato nel mio percorso accademico e in particolare in questi ultimi anni. Tutto questo non sarebbe mai potuto accadere senza il vostro aiuto. Spero sinceramente di avervi reso fieri di me.

Thank you for always being by my side.
Vi voglio bene.

# Contents

# 1. Introduction

## 1.1 Cells, the building block of life

Life, in all its complexity and diversity, is built upon a hierarchy of structures, spanning from the macroscopic level of organisms to the microscopic elements that sustain them. From towering trees to microscopic bacteria, the functioning of all living beings depends on increasingly smaller units, ultimately leading to the fundamental building block of life: the cell [1–3]. All these organisms, regardless of their size or complexity, are built upon a foundation of cells and rely on cellular activity, interaction and communication for their essential functions [3–5]. Organisms can be broadly classified into eukaryotes, which include plants, humans, and fungi, and prokaryotes, which are composed of bacteria and archaea [6]. Eukaryotic cells are typically larger in size (10-100 $\mu m$) and more complex in comparison to prokaryotes, due to their compartmentalised structures containing multiple membrane-bound organelles inserted into an intracellular liquid matrix called cytoplasm (Fig. 1.1A) [3, 7, 8]. Organelles such as the mitochondria, the Golgi apparatus, and the nucleus have specialised roles, fundamental for the cell and organism survival [8–10]. Thanks to this compartmentalisation, eukaryotic cells can finely regulate and enhance the efficiency of their fundamental biological processes [11]. The existence of these compartments is given by the presence of thin semi-permeable barriers called membranes which physically separate them from the rest of the cytoplasm. Beyond these organelles, eukaryotic cells are also encapsulated within a semi-permeable lipid-based barrier called plasma membrane, which plays a critical role not just as a protective structure, but also as a platform for complex signalling, transport processes and facilitating cell-cell communication [12–15]. This is particularly important for eukaryotic cells that are known to interact and communicate with others to form much more complex

structures that range from tissues up to organs and then living organisms.

In contrast, prokaryotic cells are smaller ($<5\ \mu m$) and simpler in structure, lacking membrane-bound organelles. This leaves essential macromolecules freely distributed within the cytoplasm (Fig. 1.1B) [6]. Despite this simplicity, archeal and bacterial domains are fundamental as it is now widely believed that they have originated eukaryotes [7, 16, 17]. This view highlighted the role of prokaryotes, which are now treated as the primary domains of life [18]. Prokaryotes are largely self-sufficient, with many - i.e. bacteria — possessing specialised external structures like pili and flagella to support movement, adhesion, and communication with their environment [19–21]. These structures, along with the outer cell membrane, enable prokaryotes to perform vital interactions that enhance survival. Across both eukaryotic and prokaryotic life, the cell membrane is not only a protective barrier but also a dynamic interface through which cells communicate, adapt, and thrive.

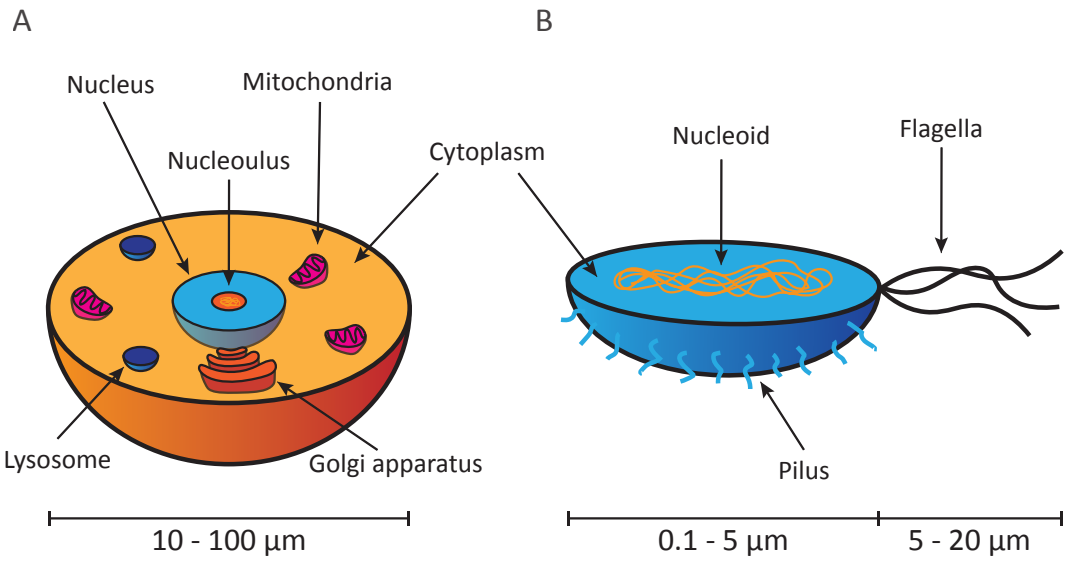


Figure 1.1: Schematic representations of eukaryotic and prokaryotic cells. (A) Eukaryotic cells are highly compartmentalised systems with multiple membrane-bound organelles immersed in the cytoplasm such as the Golgi apparatus, mitochondria, lysosomes and the nucleus where the DNA is stored. This complex organisation reflects the complexity and the multi-leveled regulation behind the biological processes involved in eukaryotes physiological functions. (B) Prokaryotic cells present a simpler structure with no membrane-bound organelles. Fundamental macromolecules such as the DNA or the ribosomes are all present within the cytoplasm without any specialised barrier or compartment. Prokaryotes such as bacteria are generally characterised by other peculiar functional elements that are bounded to the cell envelope, for example pili and flagella. These elements are fundamental to allow and regulate the mechanisms behind bacterial motility and adhesion.

Considering prokaryotes, an important subclass is represented by bacteria. These organisms have been widely studied due to their role in both physiological [22–24] and pathological processes [25–27] within human organisms. Bacteria are usually divided in Gram-positive or Gram-negative based on their response to chemical adsorption of colouring agent in the so-called Gram staining method [28]. This different response to staining agents is related to their different membrane architectures [29, 30]. Gram-positive bacteria, such as *Staphylococcus aureus*, have a single plasma membrane surrounded by a thick layer of peptidoglycan, which provides structural strength and protection [30]. This peptidoglycan layer can be up to 30 layers thick, creating a robust but relatively simple envelope. Gram-negative bacteria, for example *Escherichia coli* (*E. coli*), possess two distinct plasma membranes [30]: the inner membrane, which predominantly regulates the flow of nutrients and other molecules, and the outer membrane, which is mainly linked to protection against environmental threats like antibiotics [31]. The outer membrane contains unique molecules like lipopolysaccharides (LPS), which act as a barrier to harmful substances and are implicated in immune system recognition [32].

The understanding of these basic concepts of eukaryotic and prokaryotic cellular biology represented an essential cornerstone of scientific inquiry. Over time, researchers have dedicated extensive efforts to understanding cell structure and function, leading to our current understanding of not only cellular biology but also of complex biological processes in nature. From advancing cancer treatments to developing diagnostic tools for viral infections, many of the most fundamental scientific achievements trace back to insights gained from studying these simple microscopic units. Specifically, much of this research has relied on specific cells and organisms called model organisms [33, 34], which have served as trailblazers in the field, allowing scientists to establish foundational knowledge about cell function and structure. In most of my thesis, I focused on the *E. coli* bacterium, a model organism that fundamentally revolutionised the microbiology field, but has also been employed in other fields such as cellular biology and human biotechnology. The following section will further explore *E. coli*, focusing on its cellular structure, membrane properties, and its importance as a model organism for understanding membrane biology and membrane processes.

## 1.2 *E. coli* as model organism

*E. coli* is a Gram-negative bacterium extensively studied and employed in biotechnology. As a model organism, *E. coli* has been pivotal in advancing our understanding of fundamental biological processes. As all the model organisms [35], *E. coli* cells are usually chosen for their ease of genetic manipulation, straightforward maintenance, and well-characterised genetics. They also share key physiological processes with human cells. For instance, *E. coli* has played a crucial role in molecular biology and genetics, contributing to the development of recombinant DNA technology [36] and the discovery of the CRISPR-Cas9 system for genome editing [37]. *E. coli* stood out as a fundamental tool also for membrane biology studies as it shares several proteins and complexes with human cells [38, 39], such as proteins involved in cell division and DNA replication, making it a valuable model for understanding human cellular behaviour.

Due to its poor compartmentalisation, many of *E. coli* physiological activities are either originated or regulated along the cell envelope. This external layer acts as both a protective barrier from environment stressors and an active interface by facilitating interactions with neighbouring cells, enabling the formation of biofilms [30, 31, 40]. Additionally, the envelope is key to cell's motility, as it anchors the flagella and embeds the protein complexes that drive the movement of these filamentous structures [20, 21]. The study of *E. coli*'s envelope has therefore been beneficial for the microbiology field, allowing it to understand not only bacterial adaptation, but also broader mechanisms of microbial motility [41], environmental sensing and biofilm formation [42].

### 1.2.1 *E. coli* envelope

As previously described, *E. coli* is a Gram-negative bacterium and thus presents a complex cell envelope compared to eukaryotic cells. This envelope consists of two membranes—an inner and an outer membrane—separated by a periplasmic space that holds a robust peptidoglycan cell wall [30] (Fig. 1.2). The cell wall provides structural support and shape, interacting directly with the membranes. The peptidoglycan layer, composed of cross-linked polysaccharides and peptides, not only provides structural support and shape but also plays a critical role in

maintaining the integrity of the cell envelope under varying osmotic pressures. This rigid structure helps protecting the inner and outer membranes from mechanical stress and contributes to the overall resilience of the bacterial cell. The outer membrane is mainly composed by lipids and lipopolysaccharides (LPS) which are exposed on its extracellular surface. Thanks to the LPS presence, the outer membrane plays a crucial role for the structural integrity and protection of the cell, particularly by targeting antibiotics and detergents [30, 31]. While LPS and phospholipids dominate the outer membrane, it also contains porins and transporters that facilitate the passage of molecules into the periplasmic space, as well as larger protein complexes that can extend down to the inner membrane [43]. An example of such a complex is the flagellar motor, a bidirectional rotary system used by many bacteria to sense and propel their flagella. The motor-flagellum complex in *E. coli* has been extensively studied as a canonical system for understanding bacterial motility and serves as a reference model in bacterial movement research [44, 45].

On the other hand, the inner membrane similarly to eukaryotic membranes present a mix of lipids, proteins and sugars that mediate essential cellular functions and serves as a both physical barrier and electrochemical barrier regulating the ions passage between the inside and outside of the cells and playing a vital role in the nutrient transport [30]. This inner membrane, due to its inclusion of crucial membrane proteins for *E. coli* function and its similarity with eukaryotic membranes, has been the subject of different studies [46, 47]. Although the inner membrane composition and biophysical properties are known to adapt to the environment [48–50], some key aspects of this bilayer are highly conserved no matter the strain or the environmental conditions in which *E. coli* is grown. Following the characteristics of prokaryotes, *E. coli*'s inner membrane does not present sterols, rather hopanoids that fulfil their fluidity regulating role [51, 52]. Overall, the lipid composition of this membrane is highly conserved and includes specific classes of lipids such as phosphatidylethanolamines and phosphatidylglycerols, which will be further addressed later in this Introduction. Moreover, *E. coli* membrane is characterised by the presence of a minor lipid species called cardiolipin (CL) which in spite of its low concentration (5-10% molar ratio), plays a crucial role in in the membrane's physiological behaviour [53–55]. Thanks to its 4-lipid chains structure, CL can affect fluidity and charge density across the membrane [56] and can also influence membrane

proteins' function [46, 57], confirming its fundamental bio-active role. The presence of this lipid in the *E. coli* membrane has garnered interest, as CL is found in high concentrations within mitochondrial membranes [58]. The *E. coli*'s inner membrane can thus serve as an accessible model to explore the mitochondrial membrane-stabilising role of CL and its interactions with mitochondrial membrane proteins.

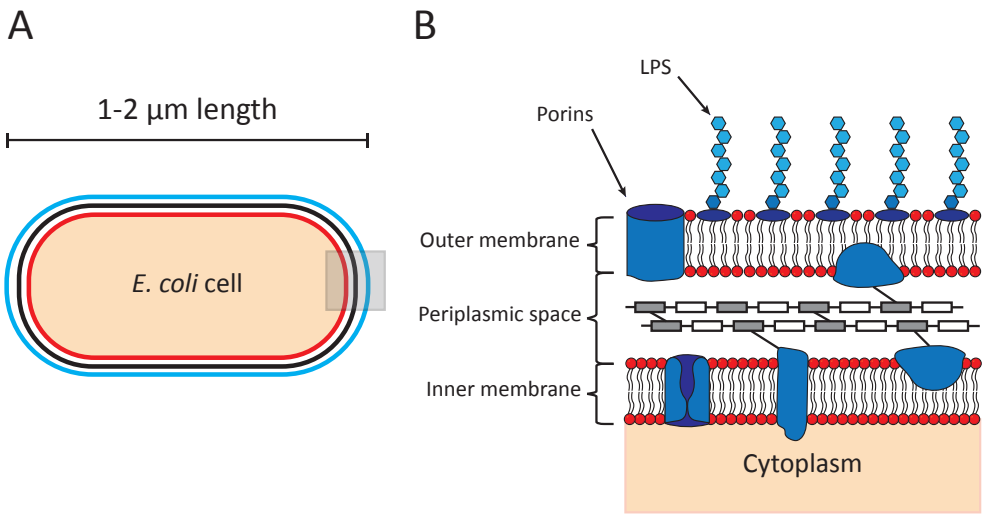


Figure 1.2: The envelope of the *E. coli* cells. (A) As all the Gram-negative bacteria, *E. coli* presents a complex cell enveloped formed by an outer membrane (blue), the periplasm (black) and finally the inner membrane (red) which all together allow to separate the inside from the outside of the cell and provide structural stability to the *E. coli*. When looking at the profile of the envelope (B), it is possible to observe that the outer membrane is a peculiar and specialised membrane thanks to the abundant presence of LPS which work as a defensive mechanism for the bacteria. Following this layer, the periplasm presents a complex bundle of peptidoglycan layers which provide structural integrity to the cell and are in direct contact with both the lipid membranes. Finally, the inner membrane represents a classic plasma membrane where both phospholipids and membrane proteins can be found. This more internal layer has the fundamental role to act as the last barrier before the cytoplasm of *E. coli*, regulating the uptake of molecules and the activation of various biological pathways.

Although this basic description of the *E. coli*'s inner membrane will be expanded in my results Chapter, it is evident from this section the importance of the inner membrane in *E. coli* physiological function and how each element within the membrane provides unique properties to this system. The fundamental roles of membranes in both eukaryotic and prokaryotic cells underscore their significance in biological research. Understanding the unique properties and behaviours of *E. coli* membranes provides valuable insights that are applicable to a wide range of

organisms. With this foundational understanding of the *E. coli*'s inner membrane in place, I will now further investigate the intricate structures and compositions of cellular membranes. This next section will explore the principles of membrane biology, including the characteristics of phospholipids, the bilayer model, and the various proteins that contribute to membrane functionality.

## 1.3 The plasma membrane

As described in the previous section, the cell membrane, or plasma membrane, covers multiple active and passive roles in cell's physiology. The plasma membrane acts as both a physical barrier dividing the inside from the outside of the cell, but also represents the headquarter of various biological processes from generating an electrochemical gradient of ions [12, 59], to transporting molecules [60] and also in motility processes [21, 41, 61].

Plasma membranes are widely studied because of their biological importance; however, much of their activity remains poorly understood (i.e. bilayer asymmetry and membrane proteins localisation) due to their inherent complexity. It has been previously addressed how membranes' composition is crucial to allow cell's ability to sense chemical and mechanical stimuli and respond by activating crucial biological pathways [62]. However, no matter the compositional difference, all cell membranes share a fundamental structural feature: they are composed of a lipid bilayer that serves as a dynamic interface for various cellular processes. This bilayer, formed primarily by phospholipids, is essential to membrane function, providing the framework in which proteins and sugars are embedded or bound. The following section delves into the composition and structure of the plasma membrane, highlighting the interplay between these components and their roles in maintaining cellular integrity.

### 1.3.1 Cell's membrane composition and structure

All plasma membranes consist of a self-assembled and self-synthesised phospholipid bilayer with a hydrophobic core in which multiple proteins, and sugars, are either bound or embedded [63]. This simple description, first framed by Singer and Nicolson in 1972, is now well-established [64] (Fig. 1.3). Singer

and Nicolson pointed out the limitations of the previous trilaminar arrangement model [65] that was used to describe membrane's structure, where a tri-layer of proteins-lipids-proteins was suggested (Fig. 1.3A). Instead, a new model called "Fluid mosaic model" was proposed by focusing on the thermodynamic principles that favour the formation of a double lipid layer in which other macromolecules can be inserted (Fig. 1.3B) [64, 66]. In this model, hydrophobic and hydrophilic covalent interactions represent the driving force for the formation of this structure. Lipids and membrane proteins generally present both a hydrophobic core (represented by the acyl chains and the non-polar aminoacids, respectively) and a hydrophilic portion (represented by the charged or zwitterionic headgroup and the charged aminoacids, respectively). The hydrophobic interactions are responsible for sequestering of hydrophobic elements away from water media, while hydrophilic interactions favour the associations of charged elements with aqueous solutions [67–69]. Although other minor noncovalent interactions such as electrostatic and hydrogen bonds are present, hydrophilic and hydrophobic forces are significantly greater by several orders of magnitude, thus acting as the dominating factors for the double layer formation. The spontaneous formation of the lipid bilayer, driven by minimising the interactions of hydrophobic chains with water, allows proteins to embed their nonpolar regions within the lipid matrix, creating a more energetically stable structure [68]. The final system is represented by a fluid lipid system where large globular proteins are inserted and able to move around, creating a mosaic structure in which protein regions are alternated by phospholipid regions in a dynamic way [64]. Although this simple description still stands and it introduced for the first time the topic of membrane's asymmetry or the ability of elements to move within the membrane, the fluid mosaic model fails to depict the complexity of the plasma membrane that has emerged over the last 40 years [66]. The presence of interactions between the membrane and the cytoskeleton filaments [70, 71], the presence of interactions with proteins [72] and the formation of specialised membrane domains [73, 74], are neglected in this interpretation and can influence the overall structure and restrict the lateral motion of membrane's molecules [66]. Furthermore, the fluid mosaic model assumes that membrane components are always in equilibrium, freely moving within the bilayer. However, this is often not the case in biological membranes. Membrane dynamics is tightly regulated in response to external chemical and physical stimuli, which can lead to localised stiffening [75], clustering

of proteins or lipids [76, 77], and interactions with scaffolding elements like the cytoskeleton [71]. These phenomena reflect an active regulation of membrane properties, rather than the random, equilibrium-based motion assumed by the fluid mosaic model. Such adaptations are essential for the cell to respond to environmental signals, mechanical stress, or changes in cellular function. A deeper understanding of these regulatory processes would enable the refinement of the fluid mosaic model into a more complete and realistic representation of the plasma membrane's natural environment.

To best understand cell membrane physiology, the next sections will describe the 2 main classes of molecules within the membrane, starting with proteins, which solve many active roles within the bilayer, and then focusing on arguably the leading component: the lipids.

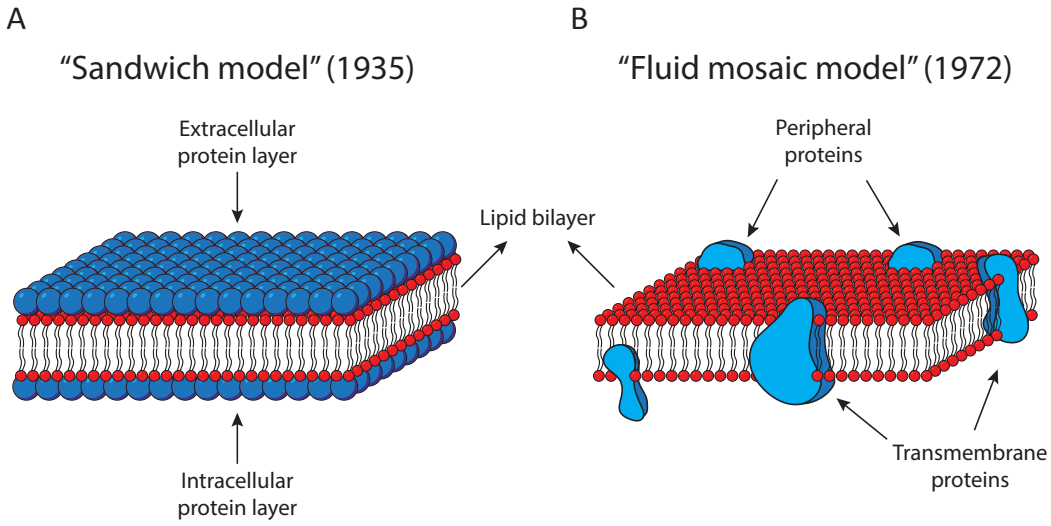


Figure 1.3: Schematic representations of past and current models of cell's membrane structure. The first description of plasma membrane framed by Davson–Danielli [65](A) has evolved into the fluid mosaic model developed by Singer and Nicolson during the early 70s [64] (B). Although this model presents some crucial limitations and lacks of fully depicting the complexity of the membrane, the fluid mosaic model is still used nowadays, also for its ability to incorporate important features including the concepts of lateral heterogeneity and the dynamic behaviour of the membrane.

### 1.3.2 The role of membrane proteins

Inside plasma membrane, proteins are the predominant molecule as the ratio by weight between proteins and lipids ranges from 1.5 to 4 depending on the specific membrane and they represent about 20-30% of the entire human proteome. Membrane proteins are vital to nearly every function that occurs at the cell's

boundary, from transporting molecules and acting as gatekeepers for ions and nutrients to transducing signals, regulating the uptake of extracellular molecules and enabling cell-cell communication [78–82]. In addition, they also participate in cell adhesion and mechano-transduction processes controlling how forces are spread across the membrane.

Membrane proteins are divided in 2 major families which have been named as peripheral and integral proteins, depending on their structure and the way they interact with the lipid bilayer [1]. Peripheral proteins generally present shorter hydrophobic regions, allowing them to partially and only temporarily insert in the bilayer and protruding just from one leaflet. On the other hand, integral proteins are permanently attached to the membrane. Integral proteins can be divided into monotopic proteins, which interact with only one leaflet of the bilayer, playing a more localised role, and polytopic proteins, also known as transmembrane proteins, which span the entire membrane and are responsible for connecting the extracellular and intracellular spaces [1]. Transmembrane proteins are the most common ones, and generally present a larger structure which is fully embedded within the membrane, sometimes presenting complex structures and multiple hydrophobic domains. These proteins present an extracellular, an intracellular and a transmembrane region respectively facing the extracellular matrix, the cytosol or the hydrophobic matrix of the membrane [83]. Thanks to their ability to directly connect the extra and intracellular spaces, transmembrane proteins can carry out some of the most fundamental biological activities that occur at the plasma membrane. Due to this wide array of tasks that they perform, transmembrane proteins can be classified based on their functions. This includes transport proteins, receptor proteins, enzymatic proteins cell adhesion proteins, and signal transduction proteins. For example, transport channels such as aquaporins are crucial to regulate the flow of water molecules across the membrane, allowing the cell survival and maintaining an osmotic balance [79]. Enzymatic proteins like transmembrane ATPases are active enzymes which provide energy to the cell by catalysing the decomposition of ATP. By cooperating with other membrane proteins and forming larger complexes, ATPases exert a crucial role in the uptake of external solutes, permitting their passage against the concentration gradient [80]. Finally, receptor proteins transmit signals by binding ligands such as hormones and triggering the cellular response. The G-protein-coupled receptors (GPCRs) are common protein complexes which after

the binding of the extracellular ligand can activate a transduction pathway through the G-protein located within the cell [81].

Although protein-protein interactions are fundamental for the formation of these complexes, the function of membrane proteins is also closely related to their lipid surrounding. The lipid environment in which proteins are inserted has a fundamental role not only by energetically stabilising their ternary structure [72], but lipids are also actively involved in regulating their function [14]. Proteins present aminoacidic regions, called motifs, which are specialised for the interaction with unique phosphate headgroups. For example, computational and experimental evidence suggests that specific lipid classes can be found inside the ternary structure of mechanosensitive channels (MSCs) [76], a peculiar family of integral proteins dedicated to sensing and responding to mechanical stress on the membrane of both eukaryotic and prokaryotic cells [84]. Here, lipids can enter and exit specific MSC pockets upon stretching of the membrane, leading to a conformational change of the MSC that can pass from an open to a close status and vice versa. Another example is given by the fact that regions of the membrane highly enriched in membrane proteins generally present a lipid pattern which is compositionally and mechanically different from the overall membrane [54, 85, 86]. The presence of these lipid domains surrounding protein complexes suggest a fundamental link between protein activity and these protein-lipid interactions. Moreover, although proteins exert the leading role when it comes to biological pathways activated along the membrane, lipids seem crucial not only because of their principal role in forming the bilayer matrix, but also by actively regulating the proteins' function.

### 1.3.3 The role and structure of lipids

Lipids are amphiphilic molecules composed of a hydrophilic polar headgroup and a hydrophobic core made up of one or more non-polar hydrocarbon chains. Due to their amphiphilic nature, lipids in aqueous solutions spontaneously arrange themselves into complexes where the hydrophobic regions are sequestered away from water [87]. This spontaneous arrangement is primarily driven by the association of the hydrophobic domains through the reduction in the ordering of water molecules in the solvent, which leads to an increase in entropy, as well as by the formation of multiple van der Waals interactions [68]. Lipids exhibit

what is known as "lipid polymorphism" [88], which refers to their capacity to form various types of superstructures depending on environmental conditions such as temperature and ionic strength, and more importantly, their chemical composition. Additionally, they can possess headgroups of different sizes, acyl chains of different lengths and with a different amount of double carbon bonds (also known as saturation degree), which significantly alters their final 3D structure. Their possible arrangement can be generally predicted by calculating the so-called packing parameter ($P$), a unitless factor depending on the area of the headgroup ($A$), the length of the chain ($L_c$) and the volume occupied ($V$) by the chain:

$$P = \frac{V}{A * L_c} \tag{1.1}$$

The value of $P$ allows predicting the shape of the lipids, for example cone, truncated cone, cylinder and inverted. Depending on their structure, it is thus possible to predict the most favourable final superstructure (Fig. 1.4).

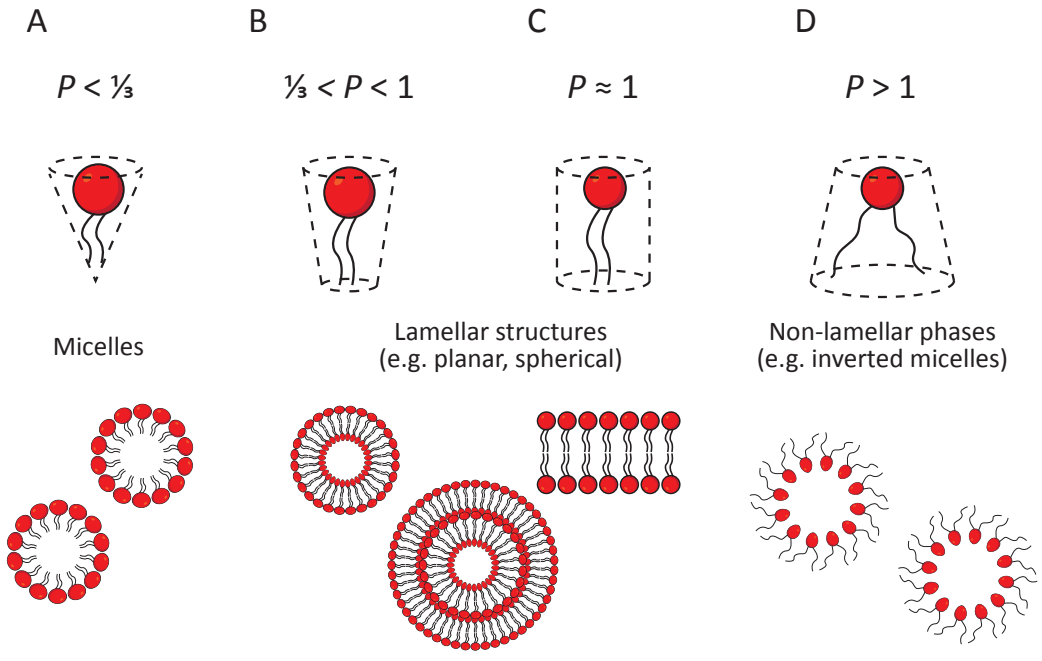


Figure 1.4: Illustration of lipid polymorphism (38). Depending on their packing parameter,$P$, lipids present different 3D shapes: conical (A), truncated conical (B), cylindrical (C) or truncated cylindrical (D). Based on their shapes, lipids then form superstructures when in aqueous solutions to minimise the free energy of the system. These structures range from monolayer micelles (A), lamellar structures (B, C) and finally more complex structures such as inverted micelles (D).

Although structures such as micelles and hexagonal phases can be found in nature, the bilayer is the most common and energetically stable superstructure for most lipids, in particular for complex lipid mixtures [3]. However, the importance of the packing parameter goes beyond merely predicting lipid structure. It plays a crucial role in the membrane curvature, as lipids with smaller $P$ can locally increase the curvature of the bilayer [89, 90]. This effect impacts processes such as vesicle formation and fusion, where membranes need to undergo significant deformation. Lipids with non-cylindrical shapes are typically found in regions of high curvature, i.e. around membrane proteins or where vesicles are formed [90, 91]. This suggests their role in both stabilising the structure of the bilayer, and facilitating these processes. The specific lipid types present in a membrane are therefore key to determine the membrane structural and functional properties. Lipids are generally divided into different classes, each differently contributing to membrane behaviour [92]:

***Phospholipids***

Phospholipids represent the major lipid class in cell membranes for both eukaryotic and prokaryotic cells. They are formed by a three-carbon backbone of glycerol, linked with two long-chain fatty acids esterified to hydroxyl groups on carbons 1 and 2 of the glycerol and with a phosphoric acid esterified to the carbon 3 hydroxyl group. The hydrophobic domain is formed by the diacylglycerol part, whereas the phosphate head is the hydrophilic domain. Phospholipids can further be classified in subclasses depending on the functional group of the phosphate head, for example phosphatidylethanolamine (PE), phosphatidylcholine (PC), phosphatidylserine (PS), phosphatidylglycerol (PG), and cardiolipin (CL), which stands out between phospholipids for its 4-chains structure [93]. In eukaryotic cells, PCs are highly abundant, representing the predominant phospholipid in human cells' membrane with an overall molar ratio of 40-60% [94, 95]. In contrast, PCs are less represented in prokaryotic membranes, with other lipids such as PEs and CLs being their main constituents [96, 97]. For example, *E. coli*'s inner membranes present a highly conserved composition composed of PEs (generally 60-80% molar ratio), followed by PGs (15-30% molar ratio) and other minor lipids, where cardiolipin (CL) is the most abundant one (5% molar ratio) [96]. Given their abundance, phospholipids play a key role in contributing to membrane properties, including fluidity, lateral organisation, and the ability to stretch.

***Sphingolipids***

This is a class of lipids containing the organic aliphatic amino alcohol sphingosine or a substance structurally similar. The simplest sphingolipids are ceramides, composed of sphingosine plus a fatty acid and are widely distributed in small amounts in eukaryotic membranes. Other sphingolipids are derived from these ceramides and usually present a higher saturation degree compared to phospholipids. The major sphingolipids in eukaryotic membranes are sphingomyelin (SM) and glycosphingolipids (GSLs) [98, 99]. While extremely common in eukaryotic cells, sphingolipids are absent in bacteria and other prokaryotic cells.

***Sterols***

Sterols are organic molecules characterised by a fused four-ring core structure and they are the most relevant non – polar lipids in eukaryotic membrane. The major sterol in animals is cholesterol, holding a fundamental role in regulating membrane fluidity along cell membrane [100–102]. Although sterols are rare or totally absent in prokaryotic cells, their function is fulfilled by other lipids called hopanoids [52, 103].

## 1.4 Lipid nanodomains in biological membranes

The compositional complexity of the plasma membrane is also reflected on its topographical features. As simply described in the fluid mosaic model, membranes present a heterogeneous surface where protein and lipid enriched regions are organised in micro or nanodomains along the membrane's surface [64]. However, multiple studies have observed that lipids can also organise themselves in nanodomains, which compositionally diverge from the rest of the membrane and presumably have an important role in the membrane's physiological functions including protein localisation and marcomolecules uptake [97, 103, 104]. Lipid nanodomains have been first discovered in eukaryotic cells [105], where high levels of sphingolipids and cholesterol have been observed to accumulate in localised areas of the membrane. These two classes of lipids have been indeed recognised as a marker for these domains in eukaryotic membrane, with cholesterol increasing lipid packing, regulating the dynamics of sphingolipids within the domains,

and contributing to their stability and functional properties [106–108]. These lipid domains present a short lifetime of the order of few milliseconds [109]. Their transient nature allows them to quickly assembly and disassembly in a dynamic way, facilitating their formation when needed. However, their nanometre size coupled with their short lifetime makes them complicated to view with traditional microscopy techniques. Because of these experimental limitations, their existence and role has generated considerable controversy over the years [110, 111]. Nonetheless, the development of new techniques and experimental approaches allowed to address these doubts [85, 109, 112–115]. For example, fluorescence-based techniques (i.e. fluorescence-lifetime imaging microscopy, FLIM, and fluorescence recovery after photobleaching, FRAP) allowed to obtain insights into the dynamic properties of these domains and identify their main constituents [109, 116–120]. Fluorescence microscopy is widely employed for its compatibility with both model membranes (i.e. vesicles) and living cells, allowing us to directly observe the native environment. However, these approaches rely on the use of fluorescent probes, which might contaminate and influence the lipid domains formation. Atomic force microscopy (AFM) has been used to study lipid nanodomains existence for its ability to image membranes in aqueous solutions with nanoscopic resolution, providing novel insights into domains' formation, role and their physical properties [98, 99, 121–125]. Nevertheless, AFM application is limited to model membranes or native patches immobilised on surfaces.

It is worth noting that lipid nanodomains are often referred to as "rafts" in the literature. While the term has sparked some controversy due to differing interpretations of their formation, properties, and functions, it is employed here primarily as a convenient shorthand. In this thesis, the term is used to emphasise the distinct physical and compositional characteristics of these lipid-based structures compared to the surrounding membrane, rather than to imply any specific biological role or function.

### 1.4.1 Lipid nanodomains relevance in cellular biology

The formation of nanodomains is thought to have crucial effects on membrane's function in both eukaryotic and prokaryotic cells. Although their role is still controversial, results over the last 20 years have strongly suggested that these domains are linked with various active processes that involve the membrane.

Their active role in the membrane's physiology has been mainly linked with the localisation of proteins within these lipid domains [86, 103, 126–135]. Thanks to the formation of transient domains, membranes can recruit and stabilise membrane proteins, localising their activity within specific regions and thereby modulating their physiological roles. Receptors involved in signalling [129–131] and trafficking [103, 132, 133] have been found in lipid domains, suggesting their critical importance in these mechanisms. In immune cells, lipid rafts serve as organisational centres for crucial receptors such as T-cell and B-cell receptors (TCRs and BCRs), which are essential for pathogen recognition and initiating immune responses [130, 136]. The localisation of these receptors within lipid rafts enhances their signalling capabilities, highlighting the rafts' importance in immune surveillance and response. Some pathogens, including viruses like SARS-CoV-2, may however exploit lipid rafts as entry tools to gain access within the cell [137]. This dual role in supporting immune function while also being co-opted by pathogens makes lipid rafts a significant area of study in immunology, as they may provide insights into both protective mechanisms and vulnerabilities within the immune system.

Specific lipid domains have been identified for their ability to work as a functional scaffold that regulate the communication between the membrane and the cytoskeleton [138], suggesting their structural relevance. Their importance has also been confirmed in prokaryotic organisms such as bacteria [139]. While prokaryotic membranes present remarkable differences with respect to eukaryotic ones for the absence of cholesterol and other classes of phospholipids, lipid domains of different phases have been experimentally observed and their role as both signalling and organisational platform has been confirmed [53, 54, 139–141]. Finally, these lipid domains are also characterised by different mechanical properties and different motility of the lipids within them [105]. This local and global mechanical reshaping of the membrane may have significant effects on the ability of the membrane to sense and respond to external stimuli, which is crucial for cell survival.

Considering the functional role of these domains, it is evident that a better understanding of lipid rafts is needed to fully capture the behaviour of plasma membranes. While many studies have focused on the functional aspects of lipid rafts, understanding how these domains form is equally important. In the next section, I will explore the fundamental concept around lipid domains formation,

which offers a theoretical framework to better explore this topic later in my thesis.

### 1.4.2 The origin of phase separated domains in the plasma membrane

A key concept around lipid raft formation is that lipids can exist in different phases. Lipids are characterised by a series of states of matter or phases in which they are stable, depending on both environmental conditions (temperature, ionic strength and pH), and structural features. Lipid domain formation is thermodynamically driven, as the system seeks to minimise its free energy [64, 66, 67, 142, 143]. This balance is achieved by maximizing entropic disorder while benefiting from stabilising lipid-lipid non-covalent interactions.

The foundational work around this lipid's property dates back to the 70s [144–146], when researchers discovered that lipids could shift between phases depending on the experimental temperature. Each lipid is characterised by a unique transition temperature ($T_m$) which describes the temperature at which it passes from a lipid phase to another (Fig. 1.5). At low temperatures, lipids are in the so-called gel phase ($S_o$), characterised by tightly packed lipids with their acyl chains fully extended and closely aligned, resulting in a rigid structure with long-range positional correlation between molecules. Upon heating, lipids increase their kinetic energy and enter a liquid-disordered phase ($L_d$), characterised by a high degree of disorder in the acyl chains, thus resulting in greater mobility and fluidity.

After these pioneering experiments, another lipid phase was discovered in biological systems; the liquid-ordered phase ($L_o$). $L_o$ phase combines the fluidity of the $L_d$ with the short-range order of the $S_o$ phase, lying in between the two extreme scenarios [143]. $L_o$ phase has been observed for the first time in lipid rafts of eukaryotic cells, where cholesterol plays a crucial role by interacting with saturated lipids to form this relatively order structure which retains lateral mobility [147]. Nonetheless, $L_o$ presence has been more recently confirmed also in bacteria [52], which do not present this sterol.

The presence of this plethora of lipids which can form different phases is at the base of the phase separation process observed in plasma membranes. This phenomenon has been now widely studied both experimentally [112, 113, 115] and theoretically [148–150]. Thanks to these works, it is well-established that at

constant environmental conditions (i.e. temperature, pH and pressure), certain class of lipids (e.g. presenting short carbon chains) preferentially stay in $L_d$ phase, maintaining a high degree of disorder and dynamicity, while others (e.g. presenting long carbon chains) tend to form highly packed and less dynamic structures such as the $S_o$ and $L_o$ phase, separating themselves from the rest of the membrane [67]. Together, the thermodynamic diversity of lipid phases and the compositional heterogeneity of membranes give rise to transient domains.

As part of my research activity, I dedicated myself to understanding not only the function of lipid rafts, but also the way these domains form in lipid membranes. Beyond the basic existence of these different lipid phases, complex lipid membrane can dynamically form lipid rafts through different molecular mechanisms which are regulated by the thermodynamic properties of these systems. As these mechanisms can influence the features of the final domains, the next section will focus on this topic, establishing a basic theoretical framework for the interpretation of my results later in this thesis.

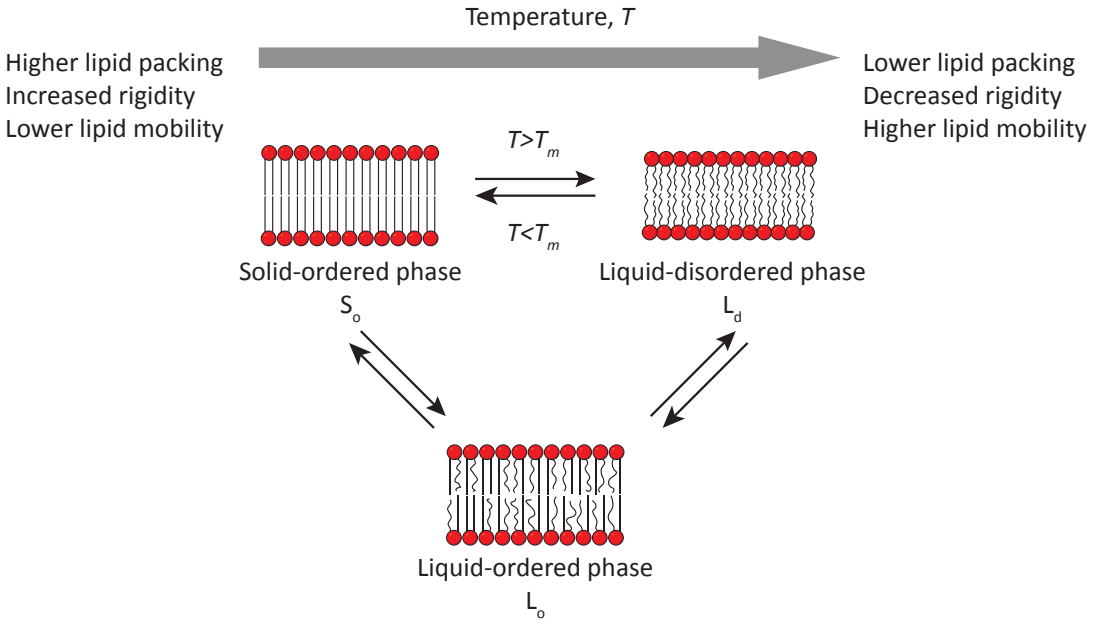


Figure 1.5: Illustration of the ability of lipids to pass through different phases varying the temperature of the system. At a temperature below their characteristic $T_m$, lipids are tightly packed and organised in the $S_o$ phase which generally present higher rigidity and lower mobility of the molecules. When the temperature is increased above $T_m$, lipids enter the $L_d$ phase, characterised by a highly dynamic and mobile molecular structure following this increase in thermal energy of the system. In native and compositionally complex systems, another phase can be found: $L_o$ phase. This lipid phase sits in-between the $S_o$ and $L_d$ extremes combining the higher rigidity of the former with a similar mobility of the latter.

### 1.4.3 Thermodynamic principles behind lipid rafts

By visualising the membrane as a simple fluid binary system composed of components A and B, it is clear that the mixing of the system is governed by two thermodynamic forces: the entropy ($S$) and the enthalpy ($H$) [151]. The entropy describes the degree of disorder of the bilayer, favouring a homogenous and mixed state where lipids can freely move. This is described by the Boltzmann's formula:

$$\bar{S} = -k_B \sum_i \phi_i \ln(\phi_i) \tag{1.2}$$

where $\phi_i$ is the probability of finding a molecule $i$ in the considered microsite. Since in a binary system one site can be either occupied by A or B, this formula can be simplified as:

$$\bar{S} = -k_B \left[\phi_A \ln(\phi_A) + \phi_B \ln(\phi_B)\right] \tag{1.3}$$

where $\phi_A$ and $\phi_B$ are the probability of finding component A and B in the specific site, respectively.

On the other hand, lipids can also interact with themselves, generating non-covalent weak interactions that influence their localisation in the bilayer and favour a more ordered and unmixed bilayer [67]. The internal energy ($U$) due to the thermodynamic unmixing contributions can be modelled as:

$$\Delta\bar{U}_{\text{mix}} = \chi\phi_A\phi_B \tag{1.4}$$

where $\chi$ is the interaction parameter that defines the energetic preference of a system for like-with-like interactions compared to unlike interactions. In the case of an ideal system with pressure being constant, the mixing internal energy can also be seen as $\Delta H_{mix}$, the mixing enthalpy.

The contribution of the two main driving mechanisms is captured by the system's Gibbs free energy ($G$). $G$ effectively describes how spontaneously a given bilayer may undergo this unmixing process leading to the formation of the separated

domains such as:

$$\Delta\bar{G}_{\text{mix}} = \Delta\bar{H}_{\text{mix}} - T\Delta\bar{S}_{\text{mix}} \tag{1.5}$$

Both the mixing entropy and enthalpy are not constant, but may change depending on the temperature of the system (Fig. 1.6A) and the interaction parameter (Fig. 1.6B), respectively [74]. This leads to the final $\Delta G_{mix}$ of the system which changes according to the specific environmental conditions the bilayer is subjected to (Fig. 1.6C). At high temperatures, the entropic contribution favours the bilayer mixing, whereas at low temperatures the enthalpic term promotes phase separation.

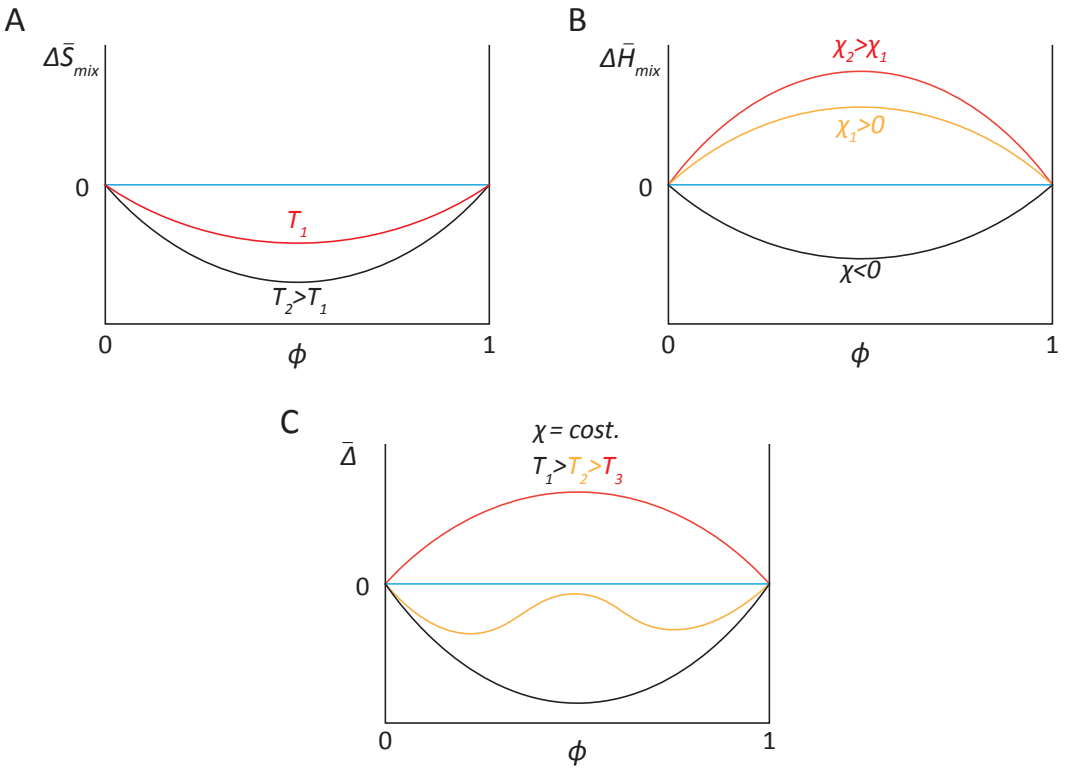


Figure 1.6: Thermodynamics of phase separation. In a relatively simple still effective model, the free energy of the system, $\Delta G$, results from two main contributions: entropy and enthalpy. Both entropy (A) and enthalpy (B) depend on the specific experimental conditions, the former being primarily influenced by the temperature and the latter by the interaction parameter of the observed system. The variations in entropy and enthalpy results in $\Delta G$ (C) also changing as a function of the temperature (as proposed in this example) or the interaction parameter. At high temperatures ($T_1$), the system remains mixed, whereas at low temperatures ($T_2$ and $T_3$) the unmixing occurs.

For the model of a binary lipid system, we can therefore propose a binary phase diagram that underlies these thermodynamic concepts (Fig. 1.7A) [142, 145, 146, 152]. Above a critical temperature ($T_c$), the components are perfectly miscible

forming a unique phase ($\alpha_0$) with the system free energy being dominated by the entropic term. This system however exhibits a miscibility gap in their phase evolution; in other words, at specific temperatures and concentrations, the components are not miscible and separate into distinct phases ($\alpha_1$ and $\alpha_2$). By decreasing the temperature of the system, molecular interactions dominate over the entropic term, favouring the unmixing and thus leading to the miscibility gap (Fig. 1.7B). This scenario is experimentally relevant when studying cellular membranes. Cells adapt their membrane composition to the environmental conditions, maintaining constant their physical properties [153–155]. For example, *E. coli* cells present critical temperatures, also known as melting temperatures, which are close to the temperature at which they are grown [49, 153, 156]. This leads to membranes being in a delicate equilibrium, where small fluctuations can easily tip the balance between entropy-dominated state or enthalpy-dominated ones. This unstable equilibrium of the plasma membrane is at the base of the dynamics for lipid raft formation in native conditions. Graphically, the miscibility gap can be represented as the binary mixture passing through the phase boundary (also known as binodal curve). In this area of the diagram, the formation of the 2 phases follows a nucleation-and-growth process when the systems is in between the binodal and the spinodal curve, whereas it follows a spinodal decomposition if the composition of the binary mixture falls within the spinodal curve [157].

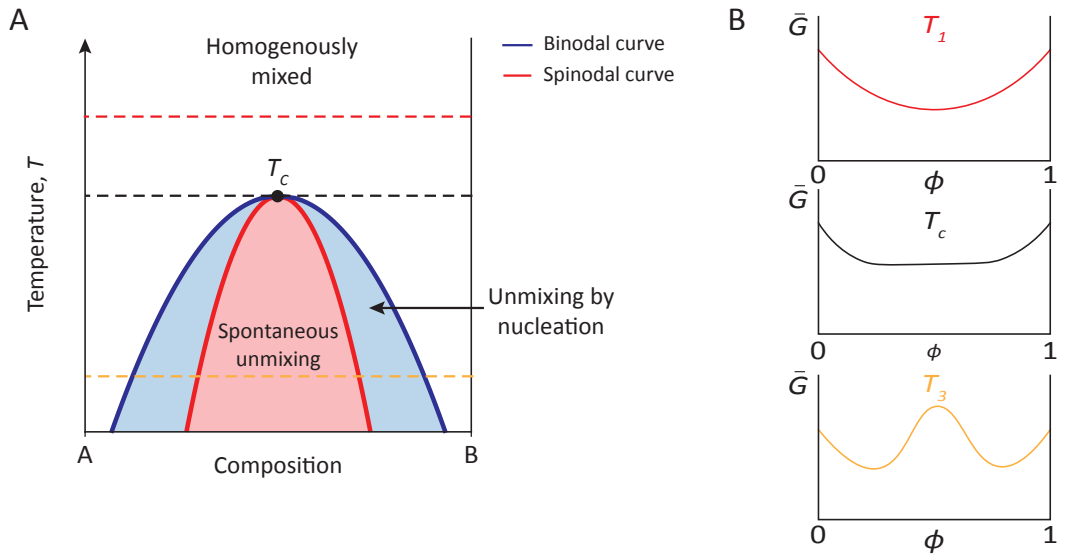


Figure 1.7: Phase diagram of simple binary mixture presenting a miscibility gap. Above the $T_c$ (which can also be referred to as $T_m$ for our case), the mixture behaves homogenously presenting a unique phase $\alpha_0$ with components A and B perfectly miscible. Once the temperature is decreased below $T_c$, a phase separation occurs leading to the formation of two different phases $\alpha_1$ and $\alpha_2$ as the system pass through the binodal curve. Within this area where the two phases coexist, another region can be found which is delimited by the spinodal curve. Depending on whether the mixture falls within this space, the phase separation process takes place with two different molecular mechanisms: nucleation-and-growth (area highlighted in blue background on the diagram) and spinodal decomposition (area highlighted in red on the diagram). (B) Examples of how the free Gibbs energy changes at different temperatures. Gradually from the upper to the lower case, the contribution of entropy decreases with decreasing temperature, leading to a different scenario where the perfectly mixed solution is not favourable anymore. The turning point is represented by $T_c$, which is an intrinsic and unique property of the system.

### 1.4.4 Mechanisms behind lipid domain's formation

This section explores the key theoretical features of the two main mechanisms that drive bilayer's unmixing: nucleation and growth and spinodal decomposition. These mechanisms differ in how and when phase domains emerge and expand within the membrane. Understanding these processes provides insight into how lipid membranes self-organise and how distinct phases arise under different conditions, ultimately contributing to the complex behaviour observed in cellular membranes. This discussion provides a foundational framework for interpreting aspects of my findings, particularly those presented in Chapter 4.

***Nucleation-and-growth***

Considering the example of a composition $X_1$ (Fig. 1.8A), once the material is slowly cooled under equilibrium conditions below $T_c$ (at a temperature that we will refer to as $T_2$), it enters within the binodal curve space of the phase diagram. While the temperature-composition phase diagram provides a practical macroscopic view of the phase stability, a deeper understanding of the unmixing of the system requires the analysis of the system's Gibbs free energy, which allows understanding the microscopic forces driving the phenomenon [158]. Therefore, the temperature-composition phase diagram can be viewed as a projection of the underlying $G$ at the specific temperature $T_2$ (Fig. 1.8B), which has a fluctuating behaviour as a function of the composition with two local minima in correspondence to the boundary between the binodal region and the homogeneous region. As the system $X_1$ crosses the binodal curve because of the cooling of the temperature, $G$ begins to change, placing it in an energetically metastable region. In this region of the phase diagram, the mixture is energetically trapped in the local minimum, meaning that small fluctuations in the concentration of the components are not sufficient to drive the system towards the phase separation. The system remains mixed because the free energy does not spontaneously decrease with these minor fluctuations. In this context, the first derivative of the free energy with respect to the composition ($dG(x)/dx$) becomes particularly important. This derivative describes the chemical potential ($\mu(x)$) of the components within the mixture, which represents the change in free energy with these small fluctuations. In this metastable region, $\mu(x)$ is uniform throughout the system and fluctuations do not lower the free energy, hence no spontaneous phase separation occurs. This uniformity of chemical potential reflects that the system is in a local minimum, where an energetic barrier must be overcome to start the phase separation. This barrier is described by the difference between the local free energy of the system at composition $X_1$ ($G_{X_1}$) and the free energy at the equilibrium ($G_{eq}$), where the system would naturally separate:

$$\Delta G_{nuc} = G_{X_1} - G_{eq} \tag{1.6}$$

Overcoming this barrier requires an energy input (nucleation energy $\Delta G$), which would initiate the phase separation through the nucleation-and-growth mechanism ($\Delta G_{nuc}$) [159]. This energy input allows initiating the first step of this

process (nucleation), where the system is perturbed, allowing the local clustering of molecules forming the so-called nuclei [160–162]. For these nuclei to grow and allow the continuation of the phase separation, they need to reach a critical size ($R_c$), which is described as:

$$R_c = \frac{2\gamma}{\Delta G_v} \tag{1.7}$$

where $\gamma$ is the interfacial energy between the two phases and $\Delta G_v$ is the Gibbs free energy per unit volume between the metastable and the new phase. The main energetic requirement behind the energetic barrier of this phase separation is the interfacial energy, $\gamma$. The formation of a new phase requires the creation of stable and sharp interfaces, which are proportional to the surface of the nuclei: the larger the surface area of the nucleus, the higher the energetic cost of their formations [162, 163]. Considering the predominant role of the interfacial energy, $\Delta G_{nuc}$ can be viewed as simply the energetic costs of creating an interface between the two newly formed phases, one enriched in A and the other one enriched in B. The whole process is favourable when $\Delta G_v$ becomes greater than the cost of the interface formation. When a nucleus smaller of $R_c$ is formed, it dissolves back into the homogeneous phase as it increases the free energy of the system. The phase separation can continue with the growth phase just when nuclei of $R_c$ dimensions are formed; this process, is described by means of the nucleation rate ($I$) [162]:

$$I = I_0 \exp\left(-\frac{\Delta G_{\text{nuc}}}{k_B T}\right) \tag{1.8}$$

where $I_0$ is a pre-exponential factor, $k_B$ is the Boltzmann's constant and $T$ the temperature. This nucleation rate is thus susceptible to $T$ and $\Delta G_{nuc}$ (Eq. 1.8). Lowering $T$ thus increases the nucleation rate, favouring the separation; at the same time, a lower temperature reduces also the thermal energy of the molecules and their mobility. Therefore, nucleation has an optimal temperature range in which these two opposite phenomena are balanced. On the other hand, $\Delta G_{nuc}$ is an intrinsic property of the system, but it can change by specific sites throughout the system such as defects or impurities [164], which locally lower the energetic barrier.

Finally, once the nuclei are formed, the growth can spontaneously start. Here, other molecules can diffuse and join the new phase following a downhill diffusion. This diffusion is characterised by the movement of the components following a concentration gradient. This diffusion drives the system closer to the equilibrium condition, reducing its free energy by approaching the local minima where $\mu(x) = 0$. This diffusion-controlled growth can be described as:

$$\chi = \frac{D}{\delta_i} \tag{1.9}$$

where $\chi$ is the growth rate, $D$ the diffusion coefficient and $\delta_i$ the length scale of the new phase. Although the growth is rapid at the beginning, it will eventually slow down due to the increase size of the new phase and the reaching of its equilibrium condition. Other growth-related phenomena may also occur such as coarsening of the nuclei, the so-called Ostwald ripening [165, 166]. Within the latter stages, smaller nuclei might dissolve in favour of the larger ones. This process has been previously described by the Lifshitz-Slyozov-Wagner (LSW) theory [167]. This theory predicts that the increase in domain size of the new phase would increase over time: $R(t) \propto t^{1/3}$, where $R$ is the radius and $t$ is time. This relationship has been confirmed through multiple studies [157, 165, 166, 168] and shows that bigger domains grow at the expense of small ones. The growth thus continues until equilibrium is reached with the final phase's morphology, which will depend on $\chi$, $\gamma$ and in general on the environmental conditions. For example, lower $\gamma$ indicates a less unfavourable interaction between the two phases, leading to an increase in the surface at the interface.

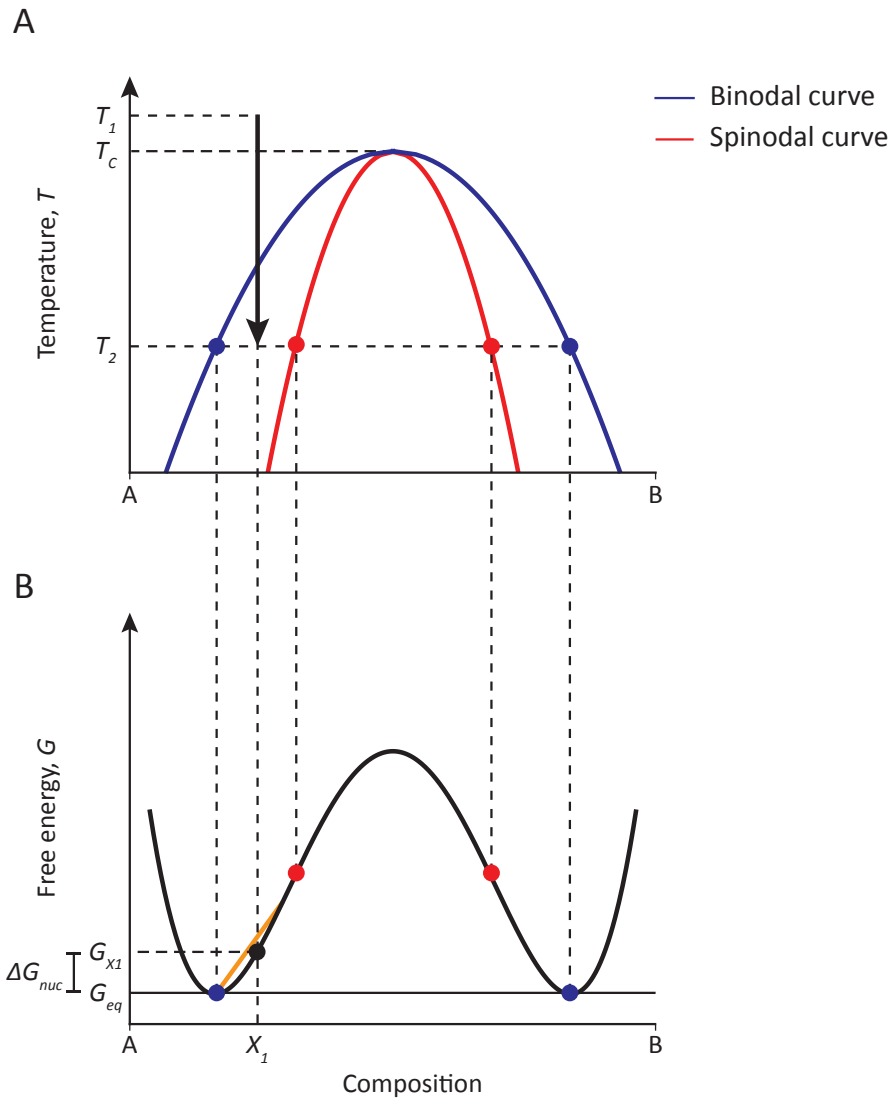


Figure 1.8: Phase separation occurring through nucleation-and-growth illustrated through phase diagrams. (A) Temperature against composition phase diagram where mixture $X_1$ is cooled below the $T_c$ at temperature $T_2$, entering the binodal space but staying outside of the spinodal curve. (B) Free energy diagram of mixture $X_1$ at $T_2$. Local composition fluctuations around the $G_{X_1}$ do not decrease the free energy of the system, rather increase it on average as showed by the orange line. This leads the system in a metastable condition, where the free energy cannot be minimised spontaneously. To reach $G_{eq}$, an external energy must be provided to the system in order to force the phase separation to occur and start the nucleation of the new phase.

### *Spinodal decomposition*

To address the spinodal decomposition case, we shall now consider the example of a second composition ($X_2$), where the system under cooling falls within the spinodal region (Fig. 1.9A). This region is delimited in the free energy phase diagram by two inflection points, which corresponds to the onset of the instability in the system. At the inflection points, the free energy with respect to composition

is zero, therefore [169, 170]:

$$\frac{d^2G(x)}{dx^2} = 0 \tag{1.10}$$

At these inflection points, not only the second derivative is zero, but the first derivative is also 0. This implies that the chemical potential is uniform across the system. Within the spinodal curve, the first derivative continues to be zero, but most importantly, the second derivative is negative, indicating the system instability to any small fluctuations. Although $G$ of the system ($G_{X_2}$) is significantly higher than $G_{eq}$ ($G_{X_2} >> G_{eq}$), small local fluctuations of the composition lower the free energy, gradually leading it towards the $G_{eq}$ and causing the phase separation of the system through a spinodal decomposition (Fig. 1.9B) [169–172]. This uniform chemical potential, coupled with the negative second derivative is behind the instability of the system which is hence more prone to the phase separation. The phase separation is thus spontaneous, rapid, does not require the formation of any nuclei and does not present well-defined and sharp interfaces between the two phases; these two phases instead are dynamic and rearrange overtime [159]. The components will follow an uphill diffusion, where counter intuitively each component diffuses from a region of lower concentration to a region of higher concentration to minimise the free energy, going against the concentration gradient. This uphill diffusion of the spinodal decomposition causes the formation of the new phases; their growth can be mathematically described through the Cahn-Hilliard equation [161, 173]:

$$\frac{\partial c}{\partial t} = \nabla \left( M \nabla \left( \frac{\partial G}{\partial c} \right) \right) \tag{1.11}$$

where $c$ is the concentration of one component, $M$ is the mobility of the components, and $\partial G/\partial c$ describes the variation of free energy as a function of the concentration. This equation describes the evolving of the concentration distribution over time, considering the nonlinear effects in spinodal decomposition. Although this equation is valid for the simple modelling of the spinodal phenomenon, parameters such as $M$ can be not necessarily constant throughout time; due to the different mechanism behind the diffusion of molecules, the temporal evolution of the phases cannot be simply modelled

with the LSW theory [167]. This means that the relationship between the size of the domains with time does not necessarily follow the growth exponent of 1/3 as previously seen. Experimental and theoretical approaches found different relationships [174–176] which seem to be dependent on the system properties, i.e. viscosity. In many systems there can be a crossover between growth exponents during the coarsening, leading to completely different early and latter stages of the domain's growth [174]. Negative growth exponents have also been found meaning a reduction of the new phase over time; this evolution can be linked to dynamic instabilities within the system (e.g. local compositional fluctuations) and competition between different diffusion mechanisms. Previous studies by Tanaka [176, 177] investigated the phenomenon of double phase separation in two-dimensional binary fluids. These works demonstrated that multiple growth exponents can arise during the rapid quenching of 2D fluid systems, leading to regimes where newly formed domains shrink. This behaviour results from the interplay between the fluidity of the mixture and the speed of the quenching process: separated liquid domains initially form through hydrodynamic processes, but due to the limited diffusivity of the components, their formation precedes the attainment of system equilibrium. Consequently, a secondary spinodal decomposition occurs within the domains, causing them to shrink and reducing the overall characteristic length scale of the system [174]. This intriguing phenomenon highlights the complexity of spinodal decomposition and its sensitivity to experimental parameters, such as the fluidity of the mixture.

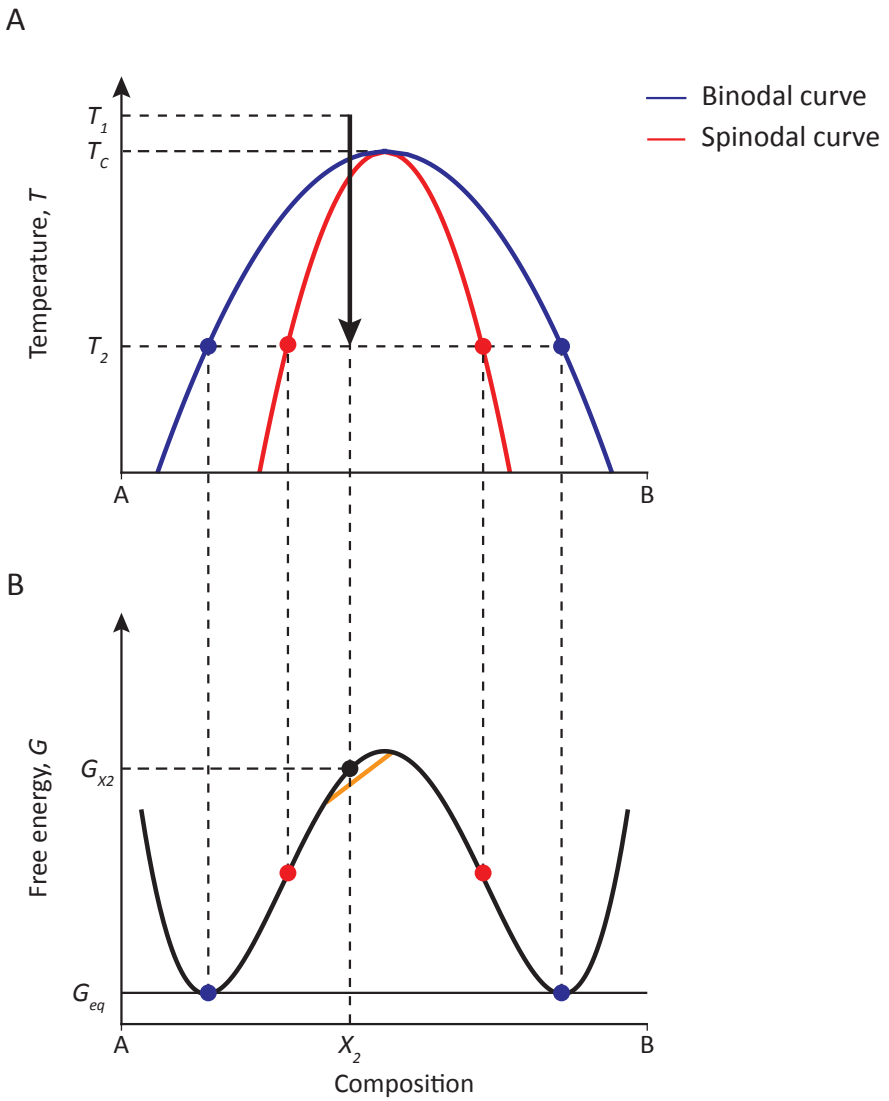


Figure 1.9: Phase separation occurring through spinodal decomposition illustrated through phase diagrams. (A) Temperature against composition phase diagram where mixture $X_2$ is cooled below the $T_c$ at temperature $T_2$, entering the spinodal space. (B) Free energy diagram of mixture $X_2$ at $T_2$. In this case, the local composition fluctuations will lower the free energy, spontaneously leading the system from $G_{X_2}$ to $G_{eq}$ and causing the phase separation. This process being spontaneous, energy input is not required for the formation of the two new phases $\alpha_1$ and $\alpha_2$.

In summary, these two mechanisms are fundamentally different and present crucial differences [159, 162, 170]:

- Driving force: while in the nucleation-and-growth presents an energetic barrier must be overcome, spinodal decomposition happens spontaneously without nucleation-needed due to the system's instability.
- Interface formation: nucleation-and-growth is characterised by the formation of sharp interfaces between the two new phases, whereas spinodal

decomposition involves continuous and dynamic interfaces that evolve dynamically.

- Diffusion mechanisms: nucleation-and-growth presents a downhill diffusion which follows the concentration gradient, while the diffusion in the spinodal decomposition is uphill, indicating that the components move against the gradient.

- Growth dynamics: the growth of the nuclei can be modelled by LSW theory following a growth exponent of 1/3 [165, 167], whereas the new phase in the spinodal decomposition evolves with a more complex and dynamic behaviour without displaying a single growth exponent [174].

Understanding this difference is fundamental, as depending on the mechanism involved, the newly formed phase presents intrinsic different compositional and physical properties. Studying the phase separation of different systems allows to predict the local and global mechanical or functional behaviour of a given material, which is indeed crucial for the case of biological membranes. For example, when lateral or out-of-plane forces are applied on the membrane, the cell must be able to sense and react against them to survive, suggesting the importance of the membrane's mechanics in this context. The presence or absence of these domains and the mechanisms behind their formation can be crucial to determine the ability to the cell to propagate this signal and survive. In this next section, I will discuss in depth the importance of sensing mechanical stimuli and the fundamental concepts behind membrane's mechanics, elucidating how it is possible to model and evaluate the mechanical profile of the membrane.

## 1.5 Mechanical properties of cell membranes

### 1.5.1 Mechanical stimuli and responses

All cells, from bacteria to eukaryotic ones, must sense and respond to mechanical forces such as shear forces, perpendicular compression or stretching, either due to external agents or arising from the intracellular molecules or cytoskeleton elements (Fig. 1.10). For example, blood cells experience compression by passing

through tight spaces within capillaries [178](Fig. 1.10A), endothelial cells need to resist to shear stress generated by the blood flow [179] (Fig. 1.10B); as a further example, any cell may experience tensile forces during their cell division [180] (Fig. 1.10C). Additional mechanical stimuli cells may be subject to include also changes in the osmotic pressure [181] (Fig. 1.10D) and pulling/stretching generated by their active cytoskeleton architecture [182] (Fig. 1.10E). Although these examples mainly focus on eukaryotic systems, prokaryotes also experience mechanical stimuli throughout their whole life cycle, for example during cell division, adhesion to external surfaces and locomotion [180, 183–185]. When sensing and processing these stimuli, membrane plays a crucial role [186] and has to collaborate with various structural components, mainly the cytoskeleton [182, 187] or the cell wall [188] depending on wheatear the cell is eukaryotic or prokaryotic. The phospholipid bilayer has a primary role in modifying its structure in response to external stimuli and then propagating signals by means of membrane proteins [189–192]. Within the membrane, a variety of membrane proteins and complexes are in charge of sensing and responding to these forces to allow cell survival, proliferation and migration. MSCs [189] and Piezo channels [193] are representative classes of proteins acting as such. Lipid mobility is a key element not only influencing the response of the membrane favouring the activation of specific proteins, but also directly allowing the membrane to deform thus relaxing an applied shear or force [76, 192]. Thanks to an intense field of research [194–199] the membrane's mechanics can be now captured by relatively a simple mathematical model. This interpretation also allows to experimentally estimate the physical properties of lipid membranes, which have been widely used [121, 200, 201]. By experimentally stretching and compressing membranes, it is possible to interpret their physical properties and compare it to others in different conditions, making these experiments valuable for any membrane-related studies. The next section will analyse the key aspects of this model.

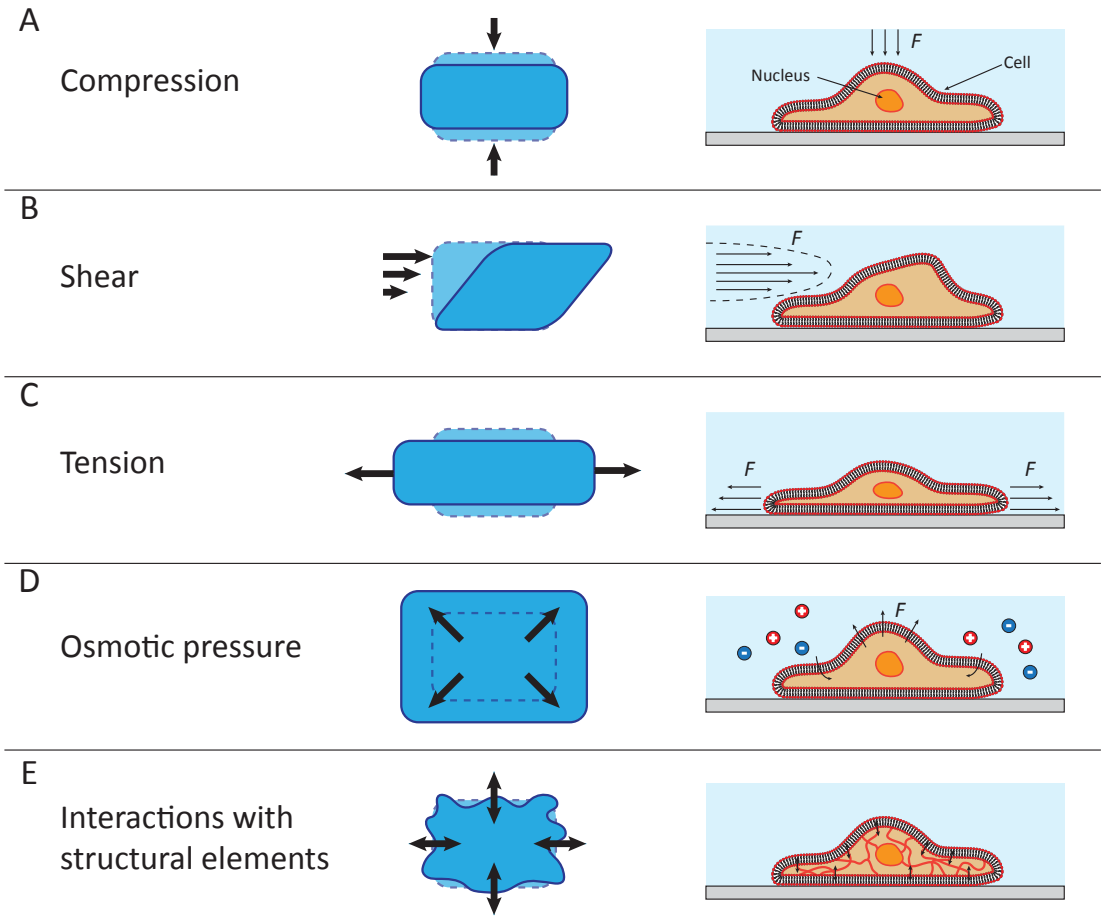


Figure 1.10: Illustration of various mechanical stimuli that can be experienced by cells and their plasma membranes. Cells are generally in contact with crowded and complex surroundings, exposing their membranes to external mechanical stimuli. It is thus fundamental for the cell to perceive these stimuli and react against them to survive. Stimuli may range from compression (A) and shear (B) to tension (C). Other types of stimuli cells are subject to include the expansion due to an osmotic stress (D) or the pulling due to the contact with structural elements such as cytoskeleton filaments (E).

### 1.5.2 Theoretical models and experimental techniques

When dealing with bodies deformed by external forces, the fundamental thermodynamics equation is:

$$dU = TdS + \sigma_{i,k} du_{i,k} \tag{1.12}$$

where $U$ is the internal energy, $T$ is the temperature, $S$ is the entropy of the system and $\sigma_{i,k} du_{i,k}$ is the mechanical work done by the internal stresses composed by $u$ the strain tensor, and $\sigma$ that is the stress tensor. It is often useful to express this relationship from the point of view of the Helmholtz free energy ($F$):

$$F = -SdT + \sigma_{i,k} du_{i,k} \tag{1.13}$$

As deformations generally occurs at constant temperature ($dT$=0), free energy just depends on the mechanical work done through stress and strain [202].
Focusing on small deformations allows the expansion of the free energy in powers of $u_{i,k}$. Assuming also an isotropic system, the undeformed state of the system ($u_{i,k}$=0) corresponds to the body without any internal stress ($\sigma_{i,k}$=0) with a constant free energy in the undeformed state, $F_0$ [202]. Expanding the free energy as a function of the strain tensor, and given the scalar nature of the free energy, two independent scalars for the strain tensor can be obtained, leading to [203]:

$$F = F_0 + \frac{1}{2}\lambda u_{i,k}^2 + \mu u_{i,k} \tag{1.14}$$

where $\lambda$ and $\mu$ are the Lamé's first and second parameter, respectively. The first term (containing $\lambda$) describes the energy stored in the material due to a change in volume, whereas the second term (containing $\mu$) describes the energy stored because of shape changes upon shear or distortion.
Although lipid membranes do not strictly conform to the assumptions of isotropic materials, classic elastic theory still offers a useful macroscopic description of their behaviour [194, 202]. Works by Helfrich [204], Canham [198], and Evans [199] have demonstrated that these theories are valid to lipid systems. Experimentally, this macroscopic approach has been extended and validated [195, 200, 205, 206]. At the microscopic level, certain key phenomena contribute to the macroscopic free energy of lipid bilayers:

- Fluidity: lipid molecules are highly dynamic and diffuse laterally along the membrane. Since they can pass each other, but not easily escape from the membrane, the energy functional must exclude in-plane shear stress, which is negligible in the fluid state of the bilayer [194].

- Stretching: altering the area per lipid molecule is a valid form of deformation and results into an energy cost. However, according to thin-plate theory, the energy associated with bending deformations (curvature changes) is typically smaller than the energy required for

stretching. Therefore, bending modes are generally more energetically favourable and are the primary deformation considered when analysing membrane behaviour, particularly for smaller vesicles or thin membranes.

- Tilting: lipids in the membrane can tilt relatively to the normal of the bilayer, which introduces an additional degree of freedom. This phenomenon is important in cases where topological changes occur in the membrane [207].

- Bilayer: in a bilayer system, the two leaflets are free to slide past each other, meaning that tangential stress between the leaflets does not contribute to the mechanical energy. However, if lipids do not easily flip between the two leaflets (i.e., they do not exchange between the inner and outer layers), this creates a constraint. This conserved quantity couples to the large-scale Hamiltonian, affecting the overall mechanical properties of the membrane.

Stretching and bending being the two most crucial deformations for the membrane, the next sections will focus on them and on the membrane's response.

***Stretching (in-plane) mechanics***

The physical model of stretching is generally more energetically relevant for vesicles and cells with relatively large sizes (>300 $nm$), as the membrane is commonly modelled as a thin shell on the order of few $\mu m$ with minimal curvature effects [197]. When considering a flat membrane of initial area, $A_0$, its isotropic stretching into a greater area $A$ (with $A > A_0$) leads to an increase in energy, expressed as:

$$E = \frac{1}{2} K_a \frac{(A - A_0)^2}{A_0} = \frac{1}{2} K_a A_0 u^2 \tag{1.15}$$

where $u$ is the area strain and $K_a$ is the area expansion modulus or stretching modulus. The resulting stress ($\Sigma_s$) is not constant, but changes linearly with $u$:

$$\Sigma_s = \frac{\partial E}{\partial A} = K_a u = K_a \frac{dA}{A_0} \tag{1.16}$$

This linear stress-strain relationship holds true until the membrane reaches the

point of rupture [205]. Although membrane rupture is traditionally treated as a material constant, this effectively depends on the loading rate applied. Under slow loading rates, the membrane ruptures at relatively small strains, as small holes are formed through a classic nucleation process. At faster rates, the membrane enters a high-strength regime of rupture due to an intermediate nucleation state [205]. The presence of these 2 regimes breaks the linear relationship previously seen (Eq. 1.16). However, by assuming the entropic contribution of the membrane on the free energy being negligible and the linear-stress relationship being maintained at slow loading rates, Eq. 1.15 allows calculating $K_a$ of the membrane [194]. Numerous experimental approaches have been indeed developed to estimate $K_a$, using for example osmotic stretching coupled with light-based techniques to track vesicle's deformation [197, 206, 208], or micropipette aspiration techniques [195, 200, 209]. By considering the linear relationship between the stress applied and the deformation of the membrane, it is possible to estimate the $K_a$ of the membrane, which has been generally found to be around 240 mN/m for artificial vesicle's systems [194].

***Bending (out-of-plane) mechanics***

Although stretching is more important when it comes to cells, the effect of bending cannot be neglected when working with smaller membrane systems (<200 $nm$) [197]. Thanks to the work of Helfrich [204], we know that:

$$F = \frac{1}{2}k(2H - C_o) + \bar{k}aK_G \tag{1.17}$$

where $k$ is the bending modulus, $H$ is the mean curvature, $C_o$ is the spontaneous curvature in absence of external forces, $\bar{k}$ is the Gaussian curvature modulus and $K_G$ the Gaussian curvature. This equation describes how the bending energy (related to the curvature of the membrane) dominates in the case of relatively small systems such as small vesicles. The bending modulus $k$ describes how resistant a membrane is upon bending, therefore the energy required to change its curvature. This is intuitively more important for smaller vesicles, where curvature is more pronounced. On the other hand, the Gaussian curvature $\bar{k}$ is associated with topological changes of the membrane such as fusion, fission and pore formation processes [194, 210]. Although these processes are biologically relevant, they are challenging to recreate experimentally with vesicles. This is

because due to closed structure of the vesicles, this term is often constant, thus not impacting the final energy.
The impact of the Gaussian curvature on the overall physical properties of the plasma membrane is however minimal, with $K_a$ dominating the evolution of the system.

***Elastic modulus and theory for a lipid membrane***

Building on the theoretical description of stretching and bending, we can expand our understanding of the mechanical properties of the membrane by using the Landau and Lifshitz elastic theory [167]. Both stretching and bending can be quantified and linked to the elastic response of the membrane upon stress, expressed with the Young's modulus ($Y$). By applying the Landau and Lifshitz elastic theory to the simplest case of a thin plate with thickness d, an intrinsic Young's modulus and a Poisson ratio ($v$), we obtain:

$$K_a = \frac{Yd}{2(1-v)} \tag{1.18}$$

The factor 2 here arises because the isotropic area strain is two times greater than the linear stain to which $Y$ typically refers. The Poisson ratio-correction accounts for the membrane's lateral deformation upon stress. This same model also predicts for a single leaflet:

$$k = \frac{Yd^3}{12(1-v^2)} \tag{1.19}$$

$$\bar{k} = \frac{Yd^3}{12(1+v)} \tag{1.20}$$

However, biological membranes consist of two interacting leaflets, each of thickness $d/2$. Due to the fluid nature of membranes, the leaflets can slide relative to each other, preventing the transmission of tangential stress. Therefore, the bending modulus for the entire membrane can be expressed as:

$$k = \frac{K_a d^2}{24(1+v)} \tag{1.21}$$

Real membranes however behave as two-dimensional fluids rather than solid structures. This adds another layer of complexity to modelling their physical properties, as the fluidity influences both bending and stretching behaviour [202]. Experimentally accessing $K_a$, $Y$ and $k$ is challenging. Techniques with high precision and accuracy are required due to the need of accurately regulate the loading rate, or the highest tension applied to the membrane. Recent advances in the last decades have improved our ability to measure mechanical properties of biological membrane, thanks to techniques such as AFM [121, 201] or the previously seen micropipette aspiration approaches [200]. However, mechanical testing of plasma membrane can be challenging when working directly with alive cells. Cells are highly complex and sub compartmented systems; it is thus hard to untangle the independent behaviour of the plasma membrane from the intercellular surroundings. To overcome this, micropipette aspiration and AFM have been vastly applied to membrane model systems, which artificially recreate the plasma membrane structure and allow the characterisation of the physical behaviour of the bilayer.

## 1.6 Model membrane systems

As extensively investigated in the previous paragraphs, membranes are highly complex systems due to their composition, morphology and dynamic ability to rearrange within short timescales. The complexity of these systems represents a challenging problem to overcome when dealing with biological questions around the plasma membrane. To solve this problem, model membranes that retain the essential lipid bilayer structure but simplify the system have been created, so that the role of individual components can be assessed, and their organisation and dynamics can be visualised [211–215]. By artificially preparing these models, membrane's composition can be tuned according to the membrane to be mimicked and the specific aim of the research. Each membrane presents a specific and highly conserved lipid composition, which is crucially linked with its overall function. When preparing a model membrane, it is important to understand the characteristics of the reference plasma membrane and design the model according to these properties. Lipidomic studies on plasma membrane prove useful to this need, as they allow picturing of these properties such as the most common

phospholipid classes or the average length of the lipid chains. This information helps developing the ideal minimalistic model for the purpose. In this context, ternary lipid systems have represented an ideal system as they offer a balance between complexity and simplicity, mimicking biological membranes while still being experimentally manageable [101, 216].

Multiple model membrane systems have been developed over the past decades and each of them presents unique characteristics depending on the biological structure or function under investigation [217–220]. Models include bulk vesicles such as giant unilamellar vesicles (GUVs) [109, 117, 221, 222], supported lipid bilayers (SLBs) [223–226], lipid nanodiscs systems [227] and also computational models [149, 213, 220]. Most of these models have found great success because of their versatility and ease of use when combined with experimental techniques such as microscopy [214, 228], Raman spectroscopy [222], and also AFM [229]. Among all these models, GUVs and SLBs are particularly popular [75, 98, 99, 109, 117, 221–226, 230, 231] for their contribution to unravelling some basic mechanisms behind different biological processes, such as rafts formation and membrane protein function.

### 1.6.1 Giant unilamellar veiscles

GUVs are large single-membrane vesicles, whose strength mainly relies on their micron-size diameter. This results in them being ideal to study membrane's behaviour. GUVs are studied under most of the microscopy techniques including light microscopy, thus offering a versatile platform. Their dimension is also helpful for the functional reconstitution of membrane proteins within these models and the study of their activity outside of the complex native environment [232, 233]. Although GUVs are highly versatile models, they also present some challenges. First, GUVs are fragile systems, which can be sensitive to any variation in osmotic pressure [234] or temperature [235] as their stability is granted only by the lipid bilayer structure. Secondly, GUVs preparation is commonly performed via electroformation [236], which requires specialised equipment. GUVs formation is also not applicable to all lipid mixtures [237] as lipid properties such as their packing parameter, charge or phase properties can significantly impact the degree of curvature and the stability of the final vesicle. Novel types of GUVs have been recently developedto overcome these limitations such as tethered systems [238].

### 1.6.2 Supported lipid bilayer systems

The very first successful attempt of preparing a bilayer on a planar surface was performed by Tamm and McConnell in 1985, which led to the birth of the SLB systems [239]. SLBs are a two-dimensional thin film coatings composed of a phospholipid bilayer, conformally suspended on top of an underlying solid surface [240] (Fig. 1.11). SLBs are produced in multiple ways including spin coating [241], Langmuir-Blodgett method [239] and the solvent-assisted lipid bilayer formation (SALB) [242] according to the surface employed. Direct lipid vesicle fusion over the solid substrate is however the most common methods due to its ease of use [243]. The method is based on the spontaneous rupture and adsorption of lipid vesicles on top of a hydrophilic surface such as mica or silica. Thanks to the attractive interactions with the surface (van der Waals and electrostatic if the lipids are charged) and to the high bending curvature of the vesicles, they are spontaneously adsorbed forming a bilayer on top of the substrate. The full mechanism behind their adsorption is however still poorly understood [244–248]. For example, the process that allows vesicle's breaking when in contact with the surface has not been clearly elucidated as AFM, theoretical predictions and quartz crystal microbalance resonant frequency and dissipation (QCM-D) approaches have shown contradictory results [249–251]. Alongside being a relatively simple preparation method to perform , the technique offers the opportunity to experimentally testing the effect of increasing incubation time and temperature using divalent anions or working at higher lipid concentrations[252]. This allows exploring and simulating different environmental conditions for the model system.

Key advantages of using SLBs as a model system include the use of a planar substrate. The substrate offers mechanical stability to the bilayer, ensuring reproducible formation and stable experimental conditions across trials. This stability enables SLBs to be paired with surface-sensitive analytical techniques, such as surface plasmon resonance (SPR) [253], QCM-D [251, 254], and AFM [75, 225, 229, 255]. Among these techniques, AFM has been fundamental for my thesis project. Due to its nanoscale resolution and sensitivity to surface characteristics, AFM enables detailed observations of membrane topography and mechanical properties. A deep historical and technical description of AFM's application will be provided in Chapter 2.

Interstingly, the lipids inside the SLB still retain a degree of lateral mobility. Thanks to NMR and X-ray observations [256], SLBs have been shown not to directly interact with substrates, but to float on top of it thanks to the presence of an adsorbed thin water layer ($<2\ nm$) (Fig. 1.11B). This allows the application of SLBs for studying lipid's dynamics within the membrane and also to reconstitute functional proteins in them. Finally, by changing the properties of the surface, SLBs allow exploring how interactions with different surrounding environments influence the membrane's structure and dynamics [257]. Multiple surfaces have been employed for SLB formation [257, 258], which allowed to observe how the surrounding and external contacts can severely affect membrane properties. Native membranes tend in general to be in close contact with structural filaments of different nature both from the intracellular space and from the connective tissues. These interactions may drastically change membrane's properties possibly influencing its phase separation [259]. By changing or functionalising the surface with specific patterns or chemical groups, it is possible thus to mimic the effect of these interactions, something that is precluded when using other lipid model systems.

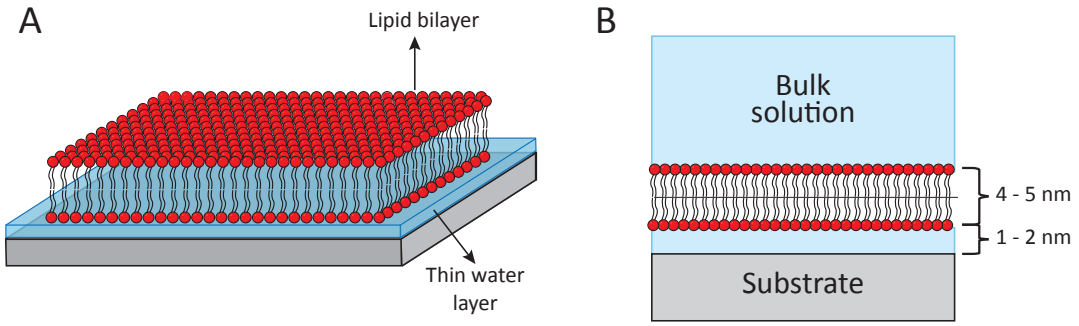


Figure 1.11: Schematic representation of SLB's structure. (A) A planar bilayer is formed on top of hydrophilic surfaces, which stabilise the lipid bilayer structure increasing its lifetime. Despite substrate-bilayer interactions, SLBs still maintain a dynamic behaviour, similar to the one of the native plasma membranes; this is thanks to the presence of a thin water layer (1-2 nm) [256] between the substrate and the bilayer as shown in (B). The adsorbed water layer provides also some space for the insertion of membrane proteins and other large marcomolecules with an intracellular-domain.

## 1.7 Open questions and purpose of the thesis

From its complex composition to its multifunctional role, it is not surprising that membranes represent one of the most interesting, but challenging systems to study in cellular biology. In this context, the unsolved questions around the nature of lipid domains in plasma membranes are multiple, from their role to the mechanisms behind their formation. The combination of model membrane systems and highly developed equipment has allowed to enhance our understanding of these structures. Nonetheless, more studies are still required to fully uncover the true nature of these dynamic systems. By fully capturing the complex nature of these domains and their role in the membrane, it would be possible to predict their effect on the native context such as the modulation of the cell's mechanical properties, the localisation of a specific protein complex, but also understand how to manipulate this phenomenon to our advantage by controlling the phase separation. Overall, a full comprehension of this phenomenon would enhance our understanding of plasma membrane's function.

The aim of this thesis is to investigate the phase separation of lipid membranes. In particular, the molecular mechanisms behind this segregation and how external factors modulate this phenomenon, but also the function of these phase separated domains and their interactions with external marcomolecules given their different mechanical and compositional properties. These investigations have been performed mainly in a newly designed model membrane system which mimics *E. coli*'s inner membrane with the aim of establishing for the first time a robust and potentially globally acknowledged model system for bacterial cells and more generally for biological studies on cell membranes. Here, a quick overview of the content of this thesis:

Chapter 2 -– Methods will focus on the main experimental techniques that have been used in my PhD work. This Chapter will highlight the key features and operational modes of Atomic Force Microscopy with some theoretical and practical explanation on how this technique can be employed for the studying and characterisation of soft biological samples such as lipid bilayers. I will then move to the explanation of Differential Scanning Calorimetry and Dynamic Light Scattering when applied to the thermodynamic and mechanical characterisation of lipid systems.

Chapter 3 – Designing of a minimalistic model membrane system for *E. coli*'s inner membrane. In this first results Chapter, I will show the development of an ideal model membrane system that mimics the compositional, thermodynamic and mechanical properties of an *E. coli*'s inner membrane. After reviewing the specific composition of this membrane thanks to previous lipidomic studies, I will then probe a series of candidate binary and ternary lipid mixtures and compare their characteristics to more complicated mixtures directly extracted from *E. coli* cells. The design and development of this model provides a fundamental platform for the next Chapter and further studies.

Chapter 4 – Substrate-induced molecular reorganisation in supported lipid membranes. This Chapter focuses on the phase separation properties of SLBs compared to free standing vesicle systems made by the simplest binary *E. coli*-like model membrane. As these 2 models only diverge in the presence or absence of an external contact with a substrate, the results show the impact of external structural elements on the phase separation properties, highlighting their ability to significantly regulate the phenomenon according also to the nature of these interactions.

Chapter 5 – Lipid bilayer fluidity and degree of order regulates small EVs adsorption on model cell membrane. The final Chapter focuses on the functional characterisation of these lipid domains. In particular, the aim is to study the role of lipid raft domains within the uptake of external macromolecules such as small extracellular vesicles. As these results have been part of a collaboration, the Chapter will mainly analyse my contribution with AFM-based tracking of the interactions between these vesicles and phase separated membrane. The Chapter highlights how the interface the complex interplay between different lipid phases and their mechanical properties in determining the overall dynamics of the system.

# References


[1] H. Lodish et al. W.H. Freeman, 2021.

[2] B. Lewin. Jones & Bartlett Learning, 2007.

[3] B. Alberts et al. W.W. Norton & Co., 2022.

[4] E. Amingol et al. *Nat Rev Genet*, 2021, 22, 71–88.

[5] T. Bechtel et al. *Nat Chem Biol*, 2021, 17, 641–652.

[6] C. R. Woese. *Microbiol Rev*, 1987, 51, 221–271.

[7] J. Vosseberg. et al. *Nature*, 2024, 633, 295–305.

[8] C. Alexia et al. *Sci Signaling*, 2013, 6, 291.

[9] A. Eisenberg-Lerner et al. *Nat Commun*, 2020, 11, 409.

[10] Y. Zhang et al. *Cell Death Discovery*, 2023, 9, 51.

[11] W. Mu et al. *Science*, 2021, 7, 191–197.

[12] K. I. M. Cooper and E. Jakobsson. *Prog Biophys Molec Biol*, 1985, 46, 51–96.

[13] C. Dias and J. Nylandsted. *Cell Discovery*, 2021, 7, 4.

[14] I. Levental and E. Lyman. *Nat Rev Mol Cell Biol*, 2023, 24, 107–122.

[15] Y. Yang et al. *Nat Cell Biol*, 2024, 26, 1878–1891.

[16] T. Williams et al. *Nat Ecol Evol*, 2020, 4, 138–147.

[17] L. Eme et al. *Nature*, 2023, 618, 992–999.

[18] T. Williams et al. *Nature*, 2013, 504, 231–236.

[19] M. Gibiansky et al. *Science*, 2010, 330, 191–197.

[20] M. Silverman and M. Simon. *Nature*, 1974, 5452, 73–74.

[21] H. Berg and R. Anderson. *Nature*, 1973, 5425, 380–382.

[22] K. Hou et al. *Signal Transduction Targeted The*, 2022, 7, 135.

[23] N. Kamada et al. *Nat Rev Immunol*, 2013, 13, 321–335.

[24] J. M. Beck, V. B. Young, and G. B. Huffnagle. *Transl Res*, 2012, 160, 258–266.

[25] M. A. Croxen and B. B. Finlay. *Nat Rev Microbiol*, 2010, 8, 26–38.

[26] J. Qiu and Z.-Q. Luo. *Nat Rev Microbiol*, 2017, 15, 591–605.

[27] P. A. Cotter and V. J. DiRita. *Ann Rev Microbiol*, 2000, 54, 519–565.

[28] A. Smith and M. Hussey. *American Society for Microbiology*, 2016.

[29] M. R. J. Salton. Elsevier Publishing Co., 1964.

[30] T. J. Silhavy, D. Kahne, and S. Walker. *Cold Spring Harbor Perspect Biol*, 2010, 2.

[31] C. Schwechheimer and M. J. Kuehn. *Nat Rev Microbiol*, 2015, 13, 605–619.

[32] H. Heine, E. T. Rietschel, and A. J. Ulmer. *Appl Biochem Biotechnol - Part B Mol Biotech*, 2001, 19, 279–296.

[33] D. Baldridge et al. *Orphanet Journal of Rare Diseases*, 2021, 16, 206.

[34] U. Irion and C. Nüsslein-Volhard. *PNAS*, 2022, 119.

[35] A. Krogh. *Science*, 1929, 70, 200–204.

[36] S. N. Cohen et al. *PNAS*, 1973, 70, 3240–3244.

[37] L. Cong et al. *Science*, 2013, 339, 819–823.

[38] M. Touchon et al. *PLOS Genet*, 2020, 16, e1008866.

[39] B. Felden and L. Paillard. *FEMS Microbiol Rev*, 2017, 41, 624–639.

[40] H. Waheed et al. *J Membr Sci*, 2022, 642, 120000.

[41] J. Rosko et al. *PNAS*, 2017, 114, E7969–E7976.

[42] L. A. Pratt and R. Kolter. *Mol Microbiol*, 1998, 30, 285–293.

[43] I. V. Mikheyeva et al. *Nat Commun*, 2023, 14, 5715.

[44] C. Lo, T. P. Y. Sowa, and B. Richard. *PNAS*, 2013, 110.

[45] H. Berg. *Ann Rev Biochem*, 2003, 72.

[46] R. A. Corey et al. *Sci Adv*, 2021, 7, 1–10.

[47] H. Liu et al. *Int J Food Microbiol*, 2004, 95, 147–155.

[48] G. Chwastek et al. *Cell Reports*, 2020, 32.

[49] H. Nakayama et al. *Biochim Biophys Acta, Biomembr*, 1980, 601, 1–10.

[50] T. Zhang et al. *Sci Rep*, 2019, 9, 1–13.

[51] J. P. Sáenz et al. *PNAS*, 2012, 109, 14236–14240.

[52] J. P. Sáenz et al. *PNAS*, 2015, 112.

[53] R. M. Epand and R. F. Epand. *Biochim Biophys Acta, Biomembr*, 2009, 1788, 289–294.

[54] S. Lopes et al. In: *Anal BioanalChem*. Vol. 398. 3. Oct. 2010, 1357–1366.

[55] J. D. Unsay et al. *Langmuir*, 2013, 29, 15878–15887.

[56] S. Lopes, G. Ivanova, and B. de Castro. *Biochim Biophys Acta, Biomembr*, 2018, 1860, 2465–2477.

[57] P. Ridone et al. *Eur Biophys J*, 2015, 44, 567–576.

[58] G. Paradies et al. *Cells*, 2019, 8.

[59] C. Hammond. In: *Cellular and Molecular Neurophysiology: Fourth Edition*. Academic Press, 2015, 39–54.

[60] Y. Liu et al. *Nature*, 2022, 610, 761–767.

[61] E. Krasnopeeva, C. J. Lo, and T. Pilizota. *Biophys J*, 2019, 116, 2390–2399.

[62] T. Harayama and H. Riezman. *Nat Rev Mol Cell Biol*, 2018, 19, 281–296.

[63] H. Watson. *Essays Biochem*, 2015, 59, 43–69.

[64] S. J. Singer and G. L. Nicolson. *Science*, 1972, 175, 720–731.

[65] J. F. Danielli and H. Davson. *J Cell Comp Physiol*, 1935, 5, 495–508.

[66] G. L. Nicolson. *Biochim Biophys Acta, Biomembr*, 2014, 1838, 1451–1466.

[67] P. F. Almeida. *Biochim Biophys Acta, Biomembr*, 2009, 1788, 72–85.

[68] J. N. Israelachvili, D. Mitchell, and B. W. Ninham. *Biochim Biophys Acta, Biomembr*, 1977, 470, 185–201.

[69] S. Tristram-Nagle and J. F. Nagle. *Chem Phys Lipids*, 2004, 127, 3–14.

[70] P. Cowin and B. Burke. *Curr Opin Cell Biol*, 1996, 8, 56–65.

[71] G. R. Chichili and W. Rodgers. *Cell Mol Life Sci*, 2009, 66, 2319–2328.

[72] S. H. White and W. C. Wimley. *Ann Rev Biophys Biomol Struct*, 1999, 28, 319–365.

[73] D. López and R. Kolter. *Genes Dev*, 2010, 24, 1893–1902.

[74] F. A. Heberle and G. W. Feigenson. *Cold Spring Harbor Perspect Biol*, 2011, 3, 1–13.

[75] K. Voïtchovsky et al. *Biophys J*, 2006, 90, 2075–2085.

[76] C. Pliotas et al. *Nat Struct Mol Biol*, 2015, 22, 991–998.

[77] R. G. Parton, M. M. Kozlov, and N. Ariotti. *J Cell Biol*, 2020, 219.

[78] Y. Zhang et al. *Nature*, 2021, 590, 509–514.

[79] P. Agre et al. *J Physiol*, 2002, 542, 3–16.

[80] J. Moller et al. *Biochim Biophys Acta, - Rev Biomembr*, 1996, 1286, 1–51.

[81] D. Rosenbaum and B. K. S. Rasmussen. *Nature*, 2009, 459, 356–363.

[82] A. Duncan et al. *Sci Rep*, 2017, 7, 16647.

[83] K. Palczewski et al. *Science*, 2000, 289, 739–745.

[84] A. J. Oakley et al. *Protein Sci*, 1999, 8, 1915–1921.

[85] L. H. Chamberlain, R. D. Burgoyne, and G. W. Gould. *PNAS*, 2001, 98, 5619–5624.

[86] V. A. M. Villar et al. *Methods in Cell Biology*, 2016.

[87] J. E. Vance and D. E. Vance. Elsevier, 2008.

[88] V. A. Frolov, A. V. Shnyrova, and J. Zimmerberg. *Cold Spring Harbor Perspect Biol*, 2011.

[89] L. Vamparys et al. *Biophys J*, 2013, 104, 585–593.

[90] S. Vanni et al. *Nat Commun*, 2014, 5, 4916.

[91] E. Beltrán-Heredia et al. *Commun Biol*, 2019, 2, 225.

[92] E. Fahy et al. *J Lipid Res*, 2005.

[93] A. Shokri and G. Larsson. *Microb Cell Fact*, 2004, 3, 1–12.

[94] R. Koynova and M. Caffrey. *Biochim Biophys Acta, Rev Biomembr*, 1998, 1376, 91–145.

[95] J. Exton. *Biochim Biophys Acta, Lipids Lipid Metab*, 1994, 1212, 26–42.

[96] C. Sohlenkamp and O. Geiger. *FEMS Microbiol Rev*, 2015, 40, 133–159.

[97] K. Simons and J. L. Sampaio. *Cold Spring Harbor Perspect Biol*, 2011, 10, a004697.

[98] F. Perissinotto et al. *Biophys Chem*, 2019, 255.

[99] C. Paba et al. *J Colloid Interface Sci*, 2023, 652, 1937–1943.

[100] A. B. García-Arribas, A. Alonso, and F. M. Goñi. *Chem Phys Lipids*, 2016, 199, 26–34.

[101] D. Marsh. *Biochim Biophys Acta, Biomembr*, 2010, 1798, 688–699.

[102] F. R. Maxfield and I. Tabas. *Nature*, 2005, 438, 612–621.

[103] M. A. Alonso and J. Millán. *J Cell Sci*, 2001, 114, 3957–3965.

[104] D. Lingwood and K. Simons. *Science*, 2010, 327, 46–50.

[105] K. Simons and E. Ikonen. *Nature*, 1997, 387, 569–572.

[106] E. London and D. Brown. *Biochim Biophys Acta, Biomembr*, 2000, 1508, 182–195.

[107] J. C. Lawrence et al. *Biophys J*, 2003, 84, 1827–1832.

[108] D. Marquardt et al. *Chem Phys Lipids*, 2016, 199, 17–25.

[109] M. Stöckl and A. Herrmann. *Biochim Biophys Acta, Biomembr*, 2010, 1798, 1444–1456.

[110] L. J. Pike. *J Lipid Res*, 2009, 50, S323–S328.

[111] I. Levental, K. R. Levental, and F. A. Heberle. *Trends Cell Biol*, 2020, 30, 341–353.

[112] J. D. Unsay, K. Cosentino, and A. J. García-Sáez. *J Visualized Exfp*, 2015.

[113] V. Kiessling, S.-T. Yang, and L. K. Tamm. In: *Current Topics in Membranes*. Vol. 75. Elsevier Ltd, 2015, 1–23.

[114] A. Dazzi et al. *Appl Spectrosc*, 2012, 66, 1365–1384.

[115] S. A. Shelby et al. *Nat Chem Biol*, 2023, 19, 750–758.

[116] D. Lingwood et al. *PNAS*, 2008, 105, 10005–10010.

[117] A. S. Klymchenko et al. *Biochim Biophys Acta, Biomembr*, 2009, 1788, 495–499.

[118] A. S. Klymchenko and R. Kreder. *Chem Biol*, 2014, 21, 97–113.

[119] B. P. Head et al. *J Biol Chem*, 2006, 281, 26391–26399.

[120] A. W. Cohen et al. *Physiol Rev*, 2004, 84, 1341–1379.

[121] L. Picas, P.-E. Milhiet, and J. Hernández-Borrell. *Chem Phys Lipids*, 2012, 165, 845–860.

[122] A. Alessandrini and P. Facci. *Soft Matter*, 2014, 10, 7145–7164.

[123] L. Picas, F. Rico, and S. Scheuring. *Biophys J*, 2012, 102, L01–L03.

[124] E. I. Goksu et al. *Biochim Biophys Acta, Biomembr*, 2009, 1788, 254–266.

[125] L. J. Johnston. *Langmuir*, 2007, 23, 5886–5895.

[126] D. A. Brown and E. London. *Ann Rev Cell Developm Biol*, 1998, 14, 111–136.

[127] K. Simons and D. Toomre. *Nat Rev Mol Cell Biol*, 2000.

[128] H. A. Lucero and P. W. Robbins. *Arch Biochem Biophys*, 2004, 426, 208–224.

[129] J. A. Allen, R. A. Halverson-Tamboli, and M. M. Rasenick. *Nat Rev Neurosci*, 2007, 8, 128–140.

[130] P. W. Janes, S. C. Ley, and A. I. Magee. *J Cell Biol*, 1999, 147, 447–461.

[131] R. Varma and S. Mayor. *Nature*, 1998, 394, 798–801.

[132] L. Pelkmans. *Biochim Biophys Acta, Mol Cell Res*, 2005, 1746, 295–304.

[133] C. Dart. *J Physiol*, 2010, 588, 3169–3178.

[134] T. Murai. *Int J Cell Biol*, 2012, 2012, 1–6.

[135] S. Donatello et al. *Am J Pathol*, 2012.

[136] P. Varshney, V. Yadav, and N. Saini. *Immunology*, 2016, 149, 13–24.

[137] H. Wang et al. *Cell Research*, 2008, 18, 290–30.

[138] B. P. Head, H. H. Patel, and P. A. Insel. *Biochim Biophys Acta, Biomembr*, 2014, 1838, 532–545.

[139] M. Bramkamp and D. Lopez. *Microbiol Mol Biol Rev*, 2015, 79, 81–100.

[140] D. Lopez. *Chem Phys Lipids*, 2015, 192, 3–11.

[141] M. Gohrbandt et al. *The EMBO Journal*, 2022, 41, 5.

[142] P. F. Almeida, A. Pokorny, and A. Hinderliter. *Biochim Biophys Acta, Biomembr*, 2005, 1720, 1–13.

[143] P. J. Quinn and C. Wolf. *Biochim Biophys Acta, Biomembr*, 2009, 1788, 33–46.

[144] D. Chapman, J. Urbina, and K. M. Keough. *J Biol Chem*, 1974, 249, 2512–2521.

[145] E. J. Shimshick and H. M. McConnell. *Biochemistry*, 1973, 12, 2351–2360.

[146] E. J. Shimshick and H. M. McConnell. *Biochem Biophys Res Commun*, 1973, 53, 446–451.

[147] J. Hjort Ipsen et al. *Biochim Biophys Acta, Biomembr*, 1987, 905, 162–172.

[148] R. X. Gu, S. Baoukina, and D. Peter Tieleman. *J Am Chem Soc*, 2020, 142, 2844–2856.

[149] J. Shearer et al. *J Chem Phys*, 2020, 153.

[150] S. K. Das, S. Roy, and J. Midya. *CR Phys*, 2015, 16, 303–315.

[151] T. J. Hill. Parts I and II. Dover, 1994.

[152] R. F. De Almeida et al. *Biophys J*, 2002, 82, 823–834.

[153] T. Mužić et al. *Biochim Biophys Acta, Biomembr*, 2019, 1861, 183026.

[154] A. Jin et al. *Biochemistry*, 1999, 38, 13275–13278.

[155] B. Cooper, L. Hammad, and K. Montooth. *Funct Ecol*, 2014, 28, 886–894.

[156] M. B. Jackson and J. E. Cronan. *Biochim Biophys Acta, Biomembr*, 1978, 512, 472–479.

[157] A. J. Bray. *Advances in Physics*, 1994, 43, 357–459.

[158] M. Kardar. Cambridge University Press, June 2007.

[159] K. Binder. *Reports on Progress in Physics*, 1987, 50, 783–859.

[160] N. T. Thanh, N. Maclean, and S. Mahiddine. 2014.

[161] J. W. Cahn and J. E. Hilliard. *J Chem Phys*, 1959, 31, 688–699.

[162] R. P. Sear. *J Phys: Condens Matter*, 2007, 19, 033101.

[163] D. Turnbull and J. C. Fisher. *J Chem Phys*, 1949, 17, 71–73.

[164] S. Teychené, I. Rodríguez-Ruiz, and R. K. Ramamoorthy. *Curr Opin Colloidal Interface Sci*, 2020, 46, 1–19.

[165] P. W. Voorhees. *J Stat Phys*, 1985, 38, 231–252.

[166] C. A. Stanich et al. *Biophys J*, 2013, 105, 444–454.

[167] I. M. Lifshitz and V. V. Slyozov. *J Phys Chem Solids*, 1961, 19, 35–50.

[168] M. H. Jensen, E. J. Morris, and A. C. Simonsen. *Langmuir*, 2007, 23, 8135–8141.

[169] J. W. Cahn. *Acta Metall*, 1961, 9, 795–801.

[170] J. Cahn and J. Hilliard. *Acta Metall*, 1971, 19, 151–161.

[171] J. W. Cahn. *J Chem Phys*, 1965, 42, 93–99.

[172] T. Lubensky. *Solid State Commun*, 1997, 102, 187–197.

[173] R. Kenzler et al. *Computer Phys Commun*, 2001, 133, 139–157.

[174] A. J. Wagner and J. M. Yeomans. *Phys Rev Lett*, 1998, 80, 1429–1432.

[175] V. M. Kendon et al. *J Fluid Mech*, 2001, 440, 147–203.

[176] H. Tanaka. *J Chem Phys*, 1996, 105, 10099–10114.

[177] H. Tanaka and T. Araki. *Phys Rev Lett*, 1998, 81, 389–392.

[178] V. Heinrich et al. *Biophys J*, 2001, 81, 1452–1463.

[179] P. F. Davies, J. A. Spaan, and R. Krams. *Ann Biomed Eng*, 2005, 33, 1714–1718.

[180] L. T. Nguyen et al. *Nat Commun*, 2019, 10, 1259.

[181] S. U. Alam Shibly et al. *Biophys J*, 2016, 111, 2190–2201.

[182] N. C. Gauthier, T. A. Masters, and M. P. Sheetz. *Trends Cell Biol*, 2012, 22, 527–535.

[183] H. Hwang et al. *Biochim Biophys Acta, Biomembr*, 2018, 1860, 2566–2575.

[184] L. A. Genova et al. *PNAS*, 2019, 116, 25462–25467.

[185] H. J. Busscher and H. C. van der Mei. *PLoS Pathog*, 2012, 8, e1002440.

[186] A. L. Roux et al. *Philosophical Transactions of the Royal Society B: Biological Sciences*, 2019, 374.

[187] P. A. Janmey. *Physiol Rev*, 1998, 78, 763–781.

[188] G. K. Auer and D. B. Weibel. *Biochemistry*, 2017, 56, 3710–3724.

[189] P. Jin, L. Y. Jan, and Y. N. Jan. *Ann Rev Neurosci*, 2020, 43, 207–229.

[190] M. Sidarta, L. Baruah, and M. Wenzel. *Pharmaceuticals*, 2022, 15, 770.

[191] J. D. Humphrey, E. R. Dufresne, and M. A. Schwartz. *Nat Rev Mol Cell Biol*, 2014, 15, 802–812.

[192] C. Kung, B. Martinac, and S. Sukharev. *Ann Rev Microbiol*, 2010, 64, 313–329.

[193] B. Coste et al. *Nature*, 2012, 483, 176–181.

[194] M. Deserno. *Chem Phys Lipids*, 2015, 185, 11–45.

[195] W. Rawicz et al. *Biophys J*, 2000, 79, 328–339.

[196] E. Evans and W. Rawicz. *Phys Rev Lett*, 1990, 64, 2094–2097.

[197] S. T. Sun et al. *Biochim Biophys Acta, Biomembr*, 1986, 860, 525–530.

[198] P. B. Canham. *J Theor Biol*, 1970, 26.

[199] E. A. Evans. *Biophys J*, 1974, 14, 923–931.

[200] Y. Sun, T. L. Sun, and H. W. Huang. *Biophys J*, 2014, 107, 2082–2090.

[201] S. Garcia-Manyes and F. Sanz. *Biochim Biophys Acta, Biomembr*, 2010, 1798, 741–749.

[202] E. A. Evans and R. Skalak. CRC Press, Jan. 2018.

[203] F. D. Murnaghan. *Am J Math*, 1937, 59, 235.

[204] W. Helfrich. *Zeitschrift fur Naturforschung - Section C Journal of Biosciences*, 1973, 28, 693–703.

[205] E. Evans et al. *Biophys J*, 2003, 85, 2342–2350.

[206] F. R. Hallett et al. *Biophys J*, 1993, 64, 435–442.

[207] M. M. Müller, M. Deserno, and J. Guven. *Phys Rev E: Stat Nonlinear Soft Matter Phys*, 2005, 72, 061407.

[208] C. A. Rutkowski et al. *Biochemistry*, 1991, 30, 5688–5696.

[209] R. M. Hochmuth. *J Biomech*, 2000, 33, 15–22.

[210] M. D. Rueda-Contreras et al. *Sci Rep*, 2021, 11, 9562.

[211] Y.-H. M. Chan and S. G. Boxer. *Curr Opin Chem Biol*, 2007, 11, 581–587.

[212] M. Eeman and M. Deleu. *Biotechnol Agron Soc Environ*, 2010, 14, 719–736.

[213] I. R. Cooke, K. Kremer, and M. Deserno. *Phys Rev E*, 2005, 72, 011506.

[214] C. Dietrich et al. *Biophys J*, 2001, 80, 1417–1428.

[215] G. J. Hardy, R. Nayak, and S. Zauscher. *Curr Opin Colloid Interface Sci*, 2013, 5, 448–458.

[216] H. J. Risselada and S. J. Marrink. *PNAS*, 2008, 105, 17367–17372.

[217] H. Ma et al. *J Phys Chem B*, 2015, 119, 14668–14682.

[218] K. Murzyn, T. Róg, and M. Pasenkiewicz-Gierula. *Biophys J*, 2005, 88, 1091–1103.

[219] W. Zhao et al. *Biochimie*, 2008, 90, 930–938.

[220] K. R. Pandit and J. B. Klauda. *Biochim Biophys Acta, Biomembr*, 2012, 1818, 1205–1210.

[221] M. Przybylo et al. *Langmuir*, 2006, 22, 9096–9099.

[222] L. Collard, F. Sinjab, and I. Notingher. *Biophys J*, 2019, 117, 1589–1598.

[223] S. J. Attwood, Y. Choi, and Z. Leonenko. *Int J Mol Scis*, 2013, 14, 3514–3539.

[224] J. M. Crane, V. Kiessling, and L. K. Tamm. *Langmuir*, 2005.

[225] S. Lansky et al. *Nature*, 2023, 621, 206–214.

[226] I. Casuso et al. *Nat Nanotech*, 2012, 7, 525–529.

[227] A. Nath, W. M. Atkins, and S. G. Sligar. *Biochemistry*, 2007, 46, 2059–2069.

[228] L. A. Bagatolli and E. Gratton. *Biophys J*, 2000, 78, 290–305.

[229] S. D. Connell, G. R. Heath, and J. A. Goodchild. In: *Methods Mol Biol.* Vol. 1886. Humana Press, New York, NY, 2019, 29–44.

[230] A. Alessandrini et al. *Biophys J*, 2012, 103, 38–47.

[231] A. Marchesi et al. *Sci Rep*, 2021, 11, 13003.

[232] M. K. Doeven et al. *Biophys J*, 2005, 88, 363–372.

[233] P. Girard et al. *Biophys J*, 2004, 87, 419–429.

[234] M. Ohno et al. *Langmuir*, 2009, 25, 11680–11685.

[235] J. Käs and E. Sackmann. *Biophys J*, 1991, 60, 825–844.

[236] L. R. Montes et al. *Biophys J*, 2007, 93.

[237] N. Kato et al. *Membranes*, 2015, 5, 22–47.

[238] C. Yoshina-Ishii et al. *J Am Chem Soc*, 2005, 127, 1356–1357.

[239] L. K. Tamm and H. M. McConnell. *Biophys J*, 1985, 47, 105–113.

[240] J. A. Jackman and N. J. Cho. *Langmuir*, 2020, 36, 1387–1400.

[241] U. Mennicke and T. Salditt. *Langmuir*, 2002, 18, 8172–8177.

[242] A. R. Ferhan et al. *Nat Protoc*, 2019, 14, 2091–2118.

[243] E. Reimhult, F. Höök, and B. Kasemo. *Langmuir*, 2003, 19, 1681–1691.

[244] P. Nollert, H. Kiefer, and F. Jähnig. *Biophys J*, 1995, 69, 1447–1455.

[245] P. S. Cremer and S. G. Boxer. *J Phys Chem B*, 1999, 103, 2554–2559.

[246] R. P. Richter, R. Bérat, and A. R. Brisson. *Langmuir*, 2006, 22, 3497–3505.

[247] C. Keller and B. Kasemo. *Biophys J*, 1998, 75, 1397–1402.

[248] J. Andrecka et al. *ACS Nano*, 2013, 7, 10662–10670.

[249] I. Reviakine and A. Brisson. *Langmuir*, 2000, 16, 1806–1815.

[250] R. Lipowsky and U. Seifert. *Mol Cryst Liq Cryst*, 1991, 202, 17–25.

[251] C. A. Keller et al. *Phys Rev Lett*, 2000, 84, 5443–5446.

[252] H. L. Wu et al. *Soft Matter*, 2013.

[253] A. L. Plant et al. *Anal Biochem*, 1995, 226, 342–348.

[254] K. Kastl et al. *Biochemistry*, 2002, 41, 10087–10094.

[255] H. M. Seeger et al. *Biophys J*, 2009, 97, 1067–1076.

[256] B. W. Koenig, H. H. Strey, and K. Gawrisch. *Biophys J*, 1997, 73, 1954–1966.

[257] H. Read, S. Benaglia, and L. Fumagalli. *Soft Matter*, 2024, 20, 5724–5732.

[258] J. A. Goodchild et al. *Langmuir*, 2023, 39, 10843–10854.

[259] S. Arumugam, E. P. Petrov, and P. Schwille. *Biophys J*, 2015, 108, 1104–1113.

# 2. Methods

## 2.1 Overview of the Chapter

To fulfil my aim of developing and studying the behaviour of a model membrane system to describe native biological processes, I conducted various experiments combining multiple techniques that allowed me to chemically, morphologically and mechanically described the properties of these systems down to the nanoscale level. Atomic force microscopy (AFM) was employed for the morphological and mechanical characterisation of the planar lipid bilayers, differential scanning calorimetry (DSC) was employed to test the thermodynamic properties of different lipid mixtures and finally dynamic light scattering (DLS) was used to characterise the mechanical behaviour of different model systems upon osmotic shock.

This Chapter aims at reviewing the most fundamental concepts behind these 3 techniques with a focus on the AFM which has been the key instrument for my project. Here, I provide a foundational introduction to these instruments to ensure a clear understanding of how they work; detailed experimental protocols and specific methods will be presented in dedicated Methods sections at the beginning of each results chapter.

## 2.2 Atomic Force Microscopy

AFM is a high-resolution imaging technique which belongs to the family of the scanning probe microscopy (SPM) techniques, which have been founded in 1981 with the invention of the scanning tunnelling microscope by Gerd Binning and

Heinrich Rohrer [1]. In 1985, Binning, Quate and Greber [2] collaborated for the invention of the very first AFM kit, which now represents the most common and well-known SPM techniques for both commercial and research purposes. SPM techniques can scan the surface of a given sample by using physical probes and allowing to observe and reconstruct the morphological properties of the material. AFM revolutionised the SPM field due to its ability to scan surfaces in both dry and liquid conditions non-invasively, achieving atomic resolution at high speed, and opening new possibilities in the material science field. Thanks to the development of new AFMs and their technical improvements over the years [3], AFM has been employed also to study thin biological interfaces that require very gentle and non-invasive approaches such as cells [4–7] or lipid bilayers [8–10]. The following sections discuss the key elements of the AFM instrument and the primary approaches for acquiring topographical and mechanical data on biological samples.

### *Structure of the AFM*

AFM works by reconstructing the properties of an interface by studying the intermolecular forces between its nanoscopic tip and the sample's surface. Thanks to the small scale of its tip, AFM can reach nanometric resolutions which are not achievable with classic fluorescence and optical microscopy limited by light diffraction [11]. In Fig. 2.1, a schematic representation of the AFM machine can be observed.

An important element of this instrument is the cantilever. This flexible block is connected to the base of the AFM, also known as the holder, and terminates with the AFM tip, making it the transducer of the interactions that are generated between the tip and the surface. While scanning the interface, the cantilever will be subject to a motion depending on the repulsive or attractive tip-surface forces which are linked with the topography of the interface. By using a laser beam which is generally placed at the base of the cantilever, the instrument tracks the tip position and any small motion of the cantilever during the scan. The beam is reflected by the cantilever top surface against a photodiode (PD) that allows the tracking of the cantilever's motion. Thanks to the presence of 4 quadrants, the PD tracks any vertical and horizontal motion of the cantilever in a precise way, currently reaching frequencies of 5MHz [12]. The PD converts this information into a voltage signal [13, 14] that activates the feedback-loop of the AFM which

will adjust the cantilever position to maintain a constant tip-sample distance or motion throughout the scan. The adjustment of the cantilever position is performed through a piezoelectric component, that interprets and converts the voltage signal from the PD in this mechanical motion.

In the next sections, I will describe the basic concepts behind the most used AFM modes and investigate the key aspects when it comes to the application of AFM for biological purposes.

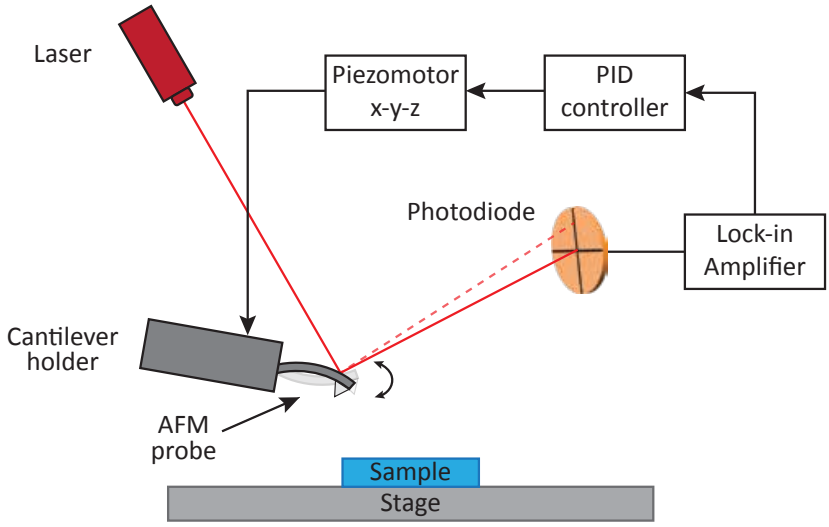


Figure 2.1: Schematic representation of the AFM machine structure. The AFM probe (composed of the cantilever and the tip) is stably mounted at its base to the cantilever holder which allows to move the entire set up on xyz directions. Once the tip is in contact with the sample, the AFM probe will eventually move due to the topographical characteristics of this surface. This bending is recorded through a laser that is reflected from the top-part of the AFM probe to a photodiode. Any variation in the position of the laser is recorded by the photodiode which sends an electronic signal to the piezomotor controlling the cantilever holder's motion forward towards the sample or moving it away. This feedback-loop system allows maintaining constant imaging conditions throughout the entire experiment.

### 2.2.1 AFM imaging concepts

As a microscopy technique, AFM is mostly known for its ability to reconstruct the surface of a given sample by scanning on top of it (Fig. 2.2A). This imaging process can be achieved through different working modes which are generally divided in two classes: static and dynamic modes (Fig. 2.2B-C) [15]. In the static mode (for example, contact mode), the AFM probe is scanned while always kept static at its base (Fig. 2.2B) [16, 17]. For example in a classic imaging approach in contact mode, the feedback loop aims to maintain a direct tip-surface

contact throughout the scan by keeping constant the repulsive interaction forces generated between the AFM tip and the surface. The direct contact between the tip and the surface can lead to damaging of the tip or of the analysed interface. By working in static mode, the AFM can be sensitive to direct adhesion with the surface and lateral friction while scanning [18, 19], allowing for example to obtain key information when looking at the lubrication properties of a surface [20]. On the other hand, the dynamic mode stood out over the past years as the main operation mode for biological applications [21]. In dynamic mode, the AFM probe is oscillated on top of the scanning surface. During the scan, the oscillating probe has an intermittent contact with the surface, reducing the risk of unintentionally damage the sample. In this thesis, the AFM probe has been oscillated at or near its resonance frequency as it reduces the noise and effectively filters out instantaneous fluctuations [22]. This has been the historically preferred non-contact method due to its robustness and ease to implement. However, off-resonance approaches have emerged during the last years such as force volume mode [23] and peakforce tapping mode [7, 24], which are generally slower, but allow for weaker tip-sample interactions and concurrent quantitative property mapping of the sample [25]. The oscillation is generally performed by acoustic excitation, where the cantilever's oscillation is excited by applying a vibrating signal to a piezoelectric actuator built within the AFM head or stage depending on the setup. However, noises given by the experimental conditions (e.g. liquid environment) and by mechanical parts reduce the stability and accuracy of the measurement [26, 27]. To overcome these limitations, other approaches have been developed such as magnetic excitation [28], electrostatic excitation [29], and photothermal excitation [30–33], which has been used in my research work. In the photothermal mode, a power-modulated laser beam is focused on the base of the cantilever. Thanks to the irradiation of the laser, the cantilever is excited by the thermal stress generated and the noise is reduced [32]. Before diving into the details of this operational mode, it is important to understand the properties of the AFM which influence this imaging mode itself.

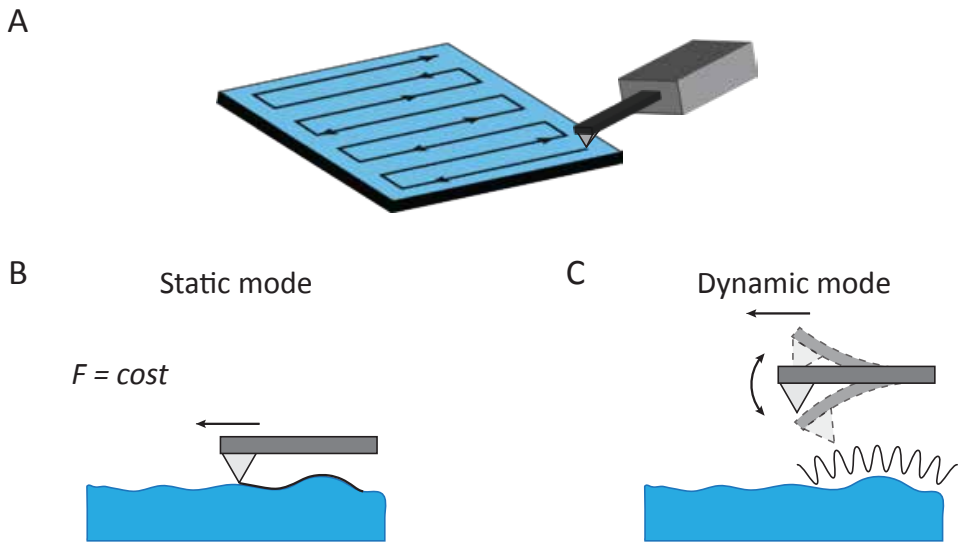


Figure 2.2: Illustration of AFM imaging through both static and dynamic mode. (A) AFM imaging works through the ability of the AFM probe to scan the surface on x,y and z axis, reconstruing a 3D image of the sample. This imaging can be done through 2 modes according to the need and the sample under study: (B) the static mode works with the AFM probe kept static with respect to its base. The example in (A) shows a classic imaging in contact mode, where the AFM tip is maintained in constant and direct contact with the surface. This is based on maintaining the same applied $F$ on the sample, which allows obtaining extra information such as the friction between the cantilever and the surface, but could eventually damage either the tip or the sample. The second method (C) is the dynamic mode, where the AFM probe is constantly oscillating near the surface. This method avoids a constant contact between the probe and the sample, allowing for a much more gentle imaging which is crucial in the case of biological samples.

### *AFM probe properties*

As previously mentioned, the AFM probe is a critical element as it enables stabilising interactions with the surface. Cantilevers can vary in dimensions, geometrical shapes, and materials, giving them peculiar characteristics which can be crucial for measuring a given sample. Generally, cantilevers have microscopic size with length, width and thickness that range 100-500 $\mu m$, 30-50 $\mu m$ and 0.5-8 $\mu m$, respectively. Any small size variation of the cantilever combined with different materials (where silicon and silicon nitride are the most common ones) and geometrical shapes (e.g. triangular, V-shape or rectangular) lead to a range of cantilevers with different mechanical properties for example impacting their ability to deflect or their disruptiveness when it comes to fragile samples [12, 34]. On the other hand, AFM tips have a pyramidal shape which is approximated as triangle near the apex, and present height, radius and opening angle that

range 8-20 $\mu m$, 30-40° and 5-15 $nm$ respectively [12, 34–36]. Thanks to the nanometre scale of its radius, the tip interacts just with a small number of surface atoms, ensuring the high resolution of the AFM. The geometrical and dimensional differences among cantilever impact their ability to bend and flex, something that is captured by the cantilever's spring constant ($k$). The cantilever is described as a Hookean spring [37–39], allowing to convert its motion into a force by using Hooke's law. The force ($F_c$) generated by the tip on the sample can be described as:

$$F_c = k_f \delta \tag{2.1}$$

where $\delta$ is the equilibrium position of the spring. The spring constant is an intrinsic property of the sample which depends on the previously named geometrical parameters following [40]:

$$k_f = \frac{Y w h^3}{4L^3} \tag{2.2}$$

where $Y$ is the Young's modulus of the cantilever, $w$ is its width, $h$ its thickness and $L$ its length. Considering the cubic dependence of $k$ on the thickness and the length of the AFM probe, any small manufacturing variation of these parameters would lead to significant higher or lower spring constants [37]. Commercial cantilevers tend present a broad range of spring constants, although, for non-disruptive imaging purposes, soft cantilevers ($k_f < 1$ N/m) are generally the preferred choice for biological applications as they reduce damages of the sample [32, 41]. The spring constant influences the ability of the cantilever to oscillate varying its angular resonance frequency ($\omega_0$) [42]:

$$\omega_0 = \sqrt{\frac{k_f}{m}} \tag{2.3}$$

where $m$ is the mass of the cantilever in the working medium. As the small mass of the cantilever is difficult to measure, another equation is generally used:

$$\omega = \omega_v \left(1 + \frac{\pi \rho w^2 \Gamma_r(\omega)}{4\mu}\right)^{-\frac{1}{2}} \tag{2.4}$$

where $\omega_v$ is the resonance of the cantilever in vacuum is used, $\mu$ the mass per unit length, $p$ the density of the medium and $\Gamma_r(\omega)$ is the hydrodynamic function that characterises the response of the cantilever in the fluid [22, 43]. In dynamic modes, the oscillation of the AFM probe needs to be finely selected with respect to its resonance frequency to enhance sensitivity to tip-sample interactions, allowing for high-resolution imaging and precise measurement of surface properties. The cantilever's oscillatory behaviour is also characterised by its Quality factor ($Q$), which is a dimensionless parameter that describes how underdamped an oscillator is [12]. Theoretically, $Q$ is defined as the ratio between the initial energy stored of the cantilever ($E_{stored}$) and the energy dissipated at each oscillation's cycle ($E_{lost}$) [44, 45]:

$$Q = 2\pi \frac{E_{stored}}{E_{lost}} \tag{2.5}$$

However, these energies are complex to experimentally evaluate, limiting our ability to obtain $Q$. Therefore, $Q$ is also expressed as a function of the oscillator's frequency and describes the sharpness of its resonance peak [42]:

$$Q = \frac{\omega_0}{\delta\omega} \tag{2.6}$$

Where $\delta\omega$ is the width of the resonance peak at half-maximum amplitude. A higher $Q$ indicates an oscillator with a sharper resonance, less energy dissipation per oscillatory cycle and low dampening. However, in fluid environments, where biological samples are commonly analysed, $Q$ decreases due to increased damping from the fluid medium. Due to the higher density of the media, the effective mass of the cantilever can increase by a factor of 10-40, reducing its resonance frequency [46, 47]. This hydrodynamic effect can therefore reduce the value of $Q$ even by two orders of magnitudes [20], impacting the imaging conditions.

### 2.2.2 AFM dynamic modes

With these key parameters established, this section will outline the main principles of AFM dynamic mode, highlighting aspects critical to cantilever motion and imaging performance.

The dynamic modes are based on the oscillation of the AFM probe, generally ranging from oscillations of 50 kHz to 500 kHz depending on its geometrical properties and the environmental conditions. The cantilever is lowered towards the surface down-to a position where the AFM tip does not directly contact the surface, making it much more gentle and limiting tip and surface damaging. The feedback loop aims at keeping the same cantilever oscillation throughout the scan, maintaining constant the intermittent tip-sample attractive interaction forces.
The goal of any AFM mode is to provide a relationship between the tip-surface forces and the microscopic properties of the given sample. However here, the nonlinear character of these forces prevents to obtain any dependence between the tip-surface interactions and either the amplitude or the phase variation throughout the measurement [48, 49]. For this scope, models have been developed to disentangle these complex interactions between amplitude, frequency, and phase. While a full derivation of the dynamic response model exceeds the scope of this thesis, it is essential to introduce its foundational assumptions and resulting equations to understand dynamic mode operation. The cantilever's motion can be approximated as a damped, point-mass harmonic oscillator subject to an external driving force $F_d$. For a cantilever with an effective mass $m$, the motion can be described by the following second-order differential equation [22, 50, 51]:

$$m\ddot{z}(t) + \gamma\dot{z}(t) + k_f z = F_{\text{exc}} + F_{\text{ts}} \tag{2.7}$$

where $z$ represents the displacement of the cantilever's free edge as a function of time $t$, $\gamma$ is a damping coefficient, and $F_{ts}$ corresponds to the tip-sample interaction forces [52, 53]. In the absence of tip-surface forces ($F_{ts} = 0$), and considering a cantilever subjected to a small-amplitude oscillatory motion, the equation simplifies to yield definitions for the cantilever's oscillation amplitude ($A$) and the phase shift ($\phi$) relative to the driving force [21]:

$$A(\omega) = \frac{F_0/m}{\left[(\omega_0^2 - \omega^2)^2 + (\omega\omega_0/Q)^2\right]^{1/2}} \tag{2.8}$$

$$\tan\phi = \frac{\omega\omega_0/Q}{\omega_0^2 - \omega^2} \tag{2.9}$$

where $F_0$ and $\omega$ are the amplitude and angular frequency of the driving force, while $\omega_0$ and $Q$ are respectively the angular natural frequency and the quality factor of the free cantilever. Here, $\phi$ represents the temporal difference between the driving force and the cantilever's response, indicating how the cantilever's oscillation is delayed or advanced in relation to the excitation. As described by Eq. 2.8, Eq. 2.9 and shown in Fig. 2.3, the amplitude at the steady-state is represented as a Lorentzian curve as a function of the driving frequency [21], while the phase shift between the steady-state motion of the cantilever and the driving force has a sigmoidal shape.

However, to model the probe when interacting with the surface, the effect of the tip-sample interactions needs to be included ($F_{ts} \neq 0$) [21]. For small motions with respect to the equilibrium position, the tip-surface force can be expressed as:

$$F_{ts}(z) = F_{ts}(0) + \left(\frac{dF_{ts}}{dz}\right)_0 z \tag{2.10}$$

This interaction is also characterised by an effective spring constant ($k_{eff}$) which is also influenced by the gradient of the force:

$$k_{eff} = k - \left(\frac{dF_{ts}}{dz}\right)_0 z = k - k_{ts} \tag{2.11}$$

This influences the effective resonant frequency ($\omega_{eff}$) and the shift from the natural resonant frequency ($\Delta\omega$) which can be calculated as:

$$\omega_{eff} = \left(\frac{k_{eff}}{m}\right)^{1/2} \tag{2.12}$$

$$\Delta\omega \approx -(\omega_0 k_{ts}/2k) \tag{2.13}$$

By applying this simple model, the AFM probe behaves as a harmonic oscillator with an effective spring constant and resonant frequency that depends on the gradient of this interaction [22]. Finally, the interaction oscillation amplitude ($A_{int}$) and phase ($\phi_{int}$) can be calculated as:

$$A_{int} = \frac{F_d/m}{\left[\left((\omega_0^2 + \Delta\omega)^2 - \omega_d^2\right)^2 + \left(\omega_d\omega_0/Q\right)^2\right]^{1/2}} \tag{2.14}$$

$$\tan(\phi_{int}) = \frac{\omega_d\omega_0/Q}{(\omega_0^2 + \Delta\omega)^2 - \omega_d^2} \tag{2.15}$$

The dependence of the amplitude on the excitation and effective resonant frequency observed in Eq. 2.14 provides a way to explain the dependence between the oscillation amplitude and the strength of the tip-surface forces. Assuming that a tip is excited at its natural frequency, the tip while approaching the surface will modify its resonant frequency, leading to a modification of the oscillation amplitude (Fig. 2.3). This new amplitude will be given by the new resonance curve at the excitation frequency of the oscillator, leading to a smaller amplitude value. This phenomenon is also called the detuning effect. The detuning occurs in both the attractive and repulsive force regime, as the nature of the tip-sample forces just change the direction of the resonance curve shift [21]. By exciting the tip slightly off resonance, the amplitude could decrease or increase depending on the new resonant frequency position with respect to the original one. Although more sophisticated models have been introduced [54, 55], the intrinsic complexity of these methods goes beyond the aim of my thesis. Moreover, this simpler harmonic oscillator model is still useful to interpret the results shown in my work [22, 42, 56, 57], where small oscillation amplitudes (1nm<) have been applied and no higher-order excitation modes have been used.

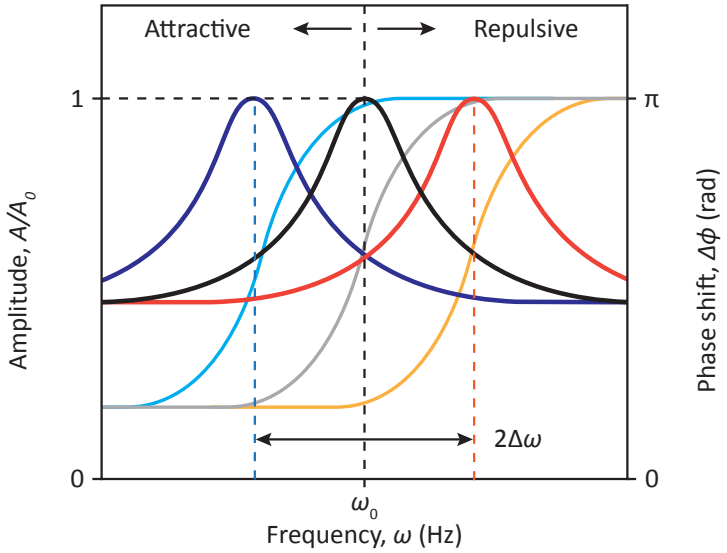


Figure 2.3: Graphical representation of detuning phenomenon in a weakly perturbed harmonic oscillator. As observed in Eq. 2.8 and Eq. 2.9, the amplitude and phase show a Lorentzian and sigmoidal dependence to the driving frequency, respectively. The oscillation amplitude and phase of the unperturbed oscillator are shown in black and gray, respectively. Once the cantilever is perturbed by weak interaction forces, both amplitude and the phase change due to the variation in the cantilever's effective resonance frequency. Attractive forces shifts the amplitude and the phase as represented by the curves blue and cyan, while the effect of repulsive forces is shown by the red and orange curves.

The dynamic modes generally diverge on the feedback parameter that the instrument uses to keep a constant oscillation. The 2 most used dynamic modes are the amplitude modulation mode (AM-AFM) and the frequency modulation mode (FM-AFM) which use respectively the amplitude and the frequency of the oscillation as the feedback parameter [58]. AM-AFM is generally favoured in biological applications due to its robustness, ease of use, and simpler instrumentation, making it suitable for softer and more fragile biological samples [34]. In this work, all AFM imaging has been performed using AM-AFM with soft cantilevers for these reasons. In AM-AFM, the amplitude of the oscillation is used as the feedback parameter and this approach can allow to obtain nanometre size details when working at relatively small oscillation amplitude (e.g. 1-2 $nm$) [12]. Another crucial aspect of this mode is that by intermittently interacting with the surface, the phase can freely vary. The variation of the phase throughout the scan can be used to reconstruct phase-contrast images [15] that contain information about the energy dissipation of the system and therefore the viscoelastic [59] and possibly chemical properties of the sample [60].

In contrast, FM-AFM uses the frequency shift of the oscillation as the feedback

parameter. The frequency is adjusted to match the resonance frequency of the cantilever, $\omega_0$, while keeping the amplitude constant. This allows for highly sensitive measurements of interaction forces and is often used in high-resolution imaging [61].

### 2.2.3 AFM force spectroscopy on biological samples

Although AFM is best known for its imaging with high resolution, it also represents a powerful tool for mechanical evaluations allowing for example the extrapolation of the elasticity of a material [62, 63] or its adhesiveness [64–66]. Given the AFM probe's ability to track interfacial forces, it has been widely used since its early development to evaluate the physical properties of samples. This has been demonstrated not only on hard surfaces [64, 67], but also on soft biological samples [68–70] such as cells [7, 15, 68, 71–73] and even thin bilayers [8, 74–76].

The AFM force spectroscopy is the AFM approach that directly measures the mechanical properties of a surface [8, 58, 77–79]. Here, the AFM probe is approached and retraced from the surface by a cyclic z-movement with its feedback loop turned off to allow free motion of the cantilever in the $z$ direction. During the AFM probe motion, the AFM tracks the motion of the cantilever ($\delta$) with respect to the displacement of the cantilever in z-axis ($z$), recording a so-called deflection curve (Fig. 2.4A). To obtain mechanical information about the sample, these curves need to be converted in the force curves, where the force generated by the tip on the sample ($F$) is related to the tip-sample distance ($d$). Here again, Hooke's law can be used (Eq. 2.1) allowing obtaining $F$ from the deflection signal from the cantilever. To calculate $d$, the length of the cantilever is neglected, and the point at which the tip contacts the surface is generally taken as the point of hard contact. These assumptions allow calculating as:

$$d = z + \delta \tag{2.16}$$

When looking at a general force curve (Fig. 2.4B), various regimes can be detected depending on the tip-sample distance. During the approaching, the cantilever does not generally experience any force at long distances from the sample.

Long-range attractive interactions such as electrostatics and capillary forces could be detected depending on the nature of the sample and the tip employed [8, 80, 81]. When these interactions are present, the probe jumps towards the surface (as shown in Fig. 2.4). The analysis of this area of the graph [82, 83] allows to characterise these long-range forces and the adhesion properties of the material under study [64–66]. In my thesis, this adhesion jump is generally not observed, as thin lipid bilayers do not show high adhesiveness considering the zwiterionic nature of their phospholipid headgroup. Moreover, silicon nitride tip have been employed in my research work, which are generally considered chemically inert due to their thin external silicon dioxide layer.

When the tip gets in contact with the surface, the probe experiences repulsive van der Waals forces as indicated by the increase in the cantilever motion and therefore the increase force generated on the sample. Once the setpoint force is reached, the retracting phase of the cantilever starts, where the AFM probe will go back to its original position. Although the mechanical properties (e.g. Young's modulus, breakthrough forces or indentation depth) are commonly extracted from the approaching part of the cycle, the retracting phase could as well contain important information regarding the nature of the sample such as its adhesiveness which is linked with the strength of the tip-sample attractive Van der Waals forces [62]. This force spectroscopy characterisation is limited to a localised nanometric area which might not fully represent the overall sample. However, with advancements in AFM technology, it is now possible to record force maps, which capture these mechanical properties over a grid of points across a sample surface [62, 84–86]. A force map consists of sequentially acquired force curves, each performed at precise, pre-defined locations, allowing for high-resolution measurements of localised mechanical characteristics. This grid-based approach enables force maps to achieve resolutions down to the nanoscale, offering a spatially resolved view of material heterogeneity and allowing for comprehensive mechanical profiling at the nanoscale.

To model tip-sample repulsive interactions, both the tip and the sample are represented as a simplified system using continuum elasticity models. Here, the probe is modelled as a triangle which ends with a sphere, cone or pyramid depending on the geometry of the tip, while the sample can be seen as an incompressible plane [72]. Models further detailing the system characteristics are however available [8, 65, 72, 77, 78, 87]. The first well-known model was

developed by Heinrich Hertz [77] in 1881 and it still represents the most used model to interpret AFM force spectroscopy data. In his work, Hertz describes the deformation of two spheres when they enter in contact upon a specific load. By half-space approximation, the model can be applied also for the interaction between a sphere and an infinite half space, allowing us to model the interaction of the tip and the sample respectively when the indentation depth is significantly smaller than the tip radius. Following his approach, the following relationship has been developed:

$$F_c = \frac{4}{3}\sqrt{Rh^3}\frac{Y}{1-\nu^2} \tag{2.17}$$

where $Y$ is the Young's modulus of the sample, $\nu$ is the Poisson's ratio of the sample, $R$ the tip radius and h the indentation depth. This approach allows to obtain a fundamental mechanical indicator such as $Y$, which describes the elastic ability of a material to resist to a stress when compressed. However, this model presents a series of criticality and assumptions when it comes to describing the sample's behaviour [87]. First, the sample needs to be homogeneous, meaning that it presents the same properties throughout. Secondly, the sample is modelled as isotropic ($\nu$=0.5) meaning that the sample is incompressible and its volume is conserved under compression, and finally the sample is considered elastic for the proportionality between stress and strain to exist. Although these assumptions fall when dealing with thin and fragile biological samples, multiple papers have demonstrated the validity of the Hertzian approach when dealing with indentations that do not exceed 5-20% of the sample's thickness. This limitation is necessary to partially avoid measuring the properties of the substrate underneath.

Although Hertz model is the most well-known one, multiple models have been developed since 1980s to best describe tip-sample interactions [65, 72, 78]. For biological purposes, researchers have been trying to correct the previously described Hertzian equation to consider part of the characteristics of bio-samples such as their finite thickness and the presence of a harder substrate underneath [78]. All the models still present limitations and critical assumptions. Thus, the quantitative values extracted from AFM spectroscopy cannot be taken as an absolute measurement, but rather relative to the experimental conditions applied

such as the tip characteristics, the chosen model, and, crucially, the method used to determine the tip–surface contact point. This latter factor is one of the most significant sources of uncertainty when estimating $Y$ from AFM data [88, 89]. It has been demonstrated that misidentifying the contact point by 50 nm can alter the estimated $Y$ value by up to an order of magnitude for thick samples [89]. In this work, where thin lipid bilayers were analysed, even small shifts of the contact point (1–2 nm) could lead to variations of up to 50% in the calculated $Y$ value — reinforcing the view that AFM-derived elastic parameters should be interpreted as relative rather than absolute. To address this, the contact point in our measurements was defined as the position where the force curve deviates from the flat baseline. This was computationally determined by incrementally fitting a linear region until a noticeable change in slope was detected. This automated approach, widely adopted in the literature, avoids subjective bias, improves reproducibility, and enables the efficient analysis of large datasets [89]. However, it is not free from limitations and can still introduce variability, particularly in soft samples and at low indentation depths. Nonetheless, these approaches still act as useful tools to compare different samples when the same conditions are met, allowing the tracking of mechanical changes or differences between different materials.

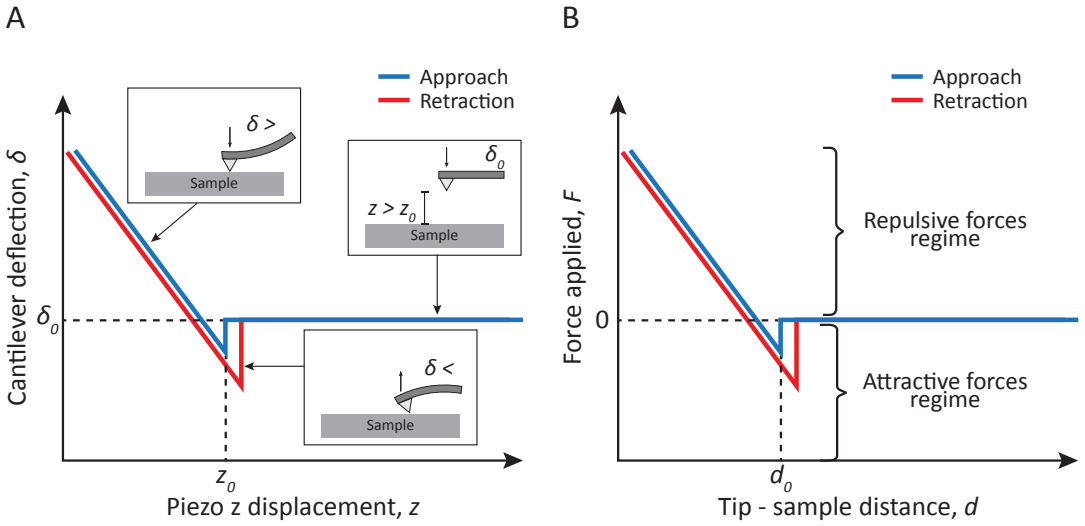


Figure 2.4: Schematic representation of the basic functioning of the AFM force spectroscopy approach and the obtained results. (A) At first, the AFM probe is too far from the sample to feel any interaction force, maintaining the original deflection while approaching the sample. Once the surface is approached ($z_0$), the cantilever will start to linearly bend and compress the sample. Finally, the AFM probe is retracted from the surface and taken back to the original piezo position. This $\sigma$ vs $z$ graph can be observed also as the $F$ vs tip-sample distance, as previously seen (B). This can allow us to extract important mechanical information from both the approach and retraction phases of the AFM probe cycle.

## 2.3 Differential Scanning Calorimetry

Differential Scanning Calorimetry (DSC) is an experimental thermo-analytical technique that was developed in 1962 by E.S. Watson and M.J. O'Neil to study the heat flow of solid materials [90]. Quickly afterwards, the technique was applied in lab research for biochemical purposes, slowly establishing it as one of the main calorimetric techniques in both academic and industrial research. DSC can directly measure the difference in heat uptake by a sample relative to a reference inert material during a temperature change process, allowing us to evaluate the thermodynamic properties of the sample. DSC can be carried out in 2 different ways which slightly differ in their recording parameter and also in the structure of the instrument. In the Heat flux DSC, both the sample and the reference material are sealed in hermetic pans and placed in 2 thermoelectric disks surrounded by a furnace. The samples are linearly heated (or cooled) with a constant rate. Due to the intrinsic difference in the heat capacity of the sample ($C_p$) and the heat capacity of the reference pan, a temperature difference between the two pans will

be generated and recorded by the DSC (Fig. 2.5A). This temperature difference ($\Delta T$) can be then converted into a heat flow ($Q$) using the thermal equivalent of Ohm's law:

$$Q = \frac{\Delta T}{R} \tag{2.18}$$

where $R$ is the gas constant. The heat flow is then linked with the sample's $C_p$ as:

$$\frac{dQ}{dt} = C_p m \beta \tag{2.19}$$

where $\beta$ is the heating (or cooling) rate and $m$ is the mass of the sample. This relationship is important because the heat capacity is a key intrinsic property that allows insight into the material's thermal behaviour.

The other operational mode of DSC is power-compensated where the sample and reference material are placed in two separate furnaces. Here, the samples are always maintained at the same temperature while getting heated up. The DSC records the thermal power generated to ensure the same temperature is maintained in the two material and then plots it against time.

Independently from the specific operational mode, DSC is capable to track the most fundamental thermodynamic properties of a sample or reaction, allowing to identify parameters such as the melting point ($T_m$), the enthalpy associated with a reaction ($\Delta H_{cal}$) or the $C_p$ of the sample before and after the reaction (Fig. 2.5B). As the $C_p$ variations in the case of lipid vesicles are pretty small [91–93], $T_m$ and $\Delta H_{cal}$ are generally used to probe and compare the thermodynamic properties of the phase transitions of lipid mixtures [94]. $T_m$ can be calculated as the peak of the endothermic or exothermic curve recorded by the instrument, and it represents the temperature where 50% of the lipids have transitioned into the new phase. $\Delta H_{cal}$ expresses the energy associated with the ordering (or disordering) of the lipids into the new phases and can be calculated as the integral of the area under the transition curve:

$$\Delta H_{cal} = \int_{T_1}^{T_2} \frac{dQ}{dt} dt \tag{2.20}$$

where $T_1$ and $T_2$ represent the initial and final temperature of the transition phenomenon. This value will then need to be normalised for the mass or the moles of lipids used, and generally lipid vesicles present $\Delta H_{cal}$ in the order of 20-40 kJ/mol [93].

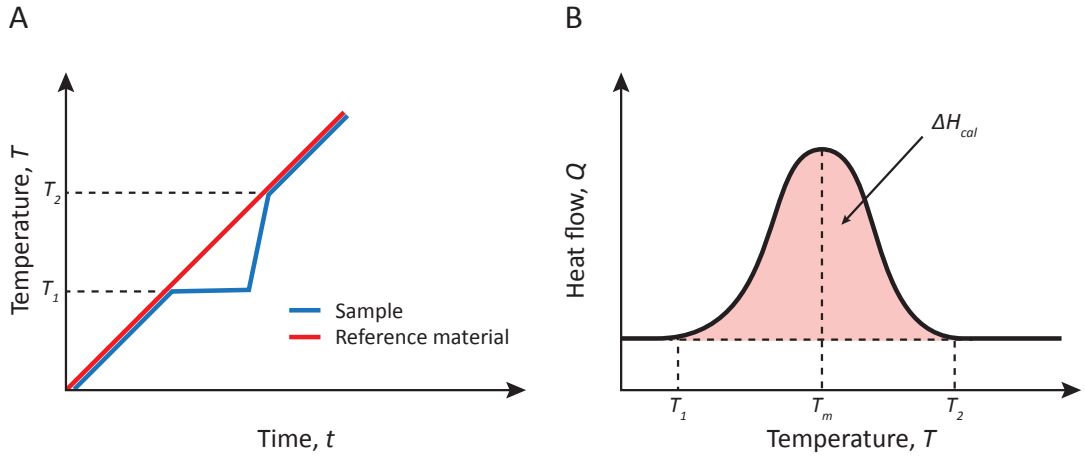


Figure 2.5: Examples of graphs to elucidate the basic functioning of heat flux DSC for studying phase transition phenomena. (A) By linearly heating both the sample and the reference material, DSC tracks temperature variations within the two pans; this temperature change is hence linked to the presence of an exothermic or endothermic (the example presented here) reaction in the observed sample. $\Delta T$ can be observed as a function of $Q$ given by the instrument to maintain the same temperature between the two pans as shown in (B). This curve contains a wide variety of thermodynamic information about the process under study such as $T_m$, $\Delta H_{cal}$ and the temperature range in which the reaction occurs.

To measure the thermodynamic properties of a given sample, such as lipid vesicles in my case, a correct DSC protocol needs to be designed. A series of critical parameters need to be taken into account:

- Temperature range. DSC operates over a wide temperature spectrum (typically from -150 °C to 700 °C, depending on the instrument). However, scanning excessively broad ranges can be time-consuming. For lipid vesicles, predicting the approximate transition temperature ($T_m$) is critical, as it helps define an appropriate scanning range. A window spanning ± 20–30 °C around the expected $T_m$ is ideal, as it generally covers the full sharp transition associated with lipid melting/freezing.

- Heating/Cooling rate. DSC can be performed in heating or cooling modes. However, the rate at which the temperature changes has a significant

impact on DSC data of any material [95–99]. For thermal analysis, a standard heating rate of 0.17 °C/s is commonly recommended, as it balances experimental speed with maintaining equilibrium conditions. Slower rates are often preferable for reducing thermal lag and ensuring the sample remains closer to equilibrium, enabling precise detection of weaker or subtler transitions such as pre-transition phenomena that have been previously observed in lipid vesicles containing phosphatidylcholine molecules [100]. However, very slow rates may increase baseline noise and obscure sharp, low-intensity peaks, such as those seen in lipid vesicle systems. Therefore, it is essential to strike a balance: a rate slow enough to approximate equilibrium conditions but fast enough to preserve signal clarity according to the specific instrument used. High heating rates often introduce thermal lag, distort transition profiles, and approach the instrumental limits, leading to greater noise and reduced resolution [98, 101, 102]. The dependence of the measured transition temperature on the scan rate has been previously described with a non-linear relationship [98, 101, 102]:

$$T_{m,\beta} = T_m + B\beta^z \tag{2.21}$$

where $T_{m,\beta}$ is the measured melting temperature at each scan rate, $T_m$ is the equilibrium or 'true' melting temperature, $\beta$ is the scan rate, and $B$ and $z$ are fitting parameters.

- Sample concentration. The sample concentration is crucial to enhance the signal of the transition, allowing to work at slower thermal rates and still maintaining a good signal to noise ratio. For lipid vesicles, high concentrations are generally required with common protocols working with samples $> 5$ mg/mL. However, it is essential to find a fine balance also in this case: while increasing the concentration can enhance the final signal, too concentrated lipid-based samples might tend to precipitate and not form vesicle's system, limiting the measurement.

- Lamellarity and dimensions of lipid vesicles. Traditionally, large multi-lamellar vesicles (LMVs) have been employed for the thermodynamic characterisation of lipid vesicles using the DSC [92, 103–105]. LMVs generally present sharp, reproducible and with high signal peaks, something

which tend to lack with smaller unilamellar systems.

## 2.4 Dynamic Light Scattering

Dynamic light scattering (DLS) is used to measure the size distribution of particles, such as vesicles or other macromolecules, in suspension [106, 107]. The system is based on directing a laser to the sample, and recording the light scattered by the sample particles by using a photodetector (Fig. 2.6A). The intensity of the scattered light fluctuates over time due to the Brownian motion of the particles. Thus, it is essential that no external forces or inertial effects influence the movement of the particles. By having a system which is dominated by the thermal energy, DLS can effectively predict the particle's size, which is linked to their diffusion and fluctuation in solution. For example, smaller particles would move more quickly, resulting in faster fluctuations (Fig. 2.6B). The fluctuations are used to calculate the diffusion coefficient ($D$) of the particles, which can then be used to calculate the hydrodynamic radius ($R_H$) via the Stokes-Einstein equation:

$$R_H = \frac{k_B T}{8\pi\eta D} \tag{2.22}$$

where $k_B$ is the Boltzmann constant, $T$ the temperature and $\eta$ the solvent viscosity. DLS can thus determine the size of the sample in the nanometre range, making it an ideal technique for monitoring particle's size (Fig. 2.6C). It is important to note that $R_H$ often differs from the actual particle size due to contributions from the solvation shell and surface interactions [108, 109]. These phenomena can overestimate the actual size of the particles. This is particularly relevant when comparing results with those from direct imaging methods such as microscopy.

Finally, the signal obtained in DLS does not directly depend on the intensity of light scattered by individual particles, which itself scales with the sixth power of the radius in the Rayleigh regime. Instead, DLS analyses the time-dependent fluctuations of this scattering, which are governed by the particles' diffusion coefficients, making the method independent of the absolute scattering intensity. This makes it versatile for particles of varying refractive indices or shapes.

DLS has been previously used to analyse lipid vesicle's size upon different treatments or environmental conditions [92, 110, 111]. Beyond the most basic aspects of DLS, there are some critical, but still simple parameters that need to be controlled when applied to vesicle's size tracking:

- Sample concentration. Low sample concentrations are generally preferred to avoid multiple scattering, which occurs when light is scattered by more than one particle before reaching the detector, lowering the apparent $R_H$ of the vesicles.

- Polydispersity index (PDI). This parameter usually provided by the DLS instrument describes the size distribution of the sample. If we need to track the size variation of a sample, it is important to work with a monodisperse system (PDI<0.1).

- Solvent and environmental properties. Solvent's viscosity and sample's temperature can influence the mobility of the vesicles, influencing the apparent $R_H$ and causing possible precipitation. DLS generally present a temperature control system to ensure consistent results between experiments. By maintaining constant the temperature, DLS ensures to maintain an equilibrium condition throughout the measurement. Rapid changes in temperature can drive the system out of equilibrium and increase the particle's motion, leading to artifacts in size determination.

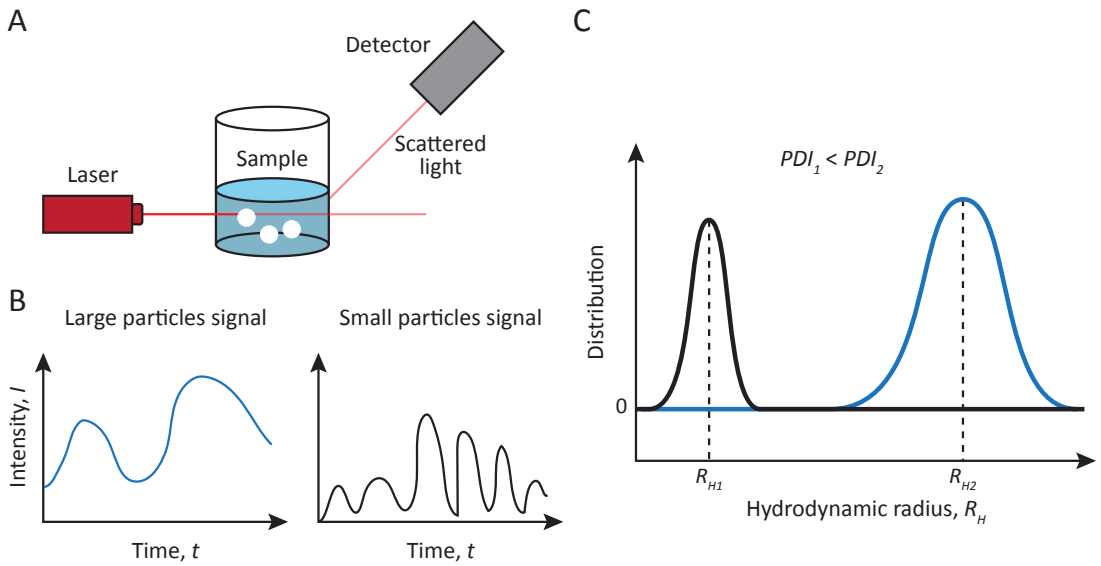


Figure 2.6: Illustration of basic concepts around DLS and results example. Schematic representation of the DLS instrument. Once the laser is pointed towards the sample, light interacts with the sample's particles. The light-particles interactions are behind the light scattering. The instrument collects the scattered light by using a detector and records the variation of the intensity of the scattered light with time as shown in (B). Here, representative datasets show the response of the system to large and small particles dispersed within the same media. Large particles generate a higher intensity of the scattered light while requiring more time to move away from the laser due to the lower $D$, whereas smaller particles are more mobile generating a more discontinuous signal. (C) Following the Stokes-Einstein equation (Eq. 2.22), the diffusion coefficient measured by DLS is used to obtain information about the size distribution of the sample, allowing us to identify the average $R_H$ and the PDI of the particles in solution.

## 2.5 Summary

This Chapter has presented the main methodologies applied within my research project with a focus on describing AFM basic principles for imaging and mechanical evaluation of biological samples. I have also covered the function of DSC and DLS which have represented fundamental complementary tools for my project.

# References


[1] G. Binning et al. *Phys Rev Lett*, 1982, 49, 57–61.

[2] G. Binning, C. F. Quate, and C. Gerber. *Phys Rev Lett*, 1986.

[3] F. Giessibl. *Rev Modern Phys*, 2003, 75, 949–983.

[4] D. J. Müller et al. *Nat Chem Biol*, 2009, 5, 383–390.

[5] A. Viljoen et al. *Nat Rev Methods Primers*, 2021, 1.

[6] L. Pasquina Lemonche et al. *Biophys J*, 2019, 116, 428a–429a.

[7] L. Pasquina-Lemonche et al. *Nature*, 2020, 582, 294–297.

[8] L. Picas, P.-E. Milhiet, and J. Hernández-Borrell. *Chem Phys Lipids*, 2012, 165, 845–860.

[9] K. Voïtchovsky et al. *Biophys J*, 2006, 90, 2075–2085.

[10] C. Paba et al. *J Colloid Interface Sci*, 2023, 652, 1937–1943.

[11] T. Ando, T. Uchihashi, and T. Fukuma. *Prog Surf Sci*, 2008, 83, 337–437.

[12] C. Cafolla and K. Voïtchovsky. *Nanoscale*, 2018, 10, 11831–11840.

[13] C. Quate. *Surf Sci*, 1994, 299, 980–995.

[14] H. Xie et al. *IEEE Sens J*, 2008, 8, 1478–1485.

[15] D. J. Müller et al. *Chemical Reviews*, 2021, 121, 11701–11725.

[16] B. Rodriguez et al. *Nanotechnology*, 2009, 20, 195701.

[17] N. M. K. Kuruppu et al. *ACS Applied Nano Materials*, 2019, 2, 2193–2203.

[18] N. Sasaki, K. Kobayashi, and M. Tsukada. *Phys Rev B*, 1996, 54, 2138–2149.

[19] C.-W. Yang et al. *Sci Rep*, 2018, 8, 3125.

[20] C. Cafolla and K. Voïtchovsky. *Nanoscale*, 2020, 12.

[21] R. Garcia and R. Perez. *Surf Sci Rep*, 2002, 47, 197–301.

[22] R. Garcia. John Wiley & Sons, Ltd, 2010.

[23] I. Medalsy, U. Hensen, and D. J. Muller. *Angew Chem Int Ed*, 2011, 50, 12103–12108.

[24] K. Xu et al. *Nanotech Rev*, 2018, 7, 605–621.

[25] P. Li et al. *Nanotech Rev*, 2023, 248, 113712.

[26] T. Schäffer et al. *J App Phys*, 1996, 80, 3622–3627.

[27] A. Buguin, O. Du Roure, and P. Silberzan. *App Phys Lett*, 2001, 78, 2982–2984.

[28] W. Han, S. Lindsay, and T. Jing. *App Phys Lett*, 1996, 69, 4111–4113.

[29] K. Umeda et al. *App Phys Express*, 2010, 3, 065205.

[30] N. Inada et al. *Beilstein Journal of Nanotechnology*, 2016, 7, 409–417.

[31] D. Ramos et al. *App Phys Lett*, 2008, 92.

[32] G. Ratcliff, D. Erie, and R. Superfine. *App Phys Lett*, 1998, 72, 1911–1913.

[33] D. Kiracofe et al. *Rev Sci Instruments*, 2011, 82, 013702.

[34] E. J. Miller et al. *J Visualized Exp*, 2016, e54924.

[35] S. Akamine et al. *App Phys Lett*, 1996, 68, 579–581.

[36] S. G. Kulkarni, S. Pérez-Domínguez, and M. Radmacher. *J Mol Recognit*, 2023, 36.

[37] D. Walters et al. *Rev Sci Instruments*, 1996, 67, 3583–3590.

[38] P. A. Wiggins et al. *Nat Nanotech*, 2006, 1, 137.

[39] M. Rief et al. *Science*, 1997, 275, 1295–1297.

[40] A. Torii et al. *Meas Sci Tech*, 1996, 7, 179.

[41] K. Voïtchovsky. *Nanoscale*, 2016, 8, 17472–17482.

[42] A. S. Paulo and R. Garcia. *Phys Rev B*, 2001, 64, 193411.

[43] R. Proksch et al. *Nanotechnology*, 2004, 15, 1344.

[44] B. Voigtländer. Springer Berlin Heidelberg, 2015. ISBN: 978-3-662-45239-4.

[45] J. Tamayo et al. *Biophys J*, 2001, 81, 526–537.

[46] C. Batchelor et al. Cambridge University Press, 2000.

[47] D. Tritton. Springer Science & Business Media, 2012.

[48] W. Xiang, Y. Tian, and X. Liu. *Precis Eng*, 2020, 64, 269–279.

[49] S.-C. Lee and A. Wacker. *Phys Rev*, 2002, 66, 115409.

[50] T. R. Rodriguez and R. Garcia. *App Phys Lett*, 2002, 80, 1646–1648.

[51] R. Garcia and A. S. Paulo. *Phys Rev B*, 1999, 60, 4961.

[52] B. Cappella and G. Dietler. *Surf Sci*, 1999, 34, 1–104.

[53] A. F. Payam, D. Martin-Jimenez, and R. Garcia. *Nanotechnology*, 2015, 26, 185706.

[54] S. Sader et al. *Nanotechnology*, 2005, 16, S94.

[55] K. Schroter et al. *Macromolecules*, 2009, 42, 1114–1124.

[56] A. J. Katan, M. H. van Es, and T. H. Oosterkamp. *Nanotechnology*, 2009, 20, 165703.

[57] Y. Song and B. Bhushan. *J Phys: Condens Matter*, 2008, 20, 225012.

[58] Y. Dufrêne et al. *Nat Nanotech*, 2017, 12, 295–307.

[59] E. Nagao and J. A. Dvorak. *Biophys J*, 1999, 76, 3289–3297.

[60] W. Trewby, J. Faraudo, and K. Voïtchovsky. *Nanoscale*, 2019, 11, 4376–4384.

[61] R. Garcia and E. T. Herruzo. *Nat Nanotech*, 2012, 7, 217–226.

[62] Y. Dufrene et al. *Nat Methods*, 2013, 10, 847–854.

[63] H.-J. Butt, B. Cappella, and M. Kappl. *Surf Sci Rep*, 2005, 59, 1–152.

[64] A. Asatekin et al. *J Membr Sci*, 2007, 298, 136–146.

[65] F. Leite et al. *Langmuir*, 2012, 13, 12773–12856.

[66] M. Sztilkovics et al. *Sci Rep*, 2020, 10, 61.

[67] R. Zangmeister, T. Morris, and M. Tarlov. *Langmuir*, 2013, 29, 8619–8628.

[68] N. Gavara. *Microsc Res Tech*, 2017, 80, 75–84.

[69] Q. Li et al. *RSC Adv*, 2016, 6, 12893–12912.

[70] W. Heinz and J. Hoh. *Trends Biotech*, 1999, 17, 143–150.

[71] T. Kuznetsova et al. *Micron*, 2007, 38, 824–833.

[72] P. Carl and H. Schillers. *Eur J Physiol*, 2008, 457, 551–559.

[73] B. Senigagliesi et al. *Nanomed Nanotechnol Biol Med*, 2022, 44, 102582.

[74] B. Gumi-Audenis et al. *Nanoscale*, 2018, 10, 23001–23011.

[75] A. Alessandrini et al. *Biophys J*, 2012, 103, 38–47.

[76] S. J. Attwood, Y. Choi, and Z. Leonenko. *Int J Mol Scis*, 2013, 14, 3514–3539.

[77] H. Hertz. *Journal fur die Reine und Angewandte Mathematik*, 1882, 1882, 156–171.

[78] P. D. Garcia and R. Garcia. *Biophys J*, 2018, 114, 2923–2932.

[79] S. Garcia-Manyes and F. Sanz. *Biochim Biophys Acta, Biomembr*, 2010, 1798, 741–749.

[80] N. A. Burnham, R. J. Colton, and H. M. Polloch. *Nanotechnology*, 1993, 4, 64–80.

[81] B. Gady et al. *Phys Rev B*, 1996, 53, 8065.

[82] J. Greenwood. *Proc R Soc Lond, A*, 1997, 453, 1277–12797.

[83] J. Israelachvili and D. Tabor. *Proc R Soc Lond, A*, 1972, 331, 19–38.

[84] Y. Efremov et al. *Sci Rep*, 2022, 12, 529.

[85] A. Kurek et al. *Cells*, 2021, 10, 219.

[86] X. Wang et al. *Sci Rep*, 2015, 5, 11097.

[87] S. V. Kontomaris, A. Malamou, and A. Stylianou. *Micron*, 2022, 155, 103228.

[88] E. K. Dimitriadis et al. *Biophys J*, 2002, 82, 2798–2810.

[89] N. Gavara. *Sci Rep*, 2016, 6, 21267.

[90] M. J. O'Neill. *Anal Chem*, 1964, 36, 1238–1245.

[91] S. M. Ohline et al. *J Chem Educ*, 2001, 78, 1251–1256.

[92] J. Drazenovic et al. *Biochim Biophys Acta, Biomembr*, 2015, 1848, 532–543.

[93] H. Ebel, P. Grabitz, and T. Heimburg. *J Phys Chem B*, 2001, 105.

[94] P. Gill, T. Moghadam, and B. T. Ranjbar. *Journal of Biomolecular Techniques*, 2010, 4, 167–193.

[95] H. Kissinger. *Anal Chem*, 1957, 29, 1702–1706.

[96] A. Yong et al. *Adv Manuf Polym Compos Sci*, 2017, 3, 43–51.

[97] G. Wang and I. R. Harrison. *Thermochim Acta*, 1994, 231, 203–213.

[98] S. Vyazovkin. *Molecules*, 2020, 25, 2813.

[99] M. V. Kök. *J Therm Anal Calorim*, 2007, 90, 817–821.

[100] K. A. Riske et al. *Biochim Biophys Acta, Biomembr*, 2009, 1788, 954–963.

[101] A. Toda, M. Hikosaka, and K. Yamada. *Polymer*, 2002, 43, 1667–1679.

[102] A. Toda. *J Therm Anal Calorim*, 2016, 123, 1795–1808.

[103] T. Kaasgaard, O. Mouritsen, and K. Jorgensen. *Biochim Biophys Acta, Biomembr*, 2003, 1615, 77–83.

[104] R. L. Biltonen and D. Lichtenberg. *Chem Phys Lipids*, 1993, 64, 129–142.

[105] R. N. Mcelhaney. *Chem Phys Lipids,* 1982, 30, 229–259.

[106] Z. Jia et al. *Colloids Interfaces*, 2023, 7, 15.

[107] J. Stetefeld, S. McKenna, and T. Patel. *Biophys Rev*, 2016, 8, 409–427.

[108] N. Jose et al. *Acta Scientific Nutritional Health*, 2019, 3, 3.

[109] C. Phelps. *Biochem Edu*, 1997, 5, 22.

[110] F. R. Hallett et al. *Biophys J*, 1993, 64, 435–442.

[111] J. Eisermann et al. *RSC Chem Biol*, 2023, 4, 386–398.

# 3. Development of a minimal model for *E. coli*'s inner membrane

## 3.1 Overview

This Chapter will describe the development of a simple model membrane system that compositionally and mechanically mimics the properties of the native *E. coli*'s inner membrane. As discussed in the Introduction, biological membranes are highly heterogeneous and challenging to investigate due to their inherent compositional complexity. To overcome this, many studies rely on the application of model membranes such as artificial vesicles and supported lipid bilayers (SLBs). The purpose of a model system is to capture the desired dominant features of the native context while remaining uniquely defined and simpler, which requires the knowledge of the most fundamental elements of the analysed membrane. Although various models have been developed throughout the years, the scientific community often lacks universally adopted model systems, which hinders the comparability of results between different research groups. For example, bacterial models have been widely used for their core importance in molecular biology, but multiple variations can be found within the published models from the lipid species applied to their molar ratio. In this part of my work, I aim to design and develop an ideal lipid-only model membrane system to mimic the thermodynamic and mechanical behaviour of the *Escherichia coli* (*E. coli*) inner membrane. By using the previously published lipidomic data about *E. coli*'s inner membrane, I designed a collection of candidate model systems reflecting the main aspects of the known native lipidomic composition and narrow down my selection based

on the systems' phase transition temperature. After identifying my candidate model systems, I independently measured their elastic properties using Atomic Force Microscopy (AFM) and compared them with native *E. coli* systems to further validate my results. I anticipate these results to be of interest for future studies making use of *E. coli* models, working as an ideal platform to investigate membrane proteins' function or macromolecule-membrane interactions.

This Chapter has been adapted from an article currently available on BioRxiv as: A minimalist model lipid system mimicking the biophysical properties of *Escherichia coli*'s membrane.

This Chapter will also include some additional challenging experiments that I have performed to test the mechanical properties of my candidate mixtures as vesicles, but which eventually failed due to the complexity of the protocol and fragility of these systems.

## 3.2 The importance of an *E. coli*'s inner membrane model

In Chapter 1, I have described how important biological membranes are for all organisms, having a multifold function, first acting as a physical barrier, but also serving as a unique environment for certain types of biological processes such as the generation of electrochemical gradients of ions, one of the main energy sources of living cells [1], transport and motility [2]. To do so, biological membranes have to sense, transmit, and respond to both chemical and mechanical stimuli. Chemical stimuli include the uptake and release of various molecules and ions [3] as well as sensing of the chemical composition outside the cell [4, 5]. While as we have seen in Section 1.5.1, mechanical stimuli arise from osmotic pressure changes [6, 7], changes in shear forces, cell-cell and cell-surface contacts [8, 9], as well as changes in the cytoskeleton [10, 11]. The transduction of these stimuli is in the charge of a large number of proteins which maintain cell physiological behaviour in collaboration with phospholipids.

Prokatyotic cells present a complex cell envelope which has been described in Section 1.2.1., where the differences between Gram-positive and Gram-negative bacteria has been highlighted. Within bacteria, I have also presented the case of *E. coli*, and how this bacteria has been widely employed for membrane

related studies in both microbial and eukaryotic studies. Specifically, the inner membrane of *E. coli* plays an important role as a barrier for ions and consequently allows the generation of their electrochemical gradients and fulfil the role of the classic plasma membrane found in eukaryotic cells. Moreover, some of the inner membrane's active membrane proteins are conserved in eukaryotic organisms [12], emphasising the importance of *E. coli*'s inner membrane as a model system. Over the last decade, a considerable amount of research has investigated *E. coli*'s membrane composition [13–16] and properties [13, 14, 17–21], highlighting several important features. For example, the composition and biophysical properties are known to adapt to the environment [15, 16, 22–29]. Additionally, *E. coli* membranes have compositional asymmetry, such as highly entropically disfavoured, unequal headgroup and acyl group asymmetries, both thought to be important for the biological function, but the origins of this asymmetry remain poorly understood [30]. These features add to the challenge of developing a model *E. coli* membrane system since it may not be unique. Various studies have nonetheless attempted to do so, each with its own approach. Some of the simplest models omit cardiolipin, a key component of *E. coli* membrane [31, 32], while others use a wide range of phospholipid headgroups with different alkyl chain lengths [22–27], with or without cardiolipin. The biophysical properties of the model membranes are rarely investigated, which makes it difficult to assess whether the systems considered accurately reflect the intrinsic properties of *E. coli* membrane. For studies of biomolecules hosted in the model membranes this is problematic because phospholipids are crucial for the structural stabilisation, active functionality, and localisation of membrane proteins [33]. Given the complexity of *E. coli* membranes and their dependence on the environment, even the best model system is unlikely to capture all of the native membrane's properties, but model systems able to replicate the native lipidomic ratios and biophysical properties would already provide a valuable basis for a wide range of studies. The goal of such 'minimal' systems is to capture some key relevant properties of the natural system while remaining compositionally much simpler and well-defined (typically composed of artificial lipids and proteins mixed with precise stoichiometry [34]).

In this part of my thesis, I systematically investigate binary and ternary lipid combinations of *E. coli*'s main lipids at stoichiometries close to those reported in lipidomic studies [20, 35–37]. I aim to create a model membrane

that replicates the *E. coli*'s inner membrane lipidic composition, thermal, as well as its mechanical properties at standard growth temperature (37°C). This work combines commercially available synthetic lipids for their ease of use and widespread availability and characterise the properties of model systems by replicating the transition temperature ($T_m$) [38] as well as comparing the in and out of plane stretching energies. Using a combination of differential scanning calorimetry (DSC), AFM, dynamic light scattering (DLS), and optical microscopy, I narrow down 18 possible combinations of the three main lipids present in *E. coli* and identify three mixtures that form stable and reproducible *E. coli* model membrane systems.

While my model systems do not include proteins or other biomolecules embedded in native *E. coli* membranes, they provide a lipid matrix that closely reflects the natural composition. Despite this simplification, the systems retain key biophysical properties, making them a valuable platform for studying *E. coli* membrane behaviour.

## 3.3 Materials and methods

In this section, I will briefly summaries the chemicals used and the protocol behind model membrane's preparation and the thermodynamic and mechanical testing used.

### 3.3.1 Chemicals

All the lipids have been purchased from Avanti Polar Lipids (Alabaster, AL). The following lipids have been purchased and dissolved in chloroform: 1-palmitoyl-2-oleoyl-sn-glycero-3-phosphoethanolamine (POPE), 1-palmitoyl-2-oleoyl-sn-glycero-3-phospho-(1'-rac-glycerol) (POPG), and 1',3'-bis[1-palmitoyl-2-oleoyl-sn-glycero-3-phospho]-glycerol (CL). 1,2-dipalmitoyl-sn-glycero-3-phospho-(1'-rac-glycerol) (DPPG) was obtained in powder form. The native *E. coli* membranes (37°C growth) have been obtained as *E. coli* Extract Polar (comprising only the polar lipids component) and *E. coli* Total Extract (full lipid extract) already dissolved in a chloroform: methanol solution. Salts (all >99% purity) have been purchased from Sigma-Aldrich (Dorset, UK) and dissolved/diluted in ultrapure water (Merck-Millipore, Watford, UK). MOPS buffer-based solution was prepared with specific ion concentrations as follows: 50 mM NaCl, 9.5 mM $NH_4Cl$, 0.5 mM $MgCl_2$, 0.3 mM $K_2SO_4$, and 1 $\mu m$ $CaCl_2$-$2H_2O$. The pH was adjusted to 6.5 prior to mixing with lipids.

### 3.3.2 Vesicles preparation

Large multilamellar vesicles (LMVs) have been used to test the stability of my candidate lipid mixture as vesicle's model systems. To prepare them, Lipids dissolved in chloroform have been mixed following the appropriate molar ratios into a 4 mL glass vial, -pre-dried under a gentle nitrogen flow, and fully dried overnight in a vacuum chamber. Large multi-lamellar vesicles have been obtained by freeze-thawing [39, 40]. Briefly, the lipid film was rehydrated in 2 mL of MOPS buffer-based solution to obtain a lipid concentration of 10 mg/mL and then briefly heated while sonicating in the sonication bath. Subsequently,

the vial was frozen (left in the freezer for 15 min). This heating-freezing process was repeated for 6 consecutive cycles to successfully form LMVs, which was confirmed by the lower turbidity of the solution and optical microscopy imaging

### 3.3.3 Supported lipid bilayers preparation

Supported lipid bilayers (SLBs) have been produced through direct lipid vesicle's fusion on top of a mica surface.
Lipids have been mixed and dried following the same protocol for the LMVs preparation. The lipid film was subsequently rehydrated in 1 mL of MOPS buffer-based solution obtaining a lipid concentration of 1 mg/mL. The vial was gently bath sonicated for 15 min at a temperature 5-10°C higher than the highest $T_m$ of the lipid species in the mixture, until the solution looked opaque and milky, indicating the formation of multilamellar vesicles. For small unilamellar vesicles (SUVs), the solution was extruded 31 times using a Mini-Extruder kit (Avanti Polar Lipids) with 1 Whatman 100 $nm$ filter (GE Healthcare Life Sciences, Little Chalfont, UK).
The SUVs solution was diluted 5 times to reach the 0.2 mg/mL concentration. 100 $\mu$L of SUVs solution have been deposited on a disk of Grade 1 freshly cleaved Muscovite mica (SPI Supplies, West Chester, PA, USA) on the AFM stage and let incubating for 20 min at 50°C covered with a Petri dish. The sample was then gently rinsed with the MOPS-buffer based solution in order to remove any non-broken lipid SUVs and finally the temperature was cooled down to 40°C and equilibrated for 15 min, as a starting point for the measurement. This process ensures the formation of a spread and uniform SLB system over the flat mica.

### 3.3.4 DSC protocol

To observe the lipids main melting transition and extract the associated melting temperature values, DSC measurements have been performed on a DSC 2500 (TA Instruments, Delaware, USA). Preliminary DSC heating tests have been performed to identify ideal lipids concentration and DSC scan parameters, and to ensure satisfactory signal to noise ratio and reproducibility of the data (Fig. 3.1): with DSC, faster scan rates tend to provide a better signal to noise

ratio. DSC test runs on binary lipid mixture have been performed with increasing lipid concentration (from 1 mg/mL up to 10 mg/mL) and heating scan rate (from 0.03 °C/s up to 0.17 °C/s) while maintaining the temperature range of -10°C – 60°C (Fig. 3.1A-B). Since the scan rate can shift the experimental melting point, DSC cooling experiments have been performed with the same increasing scan rates (from 0.03 °C/s up to 0.17 °C/s) while maintaining the same temperature range (Fig. 3.1C-D). This enables to infer the melting point of my reference mixture at 0°C/s scan rate (thermodynamic equilibrium), and therefore estimate the effect of the scan rate on the experimental melting point (Fig. 3.1E). Practically, the dependence of the measured transition temperature on the scan rate is not trivial with previous studies [41, 42] reporting the following nonlinear dependence:

$$T_m, \beta = T_m + B\beta^z \tag{3.1}$$

where $T_m, \beta$ is the measured melting temperature at each scan rate, $T_m$ is the equilibrium or 'true' melting temperature, $\beta$ is the scan rate, and $B$ and $z$ are fitting parameters. Experiments run at different scan rates enabled to determine $B$ and $z$, and correct the measured transition temperatures (Fig. 3.1). All other experiments have been performed as follows: 10 $\mu$L of LMVs solutions at 10 mg/mL have been loaded into the calorimeter and a heating rate of 0.08 °C/s was used in a temperature range of -10°C – 60°C. Samples have been equilibrated for 5 min at the starting temperature (-10°C) before starting the measurement. 3 repeats have been performed per each sample to enable statistical analysis.

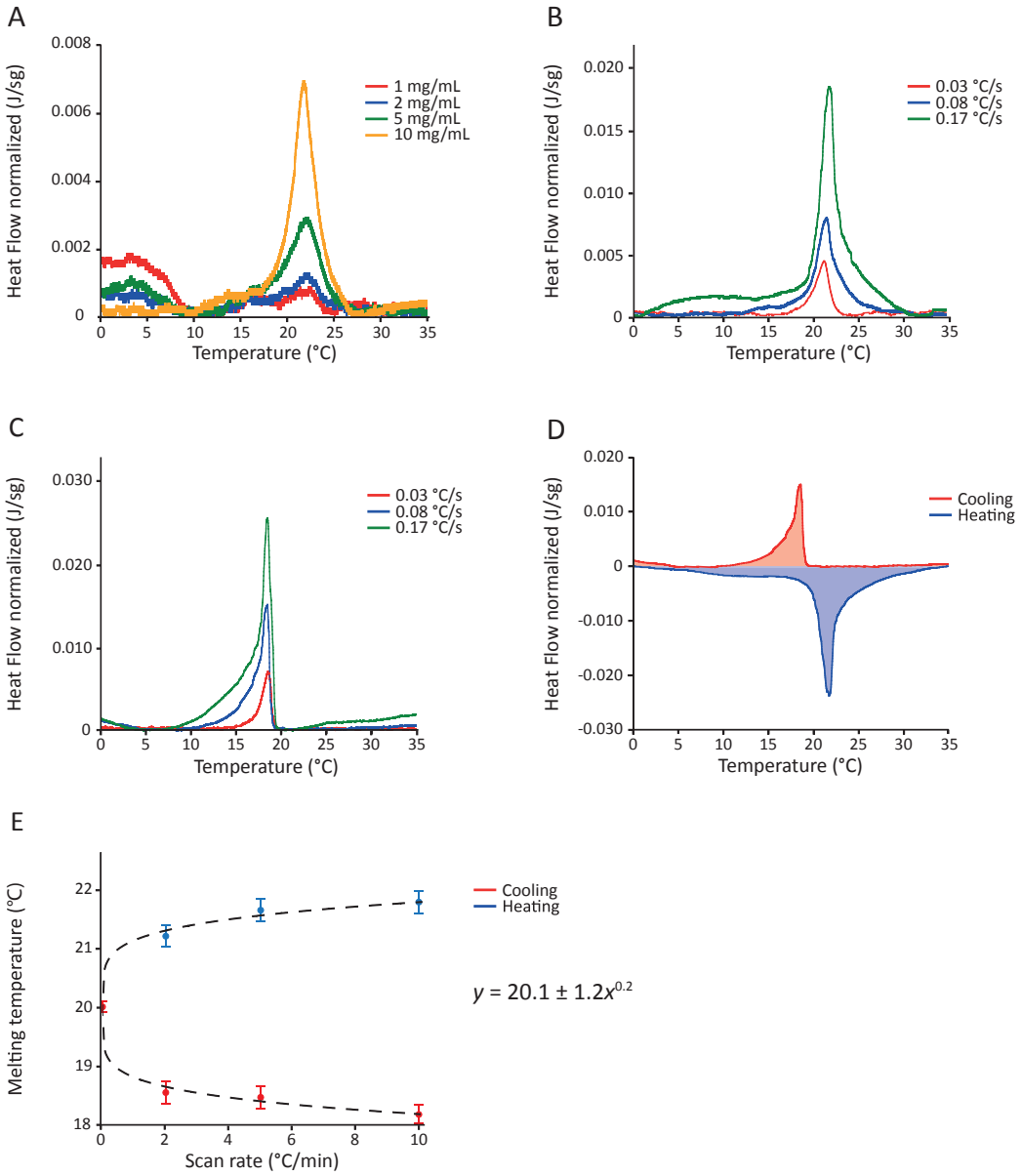


Figure 3.1: DSC thermographs of LMVs solution to optimise DSC parameters. The LMVs tested here have been formed with a mixture of POPE and POPG in 3:1 molar ratio. (A) DSC experiments varying LMVs concentration to find the optimal signal to noise (SN) at a scan rate of 0.08 °C/s. (B) DSC experiments varying heating rate to optimise the SN using LMVs solution at 10 mg/mL. Variation of scan rate up to 0.17 °C/s led to small calorimetric differences (melting point variations up to 0.4°C). The same effects are detected on both heating (B) and cooling (C) DSC thermographs, here also acquired using LMVs solution at 10 mg/mL. (D) Direct comparison between cooling and heating DSC experiments with 10 mg/mL solution using a rate of 0.08 °C/s. By using optimal concentration and heating rate, thermograph distortion is limited with relatively small variation of sample's thermodynamic parameters such as the melting point (<3°C), while still maintaining a significant signal to noise ratio. (E) The melting temperature dependence on scan rate, comparing the peaks obtained during heating and cooling can be used to infer the equilibrium transition temperature (rate of zero). The nonlinear dependence of the melting temperature with the scan rate has been previously described [41, 42] as described in Eq. 3.1. In this case, the fitting parameters are $B = 1.2$ and $z = 0.2$ after the fit (see inset). Melting temperatures have been reported with standard deviation calculated from 3 different DSC runs per condition.

### 3.3.5 Optical brightfield microscopy protocol

Images of LMVs have been taken using Eclipse E200 (Nikon) microscope with 10x and 40x phase contrast objectives. Vesicles have been imaged in a tunnel slide prepared as before [2, 43]. Briefly, two parallel strips of double-sided sticky tape have been positioned onto a microscope slide and covered with a 22x40 mm cover glass, which was pressed against the tape to form a tunnel. Approximately 10 $\mu$l of vesicles in solution was added to the tunnel for imaging. Pixel size was calibrated using a coverslip with 10 x 10 grid of 0.1mm squares (Graticules Optics).

### 3.3.6 AFM protocol

Imaging was conducted using a commercial Cypher ES AFM (Oxford Instruments, Santa Barbara, CA, USA), equipped with temperature control. SNL-10 cantilevers (Bruker Scientific Instruments, Billerica, MA, USA) with a nominal spring constant of 0.35 N/m have been used. The tip has a pyramidal shape with a tip radius $\leq 12\ nm$ at its apex. The AFM imaging was performed in amplitude mode, fully immersing the cantilever tip in the liquid. In this mode, the cantilever is acoustically oscillated at a frequency close to its resonance in liquid ($\sim$ 10 kHz).
Force spectroscopy mapping was conducted in contact mode in liquid, using SNL-10 cantilevers. A schematics illustration of the measurement principle is shown in Fig. 3.2. A force map was created from 1024 force curves (32 x 32) over a 25 $\mu m^2$ area. Calibration of the cantilever was performed by determining the inverse optical lever sensitivity by acquiring a force-distance curve on a stiff surface (mica) and the spring constant of each cantilever was determined from their thermal spectrum [44]. This allowed for more accurate derivation of the Young's modulus Y and membrane rupture force $F_r$. Both $Y$ and $F_r$ have been obtained using the same tip for all the measurements to ensure direct comparability between the results, regardless of any possible systematic offset. The emphasis is hence not placed on the absolute stiffness values [45, 46], but rather the relative differences between phases yielding the expected bimodal distribution. To minimise tip damage or contamination, AFM images have been taken before and after the measurement, also ensuring similar membrane's

topographical features. The tip was cleaned with IPA and ultrapure water before starting a new measurement.

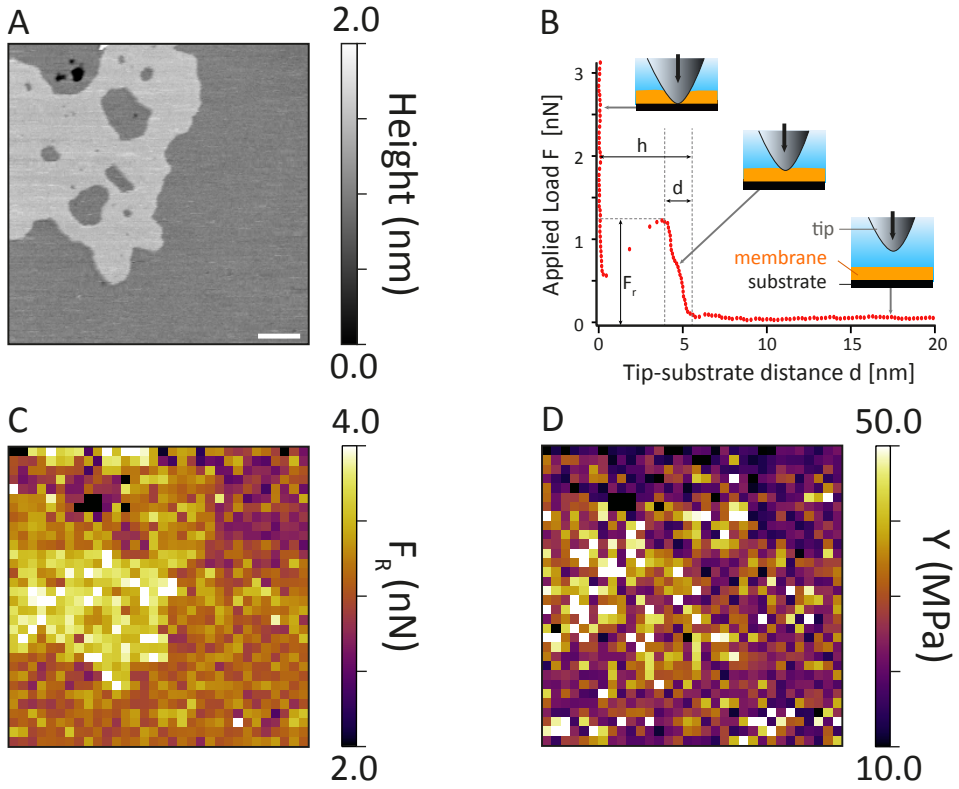


Figure 3.2: AFM force spectroscopy and force map measurement principles. (A) AFM topographical image of one of the analysed ternary mixtures below its melting point. Two lipid phases ($L_o$ and $L_d$ respect. lighter and darker gray) can be seen. (B) Schematic representation of force spectroscopy curve on lipid bilayer with images representing the experimental process. Briefly, when the AFM tip approaches the membrane from the solution, the applied load is zero. Upon contacting the membrane, the applied load begins to increase, compressing and indenting the membrane over a depth $d$, until the applied load is strong enough to puncture through the bilayer (rupture force, $F_r$) and rest on the substrate underneath. From the analysis of the load – tip distance curves, it is possible to estimate the membrane Young's Modulus, $Y$, by fitting the experimental indentation curve with a suitable model (as also discussed in the main text) [47, 48]. The total distance $h \sim 5\ nm$ between the point of membrane contact and the substrate confirms the presence of a single bilayer. (C-D) Force maps performed over the lipid membrane shown in (A) are used to extract $F_r$ and $Y$. The scale bar in (A) is 200 nm.

### 3.3.7 DLS protocol

I have also tried to test the elastic properties of the lipid vesicles using DLS. To do that, vesciles' size has been tracked upon gradual increase of the osmotic pressure. For these experiments, larger vesicles (200 $nm$ size) have been prepared with a similar experimental protocol followed for the SUVs

preparation showed in Section 3.3.2. The newly formed lipid film was rehydrated in 1 mL of MOPS buffer-based solution with 400 mM of NaCl to obtain a final lipid concentration of 1 mg/mL. The vial was then gently bath sonicated for 15 min and finally extruded 31 times using the same Mini-Extruder kit with 1 Whatman 200 $nm$ filter.
Following the vesicle preparation, the size distributions of the lipid vesicles have been determined using a commercial Malvern Zetasizer Nano ZS DLS systems (Malvern Instruments Ltd, UK). Disposable solvent resistant Micro cuvettes ZEN0040 (Malvern Instruments Ltd, UK) have been filled with 1 mL of the desired lipid solution (900 $\mu$L of solvents and 100 $\mu$L of 1 mg/mL 200 $nm$ lipid vesicles). Quickly after loading, samples have been equilibrated for 30 seconds at 37°C and 3 measurements made by 5 recordings of 10 seconds have been acquired for each sample. Considering equilibration time and setting up of the instrument before the start of the measurements, vesicle's size was measured approximately 100 seconds after the osmotic shock. A refractive index of 1.33 and a viscosity of 0.6864 cP have been used for water, while a refractive index $n = 1.38$ was chosen for lipid vesicles based on literature values [49, 50].

### 3.3.8 Data analysis

DSC results have been analysed with the TRIOS Software, provided with the instrument. The software was used to correct thermogram baselines and then obtain $T_m$ at the highest point of each calorimetric peak. DLS data have been collected with the Zetasizer Family Software v.8.01, provided with the instrument. The size and of the vesicles and its uncertainty was obtained by fitting the experimental size histograms with a Gaussian distribution. AFM images and topographical AFM data have been obtained and analysed using the Gwyddion software [51], an open-source modular program for scanning probe microscopy data visualisation and analysis. Optical microscopy images have been analysed using the open-source image processing package ImageJ/FIJI [52]. Graphs have been generated using Igor Pro Software (Wavemetrics, Lake Oswego, OR, US) and Python [53].

## 3.4 Results and discussion

### 3.4.1 Literature review on the composition of *E. coli*'s inner membrane

The starting point for this study is a literature review of previous lipidomic studies of *E. coli*'s inner membrane to identify the main components and their relative fraction in the native membrane. This is consistent with my goal to create a model system that mimics the lipidomic composition of the native membrane. Further, to control the thermal and mechanical properties of the model system, the three most important parameters are: (i) the lipid polar head distribution, as it controls lipid-lipid interactions and charge distribution along the surface, (ii) the acyl chain length, as it controls membrane thickness, fluidity and membrane packing, and (iii) acyl chain saturation degree, because it regulates lipid packing within the bilayer. Taken together, these parameters constitute the major contributors to the specific mechanical properties of the bilayer and thus need to be correctly tuned.

The composition of *E. coli* 's inner membrane obtained from previous lipidomic and mass spectroscopy assays in summarised in Table 3.1, which also includes melting temperatures obtained from previous calorimetric studies [13, 14, 54]. Because at $T_m$ the thermal energy overcomes the internal energy of the membrane, $T_m$ also offers a good indicator of how the membrane behaves mechanically: the internal energy of the membrane is the average inter-lipid interaction energy, influencing molecular order as well as dynamics within the membrane [38], and hence the propagation of any imposed mechanical stress. The results obtained from previous calorimetric studies, which did not use any modification of the membrane such as the addition of markers [55], indicate a $T_m$ value ranging from 7°C to 16°C lower than the growth temperature in the specific media. This depicts *E. coli* membrane as fluid and dynamic, rearranging the membrane composition through epigenetic reprogramming, e.g. in response to growth temperature, to shift its $T_m$ and thus maintain overall fluidity across the range of conditions.

| **Polar head distribution** | | **Lipid chain length** | |
|---|---|---|---|
| **Lipid species** | **Concentration (%)** | **Chain length** | **Concentration (%)** |
| **PE** | 75 [17, 20],70-78 [36], 80 [37], 81.7 [35], 62 [56] | **12C** | 0 [17] |
| **PG** | 19 [17],20 [20],11-18 [36], 15 [37],6.5 [35],14 [56] | **14C** | 4 [17],1-3 [36], 3-5 [54], 4.7 [35] |
| **CL** | 7-12 [36],5 [37],24 [56] | **16C** | 74.7 [17],63.73 [36], 43-74 [37],67.1 [56] |
| | | **17C** | 7-22 [36],7-29 [37],4.4 [56] |
| | | **18C** | 16.3 [17],8-21 [36], 19 [37],23.3 [56] |

(a) Polar head distribution and lipid chain length.

| **Chain saturation degree** | | ***E. coli* membrane $T_m$** | |
|---|---|---|---|
| **Saturation degree** | **Concentration (%)** | $T_G$ **(°C)** | $T_m$ **(°C)** |
| **Saturated** | 48.5 [17], 46-38.9 [18], 47-56 [36], 39.4 [35] | **17** | 10 [13, 14] |
| **Unsaturated** | 46.9 [17], 32.4-3.7 [18], 44-53 [36],64-52 [54], 60.6 [35] | **27** | 15 [13] |
| **Cyclised** | 0.7-32.5 [18] | **37** | 28.5 [13],21.3 [14], 25 [54] |

(b) Chain saturation degree and melting point in *E. coli*'s inner membrane.

Table 3.1: Summary of the *E. coli*'s inner membrane's composition and properties, when grown at standard growth temperature of 37°C (a) and variation of *E. coli* membrane melting temperature based on growth temperature (b). The data compiles results obtained from published literature.

Here, I focus on mimicking membranes at physiological growth temperature (37°C), meaning that the $T_m$ of the model membrane should be lower than at least 30°C while maintaining the lipid polar headgroup ratios, chain's length, and the overall degree of saturation as close as possible to that of the native membrane. From Table 3.1, the reported compositional ratios of *E. coli*'s inner membrane vary up to 20% [17, 20, 36, 37, 56]. However, all results suggest that the main lipid species are phosphatidylethanolamines (PEs, 60-80% molar ratio) followed by phosphatidylglycerols (PGs, 15-30% molar ratio) and other minor lipids. Within these minor species, the most abundant is cardiolipin (CL, $\sim$ 5 %), which plays a crucial role in membrane's physiological behaviour [57–59]. CL has an unusual structure comprising 4 phosphatidyl chains connected through a glycerol linker (Fig. 3.3). The fact that a single headgroup is shared by 4 acyl chains confers unique physical properties to CL which can affect fluidity and charge density across the membrane [59]. Previous studies have also reported a strong link between CL and membrane-protein interaction such as mechanosensitive channels [57]. Furthermore, more than 700 protein-binding

motifs have been identified along CL structure, which emphasises the fundamental bio-functional role of this lipid in the plasma membrane despite its small concentration [58]. I therefore include CL in my candidate model membranes. Apart from CL, most lipids in *E. coli* membrane show long carbon chains (>16C), with an even distribution between saturated and unsaturated lipid chains. Moreover, cyclised lipid chains are found in relatively high concentrations in the inner membrane [18], which significantly reduces bilayer density and lipid packing [22]. Mass spectroscopy analysis have shown that the three most common lipid chains are C16:0, C18:1, and the cyclised C17:1 (cyC17:1) [21]. Ideally, any *E. coli* model membrane should include these chains, but cyclised lipids are rare in other organisms and not commercially available. Keeping in my goal of a simple model system, I focus on more common non-cyclised lipids.

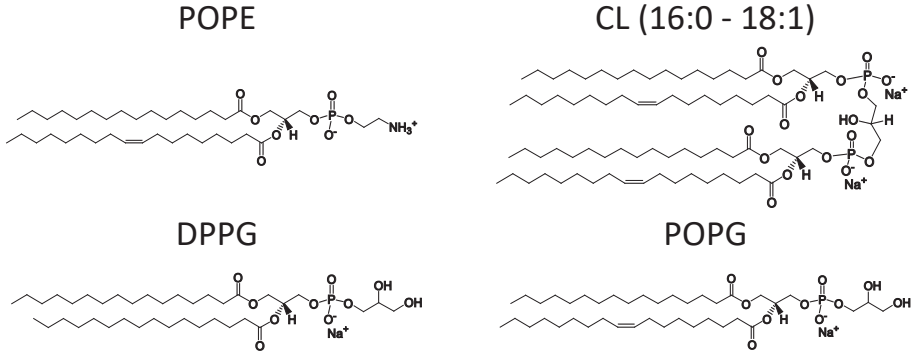


Figure 3.3: Schematic Lewis structure of lipids used to produce my lipid mixtures. Standard abbreviations have been used for the different lipid's name. The molecular structures have been reproduced from the information provided by Avanti Polar Lipid, the company from which the different lipids have been purchased.

I identify 18 possible lipid mixtures that mimic the molar ratios of *E. coli* grown at 37 °C (Table 3.2). Specifically, I use binary and ternary mixtures in the appropriate molar ratios of POPE, POPG, DPPG and CL (16:0-18:1) because they all theoretically match the structural requirements of native *E. coli* membrane (Fig. 3.3). Both POPG and DPPG could work as the PG source for the *E. coli*-like model because they exhibit the most common acyl chains in these bacteria. POPG is often used for its relatively low $T_m$ (-2°C), thus preventing phase separation in the membrane or the formation of ordered raft-like domains. In contrast DPPG has a $T_m = 41$ °C which is more likely to

induce phase separation, but its two saturated acyl chains bring the overall molar ratio of unsaturated chains closer to the native ratio. It should be noted that the charged headgroup that characterises the PG family could help prevent phase separation of DPPG, prompting to keep both POPG and DPPG in my candidate model system.

| Mixture name | POPE (%) | POPG (%) | DPPG (%) | CL (%) |
|---|---|---|---|---|
| 1-A | 80 | 20 | 0 | 0 |
| 1-B | 80 | 0 | 20 | 0 |
| 2-A | 75 | 25 | 0 | 0 |
| 2-B | 75 | 0 | 25 | 0 |
| 3-A | 70 | 30 | 0 | 0 |
| 3-B | 70 | 0 | 30 | 0 |
| 4-A | 60 | 40 | 0 | 0 |
| 4-B | 60 | 0 | 40 | 0 |
| 5-A | 80 | 15 | 0 | 5 |
| 5-B | 80 | 0 | 15 | 5 |
| 6-A | 75 | 20 | 0 | 5 |
| 6-B | 75 | 0 | 20 | 5 |
| 7-A | 70 | 25 | 0 | 5 |
| 7-B | 70 | 0 | 25 | 5 |
| 8-A | 70 | 20 | 0 | 10 |
| 8-B | 70 | 0 | 20 | 10 |
| 9-A | 65 | 25 | 0 | 10 |
| 9-B | 65 | 0 | 25 | 10 |

Table 3.2: Candidate lipid mixture for the model systems for *E. coli*'s inner membrane when grown in physiological conditions (37 °C). Each mixture is of two or three types of phospholipids: POPE, POPG, DPPG and CL (16:0-18:1). Mixtures are indicated with a number and a letter, with the number indicating a specific lipid molar ratio and the letter indicating the specific PG lipid used ("A" being POPG and "B" being DPPG).

### 3.4.2 POPG Ternary mixtures successfully mimic *E. coli*'s inner membrane transition temperature

Having identified candidate model membranes in Table 3.2, I next determine their melting temperatures as the first indicator of the average in-plane molecular interactions. For this purpose, I use lipidic LMVs samples in a MOPS buffer-based solution (see Section 3.3.2) and extract $T_m$ for each sample from the main DSC transition peaks. The composition of MOPS matches the salt concentrations of commonly used *E. coli* growth media [60–62], but without the carbon source, making it a suitable environment for exploring model systems.

And, LMVs are routinely used for this type of measurement because they enhance the signal-to-noise (SN) of the DSC compared to other types of lipid vesicles [39, 63–67]. I selected a heating rate of 0.08 °C/s to ensure on optimal signal to noise ratio, and corrected for kinetic effects [41, 42] to infer the 'true' (i.e. thermodynamic equilibrium) $T_m$ value (Section 3.3.4 and Fig. 3.1).
Apart from each candidate mixture, I analysed by DSC two *E. coli*'s inner membrane extracts as well, used here as references. Hereafter I refer to these references as *E. coli* 'Native' and *E. coli* 'Polar Extract'. The first is a direct lipid extract of the *E. coli*'s inner membrane and the second is an extract further purified by removal of unknown lipid species from the native membrane, but still maintaining the complex mixture of PE and PG phospholipids with the original broad range of acyl chains. Although these commercially available extracts are derived from a combination of the inner and outer *E. coli* membranes, they serve as reliable references for our study. The outer and inner membranes show strong similarity in their lipid composition [13], so this mixed origin does not significantly impact the analysis. The *E. coli* 'Polar Extract' is especially interesting, as the PE and PG class ratios in this preparation align closely with literature-reported values for the inner membrane previously seen in Table 3.1 , allowing it to act as an effective reference model for the inner membrane. Both lipid mixtures have been extracted from *E. coli* B (ATCC 11303) grown in Kornberg Minimal media at 37°C, as described by the commercial provider (see Chapter 3.3 for materials and methods). I note that most studies on *E. coli* membrane lipidomic composition as well as majority of modern-day microbiology studies are on K-12 strain isolates. These two commonly used *E. coli* strains present highly similar genomes, which mainly diverge in their proteomic profiles [68, 69], but no alterations have been detected in their lipidomic profile nor on the key proteins involved in phospholipid synthesis, confirming the highly conserved composition of *E. coli* membrane within different strains. Table 3.3 summarises the DSC results of my mixtures with and without the previously described correction. Predicted $T_m$ values calculated using weighted arithmetic mean [70] are also given where possible but only serve to identify the suitable temperature range for the measurements.

| Mixture name | Predicted $T_m$ (°C) | Experimental $T_m$ (°C) | Corrected $T_m$ (°C) |
|---|---|---|---|
| 1-A | 19.6 | 22.4± 0.2 | 20.7± 0.2 |
| 1-B | 28.2 | 30.8± 0.1 | 29.1± 0.1 |
| 2-A | 18.3 | 21.9± 0.2 | 20.0± 0.2 |
| 2-B | 29 | 30.3± 0.2 | 28.6± 0.2 |
| 3-A | 16.9 | 20.1± 0.2 | 18.4± 0.2 |
| 3-B | 29.8 | 31.7± 0.2 | 30.0± 0.2 |
| 4-A | 14.2 | 17.7± 0.1 | 16.0± 0.1 |
| 4-B | 31.4 | 34.7± 0.4 | 33.0± 0.4 |
| **5-A** | - | **22.6± 0.2** | **20.9± 0.2** |
| 5-B | - | 29.0± 0.3 | 27.3± 0.3 |
| **6-A** | - | **22.9± 0.2** | **21.2± 0.2** |
| 6-B | - | 30.7± 0.2 | 29.0± 0.2 |
| 7-A | - | 25.2± 0.2 | 23.5± 0.2 |
| 7-B | - | 31.2± 0.2 | 29.5± 0.2 |
| 8-A | - | 23.5± 0.2 | 21.8± 0.2 |
| 8-B | - | 30.3± 0.1 | 28.6± 0.1 |
| **9-A** | - | **22.3± 0.3** | **20.6± 0.3** |
| 9-B | - | 31.2± 0.2 | 29.5± 0.2 |
| ***E. coli* Native** | - | **22.7± 0.3** | **21.0± 0.3** |
| ***E. coli* Polar Extract** | - | **20.7± 0.4** | **19.0± 0.4** |

Table 3.3: Candidate lipid mixtures with melting temperatures theoretically calculated and experimentally evaluated with and without considering DSC scan rate effects. The reported experimental melting point temperatures are obtained through DSC experiments and the correction factor was calculated as described in Fig. 3.1 E. Not all the theoretical $T_m$ have been calculated since no information regarding the melting of pure CL is available to the best of my knowledge.

Mixtures containing POPG shows a significantly lower melting point compared to those with DPPG with an average 8 to 10°C gap between equivalent mixtures (Fig. 3.4A-B). These differences are in line with the significant $T_m$ difference between the two pure lipid species and suggest their homogeneous mixing in POPE. The presence of a unique main peak in the DSC curves further confirms homogenous mixing (Fig. 3.4A-B). If phase separation between components had occurred, I would expect to observe two distinct transitions, corresponding to the individual melting events of POPE and POPG. This observation is backed up by an average change in enthalpy of 15-43 kJ/mol as shown in Fig. 3.4C, which is generally associated with the melting of a lipid membrane [71].

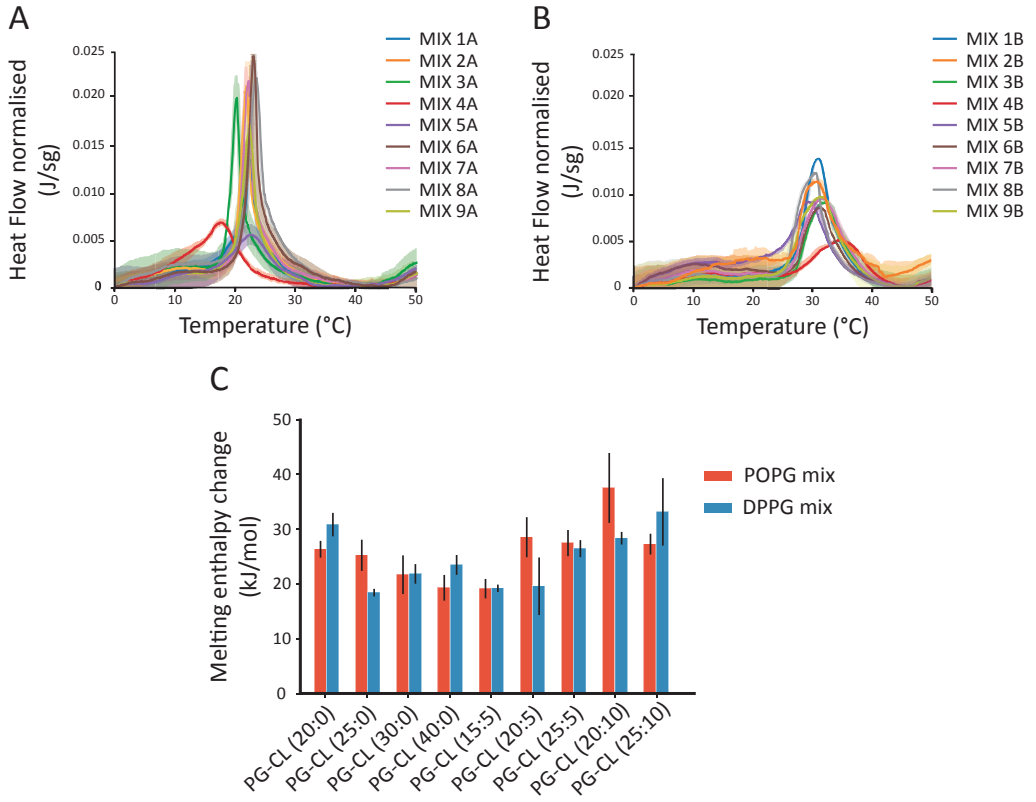


Figure 3.4: DSC thermographs of LMVs solution made of POPG (A) and DPPG (B) based mixtures. The average curve for each mixture has been plotted with standard deviation (shaded areas around average curves) and a single main peak can be observed, confirming the homogenous phase transition of the tested mixtures. (C) Plot showing the average melting enthalpy change associated with each DSC main transition peak with standard deviations. The enthalpy change ranges between 15 and 43 kJ/mol, as suggested by the literature [71]

Fig. 3.5A-C visually summarises all my candidate samples and Fig. 3.5D shows the results from my DSC analysis for each of them. *E. coli* Native and *E. coli* Polar Extract mixtures exhibit $T_m = 22.7 \pm 0.3$ °C and $T_m = 20.7 \pm 0.4$ °C, respectively. The result is in line with previous lipidomic studies (Table 3.1) and used here as a guide to set the desired $T_m$ I expect from my model system. All mixtures exhibit a $T_m$ lower than 37°C — my reference *E. coli* growth temperature -– in principle making all the mixtures still eligible for my model. Ternary mixtures exhibit more complex behaviour, without an obvious $T_m$ trend emerging. This is in line with previous studies that investigated the phase transition of CL containing bilayers and found heterogeneous behaviour. For example, CL molecules can elevate the $T_m$ from -20°C in the absence of cations, up to 30°C in their presence -– a $T_m$ even higher than for their corresponding diacyl phosphatidylglycerols [72]. Moreover, CL exhibits a small, poorly flexible structure that drives complex – and not yet fully understood – interactions with

both different and similar lipids in the bilayer. Depending on the bilayer composition, CL can be homogenously dispersed within the bilayer [73], or separate in CL-enriched domains [74]. The highly heterogeneous and not fully understood nature of CL renders its effect on membrane fluidity challenging to predict and explain compared to simpler phospholipids.

Comparing my results to both *E. coli* Native and *E. coli* Polar Extract mixture rules out the possibility of using DPPG as a PG source for my model membrane, presumably reflecting more ordered structures than in the native bilayers. However, mixtures with DPPG do not appear to phase separate despite their high $T_m$, but may form a molecularly well-packed homogenous membrane. The best match to my *E. coli* mixture references is obtained for 3 different ternary mixtures of phospholipids: 80% POPE, 15% POPG and 5% CL (composition 5-A in Table 3.2), 75% POPE, 20% POPG and 5% CL (composition 6-A in Table 3.2) and POPE 65%, 25% POPG and 10% CL (composition 9-A in Table 3.2).

It is worth noting that two binary mixtures match the native membrane behaviour: 80% POPE and 20% POPG (composition 1-A in Table 3.2) and 75% POPE and 25% POPG (composition 2-A in Table 3.2). These mixtures still reflect molecular ratios of the most abundant lipids reported for *E. coli*, are able to reproduce the $T_m$ of my reference samples, and might hence be sufficient for some studies provided the other biophysical properties also match those of the native membrane. However, this would need some caution since the lack of CL that could significantly influence any protein-related studies [57]. It is also worth noting that the most recent study on the PE composition of *E. coli* membrane, reports about 60% PE for the inner membrane, and claims previous estimates of 75-80% are an overestimate [56]. In this scenario, and particularly if further confirmed by future studies, my results would suggest a unique candidate for *E. coli* model membrane, which is POPE 65%, 25% POPG, and 10% CL (composition 9-A in Table 3.2). Interestingly, this mixture nicely matches the phosphate headgroup distribution of the *E. coli* Polar Extract (PE 67%, PG 23% and CL 10% as reported on its data sheet), backing up the validity of my results.

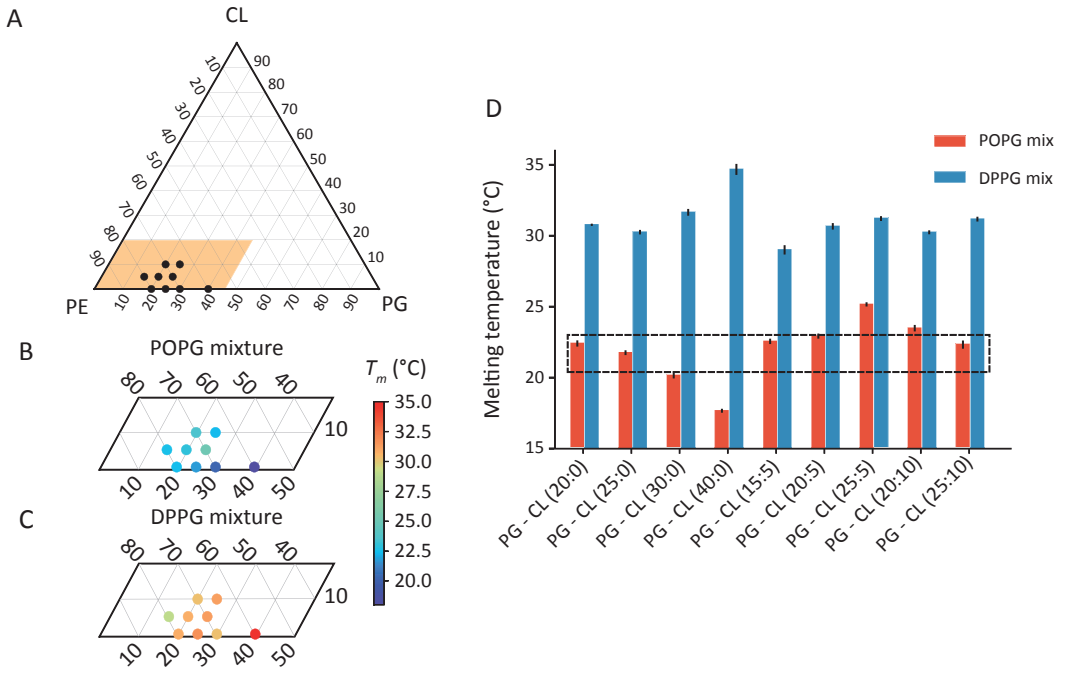


Figure 3.5: Melting temperature analysis of artificial lipid vesicles based on physiological *E. coli*'s inner membrane's compositions. (A) Ternary diagrams of PE-PG-CL model systems explored showing the physiological composition range of *E. coli*'s inner membrane. (B-C) Zoom in the ternary diagrams of POPG (B) and DPPG (C) based mixtures together with the melting temperature (obtained as discussed in the text and Materials and Methods) in each case. (D) DSC results displaying differences between POPG and DPPG systems and highlighting the native *E. coli*'s inner membrane ranges based on literature and reference experiments (dashed box).

### 3.4.3 Candidate mixtures form stable model membrane systems

Before measuring the mechanical properties of my candidate model systems, it is necessary to demonstrate that the mixtures can indeed form stable and homogenous unilamellar vesicles, as well as smooth, stable supported lipid bilayers. The formation of stable and homogenous SLBs from SUV deposition is not trivial because CL can affect the bilayer fluidity, evolution and membrane packing [75], sometimes inducing some molecular rearrangement over time and precluding the formation of stable flat SLBs [76]. Additionally, the formation of SLBs with PE and PG has been previously reported as challenging due to the negative charge of the PG headgroups, the conformation of POPE/POPG molecules [76] and the effect of PE lipids on membrane curvature [77]. To confirm the formation of stable and homogenous SUVs, I used optical

microscopy, illustrated in Fig. 3.6A-B for LMVs of composition 6-A (Table 3.2), revealing rounded vesicles which have been stable for at least 14 days. Similarly, AFM imaging of supported candidate membranes (Fig. 3.6C) reveal smooth, stable patches. Here, SLBs have been formed on an atomically flat mica using extruded 100 $nm$ SUVs (see Chapter 3.3 for materials and methods). By working at a relatively low SUV concentration, isolated membrane patches could be formed and imaged at 40°C, to confirm the formation of a single stable lipid bilayer in fluid phase. The patches thickness of 4.7± 0.1 $nm$ is in line with the expected thickness for such fluid bilayers [78] (Fig. 3.6D). Increasing the SUV concentration enabled full substrate coverage with a membrane showing only minor defects.

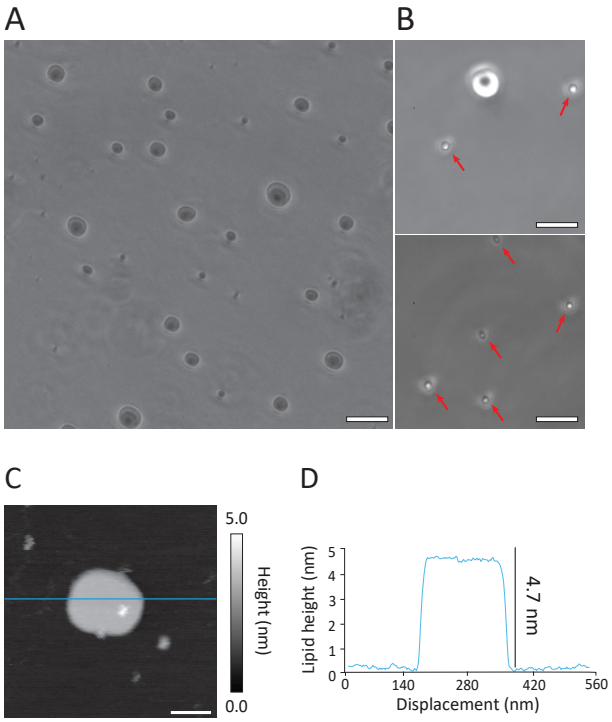


Figure 3.6: Demonstration of stable membrane formation with candidate mixtures. In bulk solution (A-B), optical microscopy (phase contrast) shows the formation of stable vesicular model membrane systems for the ternary POPE-POPG-CL mixture. Images of spherical ternary mixture's lipid vesicles have been taken with X10 (A) and 40X (B) objectives. 1 $\mu m$ size vesicles have been indicated with red arrows for clarity (B). The vesicles have been stable up to two weeks after the preparation. Stable membranes could also be formed supported on a mica substrate in solution (C-D) with patches of ternary POPE-POPG-CL mixture using low concentrated SUVs solution deposition. AFM imaging (C) reveals the thickness of a typical patch which can be quantified from the associated line profile (D). The scale bars are 50 $\mu m$ (A - 10X objective), 13 $\mu m$ (B – 40x objective) and 100 $nm$ (C).

Having confirmed the formation of stable and homogenous SUVs, as well as smooth and stable SLBs I now aim to consider mechanical properties of my model system candidates explicitly. Following the theoretical description seen in Section 1.5.2, I start by taking into account the Helmholtz free energy of a deformed *E. coli*'s inner membrane, which consists of the pressure, bending, and stretching/compression elastic energies [79, 80]. Ordinarily, *E. coli* cells are within 0.3 and 3 atm of osmotic pressure [81, 82], and it is this pressure that leads to mechanical stress in the membrane. While I mentioned such stress can be described via both the bending and stretching energy, because *E. coli* is a spherocylindrical cell 1-3 $\mu m$ in length and approximately 1 $\mu m$ in width, the inner membrane curvature is low compared to naturally occurring entropic membrane fluctuations [82, 83], and thus the bending energy can be neglected. I am, therefore, left with the elastic stretching/compression energy of the membrane under mechanical deformation. Fluid membranes cannot support in-plane shear [84] and the associated shear modulus is hence usually taken as zero.

### 3.4.4 Mixtures mimic the mechanical properties of *E. coli*'s inner membrane

#### *Perpendicular compression of the membrane*

To probe elastic properties of my candidate model systems under compression I use the nano-indentation of supported membranes with an AFM: the membrane is compressed perpendicularly, squeezed between a nanosphere and a hard substrate. Assuming the membrane to be homogenous and isotropic, its Young's modulus $Y$ (effectively an elasticity modulus in a spring analogy) can be calculated from the out-of-plane compression force at different indentation depths. In practice, it is necessary to take into account the finite thickness of the membrane and the hard substrate, bringing corrections [47, 85] to the established Hertz indentation model for a semi-infinite medium [48]. Here I use the following relationship between the applied force $F_{sphere}$, the indentation depth $\delta$, the size of the indenting sphere $R$, and membrane thickness $h$ [47]:

$$F_{sphere} = \frac{16}{9} Y \sqrt{R\delta^3} \left[ 1 + \frac{1.133\sqrt{\delta R}}{h} + \frac{1.497\delta R}{h^2} + \frac{1.469\delta R\sqrt{\delta R}}{h^3} + \frac{0.755\delta^2 R^2}{h^4} \right] \tag{3.2}$$

where $\delta \leq R$. This formula was derived assuming that the Poisson ratio, which couples in-plane and out-of-plan strain is exactly $v$= 0.5. In other words, the membrane is assumed incompressible with its volume conserved under compression. This assumption is common for bio-systems [86] and while usually a good approximation, it is not necessarily exact [87, 88]. In practice, the indentation of the membrane is carried out with an AFM tip, and while ensuring a linear indentation regime [85] to derive $Y$. I probed the Young's modulus of mixtures 6A and 9A and compared them with that of the *E. coli* Native and *E. coli* Polar extract obtained in the same manner. The mechanical assays have been also performed on two negative controls: a DPPG-based mixture 2B and a pure POPE membrane with both controls being stable when supported by a substrate. In all cases, I distinguished the liquid-disordered ($L_d$) and liquid-ordered ($L_o$) phases and conducted measurements on both separately. The $L_o$ domains are revealed upon cooling of the sampled below its $T_m$, with the $L_o$ appearing 0.5 $nm$ to 0.7 $nm$ thicker than the remaining $L_d$ phase membrane (example of SLB image in Fig. 3.2). This is consistent with the expected lipid height variation between the two phases [89, 90].

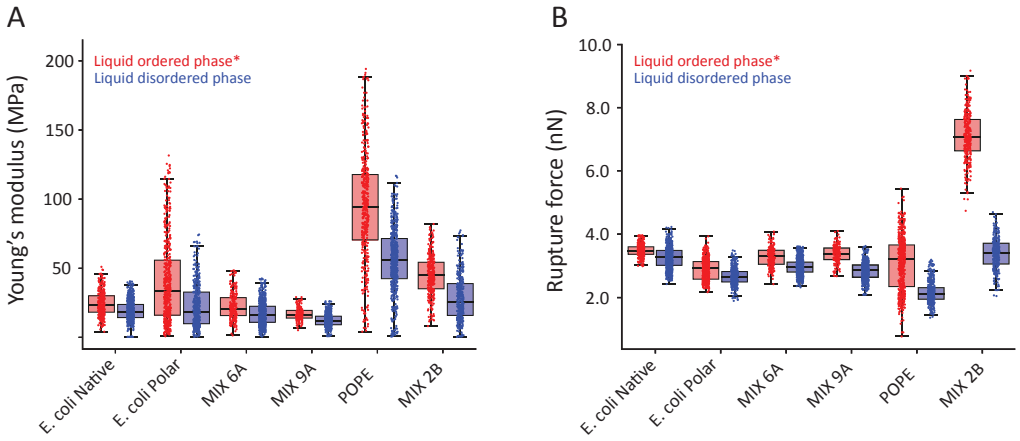


Figure 3.7: Analysis of the native and candidate membranes using AFM nanomechanical indentation. (A) Membrane average Young modulus, calculated from the indentation region of the curves (elastic indentation) and assuming a spherical tip (radius 12 nm, from manufacturer). The results confirm the mechanical similarities between the *E. coli* references and two candidate ternary POPE-POPG-CL mixtures. (B) Increasing the indentation force beyond the elastic region results in the tip puncturing the membrane. The rupture force is simply the force required to break through the lipid bilayer with the AFM tip. For (A) and (B), the data is present as boxplots distinguishing $L_o$ and $L_d$ phases. In this case, upper and lower whiskers extend to the furthest data point that is within 1.5 times the inter-quartile range, indicating the variability outside the upper and lower quartiles respectively. Note: for membrane composed of a single type of lipid (POPE), the liquid-ordered phase is solid and called 'gel phase'. The overlayed scatter plot shows the nanomechanical values for each single indentation performed on the membrane. Examples of force maps and measurement principle are illustrated in Fig. 3.2.

I then performed so-called force maps [45, 91] whereby force-distance curves – the resistance force experienced by the tip (applied load) as it presses on the membrane – are systematically acquired across randomly selected areas of the membrane. From each curve, I immediately get the rupture force $F_r$ [89] necessary for the tip to break through the membrane, and can calculate $Y$ from Eq. 3.2 (Fig. 3.7). The *E. coli* extracts, and my two candidate mixtures show comparable values on the $L_d$ phase (Y $\sim$ 17.5 MPa and $F_r \sim$ 3.0 nN) and the more ordered $L_o$ phase (Y $\sim$ 25.8 MPa and $F_r \sim$ 3.4 nN). This similarity in mechanical properties is meaningful, as confirmed by the significantly differences derived for the two negative controls: the pure POPE and the DPPG-based samples.

***In-plane stretching/compression of the membrane***

The AFM measurements use perpendicular indentation under the relatively slow indentation velocities (<1$\mu m$/s) to provide a single elasticity modulus of the membrane. In many experiments, it is, however, the in-plane stretching/compression elasticity of the membrane that is relevant. Following the description in Section 1.5.2, under the same linear elasticity assumptions [79, 92] used previously and assuming the membrane to behave as a 2D material, the in-plane stretching energy is considered [79, 92]:

$$F = \frac{1}{2}\lambda\mu_{ii}^2 = \frac{K_a}{2}\int\left(\frac{\Delta A}{A}\right)^2 dA \tag{3.3}$$

where $\mu$ is the strain tensor, $\lambda$ first Lame coefficient, $K_a$ is equivalent to $\lambda$ and often referred to as the expansion modulus [93] or elastic area compressibility [94–96] and $A$ is the surface area of the membrane. Since I have assumed the membrane behaves as a homogenous isotropic solid, the simplest model for it, with an equivalent in elastic theory, is a thin plate [93, 97]. Then, $K_a$ and $Y$ can be related with a well-known relationship:

$$K_a = \frac{Yh}{2(1-v)} \tag{3.4}$$

with $h$ the membrane thickness and $v$ the Poisson ratio. Taking $v$=0.5 and $h$= 4.7 $nm$ (obtained in Fig. 3.7D) allows calculation of a $K_a$ from the measured $Y$. The result, given in Fig. 3.8, suggests $K_a$ values slightly lower than the average 0.2 N/m values obtained from previous reports [94–96, 98, 99], where both artificial lipid vesicles and native *E. coli* spheroplast [100] have been measured through micropipette aspiration. However, my results still match the correct order of magnitude and fit within the expected range between 0.1 N/m and 0.2 N/m. Thus, both my out-of-plane and in-plane mechanical measurements/estimates support mixtures 6A and 9A as suitable composition to reproduce the biophysical properties of *E. coli*'s membrane lipids. Specifically, the match between the mechanical properties of mix 6A, 9A and *E. coli* Polar mixture suggest the similarity of these lipid compositions with the *E. coli*'s inner membrane.

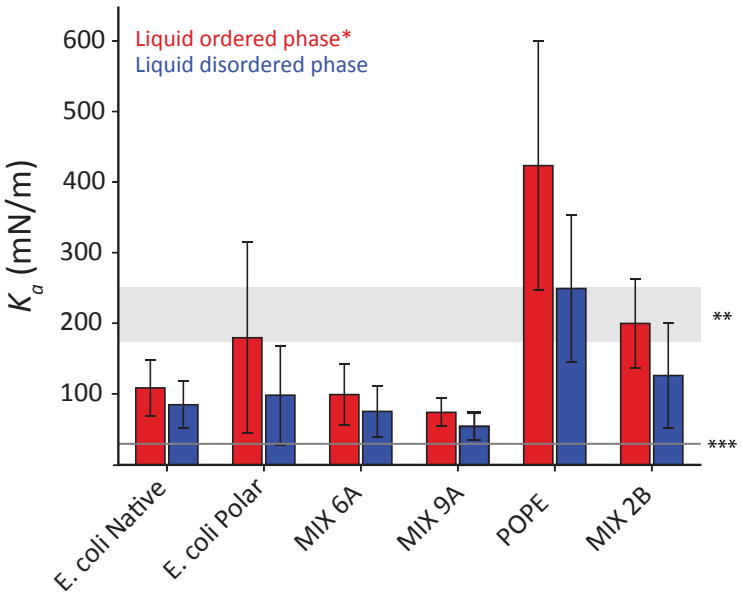


Figure 3.8: Comparison of the elastic area compressibility, $K_a$ values derived from the values obtained for Young's modulus, $Y$. The values are derived separately for the $L_o$ and $L_d$ domains of the different candidate membranes using Eq. 3.4 in conjunction with the data of Fig. 3.4 A and standard deviation has been used as error bar. Values from a previous study [100] have been used to visually compare my $K_a$ results.
** $K_a$ values for artificial giant lipid vesicles (light grey box), *** $K_a$ values for metabolically active *E. coli* spheroplast (dark grey light), confirming the correct order of magnitude of my results that fits within this range.

The indirect measurement of membrane area expansion modulus, $K_a$ , through vesicle response upon stretching can also be assessed directly using other methods, as previously discussed in Section 1.5.2. Tracking the size of lipid vesicles upon external stimuli represents a possible approach [95, 101], beyond the most common micropipette aspiration [93, 94, 100, 102]. Here, I generated monodispersed unilamellar vesicles of approximately 200 *nm* diameter in a high-salt solution (400 mM NaCl, as illustrated in Fig. 3.9A). By diluting the NaCl concentration in the surrounding solution, the vesicles experience osmotic pressure changes, resulting in size expansion that is measurable via dynamic light scattering (DLS). The 200 *nm* size choice was crucial for consistency, as larger vesicles could not be reproducibly prepared (Fig. 3.9B). Following this setup, I compared the behaviour of the candidate lipid mixtures with vesicles made from both *E. coli* Native and *E. coli* Polar extracts, alongside negative control mixtures. As NaCl concentration in the vesicle medium decreases, water influx across the membrane causes vesicle expansion, which is then tracked

(example of vesicles enlargement is shown in Fig. 3.9C).

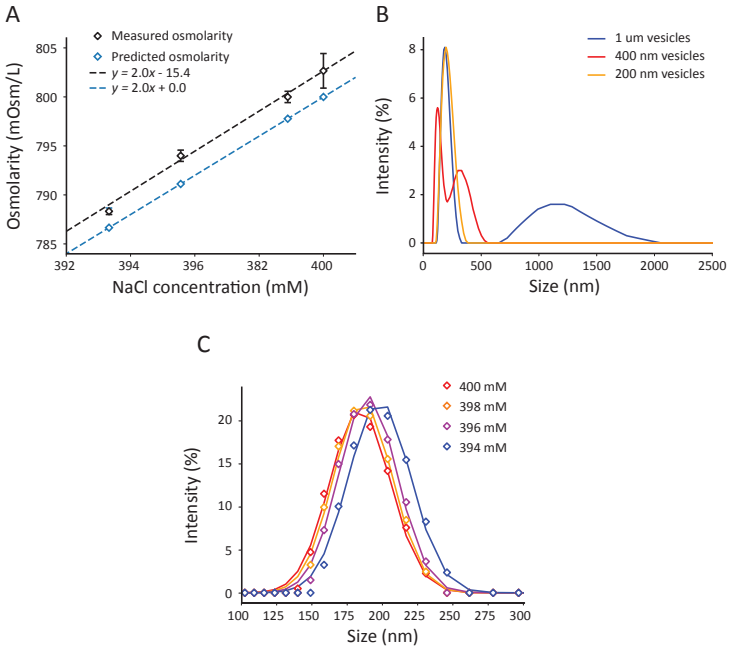


Figure 3.9: Preliminary experiments and examples of vesicles' size analysis with DLS. (A) Osomolarity check of the 400 mM NaCl solution prepared with different dilutions. (B) Vesicles do not form stable structures above 200 nm. Although the lipid solutions have been extruded using filter of different pore size, vesicles seem to preferentially form 200 *nm* size systems. (C) Example of vesicles' DLS signal. As the concentration of NaCl in the solvent is diluted, vesicles enlarge thanks to the water influx.

Data analysis was based on established literature methods [94–96, 99–101], where the osmotic pressure ($\Delta p$) is simply related to the tension ($\tau$) in the membrane through the Laplace equation which for a vesicle of radius $R$ yields:

$$\Delta p = \frac{2\tau}{R} \tag{3.5}$$

Given that $\Delta p$ and $R$ are either controlled or measured, $\tau$ can be calculated directly, allowing us to derive the apparent $K_a$ value of the vesicles through Eq. 1.15 (Fig. 3.10).

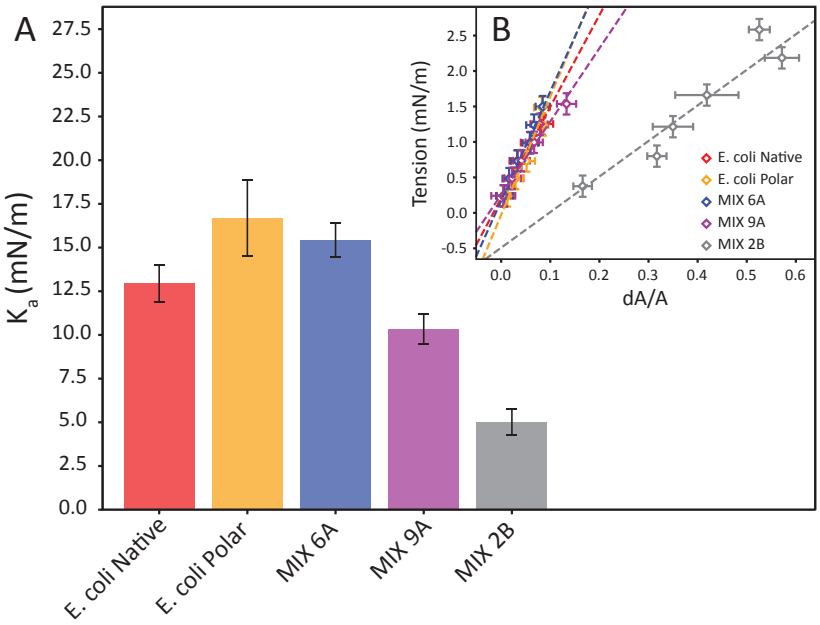


Figure 3.10: Expansion modulus $K_a$ of the candidate and *E. coli* membranes from osmotic shock measurements with DLS. (A) Scatter plot showing the measured increase in membrane tension as a function of the normalised vesicles enlargement ($dA/A_0$). Dashed lines represent linear fits of each data set, imposing for the curves to go through the origin (no area change if no osmotic is applied). The value of $K_a$ in each case is simply the gradient of the curve [100]. (B) Bar plot of the $K_a$ values derived for the vesicles prepared with the two *E. coli* extract, two candidate mixtures (MIX 6A and MIX 9A) and one negative control (MIX 2B).

Results show a similar response in osmotic stress for candidate mixtures and *E. coli* extract vesicles, with $K_a$ values ranging between 10–20 mN/m, aligning with the trend observed in Fig. 3.7 and 3.8. In contrast, MIX 2B exhibits a significantly less elastic membrane ($K_a$ =5 mN/m). Pure POPE vesicles have been also tested but failed to remain stable in high NaCl concentrations, aggregating within minutes and precluding meaningful measurements. Interestingly, $K_a$ values obtained here are approximately an order of magnitude lower than the predicted ones [100]. This suggests that small shocks ($\sim$ 1mM to 6mM) cause a significant enlargement of the vesicles which grows linearly with the osmotic pressure (Fig. 3.10B), but reaching relative expansions that exceed

the one that can be found in the literature [100]. This suggests that this DLS-based method may overestimate initial expansion due to limitations in directly tracking vesicles' equilibrium state, unlike single-vesicle micropipette aspiration. Measurements have been taken within minutes of exposure to NaCl dilution, likely reflecting maximal initial expansion before vesicles reach a final equilibrium state. Previous research [101] reported meaningful measurements only after 1–2 days of equilibration, an impractical and demanding duration for this study.Additionally, the vesicle population analysed by DLS may not be strictly monodisperse. As DLS signal intensity scales with the sixth power of particle size, larger vesicles within a polydisperse distribution could disproportionately bias the measurement, artificially inflating the apparent expansion. This reinforces the limitations of bulk methods like DLS and highlights the importance of directly tracking single-vesicle behaviour to ensure accurate interpretation of vesicle mechanics under osmotic stress. Finally, fusion between vesicles or transient pore formation may also contribute to the observed expansion [103]. Addressing these factors and testing the hypotheses above would require continuous observation of vesicles under controlled conditions. In future experiments, micropipette aspiration would provide a more robust single-vesicle approach to these measurements, though this specialised instrumentation was not available for this study.

## 3.5 Summary

In this Chapter, I have developed model systems that mimic *E. coli*'s inner membrane lipid composition and mechanical properties based on commercially available lipid mixtures. I find that DPPG is not suitable as a PG source for model *E. coli* membranes under standard growth conditions. Instead, my results indicate the suitability of three ternary mixtures of POPE, POPG and CL as model systems. The mixtures form stable bilayers both in bulk solution and supported. They also match the composition of *E. coli* membrane's main lipid constituents, the melting temperature of the membrane and its mechanical properties. The fact that the model systems reproduce the main elements of the membranes' biomechanical proprieties may help future studies where active molecules or forces are at play. For example, I anticipate use of the model

systems for investigations of force transduction within membranes, in particular active response to stimuli achieved through integral proteins such as mechanosensitive channels and PIEZO proteins. The transduction and lateral transfer of forces over suitable range and with relevant magnitude, relies on a complex interplay hinging on the local molecular interactions [104] – the local biomechanical properties of the membrane. In the case of *E. coli*, the dynamical shift of $T_m$ as a function of the growth environment indicates a clear correlation between the membrane functionality, the activity of embedded macromolecules and the overall physiological transduction of these stimuli across the cell. Generally, the detection and propagation of mechanical stimuli over controlled distances remains an active research topic with many open questions related to mechano-transduction and the function of these proteins [104, 105]. The model systems could also be used to investigate the passive mechanisms behind lipid bilayer asymmetry, an intrinsic property of biological membranes [30], and its effects on the functional features of native membranes. Recent work [106] highlighted how CL can show leaflet preferentiality depending on vesicles curvature, suggesting the possibility of developing model membrane system with controlled compositional asymmetry that could be employed to explore this phenomenon in future work. Additionally, more sophisticated models will be needed to account for the significant local variations in native membrane's macromolecular content [107]. This is important to underpin experimental [108, 109] and computational [105] studies. On the other hand, a simpler bi-component mixture comprising only POPE and POPG could also match native *E. coli* 's transition temperature, suggesting its useful for more basic studies where specific molecular interactions or proteins activity is not crucial. Lastly, I note that the consistency between the $L_o$ and $L_d$ measurements and the general agreement with existing literature supports my present approach when estimating $K_a$, even if it is a simplification, the results need to be taken with caution because the lipid bilayer is not an isotropic 3D material as assumed with the thin plate model.

# References


[1] C. Hammond. In: *Cellular and Molecular Neurophysiology: Fourth Edition*. Academic Press, 2015, 39–54.

[2] J. Rosko et al. *PNAS*, 2017, 114, E7969–E7976.

[3] K. I. M. Cooper and E. Jakobsson. *Prog Biophys Molec Biol*, 1985, 46, 51–96.

[4] R. Santos et al. *Nat Rev Drug Discovery*, 2016, 16, 19–34.

[5] K. Sato et al. *Nature*, 2008, 452, 1002–1006.

[6] I. Khmelinskii and V. I. Makarov. *Sci Rep*, 2020, 10, 1–9.

[7] C. Laroche et al. *App Microbiol Biotech*, 2001, 56, 249–254.

[8] J. G. Dumortier et al. *Science*, 2019, 365, 465–468.

[9] J. L. Maître and C. P. Heisenberg. *Curr Opin Cell Biol*, 2011, 23, 508–514.

[10] F. C. Tsai and G. H. Koenderink. *Soft Matter*, 2015, 11, 8834–8847.

[11] A. Mogilner and G. Oster. *Biophys J*, 1996, 71, 3030–3045.

[12] W. Kühlbrandt. *Ann Rev Biochem*, 2019, 88, 515–549.

[13] H. Nakayama et al. *Biochim Biophys Acta, Biomembr*, 1980, 601, 1–10.

[14] T. Mužić et al. *Biochim Biophys Acta, Biomembr*, 2019, 1861, 183026.

[15] A. B. Carey, A. Ashenden, and I. Köper. Vol. 14. 1. Springer Berlin Heidelberg, 2022, 111–143.

[16] E. Krok et al. *Biochim Biophys Acta, Biomembr*, 2023, 1865, 184194.

[17] S. Morein et al. *J Biol Chem*, 1996, 271, 6801–6809.

[18] M. A. Casadei et al. *App Environ Microbiol*, 2002, 68, 5965–5972.

[19] K. Pluhackova and A. Horner. *BMC Biol*, 2021, 19, 1–22.

[20] C. Sohlenkamp and O. Geiger. *FEMS Microbiol Rev*, 2015, 40, 133–159.

[21] D. Oursel et al. *Rapid Communications in Mass Spectrometry*, 2007, 21, 1721–1728.

[22] K. R. Pandit and J. B. Klauda. *Biochim Biophys Acta, Biomembr*, 2012, 1818, 1205–1210.

[23] J. Shearer et al. *J Chem Phys*, 2020, 153.

[24] H. Hwang et al. *Biochim Biophys Acta, Biomembr*, 2018, 1860, 2566–2575.

[25] T. J. Piggot, D. A. Holdbrook, and S. Khalid. *Biochim Biophys Acta, Biomembr*, 2013, 1828, 284–293.

[26] K. Murzyn, T. Róg, and M. Pasenkiewicz-Gierula. *Biophys J*, 2005, 88, 1091–1103.

[27] S. Li et al. *Membranes*, 2022, 12, 906.

[28] B. Kiss et al. *Nanoscale Adv*, 2021, 3, 755–766.

[29] T. Zhang et al. *Sci Rep*, 2019, 9, 1–13.

[30] M. Bogdanov. *Emerging Topics in Life Sciences*, 2023, 7, 137–150.

[31] G. Carranza et al. *Biochim Biophys Acta, Biomembr*, 2017, 1859, 1124–1132.

[32] S. Lopes et al. In: *Anal BioanalChem*. Vol. 398. 3. Oct. 2010, 1357–1366.

[33] M. Bogdanov, E. Mileykovskaya and W. Dowhan. *Sub-cellular Biochemestry*, 2004, 32, 1051–1056.

[34] Y.-H. M. Chan and S. G. Boxer. *Curr Opin Chem Biol*, 2007, 11, 581–587.

[35] E. J. Lugtenberg and R. Peters. *Biochim Biophys Acta, Lipids Lipid Metab*, 1976, 441, 38–47.

[36] A. Shokri and G. Larsson. *Microb Cell Fact*, 2004, 3, 1–12.

[37] P. M. Oliver et al. *J Bacteriol*, 2014, 196, 3386–3398.

[38] G. Cevc. *Biochemistry*, 1991, 30, 7186–7193.

[39] R. Baccouch et al. *Biochim Biophys Acta, Biomembr*, 2023, 1865.

[40] C. B. Giuliano et al. *ChemSystemsChem*, 2021, 3.

[41] A. Toda, M. Hikosaka, and K. Yamada. *Polymer*, 2002, 43, 1667–1679.

[42] A. Toda. *J Therm Anal Calorim*, 2016, 123, 1795–1808.

[43] E. Krasnopeeva, C. J. Lo, and T. Pilizota. *Biophys J*, 2019, 116, 2390–2399.

[44] H. J. Butt and M. Jaschke. *Nanotechnology*, 1995, 6, 1–7.

[45] L. Picas, P.-E. Milhiet, and J. Hernández-Borrell. *Chem Phys Lipids*, 2012, 165, 845–860.

[46] C. Gabbutt et al. *Sci Rep*, 2019, 9, 1–8.

[47] P. D. Garcia and R. Garcia. *Biophys J*, 2018, 114, 2923–2932.

[48] H. Hertz. *Journal fur die Reine und Angewandte Mathematik*, 1882, 1882, 156–171.

[49] J. Eisermann et al. *RSC Chem Biol*, 2023, 4, 386–398.

[50] D. L. M. Rupert et al. *Langmuir*, 2018, 34, 8522–8531.

[51] D. Nečas and P. Klapetek. *Cent Eur J Phys*, 2012, 10, 181–188.

[52] J. Schindelin et al. *Nat Methods*, 2012, 9, 676–682.

[53] G. V. Rossum and F. L. Drake. *Bioinf*, 2006, 22, 9117–9129.

[54] M. B. Jackson and J. E. Cronan. *Biochim Biophys Acta, Biomembr*, 1978, 512, 472–479.

[55] X. Jiang et al. *Sci Rep*, 2018, 8, 1–10.

[56] M. Bogdanov et al. *Sci Adv*, 2020, 6.

[57] P. Ridone et al. *Eur Biophys J*, 2015, 44, 567–576.

[58] R. A. Corey et al. *Sci Adv*, 2021, 7, 1–10.

[59] S. Lopes, G. Ivanova, and B. de Castro. *Biochim Biophys Acta, Biomembr*, 2018, 1860, 2465–2477.

[60] F. C. Neidhardt, P. L. Bloch, and D. F. Smith. *J Bacteriol*, 1974, 119, 736–747.

[61] M. Scott et al. *Science*, 2010, 330, 1099–1102.

[62] T. Honda et al. *PNAS*, 2022, 119, 1–8.

[63] R. L. Biltonen and D. Lichtenberg. *Chem Phys Lipids*, 1993, 64, 129–142.

[64] K. A. Okotrub et al. *Biochim Biophys Acta, Biomembr*, 2021, 1863, 183514.

[65] J. Drazenovic et al. *Biochim Biophys Acta, Biomembr*, 2015, 1848, 532–543.

[66] R. N. Mcelhaney. *Chem Phys Lipids,* 1982, 30, 229–259.

[67] M. Chiu and E. Prenner. *Journal of Pharmacy and Bioallied Sciences*, 2011, 3, 39–59.

[68] M. J. Han. *J Biosci Bioeng*, 2016, 122, 1–9.

[69] S. H. Yoon et al. *Gen Biol*, 2012, 13.

[70] R. J. Cordina, B. Smith, and T. Tuttle. *J Phys Chem B*, 2023.

[71] G. Cevc and D. Marsh. *J Cell Sci*, 1988, 6, 147–147.

[72] R. N. Lewis and R. N. McElhaney. *Biochim Biophys Acta, Biomembr*, 2009, 1788, 2069–2079.

[73] S. Nichols-Smith, S. Y. Teh, and T. L. Kuhl. *Biochim Biophys Acta, Biomembr*, 2004, 1663, 82–88.

[74] Ò. Domènech et al. *Biochim Biophys Acta, Biomembr*, 2006, 1758, 213–221.

[75] B. A. Wilson, A. Ramanathan, and C. F. Lopez. *Biophys J*, 2019, 117, 429–444.

[76] T. K. Lind, M. W. Skoda, and M. Cárdenas. *ACS Omega*, 2019, 4, 10687–10694.

[77] H. T. McMahon and E. Boucrot. *J Cell Sci*, 2015, 128, 1065–1070.

[78] D. Regan et al. *Langmuir*, 2019, 35, 13805–13814.

[79] F. Wong and A. Amir. *Biophys J*, 2019, 116, 2378–2389.

[80] K. E. Daly et al. *Phys Rev E: Stat Nonlinear Soft Matter Phys*, 2011, 83.

[81] Y. Deng, M. Sun, and J. W. Shaevitz. *Phys Rev Lett*, 2011, 107, 7–10.

[82] D. S. Cayley, H. J. Guttman, and M. T. Record. *Biophys J*, 2000, 78, 1748–1764.

[83] T. Betz and C. Sykes. *Soft Matter*, 2012, 8, 5317–5326.

[84] S. A. Safran. CRC Press, Mar. 2018, 1–266.

[85] E. K. Dimitriadis et al. *Biophys J*, 2002, 82, 2798–2810.

[86] K. Voïtchovsky et al. *Biophys J*, 2006, 90, 2075–2085.

[87] E. Geissler and A. M. Hecht. *Macromolecules*, 1981, 14, 466.

[88] R. E. Mahaffy et al. *Phys Rev Lett*, 2000, 85, 880–883.

[89] J. D. Unsay, K. Cosentino, and A. J. García-Sáez. *J Visualized Exp*, 2015, 1–9.

[90] A. Alessandrini and P. Facci. *Soft Matter*, 2014, 10, 7145–7164.

[91] S. Garcia-Manyes and F. Sanz. *Biochim Biophys Acta, Biomembr*, 2010, 1798, 741–749.

[92] F. Behroozi. *Langmuir*, 1996, 12, 2289–2291.

[93] M. Deserno. *Chem Phys Lipids*, 2015, 185, 11–45.

[94] W. Rawicz et al. *Biophys J*, 2000, 79, 328–339.

[95] S. T. Sun et al. *Biochim Biophys Acta, Biomembr*, 1986, 860, 525–530.

[96] C. A. Rutkowski et al. *Biochemistry*, 1991, 30, 5688–5696.

[97] E. M. Lifshitz, A. M. Kosevich, and L. P. Pitaevskii. 3rd ed. Vol. 7. Elsevier, 2012, 1–187.

[98] E. Evans et al. *Biophys J*, 2003, 85, 2342–2350.

[99] E. Hantz et al. *Biochim Biophys Acta, Biomembr*, 1986, 862, 379–386.

[100] Y. Sun, T. L. Sun, and H. W. Huang. *Biophys J*, 2014, 107, 2082–2090.

[101] F. R. Hallett et al. *Biophys J*, 1993, 64, 435–442.

[102] R. M. Hochmuth. *J Biomech*, 2000, 33, 15–22.

[103] O. Sandre, L. Moreaux, and F. Brochard-Wyart. *PNAS*, 1999, 96, 10591–10596.

[104] E. S. Haswell, R. Phillips, and D. C. Rees. *Structure*, 2011, 19, 1356–1369.

[105] C. Pliotas et al. *Nat Struct Mol Biol*, 2015, 22, 991–998.

[106] M. M. Elmer-Dixon et al. *J Phys Chem B*, 2019, 123, 9111–9122.

[107] T. Harayama and H. Riezman. *Nat Rev Mol Cell Biol*, 2018, 19, 281–296.

[108] I. P. Uray and K. Uray. *Int J Mol Sci*, 2021, 22, 11566.

[109] D. W. Barrett et al. *Sci Rep*, 2019, 9, 6718.

# 4. Substrate - induced effects on supported membranes

## 4.1 Overview

Biological membranes frequently come into contact with external structures, including the cytoskeleton, subcellular assemblies, organelles, and macromolecules [1–3]. While specific molecular interactions with the membrane have been widely studied, the effects of non-specific physical contacts on the membrane's local molecular organisation and behaviour remain less understood. This knowledge gap is partly due to the complexity of biological membranes, which often exist near their transition temperature, adjusting both composition and structure in response to external forces and functional needs.

Here, I use one of the binary lipid systems developed in the previous Chapter 3 to examine how contacts with substrates affect membrane organisation at the nanoscale, particularly when close to the transition temperature ($T_m$). Contact with the surface increased the $T_m$ of the lipid mixture by approximately 10 °C compared to suspended vesicles, consistent with previous findings linking this thermodynamic effect to the stabilising role of the substrate on the bilayer [4]. Additionally, the phase transition properties of the supported membrane are significantly altered, showing transition kinetics nearly two orders of magnitude slower than those observed in solution. This interaction induces a spontaneous spinodal-like molecular reorganisation in the membrane, which alters the topography of the membrane and leads to the mechanical stiffening of its nanodomains. By performing these experiments on different substrates, this Chapter demonstrates that this process is substrate-specific and evolves over substrate-dependent time frames.

The overall reorganization is consistent with substrate-enabled lipid flip-flop, inducing local compositional fluctuations and possibly leaflet-asymmetric lipid distribution within the membrane. The results, confirming previous theoretical predictions, demonstrate that simple physical contact is able to induce significant changes in the local composition and biophysical properties of the membrane, with obvious consequences for its function.

## 4.2 The role of membrane's interactions with structural biological elements

Biological membranes are essential elements of cells and control multiple active pathways such as signaling, regulating the uptake of macromolecules and the electrochemical gradient between the inside and outside of the cell [5–7]. Most biological membranes comprise mainly phospholipids organised in a bilayer structure together with other amphiphilic molecules, and embedding a large number macromolecules such as proteins and sugars supporting the membrane's function [7]. The membrane composition is heterogeneous at the nanoscale and evolve dynamically in response to external stimuli and to support the membrane's activity [8, 9]. As a result, cell membranes typically present different coexisting lipid phases with different compositional and physical characteristics [10, 11]. Highly packed lipids can form micron-scale domains referred to as solid-ordered ($S_o$) or liquid-ordered ($L_o$), depending on their composition, where the molecular mobility and mechanical properties differ from the more disordered and dynamic regions known as liquid-disordered ($L_d$). In native biomembranes, ordered domains often include numerous proteins and biomolecules and are referred to as rafts [8] which underpin various cellular functions both in physiological and pathological conditions [10, 12–14]. The existence of multiple phases in eukaryotic membrane has been extensively studied and debated over the last decade [15] because of their complex origins and challenging detection with standard microscopy techniques. Nonetheless, the existence of rafts is now well-established, and have been show to participate in processes such as the uptake of extracellular vesicles [16] or mechanosensing [17].

Unlike for eukaryotic membranes, little attention has been given to prokaryotic systems in the context of membranes micro-domains. For decades, bacteria and

archaea have been considered simpler organisms which do not require of such a complex lateral organisation to fuflil their basic membrane's functions. This hypothesis was also supported by the absence of cholesterol, linked to lipid raft formation in eukaryotes [18]. However, studies performed on bacteria over the last decade [19–23] have been able to verify the presence of equivalent membrane domains with signaling, transporting and secreting functions [23]. This was first achieved by observing the local accumulation of bacterial flotillin [22], a prokaryotic homolog to the human flotillin and known to be localised in lipid rafts where it plays a functional role [8, 24]. Bacterial membrane domains, also referred to as rafts or functional membrane microdomains, are fundamental to organise membrane proteins and are enriched in specific lipids which are predominantly found in prokaryotes such as cardiolipin, hopanoids and other phospholipid classes [23]. However, unlike for eukaryotic membranes, the extent to which these microdomains play similar roles in bacterial membranes remains largely unexplored despite similarities suggesting common roles and importance. For both eukaryotic and prokaryotic membranes, interactions between the membrane and surrounding entities coming into close proximity can play a significant role in the formation and fate of rafts. Biological membranes are always in contact with different structural elements such as protein scaffolds [25], cytoskeleton filaments [26, 27] and other polymeric layers such as the peptidoglycan wall in bacteria [28]. In eukaryotes, the interactions between rafts and these elements have been partially addressed [29–32] with the formation, function and evolution of the lipid domains influenced by the interactions with specific scaffolds such as caveolins [33] or the cytoskeleton filaments [29]. Little is known about similar interactions in bacteria [3] which also present a cytoskeleton, albeit less developed, and other structural elements that are always in contact with the membrane: the peptidoglycan cell wall and other membrane scaffolds such as the MinD-MinE complex [34]. In most cases, contacts between the membrane and surrounding entities are simply mechanical and do not involve specific interactions. This allows the membrane to be modelled as a bilayer that merely 'touches' a support, providing a simplified framework to approach the study of membrane-support interactions.

From a biophysics perspective, simple contacts can in principle locally alter the membrane molecular dynamics through reduced configurational entropy [35] without any need for specific interactions. With many membrane naturally

existing close to their transition temperature [36, 37], points of contact could be enough to trigger local phase transition or molecular reorganisation in the membrane. If verified, this could also offer a general mechanism for the spontaneous formation of nanodomains exhibiting different properties from the rest of the membranes.

To answer this question, it is useful to focus on the fundamental biophysics of the membrane using artificial model membrane systems which allow more controlled studies down to the single molecule level [38]. Supported lipid bilayer (SLB) offer an obvious platform to investigate the impact of physical contact between the membrane and an external object, and are compatible with techniques such as fluorescence microscopy [39] and atomic force microscopy (AFM) [40–42]. SLBs have enabled investigation of the $S_o$ phase formation, its properties and links with biological processes. This is typically achieved by controlling the temperature and composition of the model membrane which can be tuned to create different phases. Previous studies have already demonstrated the impact of the support on the membrane's thermodynamic behaviour, with melting temperature ($T_m$) often lowered by several degrees [43–50]. The impact of the substrate on the membrane kinetics is less clear with conflicting results on the lipid mobility [51–53] but a facilitation of lipid flip-flop between leaflets [54–57]. The flip-flop process typically occurs within hours [54, 58, 59] and theoretical predictions [54, 60] suggest that the substrate could not only facilitate it, but also bias it through differential interactions between the each leaflet and the solid, effectively providing a mechanism for spontaneous substrate induced molecular reorganisation.

Here I comparatively investigate the phase transition and evolution of a model binary lipid membrane when supported in on different solids or suspended in solution. The model membrane is one of the simple binary mixtures identified in Chapter 3, which mimics the main lipid composition and temperature transition of *E Coli*'s inner membrane. Using a combination of differential scanning calorimetry (DSC) and AFM, I explore the rapid changes occurring in the membrane upon cooling below the transition temperature and the longer term (<24h) evolution, including possible molecular rearrangements and local changes in mechanical properties of the membrane as a result of contact with the substrate. This Chapter demonstrate that surface interactions play a drastic role in modulating phase separation in lipid bilayer systems, modifying their

thermodynamic properties and the molecular organisation along the SLBs over longer timescales.

## 4.3 Materials and methods

In this section, I will briefly summarise the chemicals used and the protocol behind model membrane's preparation and the thermodynamic and mechanical testing used.

### 4.3.1 Chemicals

The commercially available lipids,
1-palmitoyl-2-oleoyl-sn-glycero-3-phosphoethanolamine (POPE) and
1-palmitoyl-2-oleoyl-sn-glycero-3-phospho-(1'-rac-glycerol) (POPG), have been purchased and dissolved in chloroform from Avanti Polar Lipids (Alabaster, AL). Salts (all>99% purity) have been purchased from Sigma-Aldrich (Dorset, UK) and dissolved in ultrapure water (Merck-Millipore, Watford, UK) to prepare MOPS buffer-based solution with specific ions concentration as follows: 50 mM NaCl, 9.5 mM $NH_4Cl$, 0.5 mM $MgCl_2$, 0.3 mM $K_2SO_4$, and 1 $\mu m$ $CaCl_2$-$2H_2O$. The pH was adjusted to 6.5 prior to mixing with lipids.

### 4.3.2 Vesicles preparation

For the large multilamellar vesicles (LMVs) preparation, 10 mg of lipids dissolved in chloroform have been mixed following the correct molar ratios and deposited in a 4 mL glass vial. To allow chloroform evaporation, the lipids have been then pre-dried under a gentle nitrogen flow and finally placed overnight in a vacuum chamber. Lipids have been then rehydrated with 1 mL of MOPS buffer-based solution obtaining a final concentration of 10 mg/mL and large multilamellar vesicles have been obtained through freeze-thawing. In short, the lipid solution was heated while sonicating in a bath sonicator and subsequentially, the lipids have been frozen by leaving the glass vial for 15 minutes in a freezer. This heating-freezing was repeated for 6 consecutive cycles to ensure vesicles formation, as indicated by the lower turbidity of the final

vesicles' solution.
Similarly to LMVs preparation, lipids have been mixed and dried in a 4 mL glass vial before being rehydrated in the MOPS buffer-based solution. The lipid solution was gently bath sonicated for 15 minutes at 45°C, until the solution looked opaque and milky, indicating the dissolving of lipids in the solvent. The solution was extruded 31 times using a Mini-Extruder kit (Avanti Polar Lipids) with 2 Whatman 100 $nm$ filter (GE Healthcare Life Sciences, Little Chalfont, UK) to form small unilamellar vesicles (SUVs). Appropriate final SUVs concentration was prepared depending on the surface used for the supported lipid bilayer preparation.

### 4.3.3 DSC protocol

To observe the effects of the scan rate on the thermodynamic properties of lipid vesicles, DSC measurements have been performed on a DSC 2500 (TA Instruments, Delaware, USA). 10 $\mu$L of LMVs solution at 10 mg/mL have been loaded into the calorimeter and the sample was equilibrated before the measurement for 5 min at the starting temperature. DSC runs on vesicles have been performed with varying cooling rate (from 0.03 °C/s up to 0.67 °C/s) within a temperature range of 60 °C to -10 °C. DSC runs have been repeated 3 times per each sample to ensure reproducibility. To test compositional rearrangement in the vesicle's membrane, a series of DSC cycles have been performed with the same DSC 2500 instrument. After loading the LMVs in the same volume and concentration as previously described, the vesicles have been equilibrated at 45°C for 5 minutes. The sample was then cooled down at 16°C with a rate of 0.08 °C/s and equilibrated at this temperature for a variable amount of time. At the end of this isothermal phase, the sample was heated back up at 45°C with a rate of 0.08°C/s and equilibrated at this temperature before the start of the next cycle.

### 4.3.4 PDMS surface preparation

Sylgard 184 silicon elastomer kit was purchased at Dow Corning Corporation (Michigan, USA). Silicon elastomer and curing agent have been gently mixed in a 10:1 weight ratio in a glass container. Subsequently, the mixture was degassed

in a vacuum chamber for at least 1 hour to remove any air bubble in the solution. The PDMS solution was then deposited on top of a cleaved Muscovite mica disk (SPI Supplies, West Chester, PA, USA) and placed inside a WS-650Mz-23NPPB spin-coater (Laurell Technologies Corporation, Landsalle, PA, USA) to allow a homogenous distribution of the PDMS over the surface. Spin-coating was performed for 10 minutes at 1000 RPM at room temperature. Finally, the PDMS-coated disk was placed in an oven at 50°C overnight to ensure the curing of the PDMS layer.

### 4.3.5 Supported lipid bilayers (SLB) and monolayer (SLM) preparation

The SUVs solution was diluted to an appropriate concentration to ensure full bilayer or monolayer formation depending on the surface used. To form SLB on a mica surface, 100 $\mu$L of 0.2 mg/mL SUV solution have been deposited on a freshly cleaved Muscovite disk (SPI Supplies, West Chester, PA, USA) placed on the AFM stage and let incubating for 30 minutes at 50°C covered with a Petri dish. To form SLB on PDMS, 100 $\mu$L of 1 mg/mL SUV solution have been deposited on the cured PDMS surface for 30 minutes at 50°C. Finally, to form lipid monolayer on top of highly ordered pyrolytic graphite, 100 $\mu$L of 0.4 mg/mL SUV solution have been deposited on freshly cleaved HOPG surface (SPI Supplies, West Chester, PA, USA) for 30 minutes at 50°C. All the samples have been subsequently gently rinsed with the solvent to remove any un-broken vesicle and the temperature was cooled down at 40°C for 15 minutes before starting the experiment.

### 4.3.6 AFM protocol

Imaging was conducted using a commercial Cypher ES AFM (Oxford Instruments, Santa Barbara, CA, USA), equipped with temperature control. SNL-10 cantilevers (Bruker Scientific instruments, Billerica, MA, USA) with nominal spring constant of 0.35 N/m have been used. The tip has a pyramidal shape with a nominal radius $\leq 12\ nm$ at its apex. The AFM imaging was performed in amplitude mode, where the tip was oscillated at a frequency close to its resonance while fully immerse in the liquid. By adjusting cantilever

oscillations, the imaging conditions have been kept as soft as possible ensuring neither tip contamination nor damaging of the sample. Force spectroscopy curves and map have been conducted by working in contact mode with a SNL-10 cantilever. Force maps have been created from 1024 force curves (32 x 32) over a 6.25 $\mu m^2$ area. Through the acquired force curved, membrane's mechanical features such as $F_r$ and $Y$ have been calculated based on commonly used AFM force spectroscopy approaches with thin biological systems [61, 62]. The Young's modulus has been calculated through a corrected version of the well-established Hertzian indentation model for a semi-infinite medium [63, 64] which takes into account the thinness of the bilayer and the presence of a hard substrate underneath it [65]:

$$F_{sphere} = \frac{16}{9} Y \sqrt{R\delta^3} \left[ 1 + \frac{1.133\sqrt{\delta R}}{h} + \frac{1.497\delta R}{h^2} + \frac{1.469\delta R\sqrt{\delta R}}{h^3} + \frac{0.755\delta^2 R^2}{h^4} \right] \tag{4.1}$$

where $F$ is the force applied with our tip which is described as a sphere, $R$ is the indenting radius, $\delta$ is the indentation depth and h is the membrane's thickness. The formula was derived by assuming an incompressible membrane (Poisson ratio, $v$= 0.5), and to limit surface's contribution, indentation was kept below 20% of the bilayer's thickness so that $\delta \leq R$. It's important to notice that these commonly used assumptions are not necessarily true for biological systems [66, 67] and therefore the results are still influenced by various experimental parameters such as the material of the tip, its geometrical properties and the properties of the surface used. To compare the obtained results, the same cantilever has been used for the maps and tip calibration was performed before and after the experiment. This allows us to obtain the spring constant of the tip used and ensure the absence of impurities or damaging on the cantilever after the measurements. Calibration was obtained by determining the inverse optical lever sensitivity by recording a force-distance curve on a stiff mica surface and the spring constant was determined through the cantilever's thermal spectrum.

### 4.3.7 Data analysis

DSC results have been analysed with the TRIOS Software, provided with the instrument. The software was used to correct thermogram baselines and then obtain Tm at the highest point of each calorimetric peak. AFM images and

topographical AFM data have been obtained and analysed using the Gwyddion software [68], an open-source modular program for scanning probe microscopy data visualisation and analysis. Graphs have been generated using Igor Pro Software (Wavemetrics, Lake Oswego, OR, US) and Python [69].

## 4.4 Results and discussion

### 4.4.1 Kinetics of phase transition in SLBs

To understand the influence of a contacting substrate on the phase behaviour of my *E. coli* model membrane, I comparatively track the phase transition of unsupported bilayers using DSC [70–73] and of planar SLBs using AFM. The unsupported bilayers are formed of large vesicles (LMVs) in aqueous solution and have an identical lipid composition to the SLBs (see Section 4.3.2). Working in identical experimental conditions allows for a direct comparison between both systems, with the only difference being the presence of a solid substrate on one side of the membrane in the case of SLBs. While DSC is a well-established technique for characterising the thermodynamic properties of unsupported lipid systems, AFM allows direct quantification of the fractions of $L_d$ and $S_o$ phases at each temperature over a given transition. In both cases, the measurements are taken upon cooling the sample down from a purely $L_d$ phase to a fully $S_o$ phase. I explored a range of temperature and cooling rates relevant to the $L_d \rightarrow S_o$ transition of the system.
The DSC results always exhibit a single peak regardless of the cooling rate (Fig. 4.1A). The peak is characteristic of standard first-order phase transition, with the cooling rate slightly influencing the transition temperature $T_m$ (position of the maximum in Fig. 4.1A): faster rates yield lower apparent $T_m$ values (Fig. 4.1B). This indicates that some kinetic effects are already at play as the temperature is changed too rapidly for the system to fully equilibrate across the transition. This drives the system further out of thermodynamic equilibrium as the cooling rate increases. The effect is however subtle, with a maximum of $\sim 1$ °C shift in $T_m$ within the range of rates accessible here. In fact, the onset temperature $T_o$ – the temperature at which the transition begins – does not show any clear dependence on the cooling rate within error, with an

average value of $T_o = 19.1 \pm 0.2$ °C (Table 4.1). The slowest rate probed shows a transition temperature of $T_m = 18.6 \pm 0.1$ °C. By comparing the $T_m$ on both cooling and heating experiments, it's possible to infer an equilibrium transition temperature of 20± 0.1 °C (quasistatic cooling rate close to 0°C/s as calculated in Chapter 3).

Finally, the change in enthalpy $\Delta H_{\text{cal}}$ associated with the transition can be calculated by temporal integration of the transition peak (Table 4.1), yielding an average value of $\Delta H_{\text{cal}} = 26.7 \pm 2.5$ kJ/mol. This is in line with results from previous calorimetric studies on similar vesicular systems [45] and within the expected value range for lipid membranes [74].

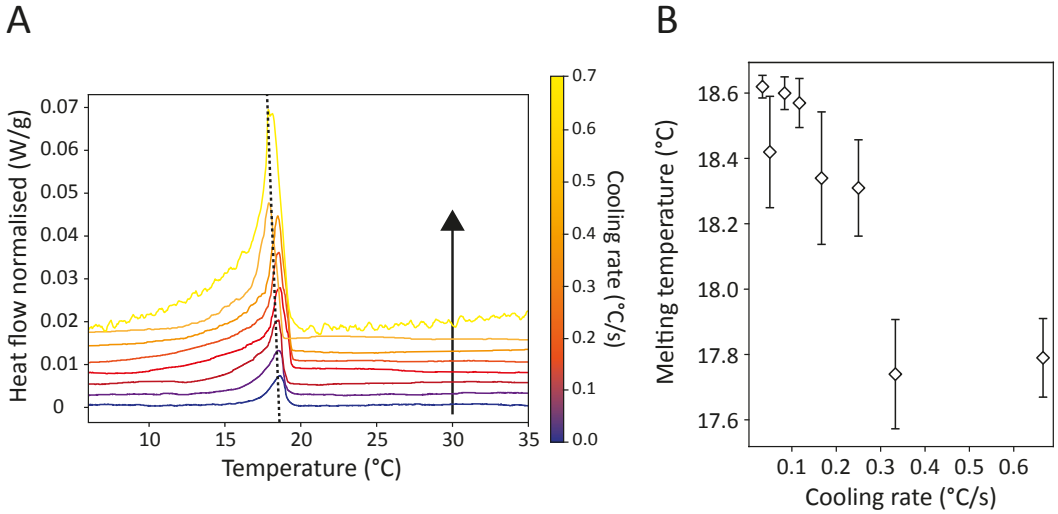


Figure 4.1: Calorimetric analysis on unsupported lipid vesicles. (A) DSC thermographs on lipid vesicles at different cooling rate. Curves have been vertically offset for clarity, evidencing the peak shift to lower temperatures as the rate increases. The associated $T_m$ shift is shown in (B) where a maximum of 1°C shift can be observed due to the approach of the instrument limits. All the raw values are presented in Table 4.1

| **Cooling rate (°C/s)** | $T_m$ **(°C)** | $\Delta H_{\text{cal}}$ **(kJ/mol)** | $T_o$ **(°C)** |
|---|---|---|---|
| Equilibrium ($\sim 0$) | 20°C ± 0.1 | — | — |
| 0.03 | 18.62 ± 0.03 | 21.68 ± 0.91 | 19.18 ± 0.04 |
| 0.05 | 18.42 ± 0.17 | 27.79 ± 3.46 | 18.93 ± 0.13 |
| 0.08 | 18.60 ± 0.09 | 27.50 ± 0.94 | 18.99 ± 0.09 |
| 0.12 | 18.57 ± 0.05 | 29.38 ± 3.86 | 19.30 ± 0.05 |
| 0.17 | 18.34 ± 0.30 | 28.36 ± 1.98 | 19.11 ± 0.30 |
| 0.25 | 18.31 ± 0.12 | 25.73 ± 2.76 | 19.23 ± 0.12 |
| 0.33 | 17.74 ± 0.21 | 16.13 ± 2.88 | 18.59 ± 0.21 |
| 0.67 | 17.79 ± 0.10 | 15.93 ± 3.15 | 19.20 ± 0.10 |

Table 4.1: Table summarising the results from the DSC experiments on lipid vesicles reporting the melting temperature, the calorimetric enthalpy and the temperature onset at each cooling rate.

The same transition explored by AFM for SLBs allows direct visualisation of the $L_d$ to $S_o$ transition as the lipids pack more tightly upon cooling (Fig. 4.2) [75]. However, unlike for LMVs in solution, two different $T_m$ values can be observed, reflecting the decoupled transitions of the distal and proximal leaflet. The interaction between the lipid molecules in the proximal leaflet increases its $T_m$ relative to the distal leaflet exposed to the bulk liquid. This decoupling can be directly observed at certain temperatures upon cooling (Fig. 4.2B). The effect is well-documented [4, 45] and also occurs at thermodynamic equilibrium. Here, since the experiments are systematically conducted cooling down the sample, I focused on the first transition observed in an experiment: the transition of the proximal leaflet. This is sufficient to best capture the effect of the substrate as this bilayer leaflet is the one in direct contact with the surface which represents the aim of this work. This approach also allows me to avoid having to track the membrane over tens of degrees, a demanding experiment. Significantly, the distal transition always occurs after the proximal transition in any given location, thereby emphasising the importance of the proximal transition for the purposes of the present study.

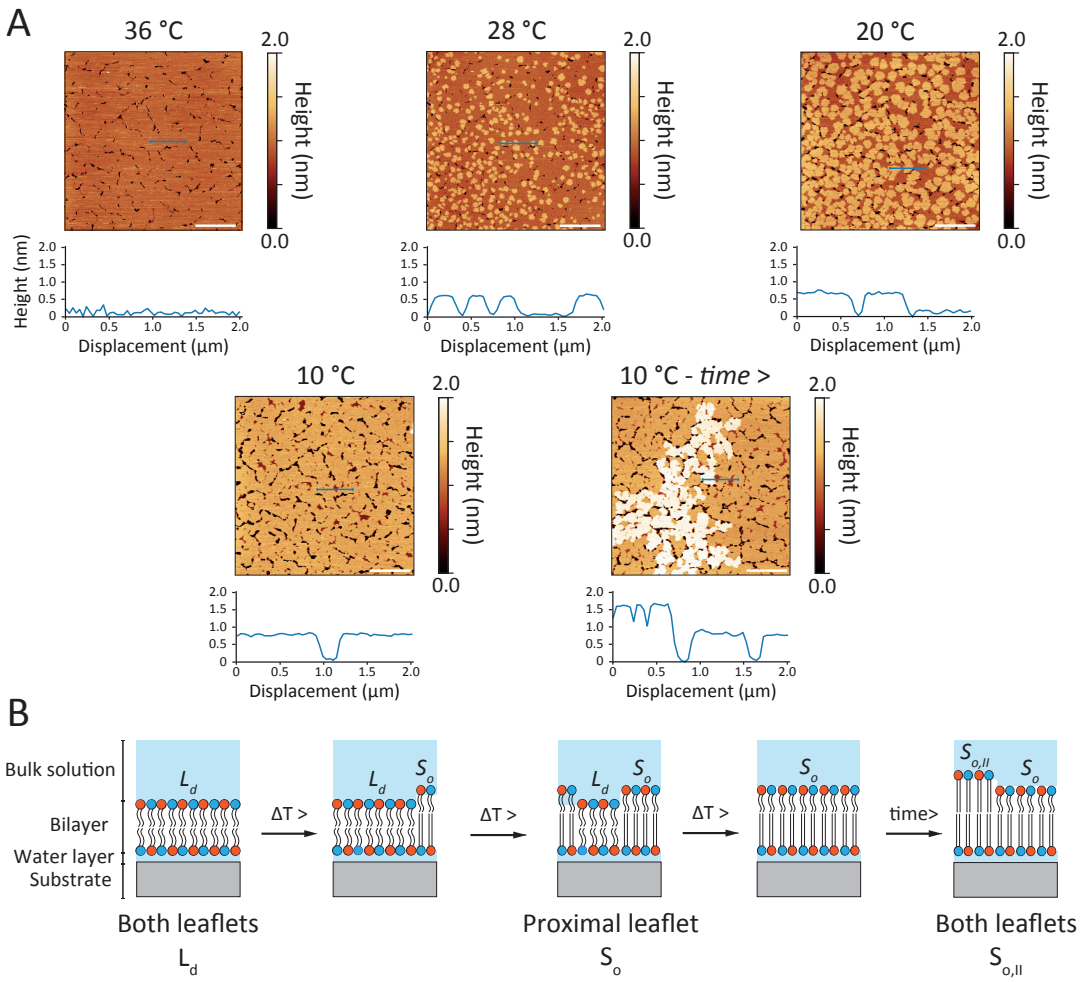


Figure 4.2: Thermal analysis on SLBs at different cooling rates. (A) AFM topography images of an SLB undergoing phase transition captured at different temperatures. The better packing of the lipids in the $S_o$ phase results in taller membrane domains. The schematic representation of the change in molecular arrangement during the transition is shown in (B). The proximal leaflet transitions at higher temperatures because of its interactions with the substrate and reduced configurational entropy. The transition is fully complete at lower temperatures (here shown at 10° C). The scale bar is 2 $\mu m$ for all the AFM images (A).

Using a Van't Hoff analysis of the experimental data, the $T_m$ of the proximal leaflet can be derived: the area fractions of $L_d$ and $S_o$ phases are assumed to follow a sigmoidal evolution with temperature, with $T_m$ marking the position of the transition [46, 76, 77] (Table 4.2 for fitting results). As expected, the SLB presents a higher $T_m$ (almost 10°C) than for the LMVs, and a much stronger dependence on the cooling rate (Fig. 4.3A). Close to equilibrium, $T_m = 27.2 \pm 0.6$ °C, progressively decreasing to $T_m = 13.9 \pm 0.6$ °C at the fastest cooling rate used here (0.02 °C). I hypothesise that this strong rate dependence originates from a thermal lag between the AFM stage temperature and the effective temperature experienced by the lipids in the supported bilayer. This

lag may arise because the close interaction between the bilayer and the solid substrate hinders lipid mobility, limiting the system's ability to respond promptly to changes in temperature. As a result, the phase transition appears kinetically delayed at faster cooling rates. In contrast, the $T_o$ value remains relatively conserved between the different experiments (29.5 ± 1.5 °C) while the Van't Hoff enthalpy ($\Delta H_{\mathrm{VH}}$) obtained varies significantly with the cooling rate (see Table 4.2 for the specific values), further supporting a kinetically regulated process in the SLB systems.

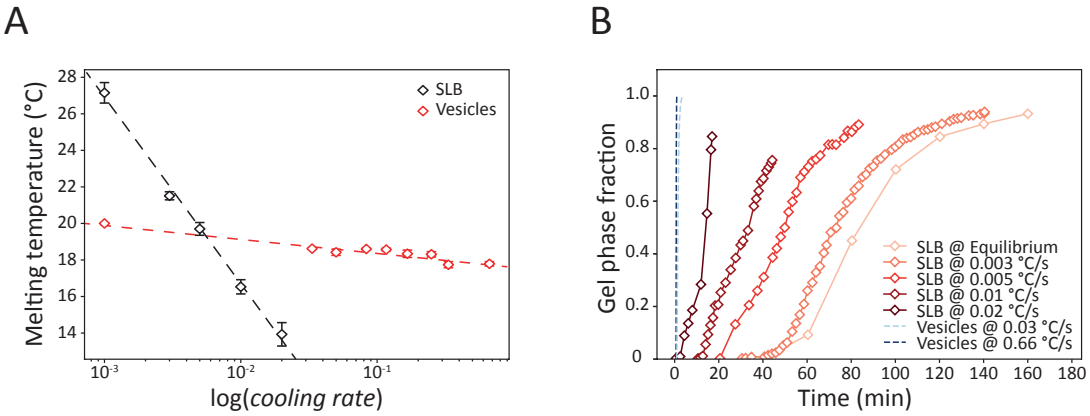


Figure 4.3: Comparison between the effect of the cooling rate on the phase transition of unsupported vesicles and SLBs. (A) Semi log plot comparing the $T_m$ variation as a function of cooling rate in SLB and vesicles' systems. The predicted $T_m$ value of unsupported vesicles at the theoretical slowest rate (cooling rate close to 0°C/s) has been added for reference. (B) Curves representing time required to complete the transition process in the SLBs (proximal leaflet, diamond marked lines) and bulk vesicles (dashed lines) at varying cooling rates. The curves have been horizontally offset for clarity. Longer timescales (>2 hours) are required to fulfil phase transition in SLBs, compared to the rapid transition (few minutes) for the vesicles.

| **Cooling rate (°C/s)** | $T_m$ **(°C)** | $\Delta H_{\mathbf{VH}}$ **(kJ/mol)** | $T_o$ **(°C)** |
|---|---|---|---|
| Equilibrium (∼ 0) | 27.15 ± 0.59 | 448.97 ± 56.7 | 30.00 ± 0.56 |
| 0.003 | 21.51 ± 0.21 | 328.70 ± 10.9 | 29.56 ± 0.22 |
| 0.005 | 19.70 ± 0.20 | 198.80 ± 5.53 | 29.50 ± 0.35 |
| 0.01 | 16.53 ± 0.36 | 123.79 ± 20.9 | 29.56 ± 0.39 |
| 0.02 | 13.93 ± 0.60 | 205.84 ± 14.0 | 27.32 ± 0.64 |

Table 4.2: Table summarising the results from the calorimetric AFM experiments on SLB reporting the melting temperature, the Van't Hoff enthalpy and the temperature onset at each cooling rate.

While both suspended LMVs and SLBs show qualitatively similar behaviour with increasing the cooling rate, it is immediately obvious that not only the equilibrium phase thermodynamics but also the kinetics of the membrane evolution are drastically different. Fig. 4.3B presents comparatively the results obtained on both systems, showing LMVs to reach thermodynamic equilibrium in a few minutes at most while SLBs require hours. This is all the more remarkable considering the relatively weak interaction between lipid headgroups and the substrate underneath; several layers of water are present in-between with an overall water thickness ranging from 1 to 2 nm [78–80]. Additionally, several studies did not find significant differences in molecular mobility between LMVs, native membranes and SLBs [52, 53, 81, 82], although usually without distinguishing the leaflets.

Interestingly, the present results indicate that careful control of the phase behaviour is needed for studies relying on SLBs, where the slow kinetics may preclude reaching equilibrium over the course of the experiments, depending on the temperature history of the system.

### 4.4.2 Molecular reorganisation in SLBs

To explore in more detail the substrate-lipid interactions and the consequences for the fate of the membrane, I investigated the SLB system over longer timescales when near its transition temperature. SLBs have been first equilibrated at 40 °C, far above their $T_m$ (27.2 ± 0.6 °C near equilibrium), then rapidly quenched (cooling rate of 1°C/s) down to a set temperature a few degrees below the $T_m$ (25.0 ± 0.1 °C or 23.0 ± 0.1 °C). The SLBs have been subsequently imaged by AFM over 24 hours inside a sealed chamber, while subsequently kept at that quenching temperature. From a thermodynamics perspective, the experiment follows the membrane evolution through an isothermal phase transition at equilibrium.

For a uniform, homogenous membrane, I expect the nucleation and growth of $S_o$ domains to progress until full coverage of the observed area, albeit with a relatively slow kinetic due to the substrate-SLB interactions. However, this simple phase transition was not observed for my model *E. coli*'s binary membrane, which shows a significantly more complex behaviour (Fig. 4.4A) despite DSC measurements indicating a single, full transition. The early stages

of the transition follow the expected classical nucleation and growth behaviour with initially small, randomly distributed $S_o$ domains that grow over time. However, between 1 and 3 hours into the experiment, a sudden slowdown in the growth of the $S_o$ domains occurs, coupled with the formation of new $L_d$ domains within the $S_o$ domains (Fig. 4.4A). This apparent reorganisation of the membrane not only stops the phase transition in its tracks, but it also transforms the morphology of the different domains over 24h. The elongated structures of the late-stage domains are reminiscent of structures formed by classical spinodal decomposition [83].

To obtain a more quantitative handle on these observations, I conducted a form factor analysis of all the domains visible in the AFM images (Fig. 4.4B). The evolution of the form factor $S_k$ over time $t$ is expected to follow a power law $S_k \propto t^{\alpha}$ with $\alpha$ characteristic of the process at play [84, 85]. An average $S_k$ value can be obtained through Fourier analysis of the real space AFM images [84, 86, 87]:

$$|S_k| = |L^d g(kL)| \tag{4.2}$$

where $d$ is the spatial dimensionality (here $d$=2), and $g(x)$ is the Fourier transform of my images. In practice, each AFM image was first background-flattened and contrast-normalized before performing a 2D fast Fourier transform (FFT). I then computed the radial average of the power spectrum to extract $S_k$ as a function of spatial frequency $k$, and tracked the position of its peak over time. This peak corresponds to the most frequent domain size formed during the phase separation of the proximal membrane leaflet, allowing quantitative monitoring of domain coarsening. To improve signal clarity, I excluded both very low and very high frequencies from the spectrum, which can be affected by edge effects and image noise, respectively. Finally, only areas displaying a single-layer transition were included in the analysis; regions showing signs of the second leaflet transition were excluded from the form factor calculation.

By analysing the images obtained on atomically flat mica substrates to avoid roughness effects (FIG. 4.4 A), the analysis of $\ln S_k$ vs $\ln t$ suggests three distinct regimes in the evolution of the system (FIG. 4.4 B): first, a classical post-nucleation growth takes place over $\sim$ 45 mins, characterised by the expected $\alpha$=1/3 [88]. This is followed by a plateau which coincides with the

slowdown of the domain's growth and the onset of formation of the secondary $L_d$ domains. $S_k$ remains unchanged within error over the plateau, implying that $\alpha \sim 0$. Finally, the third regime appears after $\sim$ 3 h and is characterised by a growth exponent of $\alpha$=$-1/3$, suggesting a decay in the $S_o$ phase size in favour of the $L_d$ phase. This exponent value has been previously observed in computer simulations of spinodal processes [89, 90]. However, given the spontaneous nature of spinodal processes [85], its formation in the later stages of the experiment can only be explained by an associated slow kinetics or the late development of suitable conditions. In fluids, several molecular reorganisation mechanisms can coexist during the late stages of phase-separating fluids if diffusivity is low [86, 91]. In the case of SLBs, multiple studies [52, 53, 81, 82] have confirmed that the diffusivity of the lipid molecules is not drastically affected by the presence of a substrate, ruling out diffusion-related kinetic effects. Additionally, the fact that classical nucleation, growth and spinodal processes all take place consecutively in a same system suggests the intervention of a different mechanism with its own kinetics. Consistently, repeating the experiment at different quenching temperatures uniformly changes the kinetics of the process through all three regimes, with slower kinetics further from $T_m$ (Fig. 4.4B). To the best of my knowledge, such a complex evolution has never been reported for lipid membranes.

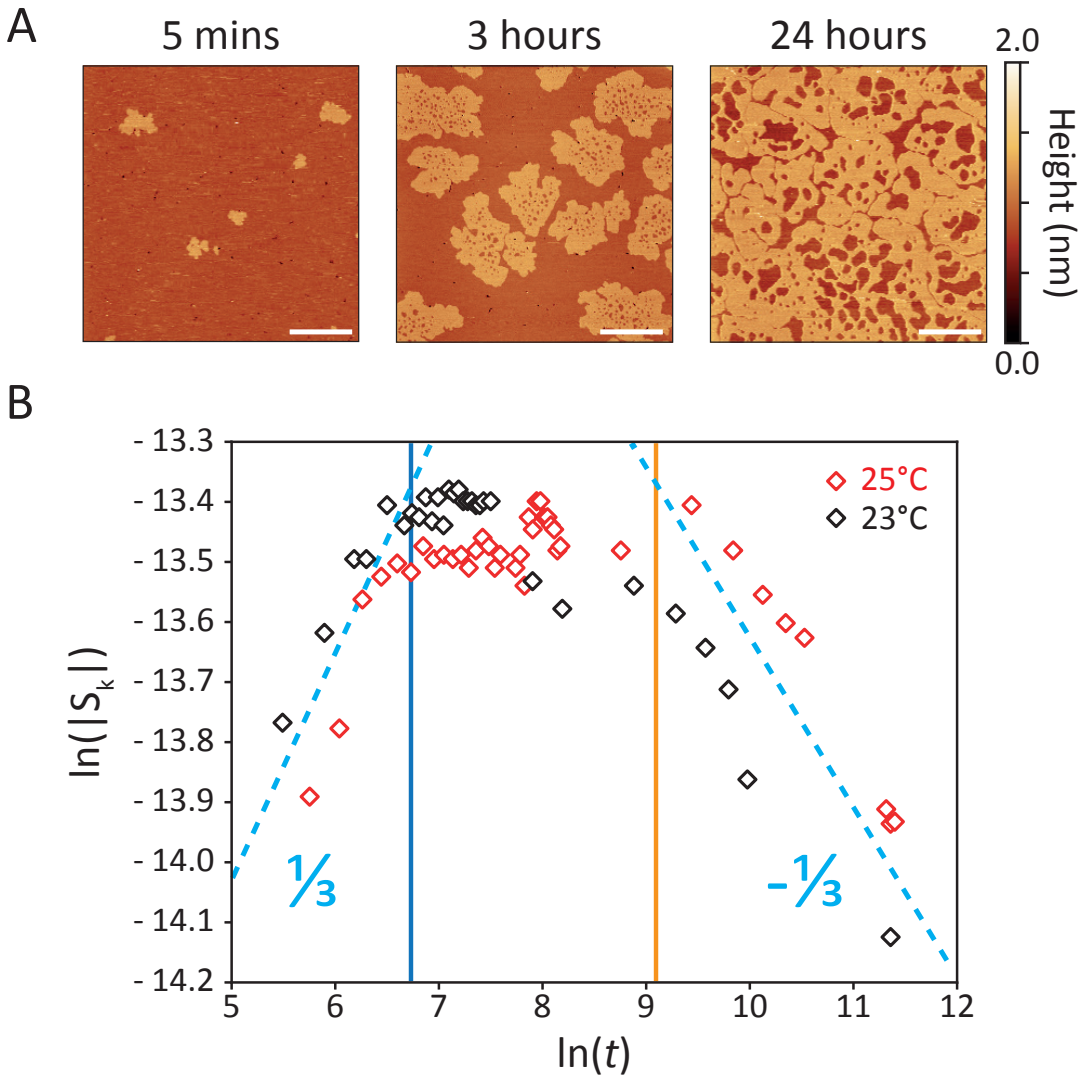


Figure 4.4: Evolution of the SLB over 24h and characterisation of its form factor. (A) Consecutive AFM topography images of the same SLB region acquired at different times. The temperature is fixed at 25 °C. (B) Evolution of the factor analysis against time (of $\ln S_k$ vs $\ln t$) for two different fixed temperatures. For both temperatures, the data correspond to single experimental samples. At each time point, three distinct membrane regions were imaged and analysed. The dashed light blue lines highlight the growth exponent (here reveals as line gradient). Two coloured lines have been used to indicate the separation between the three regimes of the process. The scale bars are 2 $\mu m$ in (A).

### 4.4.3 The molecular reorganisation is substrate specific

I propose that the spinodal process observed during the third regime is due to substrate-induced molecular reorganisation of the SLB, thereby creating domains with different lipid composition: depleted or enriched in one of the two lipid species. The associated slow timescale points to inter-leaflet lipid reorganisation in the $S_o$ phase being the limiting factor, a process called flip-flop

[54, 92, 93]. Both lateral and rotational diffusion occur rapidly in synthetic and native biological membranes [7, 94], but the flip-flopping process is considerably slower without the involvement of enzymes called flippase [59, 95] due to the energetic cost for the hydrophilic headgroup have to pass through the hydrophobic interior of the bilayer. Although spontaneous, the timescales of flip-flop are biologically long [54, 58, 59] and can be significantly affected by environmental parameters such as temperature [54] or the presence of defects in planar bilayers [58].

Here, the experimental observations are all consistent with the substrate biasing the spontaneous flip-flop process, hence creating compositional asymmetry between the leaflets and local molecular reorganisation. First, the third regime is only observed when at least two different lipid species are present on the substrate (FIG. 4.5). Mono component membrane undergoes a classic nucleation and growth where the $S_o$ domains slowly cover the full scanned area (Fig. 4.5A). On the other hand, binary mixtures always present this complex behaviour, reaching a final $S_o$ coverage in line with the molar ratio of the used lipid species (Fig. 4.5B-C).

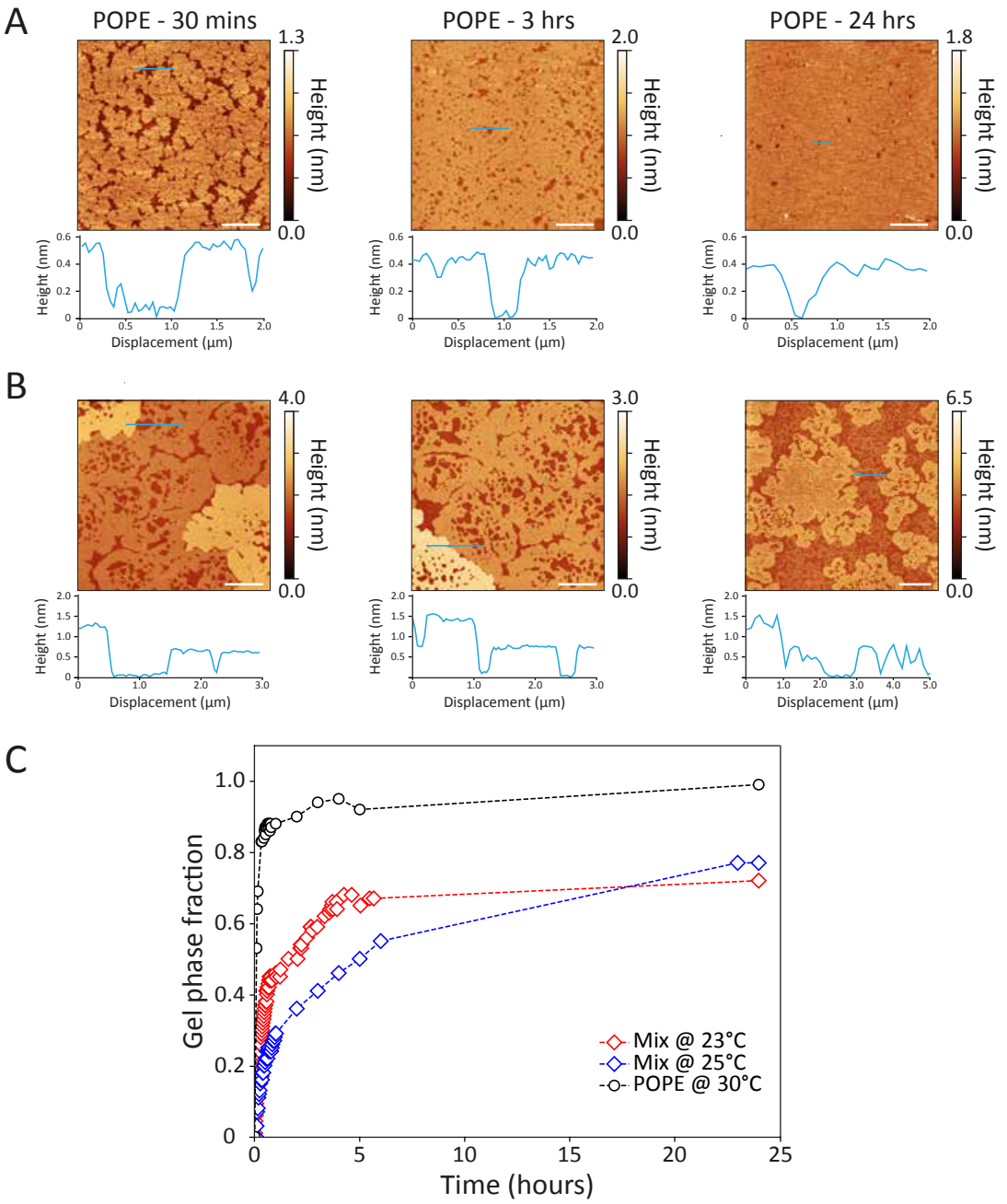


Figure 4.5: Binary supported membrane present multiple phases coexistence and interesting morphological features at latter stages of the phase transition process, not completing the full transition. (A) Mono component POPE membrane undergoes full phase transition within the 24 hours explored with AFM.
(B) On the other hand, binary SLB at 25°C (left and middle) and 23°C (right) do not fuflil the phase transition and develop an unusual morphology. The images reported here are examples of the binary system after 24 hours. Each image in (A) and (B) has been presented with a height profile to show lipid domain's height.
(C) Graph showing the gel phase fraction growth against time after quenching the temperature below the melting point compared with mono-component membrane behaviour. In binary systems, full $S_o$ transition is not observed with a final $S_o$ phase coverage of approximately 75% at both 23°C and 25°C. This $S_o$ fraction is in line with the composition of the binary membrane. The scale bar of the AFM images is 2 $\mu m$ for all images in (A), while it is 2 $\mu m$ (left and middle) and 5 $\mu m$ (right) for images in (B)

Second, the timescale of the third regime is consistent with that of the spontaneous flip-flop process for natural and synthetic biomembranes. Third, the substrate provides an obvious route to bias the flip-flopping process since both lipid species are unlikely to interact identically with the substrate in the proximal leaflet. This has been theoretically predicted [58], but never observed experimentally for lipid membranes. Finally, supported lipid monolayers with the same binary composition only undergo the phase transition in the first regime, with no spinodal process taking place (Fig. 4.6A). This confirms beyond any doubt that both leaflets are involved in the process, as necessary for flip flop. This also explains how the observed spinodal behaviour in bilayers can take place in the third regime while being spontaneous: it is limited by the flip-flopping rate of the lipids.

To confirm this interpretation and better quantify the underpinning energetics I conducted control experiments with DSC, and with AFM on different substrates. In the DSC experiment, vesicles have been initially cooled down $\sim 2$ °C below their melting temperature (as determined by DSC) and then allowed to evolve isothermally for a set amount of time (from 1 min to 1 hour). This is equivalent to the AFM experiments presented in Fig 4.4, but with isothermal times reaching max 1 hour considering the limitations of the instrument employed. Following the evolution, the sample was heated back to the starting temperature and subsequently cooled down again to observe any change resulting from the isothermal evolution: compositional asymmetry between leaflets or the formation of heterogenous domains is likely to affect the transition peak. The results do not show any variation in the peak with error, regardless of the length of the isothermal evolution (Table 4.3 for the $T_m$ values of each DSC cycle). This confirms the need for a substrate to drive the third regime of membrane evolution.

| | **Isothermal time (min)** | | | | | |
|---|---|---|---|---|---|---|
| $T_m$ **(°C)** | **1** | **5** | **10** | **20** | **30** | **60** |
| **Cooling cycle** | 18.7 | 18.84 | 18.66 | 18.65 | 18.70 | 18.60 |
| **Heating cycle** | 21.91 | 21.96 | 21.96 | 21.95 | 21.84 | 21.84 |

Table 4.3: Table summarising the melting point of each DSC cycle performed on the lipid vesicles with varying isothermal time. Melting points seem to be relatively consistent and do not variate upon quenching, suggesting the absence of any compositional rearrangement or segregation along the bilayer.

The AFM experiment of Fig. 4.4 was then repeated on a different substrate to alter the lipid-substrate interactions and hence the presumed bias over the flip-flop. I selected oxidised polydimethylsiloxane (PDMS, see Section 4.3.4) due to its different surface chemistry and increased roughness, which enables higher lipid mobility and local curvature. This naturally makes the formation of defect-free membranes and AFM experiments more challenging [96], but a qualitatively similar behaviour as presented in Fig. 4.4 can be observed (Fig. 4.6B). The $S_o$ domains form too rapidly to allow for imaging of the first regime and topographical features consistent with the spinodal process can already be observed after $\sim$ 30 min, with the formation of the $L_d$ domains inside the $S_o$ phase. The SLB's poor stability made it impossible to follow the membrane for 24 hours and the deduced $S_k$ values exhibit a larger error, but the results nonetheless confirm the same phenomenon as on mica, albeit with a faster dynamic. This is to be expected due to the significant increase in local surfaces features such as curvature and defects known to enhance the flip-flop rate [58].

The fastest substrate-induced evolution was observed for lipid bilayers supported by another bilayer (Fig. 4.6C). In bilayer stacks, the interaction between bilayers drives the molecular reorganisation with the formation of $S_o$ domains and circular $L_d$ inclusions appearing within minutes of quenching the temperature below $T_m$. Numerous defects are visible and with the 'substrate' itself being mobile the molecular reorganisation is further enhanced, inducing the immediate reorganisation of the system. While unhelpful to accurately quantify the characteristics of the stack's evolution (FIG 4.5 D), the experiment highlights the fact membrane-membrane interactions –arguably one of the most common forms of physical contact between biological membranes– can dramatically and rapidly alter the local biophysical properties of the membrane.

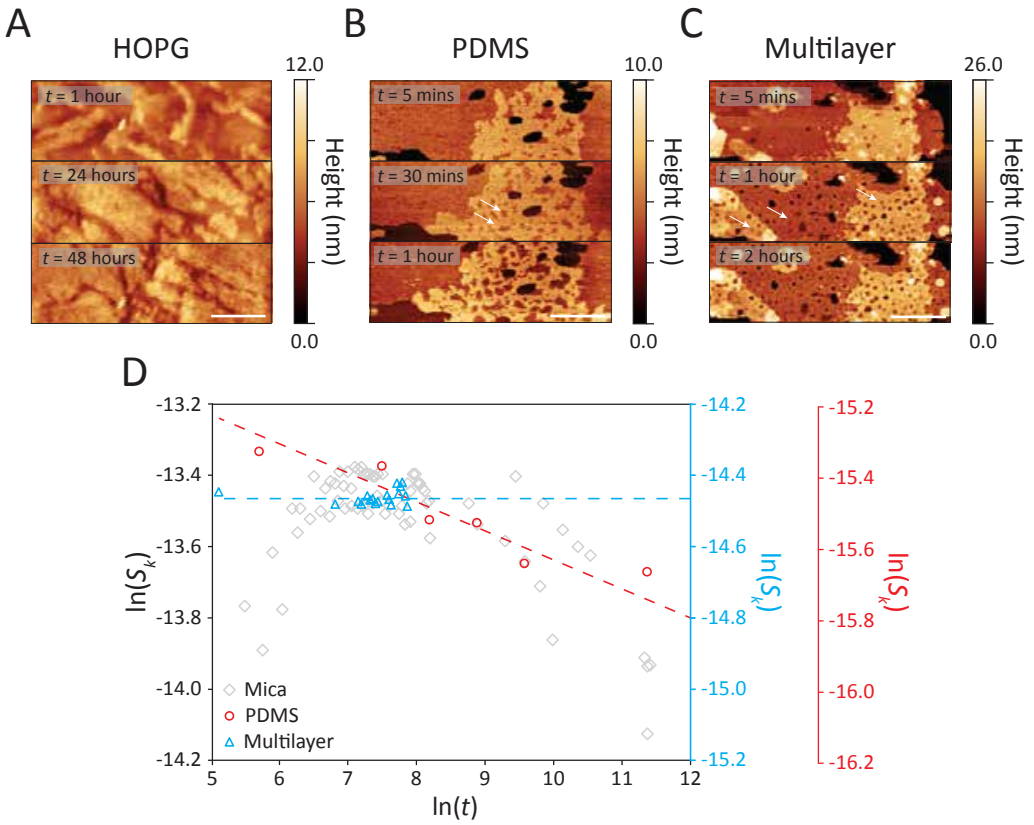


Figure 4.6: Evolution of binary supported bilayers and monolayers on different substrate imaged by AFM. When the temperature is quenched below the transition point, monolayer prepared on HOPG (A) shows slower kinetics $S_o$ domains forming progressively over 24h, proceeding from substrate step edges. The domains eventually cover the whole surface without any $L_d$ domain ever appearing. Similar experiments have been conducted on PDMS (B) and bilayers stacks (C), where the $S_o$ domains appear as soon as the temperature is lowered below the transition temperature. $L_d$ domains form within $\sim$ 30 min on PDMS and almost immediately on the bilayer stacks (white arrow). (D) Evolution of the form factor for the lipid bilayer on PDMS and the multilayer system compared to the previously observed data on top of mica. The evolution of $S_o$ domains occur rapidly within the very first minutes for the PDMS system, showing a similar trend as for mica. Multi-bilayer phase separation occurs almost immediately once the temperature is decreased, precluding accurate quantification of its progress. The scale bars are 200 $nm$ (A) 500 $nm$ (B) and 2 $\mu m$ (C).

### 4.4.4 Effects on membrane's mechanics

Taken together, the previous experiments establish the origins of the molecular reorganisation in the *E. coli* model membrane. However, directly quantifying its extent is challenging because it would require high-resolution chemical mapping of the two lipid species at different times, and all my attempts proved unsuccessful. The first approach involved incubating the membrane, at different time intervals, using cinnamycin, which is an antibacterial peptide able to

recognise PE headgroups [97, 98]. Although cinnamycin adsorption of the bilayer is observable with AFM, the marker does not spread homogenously across the surface even at high temperature where the mixture is perfectly mixed. Instead, cinnamycin tends to accumulate mainly along bilayer defects, likely due to interactions between it and the underlying surface. As an alternative, I have employed caesium ions (positively charged), which I hypothesised would preferentially interact with PG headgroups (negatively charged) due to the favourable electrostatic interactions. Given caesium's large radius, I expected to observe some topographical variations while gently imaging the sample with AFM. Unfortunately, the experimental conditions proved to be particularly challenging, and no morphological signal was detected from the caesium ions. This is likely due to the fragility of the electrostatic interactions which might be impaired by the AFM probe motion. Changing the solution's pH would have increased the strength of these interactions, but inevitably modifying the phase transition properties. Other approaches could have been employed, but each of them presents criticalities for the purpose of my research. For example, the use of fluorescently labelled lipids would significantly change the flip-flop rate in the SLBs, while techniques such as neutron diffraction [99, 100] or nano-Raman in solution [101] are particularly challenging for achieving single leaflet resolution on unmodified SLBs.
In the absence of direct compositional mapping of the SLB, I tracked the membrane's mechanical properties throughout its evolution using AFM. The membrane mechanics depends on its composition [102] and domain-specific evolution can hence provide a signature of the associated molecular rearrangements. This also quantifies the impact of the spinodal process on the biophysical properties of the membrane and is therefore highly relevant for the system. Using the same bilayer as shown in Fig. 4.4 on mica in solution, I track the evolution of both the $S_o$ and $L_d$ domains and employ force spectroscopy mapping to correlate the membrane's mechanics at any given location with the corresponding bilayer domain (Fig. 4.7). Specifically, I calculate the membrane rupture force ($F_r$) and Young's modulus ($Y$) from the spectroscopy curves [62] (protocol in Section 4.3.6 and values in Table 4.4). As expected $S_o$ regions appear stiffer and harder to break compared to the $L_d$ phase due to higher molecular packing density in the $S_o$ phase [61, 62]. However, both types of domains undergo an evolution in the mechanical properties (Fig. 4.7D).

Comparing the ratio of the average $F_r$ and $Y$ values obtained over the apparent $L_d$ and $S_o$ domains reveal a significant stiffening of the $S_o$ phase compared to the $L_d$ regions. Interestingly, the stiffening does not occur progressively, but rapidly $\sim$ 3 hours from the start of the experiment, at the onset of the spinodal process. The associated change in the local mechanical properties is considerable, with obvious consequences for biological membranes in contact with supporting structures and external entities. I note that the absolute value of the stiffness derived from AFM measurements carries a significant error, also due to possible degradation of the measuring tip over the course of the experiment. However, the emphasis is placed on the ratio between the values derived over different domains since it compares data acquires with a same tip and at a same time (within minutes).

| **Time (mins)** | **Rupture force (nN)** | | **Young's modulus (MPa)** | |
|---|---|---|---|---|
| | $L_o$ phase | $L_d$ phase | $L_o$ phase | $L_d$ phase |
| 5 | 0.31 ± 0.21 | 0.22 ± 0.10 | 5.45 ± 5.36 | 9.12 ± 5.13 |
| 30 | 0.35 ± 0.16 | 0.30 ± 0.14 | 11.32 ± 4.19 | 10.65 ± 4.3 |
| 60 | 0.48 ± 0.26 | 0.25 ± 0.18 | 16.01 ± 8.87 | 11.52 ± 4.41 |
| 120 | 0.32 ± 0.12 | 0.19 ± 0.07 | 21.60 ± 17.00 | 18.00 ± 13.00 |
| 180 | 0.39 ± 0.19 | 0.27 ± 0.16 | 16.00 ± 15.36 | 10.00 ± 6.50 |
| 240 | 1.35 ± 0.42 | 0.36 ± 0.30 | 46.99 ± 7.09 | 8.34 ± 7.94 |
| 300 | 1.35 ± 0.41 | 0.43 ± 0.40 | 41.00 ± 17.00 | 4.62 ± 3.79 |
| 360 | 1.62 ± 0.47 | 0.43 ± 0.38 | 52.16 ± 2.28 | 4.60 ± 3.22 |
| 420 | 2.06 ± 0.58 | 0.62 ± 0.56 | 58.61 ± 4.05 | 6.83 ± 4.10 |
| 720 | 2.32 ± 0.50 | 0.86 ± 0.79 | 64.27 ± 13.55 | 11.55 ± 10.05 |

Table 4.4: Table summarising the results from the force spectroscopy measurements on the different phases of SLB over time, reporting both the rupture force and Young's modulus values.

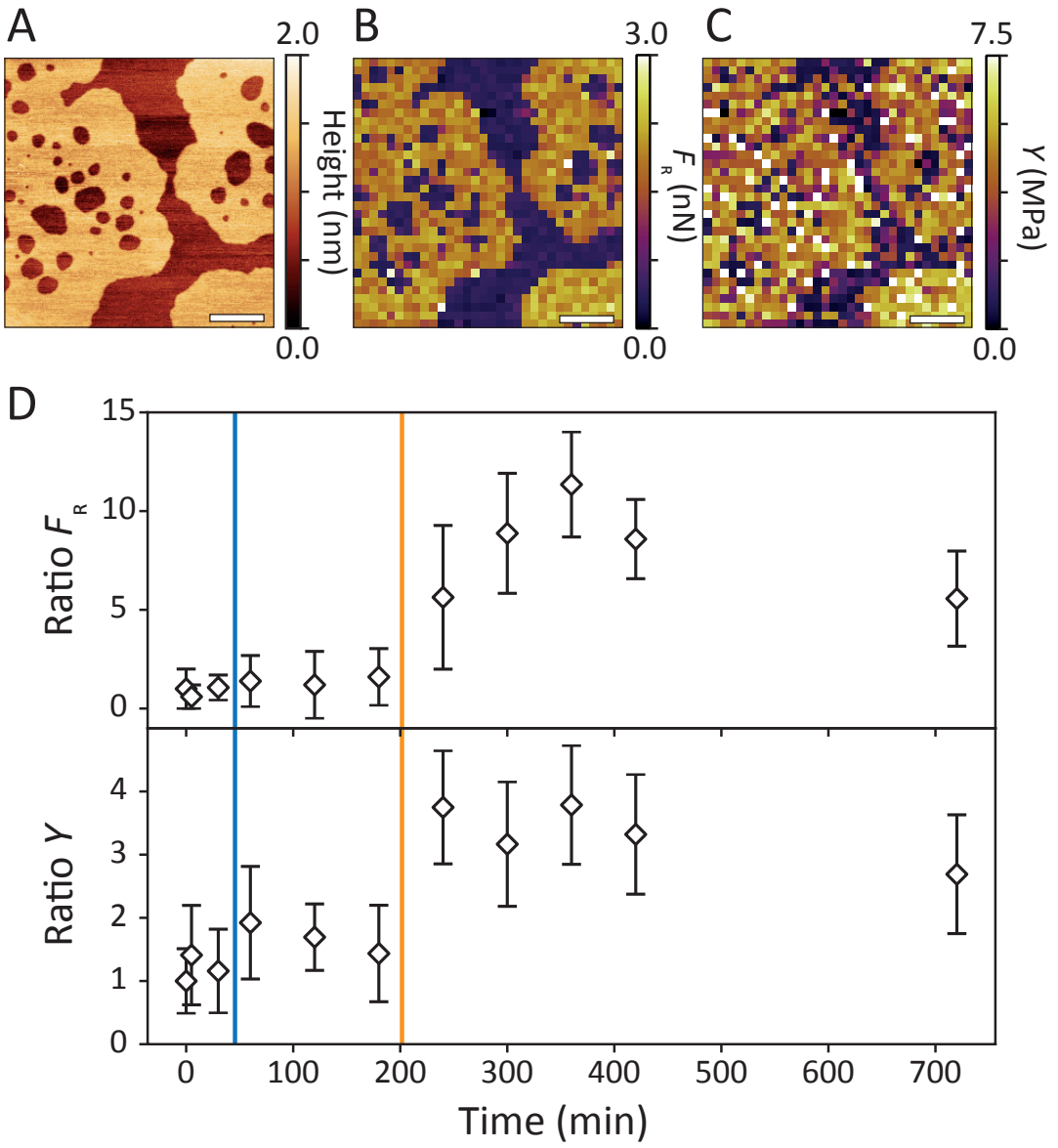


Figure 4.7: Mechanical evolution of the $S_o$ and Ld domains over time. (A) AFM topography image of a binary bilayer on mica after 6 hours from the start of the experiment. (B-C) AFM force maps displaying rupture force values and Young's modulus values respectively. (D) Ratio between gel and liquid $F_r$ (upper panel) and $Y$ (lower panel) plotted against time. The absolute values of $F_r$ and $Y$ for both phases can be found in Table 4.4. Two coloured lines matching Fig. 3B have been added to indicate the 3 regimes previously seen. The scale bar is 500 $nm$ on the AFM images (A-C).

## 4.5 Summary

Most natural biomembranes are constantly in contact with their surroundings, from the cell wall or the cytoskeleton to compartments within the cell. Here, I investigate the impact of such 'physical' contact on the molecular organisation and evolution of a model binary membrane designed to mimic the phase behaviour of *E. coli*.

My results indicate that interactions between the membrane and a surface can dramatically affect both the local molecular composition and mechanical properties of the membranes without requiring energy consuming processes or chemical reactions. Instead, the relatively weak and non-specific interaction between lipids and the surface bias the thermodynamics of the system towards a different equilibrium. While the effect can alter the local molecular diffusion within the membrane, substrate-influenced flip-flop provides a mechanism to reorganise the lipid composition and induce leaflet asymmetry, with the associated timescale depending on the properties of the contacting surface. Given the fact that my experiments are conducted in-vitro and on model membranes, the prevalence of this effect in natural systems remains to be assessed. However, my results make it possible to identify some of the key conditions and characteristics of the process, both from a thermodynamic and kinetic perspective. First, in order for the molecular reorganisation to take place, the membrane needs have one leaflet in the $S_o$ phase, a key condition for the subsequent spinodal process to take place. This requires the membrane to be close to its transition temperature, but remain slightly below in order for the phase transition to proceed differentially. If below $T_m$, the higher the temperature, the faster the spinodal process takes place for a given system (Fig. 4.4), consistent with the idea of a flip-flop-limited evolution. Second, the effect depends on the balance of lipid-lipid and lipid-substrate interactions (Fig. 4.6). This implies that both the lipid composition of the membrane and the surface chemistry and topography of the contacting object determine the extent and the kinetics of the molecular reorganisation. Here, substrates able to enhance the flip-flop rate have been able to dramatically accelerate the process, but the final balance of domains is not necessarily conserved pointing to variations in both kinetics and final equilibrium local composition of the membrane. In native membranes, a punctuate area of contact (e.g. anchoring or support point) is likely to create a local singularity in terms for diffusion or geometry, which in turns may enhance the flip-flopping rate and trigger a rapid local molecular reorganisation. Compositional rearrangement of the membrane's leaflets is a key feature in the native membrane's activity [9, 103].
More work is needed to investigate 'contact-induced' molecular reorganisation in more realistic biological membranes [104] and assess its prevalence and kinetics, but the present results already suggest the effect to be the norm in nature.

# References


[1] S. Arumugam, E. P. Petrov, and P. Schwille. *Biophys J*, 2015, 108, 1104–1113.

[2] J. A. Allen, R. A. Halverson-Tamboli, and M. M. Rasenick. *Nat Rev Neurosci*, 2007, 8, 128–140.

[3] S. Wang and N. S. Wingreen. *Biophys J*, 2013, 104, 541–552.

[4] A. Alessandrini and P. Facci. *Soft Matter*, 2014, 10, 7145–7164.

[5] C. Hammond. In: *Cellular and Molecular Neurophysiology: Fourth Edition*. Academic Press, 2015, 39–54.

[6] J. Rosko et al. *PNAS*, 2017, 114, E7969–E7976.

[7] H. Watson. *Essays Biochem*, 2015, 59, 43–69.

[8] K. Simons and E. Ikonen. *Nature*, 1997, 387, 569–572.

[9] S. A. Shelby et al. *Nat Chem Biol*, 2023, 19, 750–758.

[10] Y. Shin and C. P. Brangwynne. *Science*, 2017, 357, 6357.

[11] R. Welti and M. Glaser. *Chem Phys Lipids*, 1994, 73, 121–137.

[12] V. Martín et al. *J Alzheimer's Disease*, 2010, 2, 489–502.

[13] T. Murai. *Int J Cell Biol*, 2012, 2012, 1–6.

[14] D. Lingwood and K. Simons. *Science*, 2010, 327, 46–50.

[15] I. Levental, K. R. Levental, and F. A. Heberle. *Trends Cell Biol*, 2020, 30, 341–353.

[16] C. Paba et al. *J Colloid Interface Sci*, 2023, 652, 1937–1943.

[17] E. N. Petersen et al. *Nat Commun*, 2016, 7, 13873.

[18] J. R. Silvius. *Biochim Biophys Acta, Biomembr*, 2003, 1610, 174–183.

[19] R. M. Epand and R. F. Epand. *Biochim Biophys Acta, Biomembr*, 2009, 1788, 289–294.

[20] M. Gohrbandt et al. *The EMBO Journal*, 2022, 41, 5.

[21] D. Lopez. *Chem Phys Lipids*, 2015, 192, 3–11.

[22] D. López and R. Kolter. *Genes Dev*, 2010, 24, 1893–1902.

[23] M. Bramkamp and D. Lopez. *Microbiol Mol Biol Rev*, 2015, 79, 81–100.

[24] G. P. Otto and B. J. Nichols. *J Cell Sci*, 2011, 124, 3933–3940.

[25] O. Daumke, A. Roux, and V. Haucke. *Cell*, 2014, 156, 882–892.

[26] G. R. Chichili and W. Rodgers. *Cell Mol Life Sci*, 2009, 66, 2319–2328.

[27] P. Cowin and B. Burke. *Curr Opin Cell Biol*, 1996, 8, 56–65.

[28] W. Vollmer, D. Blanot, and M. A. De Pedro. *FEMS Microbiol Rev*, 2008, 32, 149–167.

[29] J. W. Kok, K. Klappe, and I. Hummel. *Adv Biol*, 2014, 2014, 1–11.

[30] B. P. Head, H. H. Patel, and P. A. Insel. *Biochim Biophys Acta, Biomembr*, 2014, 1838, 532–545.

[31] B. P. Head et al. *J Biol Chem*, 2006, 281, 26391–26399.

[32] J. Gómez-Llobregat, J. Buceta, and R. Reigada. *Sci Rep*, 2013, 3, 2608.

[33] A. W. Cohen et al. *Physiol Rev*, 2004, 84, 1341–1379.

[34] Z. Hu, E. P. Gogol, and J. Lutkenhaus. *PNAS*, 2002, 99, 6761–6766.

[35] S. Ramaswamy, J. Toner, and J. Prost. *Phys Rev Lett*, 2000, 84, 3494–3497.

[36] H. Nakayama et al. *Biochim Biophys Acta, Biomembr*, 1980, 601, 1–10.

[37] T. Mužić et al. *Biochim Biophys Acta, Biomembr*, 2019, 1861, 183026.

[38] Y.-H. M. Chan and S. G. Boxer. *Curr Opin Chem Biol*, 2007, 11, 581–587.

[39] J. M. Crane and L. K. Tamm. *Methods Mol Biol*, 2007, 400, 481–488.

[40] S. Ahmed, Z. Nikolov, and S. L. Wunder. *J Phys Chem B*, 2011, 115, 13181–13190.

[41] Z. V. Leonenko et al. *Biophys J*, 2004, 86, 3783–3793.

[42] S. J. Attwood, Y. Choi, and Z. Leonenko. *Int J Mol Scis*, 2013, 14, 3514–3539.

[43] A. Charrier and F. Thibaudau. *Biophys J*, 2005, 89, 1094–1101.

[44] H. Read, S. Benaglia, and L. Fumagalli. *Soft Matter*, 2024, 20, 5724–5732.

[45] H. M. Seeger et al. *Biophys J*, 2009, 97, 1067–1076.

[46] O. Enders et al. *Biophys J*, 2004, 87, 2522–2531.

[47] Y. Jing et al. *Soft Matter*, 2014, 187–195.

[48] M. V. Kök. *J Therm Anal Calorim*, 2007, 90, 817–821.

[49] G. Wang and I. R. Harrison. *Thermochim Acta*, 1994, 231, 203–213.

[50] A. Toda. *J Therm Anal Calorim*, 2016, 123, 1795–1808.

[51] M. Przybylo et al. *Langmuir*, 2006, 22, 9096–9099.

[52] T. Baumgart and A. Offenhäusser. *Biophys J*, 2002, 83, 1489–1500.

[53] F. Pincet et al. *PLOS ONE*, 2016, 11, e0158457.

[54] L. Porcar and Y. Gerelli. *Soft Matter*, 2020, 16, 7696–7703.

[55] B. Wah et al. *Langmuir*, 2017, 33, 3384–3394.

[56] R. L. Schoch et al. *J Chem Phys*, 2018, 148.

[57] Y.-H. Ma et al. *J Phys Chem C*, 2019, 123, 17899–17907.

[58] D. Marquardt et al. *Langmuir*, 2017, 33, 3731–3741.

[59] R. D. Kornberg and H. M. Mcconnell. *Biochemistry*, 1971, 10, 1111–1120.

[60] Y. Gerelli. *Phys Rev Lett*, 2019, 122, 248101.

[61] L. Redondo-Morata et al. *Biophys J*, 2016.

[62] L. Picas, P.-E. Milhiet, and J. Hernández-Borrell. *Chem Phys Lipids*, 2012, 165, 845–860.

[63] H. Hertz. *Journal fur die Reine und Angewandte Mathematik*, 1882, 1882, 156–171.

[64] S. V. Kontomaris, A. Malamou, and A. Stylianou. *Micron*, 2022, 155, 103228.

[65] P. D. Garcia and R. Garcia. *Biophys J*, 2018, 114, 2923–2932.

[66] E. Geissler and A. M. Hecht. *Macromolecules*, 1981, 14, 466.

[67] R. E. Mahaffy et al. *Phys Rev Lett*, 2000, 85, 880–883.

[68] D. Nečas and P. Klapetek. *Cent Eur J Phys*, 2012, 10, 181–188.

[69] G. V. Rossum and F. L. Drake. *Bioinf*, 2006, 22, 9117–9129.

[70] R. L. Biltonen and D. Lichtenberg. *Chem Phys Lipids*, 1993, 64, 129–142.

[71] J. Drazenovic et al. *Biochim Biophys Acta, Biomembr*, 2015, 1848, 532–543.

[72] K. A. Okotrub et al. *Biochim Biophys Acta, Biomembr*, 2021, 1863, 183514.

[73] R. N. Mcelhaney. *Chem Phys Lipids,* 1982, 30, 229–259.

[74] G. Cevc and D. Marsh. *J Cell Sci*, 1988, 6, 147–147.

[75] S. D. Connell, G. R. Heath, and J. A. Goodchild. In: *Methods Mol Biol*. Vol. 1886. Humana Press, New York, NY, 2019, 29–44.

[76] J. T. Mason. *Methods Enzymol*, 1998, 295, 468–494.

[77] F. Tokumasu, A. J. Jin, and J. A. Dvorak. *Journal of Electron Microscopy*, 2002, 51, 1–9.

[78] T. M. Bayerl and M. Bloom. *Biophys J*, 1990, 58, 357–362.

[79] J. Kim, G. Kim, and P. S. Cremer. *Langmuir*, 2001, 17, 7255–7260.

[80] S. J. Johnson et al. *Biophys J*, 1991, 59, 289–294.

[81] L. Zhang and S. Granick. *J Chem Phys*, 2005, 123.

[82] M. Rose et al. *Membranes*, 2015, 5, 702–721.

[83] C. Datt, S. P. Thampi, and R. Govindarajan. *Phys Rev E: Stat Nonlinear Soft Matter Phys*, 2015, 91, 010101.

[84] A. J. Bray. *Advances in Physics*, 1994, 43, 357–459.

[85] A. Onuki. Cambridge University Press, 2002.

[86] A. J. Wagner and J. M. Yeomans. *Phys Rev Lett*, 1998, 80, 1429–1432.

[87] V. M. Kendon et al. *J Fluid Mech*, 2001, 440, 147–203.

[88] I. M. Lifshitz and V. V. Slyozov. *J Phys Chem Solids*, 1961, 19, 35–50.

[89] H. Tanaka. *J Chem Phys*, 1996, 105, 10099–10114.

[90] H. Tanaka and T. Araki. *Phys Rev Lett*, 1998, 81, 389–392.

[91] T. Sigehuzi and H. Tanaka. *Phys Rev E: Stat Phys Plasmas Fluids Relat Interdiscip Top*, 2004, 70, 8.

[92] J. Lin, R. Dargazany, and A. Alexander-Katz. *Small*, 2017, 13, 1603708.

[93] J. S. Allhusen and J. C. Conboy. *Accounts Chem Res*, 2017, 50, 58–65.

[94] T. Schmidt et al. *PNAS*, 1996, 93, 2926–2929.

[95] J. C. Holthuis and T. P. Levine. *Nat Rev Mol Cell Biol*, 2005, 6, 209–220.

[96] J. A. Goodchild et al. *Langmuir*, 2023, 39, 10843–10854.

[97] G. Machaidze and J. Seelig. *Biochemistry*, 2003, 42, 12570–12576.

[98] M. Vestergaard et al. *ACS Omega*, 2019, 4, 18889–18899.

[99] V. K. Sharma and E. Mamontov. *Prog Lipid Res*, 2022, 87, 101179.

[100] S. J. Bryant et al. *Adv Colloid Interface Sci*, 2024, 326.

[101] L. Collard, F. Sinjab, and I. Notingher. *Biophys J*, 2019, 117, 1589–1598.

[102] S. Garcia-Manyes and F. Sanz. *Biochim Biophys Acta, Biomembr*, 2010, 1798, 741–749.

[103] S. H. w. Wu and H. M. McConnell. *Biochemistry*, 1975, 14, 847–854.

[104] S. M. Sterling et al. *Biophys J*, 2015, 108, 1946–1953.

# 5. Role of lipid rafts in the uptake of small extracellular vesicles

## 5.1 Overview

One of the key activities of the plasma membrane is to regulate cell-cell communication and intracellular signalling pathways. Beyond its role as a selective barrier, the plasma membrane is a platform for vesicle formation, fusion, and trafficking—mechanisms that are essential in mediating intercellular interactions. Among these, lipid vesicles originated from the plasma membrane such as small extracellular vesicles (sEVs) play a pivotal role in transferring biological information across cells and tissues, with significant implications in health and disease.

This Chapter explores the fusion behaviour of sEVs from a cellular model of triple-negative breast cancer with various synthetic lipid bilayers designed to mimic different regions of the plasma membrane. In contrast with my previous Chapters, these model membranes have been engineered with and without cholesterol to simulate 'raft'-like nanodomains present in eukaryotic cells in line with the sEVs employed. Using time-resolved Atomic Force Microscopy, we tracked the interactions and fusion events of sEVs with these model membranes, revealing a strong dependence on the local membrane order. Notably, fusion was most pronounced over ordered, less fluid regions, with sEVs even able to disrupt these domains in membranes with high cholesterol content. These findings underscore the importance of plasma membrane biophysical properties in modulating sEV uptake, offering new insights into the influence of lipid composition on sEV fusion dynamics and intercellular communication.

The bulk of this Chapter is based on an article titled "Lipid bilayer fluidity and degree of order regulates small EVs adsorption on model cell membrane" which has been recently published on Journal of Colloid and Interface Science. After a brief introduction to extracellular vesicles and their role, I will describe my contribution to this work in characterising the topographical properties of the employed model membrane systems and detecting the interaction within sEVs and SLBs using high-resolution Atomic Force Microscopy.

## 5.2 The role of extracellular vesicles

Extracellular vesicles (EVs) represent a heterogeneous family of lipid bilayer-enclosed structures, which are actively synthesised, secreted and eventually adsorbed by a myriad of cells ranging from eukaryotes to prokaryotes [1]. The proposed mechanism of formation of these vesicles involves the formation of a multi-vesicular body (MVB) and its subsequent fusion with the plasma membrane, leading to the final release of the EV in the extracellular space [2]. Once secreted, EVs serve as crucial bioactive carriers transporting a plethora of different cargos including proteins, transcription factors and nucleic acids. Their presence and active role have been studied and documented in both physiological and pathological processes [3–6]. EVs have been found to contribute to pathological diseases such cancer development. For example, thanks to their molecular content, EVs are able to allow the communication between cancer cells [5], while also contributing to cancer progression and the development of more aggressive phenotypes, eventually leading to metastasis [6]. However, healthy cell also rely on EVs presence, allowing for fundamental physiological processes such as cell proliferation, and stimulation of the adaptive and innate immunoresponse [3, 4, 7, 8]. Finally, EVs have also been studied for their possible applications as nano-drug delivery systems [3, 7, 9, 10]. Thanks to their biocompatibility and ease of preparation, artificial EVs could be modified to target unhealthy cells and transport small drugs in situ.

EVs are now widely accepted for their role, but the classification of these encapsulated structure is not trivial as they can significantly diverge in composition and occasionally on their formation mechanism [10]. Since the different vesicles isolation methods rely on size-based separation, EVs are

nowadays divided based on their vesicle's size, with small-EVs (sEVs) which are smaller than 200 nm, and medium/large-EVs which are generally bigger than 200 nm. Specifically, sEVs have emerged as potential cancer biomarkers as their molecular composition reflects that of the originating cells; they are also considered optimal delivering nanocarriers as they mediate the communication between tumor and tumor-associated cells, escaping the immune response [11]. This landscape is further complicated by the presence of different pathways for sEVs to deliver their molecular cargo. One of these pathways is lipid raft mediated endocytosis, where the rafts are continuously assembling/disassembling to maintain cell homeostasis and regulate vesicle trafficking [12]. Delivery of the cargo can also occur through a mechanism initiated by some degree of fusion with the target membrane, a pathway mostly adopted by viruses. This last pathway induces a level of mixing of the sEV and target membranes which become contiguous, something recently observed with umbilical cord mesenchymal stem cells (UC-MSC) sEVs from GMP production and a model membrane containing lipid rafts [13]. However, details on the dynamics of the interaction pathways of sEVs with target cells and on the specific role of each molecular player are still scarce and highly debated in the literature [7, 13]. This is related to the small size and the high heterogeneity of sEVs [14], as well as to the high spatial and temporal resolution required for the detection of lipid rafts dynamics. Several recent studies have investigated the role of the biophysical properties of the cell membrane on vesicle fusion and agglomeration rate, showing that the mechanical properties such as membrane curvature, fluidity and rigidity, all highly regulated by cholesterol content, can affect vesicle fusion kinetics [13–15].

In this study, we follow up on the raft-based pathway for regulating vesicle uptake and investigate the interaction of single sEVs isolated from a triple-negative breast cancer cell line (TNBC) with model supported lipid bilayers (SLBs) with different fluidity, ordered nanodomains, and cholesterol concentration. Using Atomic Force Microscopy (AFM) in solution, we aim to explore sEVs fusion with membranes exhibiting quasi-physiological cholesterol concentration and compositions reflecting the raft structures of in vivo systems. In particular, we focus on lipid membranes with the coexistence of two lipid phases: a tightly packed and ordered state called liquid-ordered phase ($L_o$) made of sphingolipid and cholesterol molecules, coexisting with a more fluid and disordered phase called liquid-disordered ($L_d$) phase enriched with unsaturated phospholipid. The use of

AFM enables me to track single EVs interacting and fusing with the membrane in situ and with nanoscale precision, and the subsequent evolution of the target membrane.

## 5.3 Materials and methods

### 5.3.1 Chemicals

The lipids, 1,2-dioleoyl-sn-glycero-3-phosphoCholine (18:1 (Δ9 - Cis) PC), 1,2-dipalmitoyl-sn-glycero-3-phosphoCholine (DPPC, 16:1), Sphingomyelin (brain, porcine, SM), and cholesterol (ovine wool, >98%), have been purchased from Avanti Polar Lipids (Alabaster, AL). Salts (all>99% purity) have been purchased from Sigma-Aldrich (Dorset, UK) and dissolved in ultrapure water (Merck-Millipore, Watford, UK) to prepare TRIS buffer solution (10 mM concentration, pH = 7.4).

### 5.3.2 Small unilamellar vesicles preparation

The single lipids suspended in chloroform have been mixed and dried in a 4 mL glass vial before being rehydrated in the TRIS buffer to obtain a final concentration of 1 mg/mL. The lipid solution was gently bath sonicated for 40 minutes at 45°C, until the solution looked opaque and milky, indicating the dissolving of lipids in the solvent. Then the solution was vortexed and extruded 51 times using a Mini-Extruder kit (Avanti Polar Lipids) with 2 Whatman 100 $nm$ filter (GE Healthcare Life Sciences, Little Chalfont, UK) at 40°C to form small unilamellar vesicles (SUVs).

### 5.3.3 Supported lipid bilayers preparation

Lipids have been combined in three lipid mixtures: DOPC-SM (2:1 molar ratio) with Chol (5, 10, 17 mol%), DOPC-SM and DOPC-DPPC in a fixed molar ratio of 2:1, and lastly, DOPC and DPPC alone. The obtained extruded solution was diluted in TRIS/$CaCl_2$ buffer to a final concentration of 0.4 mg/mL with 2 mM $CaCl_2$. For all compositions, the vesicle fusion method was adopted as a standard

procedure for planar lipid bilayer preparation. The sample was deposited on a freshly cleaved mica substrate (Nano-Tec V-1 grade, 0.15 - 0.21 mm thickness, 10 mm diameter), incubated at 50°C for 30 min, and slowly cooled to 27°C, then extensively washed with TRIS buffer 10 mM.

### 5.3.4 Atomic Force Microscopy imaging

AFM was performed on commercially available microscope (Cypher ES from Asylum Research), working at 27 °C in high resolution AC mode. Sharp nitride levers (SNL-10 with A geometry from Bruker Corporation) have been used to perform the imaging in liquid conditions. Images have been acquired at 512 x 512 pixel frames at 2.44 Hz.

## 5.4 Results and discussion

### 5.4.1 Characterisation of eukaryotic-like SLBs

As a first step towards characterising the sEVs uptake mechanism, the design and development of a correct model membrane system is crucial. Considering that, we first performed a careful topographic characterisation of several multicomponent-SLB by means of AFM. To emulate the classic composition of human's plasma membrane and their microdomains [16], 3 lipid species have been employed: DOPC which is a neutral and monosaturated phospholipid (18:1) which is one of the main lipids in eukaryotic systems [17, 18], sphingomyelin (SM) that represents one of the most abundant sphingolipids in the plasma membrane, and is characterised by long saturated fatty acyl chains [19], and cholesterol (Chol) that sterically interacts with the acyl chains of other lipids and preferentially with saturated phospholipids such as SM [20]. As described in Section 1.4.1, Chol is a well-known lipid raft element, which regulates the fluidity of the membrane and the packing of these microdomains [20–22]. It is therefore important to identify the correct concentration of Chol to use, by matching the native molar ratios, while considering the experimental limitations. Three cholesterol molecular concentrations have been tested: 5 mol%, 10 mol% and 17 mol%, with DOPC and SM kept at a fixed 2:1 molar ratio. In the following

sections the sample composition with 17 mol% will be described in more depth and compared with a bilayer that has no sterol content. The 17 mol% Chol falls in the typical biological range of 15-50% for the sterol component, and offers good reproducibility and stability when performing AFM imaging in liquid conditions [23, 24].

Examples of lipid phase separation in eukaryotic-like SLBs observed in AFM are presented in Fig 5.1. As previously seen in Chapter 3 and 4, the more ordered domains (in this case, liquid-ordered, $L_o$) are visible as they protrude from the overall liquid disordered ($L_d$) phase with different height, area and number according to the cholesterol content of the mixture. The taller $L_o$ bilayer domains exhibit a maximum diameter of around 0.5 $\mu m$ with 5 mol% Chol, a value that increases with Chol and reaches around 1.5 $\mu m$ at 17 mol%. The apparent number of domains changes very little with increasing cholesterol percentage as reported in Fig. 5.2, varying from an average value of 113 $\pm$ 7.07 to 128 $\pm$ 5.65 and 135 $\pm$ 14.36 respectively. The increase of the area occupied by $L_o$ domains is accompanied by a decrease of their relative height with respect to the surrounding DOPC. The total area occupied by $L_o$ domains is directly related to the Chol in agreement with the theory of the preferential mixing of cholesterol with saturated lipids such as SM. This results in the increase of the area per lipid [25, 26], and a 'cholesterol-condensing effect' on phospholipids thickening of the $L_d$ phase and a reduced height difference with the $L_o$ domains [25]. Lastly, it has been demonstrated that the transition temperature of a phospholipid system decreases with increasing cholesterol concentration [24]. This explains the lower number of $L_o$ domains per scanned area observed for the 5 mol%, where the transition starts at 30 °C, when compared with the 10 mol% and 17 mol% where lower thermal fluctuations are required to promote the $L_o$ phase nucleation. While helpful to explain the AFM observations, a full description of the systems should also take into account the impact that a rigid substrate and the kinetics of the temperature control during sample cooling, which have severe effects on the bilayer properties as previously investigated in Chapter 4.

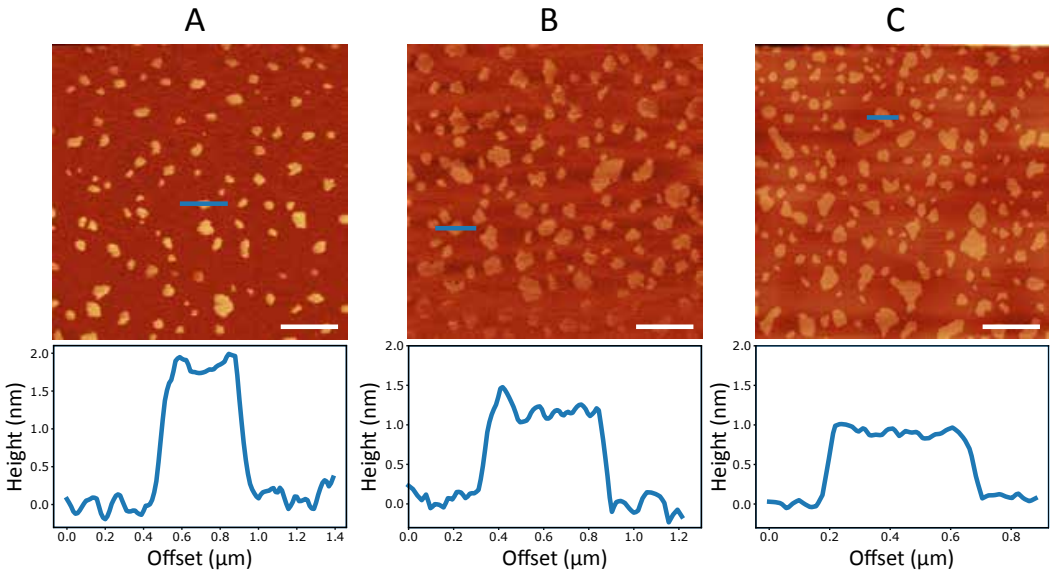


Figure 5.1: AFM topographical characterisation of DOPC-SM (2:1 molar ratio) SLBs with varying Chol concentration. The SLB contain 5% (A), 10% (B) and 17% (C) of Chol. In each image, a profile is shown to highlight the hight of the $L_o$ domains from the $L_d$ phase. The scale bar in all the images is 2 $\mu m$. The colour scale of all the images is 3 nm.

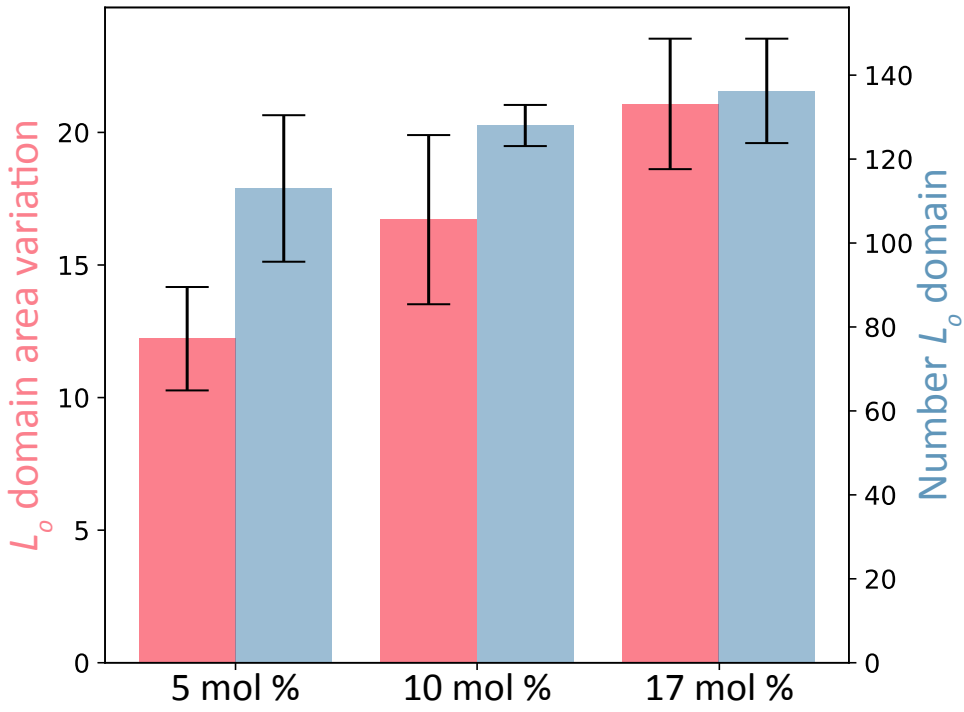


Figure 5.2: Comparative analysis of the area and number variations of the $L_o$ domains present in the SLB showed in Fig.. 5.1 with increasing Chol concentration. With increasing Chol concentration, $L_o$ domains appear wider and more abundant, confirming Chol preferential localisation in these domains. This graphical representation has been made by Carolina Paba. However, the colours have been here modified to emphasise the different y-axis.

### 5.4.2 Adsorption of sEVs and local biophysical changes

With this brief topographical characterisation of our basic model system, we then explore the interaction of sEVs isolated from the TNBC MDA-MB-231 cell line (isolation performed by C. Paba). TNBC represents one of the most aggressive breast cancer subtypes, with a poor prognosis due to the absence of targetable receptors, high propensity for metastatic progression and lack of effective chemotherapy treatments [27]. The role of sEVs in TNBC has been previously addressed [28], highlighting their role in the cancer progression. TNBC-derived sEVs induce morphological and biomechanical changes in non-metastatic cancer cells toward higher aggressiveness, representing a possible fundamental pathway for TNBC metastatic progression.

Here, the vesicles have been put in interaction with our model membranes. The system evolution was followed in real time within a few minutes from the sEVs injection. A representative AFM image of sEVs adsorption on the 17 mol% Chol membrane is shown in Fig. 5.3A. The adsorption of sEVs induces small protrusions $\sim 1\ nm$ above the height over the $L_o$ domains, accompanied by a local destabilisation of the $L_o$ region at the edges of the interaction's site. This destabilisation appears as fluid-like regions surrounding the protrusions (blue arrows in Fig. 5.3) and the formation of pores confined at the level of the outer leaflet of the supported lipid bilayer. Given the typical 5-6 $nm$ thickness of the membrane as measured from the SLB defects [13, 29], we interpret the localised protrusions as portions of sEVs clusters which strongly interacted with the SLB through an adsorption process involving their partial fusion and mixing with the membrane, and the possible molecular cargo release due to pore formation. However, even if we cannot discard the hypothesis that sEVs docking might be favored by the presence of defects in the SLB, it is a matter of fact that no morphological changes have been observed at the DOPC ($L_d$) level, and that only the interaction between sEVs and $L_o$ domains was detectable. To understand whether the protrusions are EV-related components or the result of the $L_o$ degradation process, a time-resolved analysis was performed to track the process evolution (Fig. 5.3A-C). A drastic rearrangement of the $L_o$ domains is visible with a progressively melting into the surrounding SLB, in favour of positive growth for both the area occupied by the lipid-vesicles protrusions and SLB invaginations. The sum of the area occupied by the small protrusions

and the one of the $L_o$ domains stays constant during time, pointing to a lipid rearrangement between the two phases, with one growing at the expenses of the other. The area occupied by $L_o$ domains progressively decreases starting from the small defects of the $L_o$ phase characterised by high curvature and evolving laterally until the melting with the $L_d$ phase expansion is completed. Simultaneously, a slight increase in the area occupied by pores and the $L_o$ phase takes place.

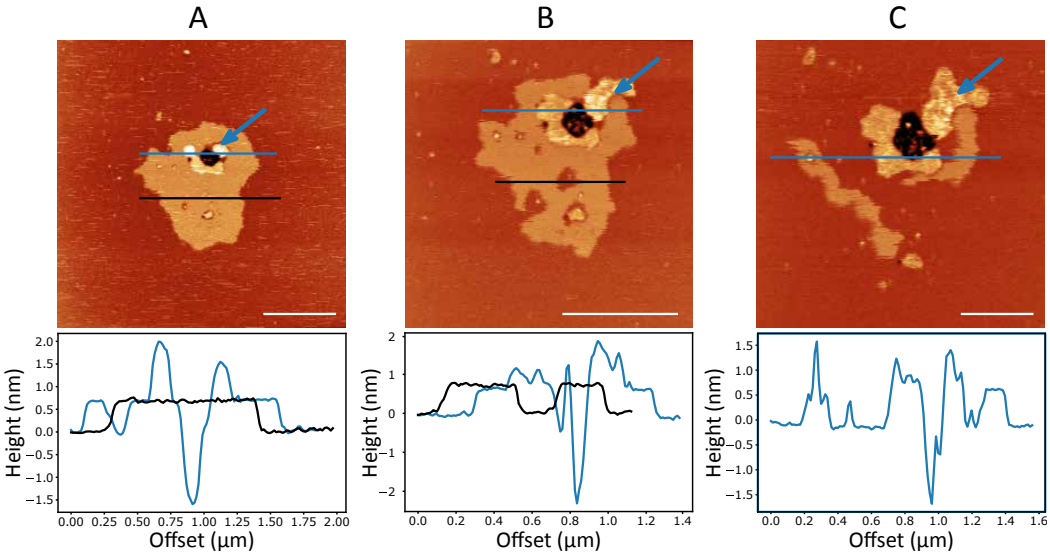


Figure 5.3: Time-resolved AFM topographic images of the interaction between sEVs and the SLB made of DOPC-SM (2:1) with 17% Chol. Each image presents a line profile to show the height of the original lipid domains (in black) and the height of the protrusion generated by sEVs interaction (in blue). Blue arrows have been used to indicate the protrusion position and disruptive enlargement with time. The images have been acquired at 27°C and within 10 minutes from sEVs injection. The scale bar in all the images is 1 $\mu m$ for (A-B), and 500 $nm$ for (C). The colour scale of the images is 4 nm (A,C) and 5 nm (B).

The 'melting' effect of sEVs on planar lipid bilayer has previously been observed by our collaborator's group [13], where sEVs from UC-MSC cell line have been tested in the interaction with a SLB enriched with 5 mol% cholesterol. Here, sEVs lead to a dramatic fluidification of the $L_o$ phase, in contrast to the previous study where a mixing between sEVs and the $L_o$ was observed instead, with the formation of high granularity patches protruding 4 $nm$ above the SLB. These apparent differences in docking process and the resulting impact on the SLB suggests possible intrinsic differences in the EV adsorption process based on sEVs origin and cholesterol content of the target membrane. To further investigate the impact

of the sEVs origins, we tested the behaviour of sEVs isolated from the UC-MSC cell line with the same target membrane containing 17 mol% Chol, resulting in qualitatively similar results to those previously reported [13] (Fig. 5.1). Given the relevance of lipid raft integrity in regulating cell proliferation, adhesion, and invasion [30], these results further strengthens the idea of EV potency altering the membrane properties. It also underlines the need for screening approaches that consider, other than EV's molecular cargo and surface properties, the cell membrane molecular composition in order to be able to investigate their ability to alter the membrane properties of recipient cells, such that both faces of the interaction process can be explored.

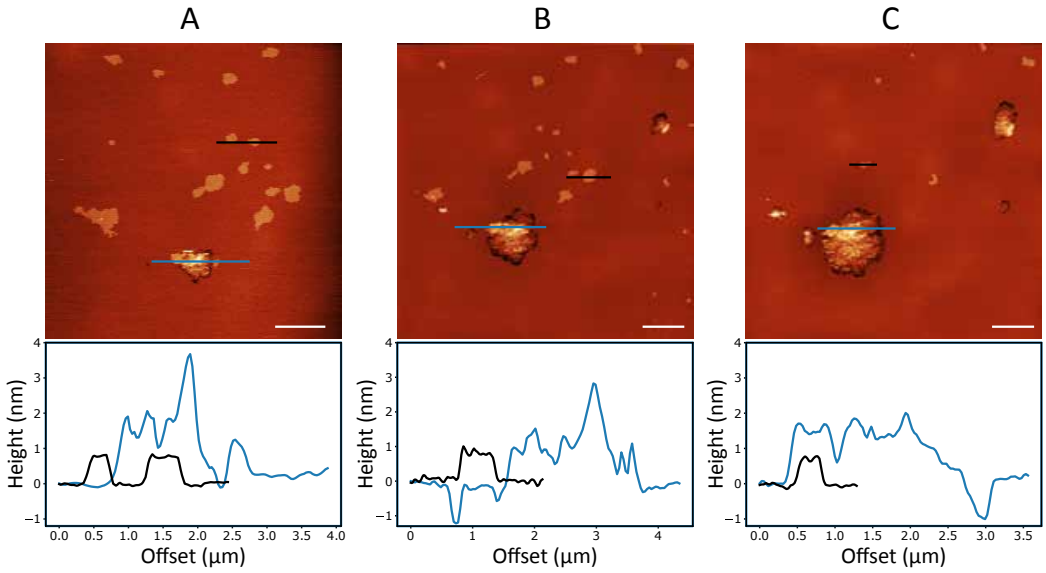


Figure 5.4: Time-resolved AFM topographic images of EVs (UC-MSC cell line) interacting with DOPC-SM (2 : 1) SLB with 17 mol% Chol with corresponding height profiles, acquired at 27 °C, with a time-lapse of 10 minutes The scale bar in all the images is 2 $\mu m$. The colour scale in all the images is 5 nm.

### 5.4.3 sEVs interaction is regulated by lipids mobility

The previous results highlight the importance of ordered nano-domains on the adsorption and fusion of sEVs. The well-established importance of cholesterol in modulating the emergence, stability and fate of these nano-domains makes it an obvious agent for indirectly modulating sEVs uptake in recipient cells. It is however not clear at this stage to what extent the effect is physical in terms of membrane biomechanics and fluidity or chemical through specific interactions between cholesterol and adsorbing sEVs. To further study the impact of membrane fluidity on modulating the sEVs adsorption, two control

compositions with 0% Chol content have been also analysed containing either DOPC and SM 2:1 or DOPC and DPPC 2:1 at 27°C. In these conditions, SM domains are expected to form an ordered phase also called solid-ordered ($S_o$), characterised by a higher degree of order and less fluidity, surrounded by fluid DOPC. Similarly, DPPC domains should form highly ordered gel-phase domains within the DOPC. For both membranes, AFM imaging confirms the expectations (Fig 5.5A-B), with SM forming smaller domains covering an average percentage area of 1.17% and protruding 1.75 $nm$ over the DOPC layer, compared to bigger DPPC domains, occupying an average 2.8% of the membrane and with a relative height of 2 $nm$ over the surrounding DOPC. The SM $S_o$ domains are also more irregular in height than DPPC, showing two different levels at 0.75 $nm$ and 1.75 $nm$ above the DOPC layer, suggesting that the phase transition of the SM during the cooling is not uniform. Indeed, the two levels can be explained by a leaflet-by-leaflet phase transition where the SM molecules in contact with the substrate solidify first [31, 32].

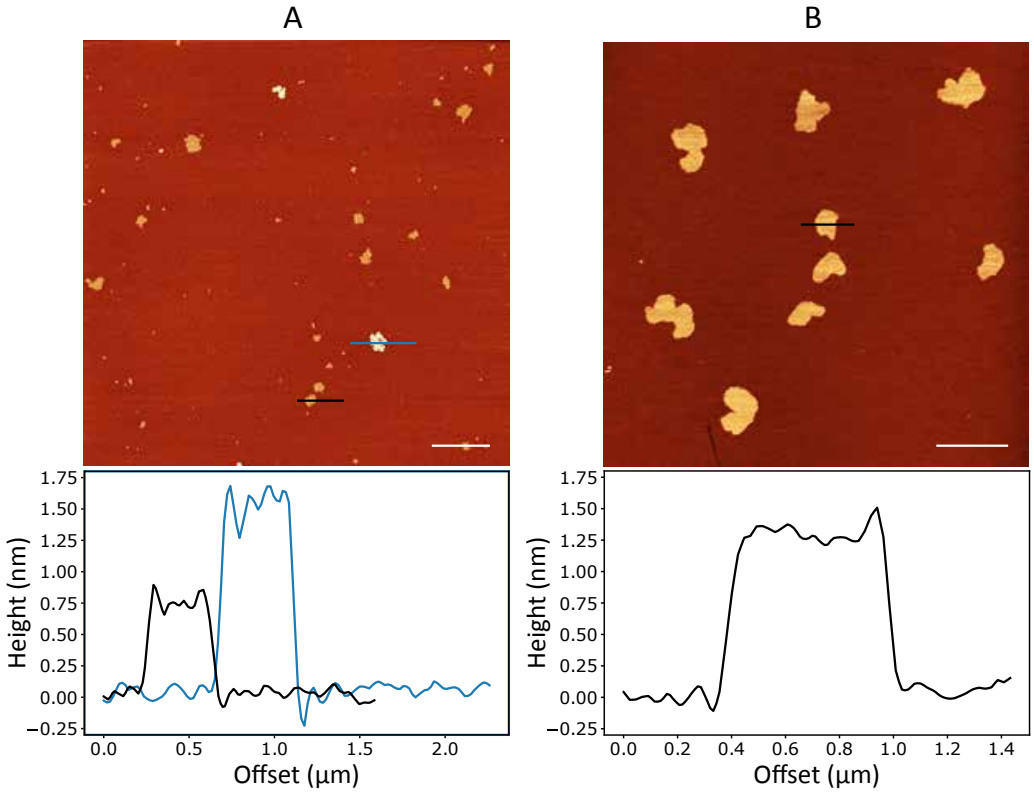


Figure 5.5: AFM topographic images of (A) DOPC/SM and (B) DOPC/DPPC (2 : 1) SLB with corresponding height profiles, acquired at 27°C. Each image is presented with line profiles showing the height of the $S_o$ domains with respect to the $L_d$ phase. The scale bar is 2 $\mu m$ for both images. The colour scale in both images is 2 nm.

The first test of sEV-SLB interaction is reported in Fig. 5.6, acquired within few minutes after vesicles' addition to the DOPC-SM (2:1) model membrane. A preferential interaction of sEV-MDA-MB-231 with the SM domains is here observed. Upon sEVs-membrane interaction, protrusion of circa 3-6 $nm$ above the lipid domains. Interestingly, it would be expected to have a preferential insertion of the sEVs at the interface of the two SM asymmetric leaflets, or along the phase borders of the two lipid phases, as both would represent two energetically favorable sites for molecule interaction. However, the sEVs protrusions only localise over the symmetric part of the $S_o$ domains. Moreover, by analysing the same area in a time scale of 1 hr an overall height increase of the protrusions can be noted, with no morphological variations in the area surrounding the site of interaction. This suggests that sEVs are no longer able to mix with their lipidic component within the SLB in absence of cholesterol. Finally, the number of interaction sites per scanned area is higher compared to the membrane with 17% of cholesterol, indicating an enhanced EV interaction with the planar bilayer.

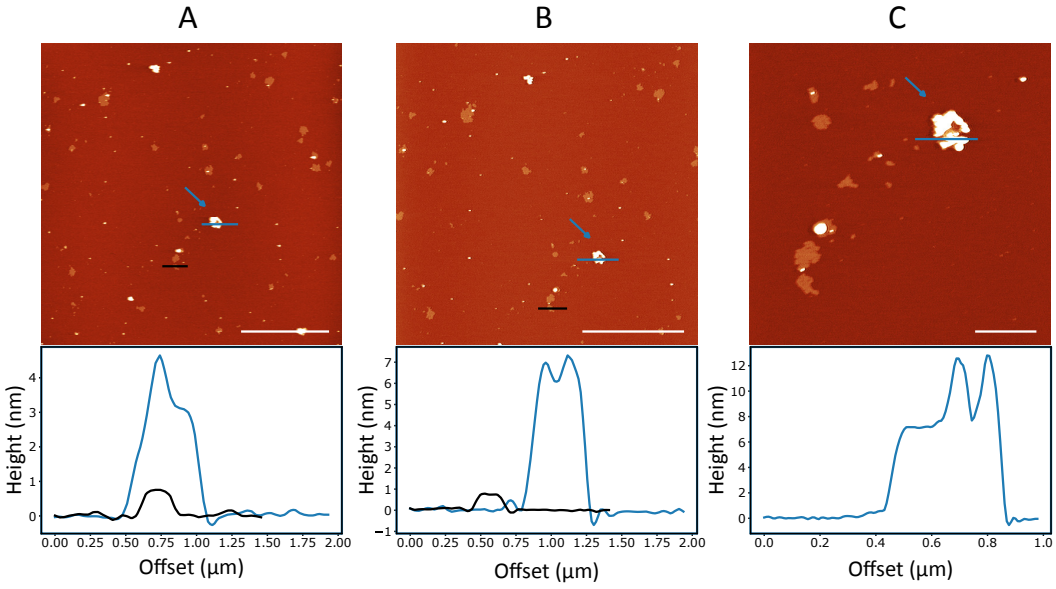


Figure 5.6: Time-resolved AFM topographic images of sEVs (MDA-MB-231 cell line) interacting with DOPC-SM (2 : 1) SLB with corresponding height profiles, acquired at 27°C in Tris buffer 10 mM , with a time-lapse between (A) and (B) of 1 h. Image (C) is a magnification of image (B), acquired within a few minutes. The scale bar is 5 $\mu m$ for images (A-B), and 1 $\mu m$ for the image in (C). The colour scale is 4 nm (A), 5 nm (B) and 7 nm (C).

The comparative experiment conducted on the DOPC-DPPC membrane displays a similar degree of order and level of saturation to the model system with SM,

ruling out a chemical affinity of the sEVs with SM. Also in this scenario, sEVs show preferential interaction with lipid ordered domains and protrusions ranging from 4 to 12 $nm$ start to emerge. However, contrary to SM domains, a mixing with the vesicles is visible, inducing an increase of the relative height of the $S_o$ domains (Fig. 5.7). The initial difference between the $L_d$ and $S_o$ phase of 1.5 – 2 $nm$ (Fig. 5.6), gives space to a much higher step width of 8 $nm$ (Fig. 5.7). This is confirmed by AFM revealing the overlapping of multiple layers and the presence of a 'vesicle-like' morphology over the DPPC domains. A possible explanation of this process would be the vesicles engulfment by the DPPC domains, whose mechanism consists of the spreading of the molecules/vesicles onto the membrane, followed by their partial or complete engulfment within the membrane.

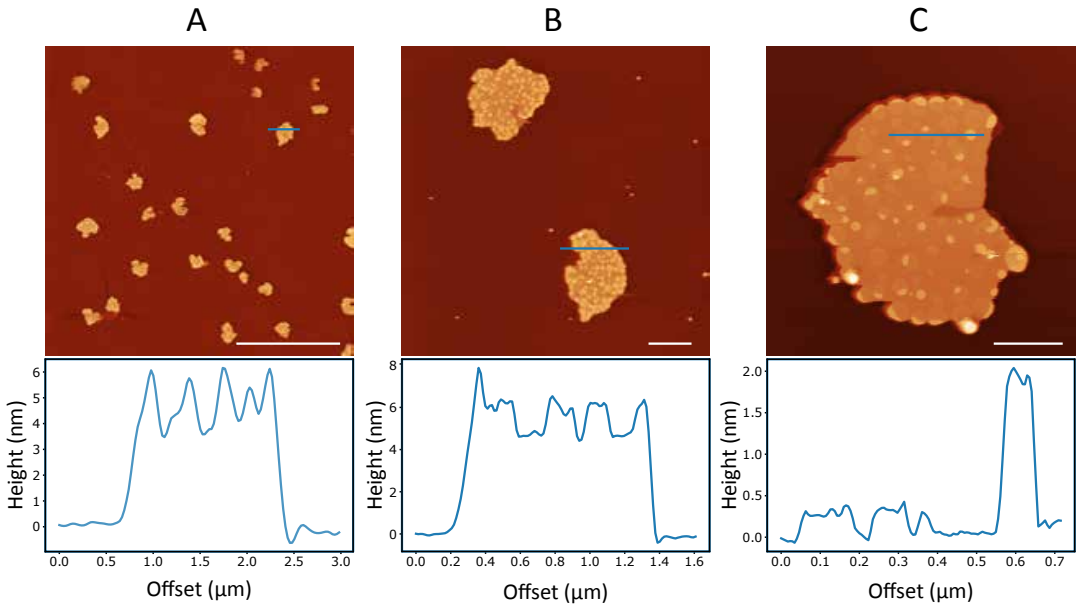


Figure 5.7: AFM topographic images of EVs (MDA-MB-231 cell line) interacting with DOPC-DPPC (2 : 1) SLB with corresponding height profiles, acquired at 27°C, with a time-lapse of 15 minutes. The scale bar in all the images is 10 $\mu m$ for (A), 1 $\mu m$ for (B) and 500 $nm$ for (C). The colour scale in all images is 7 nm.

To fully confirm the hypothesis of sEVs preferential mixing with high-ordered domains, two control experiments have been performed using single-component SLB made of either pure DOPC or pure DPPC, representing a full disordered and fully ordered system at room temperature, respectively. The results, reported in Fig. 5.8, confirm that sEVs do not interact with the disordered DOPC SLB, while a maximal interaction can be observed for the DPPC SLB, resulting in the SLB

morphology reshaping over a larger time scale compared to the system enriched with cholesterol. These results highlight the need of lower system fluidity for the 'lipid raft' domains in order to have a fast EV adsorption process and cargo release over the SLB. Moreover, the structural SLB modification leading to a 'lipid rafts' fluidification further stresses the importance of the molecular orientation and packing in the recipient membrane lipids to control interaction and uptake of sEVs over time. These results pave the basis for further investigating the physicochemical mechanisms of the cell membrane, and in particular of lipid rafts as a preferential route of interaction with the sEVs.

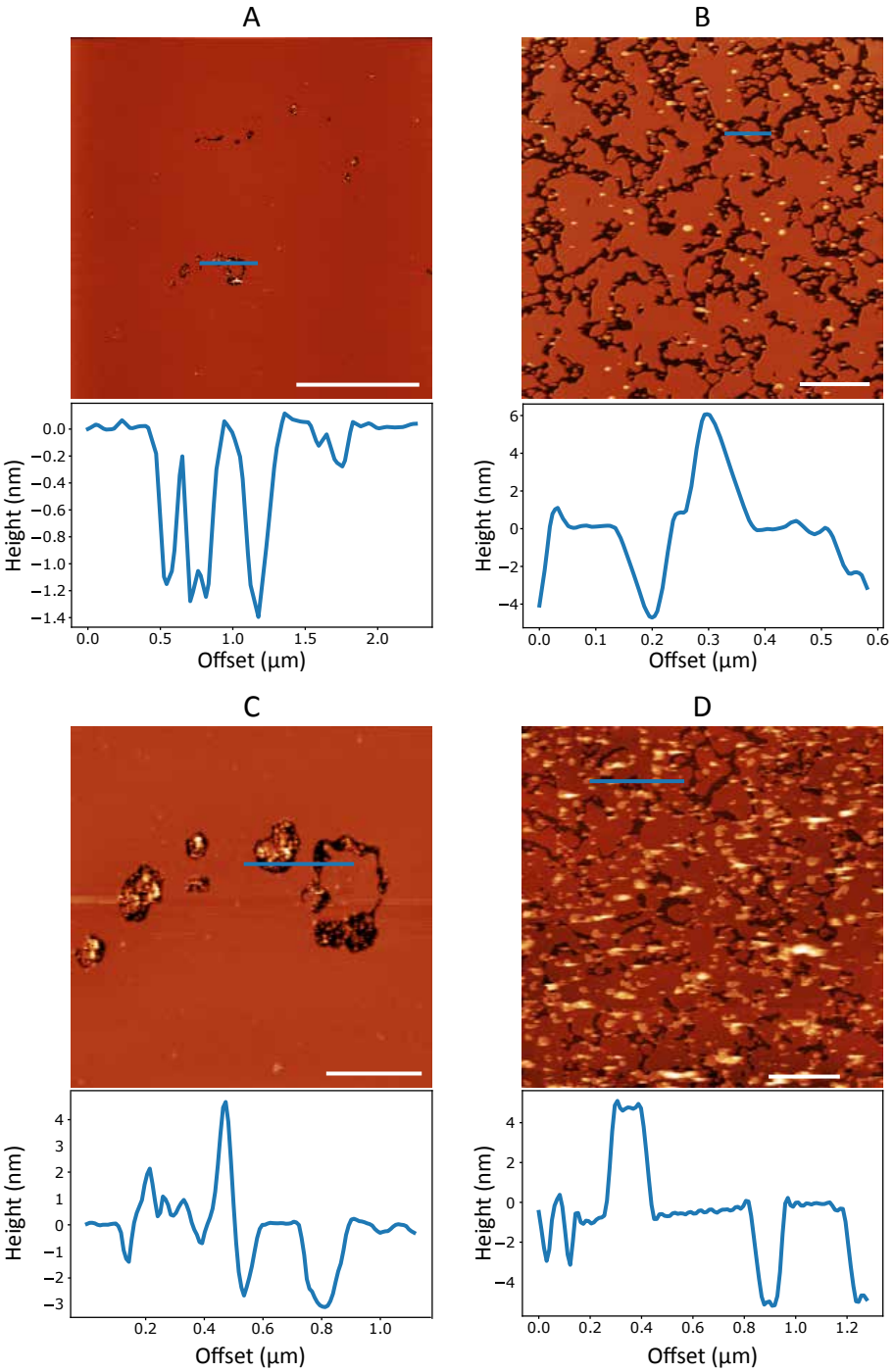


Figure 5.8: AFM topographical characterisation of full DOPC and full DPPC SLBs before (A-B, respectively) and after (C-D, respectively) addiction of sEVs. Each image present a line profile to show bilayer height and eventual sEVs interacting with the surface if detected. The scale bar is 5 $\mu m$ for (A) and 1 $\mu m$ for (B-D). The colour scale is 5 nm (A,C) and 7 nm (B,D).

## 5.5 Summary

The development of a multi-component SLB mimicking the 'lipid-raft' structure of cell model membranes, allowed to study the driving forces regulating the sEVs uptake for vesicles isolated from breast cancer cell lines. Our findings, based on time-resolved AFM topographic imaging, indicate a preferential sEV affinity for the ordered lipid raft-like domains. However, the adsorption process undergoes different pathways depending on lipid bilayer composition and fluidity. Working at the submicrometric level and performing a time-resolved analysis it was possible to identify two interaction pathways. For a fluid SLB enriched with cholesterol, the adsorption process is featured by the formation of sEV clusters protruding over the outer layer of the model system. In the same frame, a pore-opening close to the interaction site occurs, followed by a fluidification step that leads to lipid raft integrity loss. Whereas, for a rigid system without cholesterol, the adsorption pathway follows the budding-fission mechanisms [33], with maximal affinity with the solid-ordered domains. This alternative mechanism is described by the fusion of the vesicles with the outer layer of the model membrane and the formation of an intermediate regular lipid phase due to full lipid mixing with the vesicles. In such a rigid system, the extent of the interaction is featured by the formation of a stable state not prone to fracture, which leads to a large-scale shape modification over time. Our study provides evidence that the degree of sEV mixing with lipids is highly regulated by the vesicle origin but also by the fluidity of the SLB. Although the lipid composition is limited to a restricted choice of lipids and cholesterol range, we believe that our results provide a strong message in light of the chemical and physical forces regulating the vesicle uptake, underlying that both cell membrane composition and lateral organisation must be taken into consideration to rationalise sEV interaction and cargo release in the recipient cell. Moreover, it is also evident that the side effects on lipid raft integrity are not negligible as well, as it has been demonstrated that membrane domain disruption is fundamental for the regulation of molecules trafficking across the membrane and cell survival [30]. Furthermore, it is interesting to note that this versatile platform can be applied to study the impact of surface functionalization strategies (e.g. fusogenic proteins) on the vesicle uptake pathways [34], but it can also be easily integrated,

besides cholesterol molecules, with other lipids and proteins. In particular, the reconstitution of transmembrane proteins in the proposed model would be an innovative approach for studying transmembrane proteins localisation and activity, when the planar lipid bilayer is fabricated over a pore spanning membrane [35, 36]. We foresee that, with some implementation of the model, we can develop a versatile and broadly accessible platform for the investigation the sEVs uptake pathways.

# References


[1] M. Kumar et al. *Signal Transduction Targeted Ther*, 2024, 9, 27.

[2] E. Bazzan et al. *Int J Mol Scis*, 2021, 22, 6417.

[3] S. Araujo-Abad, M. Saceda, and C. de Juan Romero. *Adv Drug Delivery Rev*, 2022, 182, 114–117.

[4] T. Huyan et al. *Int J Nanomedne*, 2020, 15, 6485–6502.

[5] M. Bebelman et al. *Pharmacol Ther*, 2018, 188, 1–11.

[6] A. Becker et al. *Cancer Cell*, 2016, 30, 836–848.

[7] I. Herrmann, M. Wood, and G. Fuhrmann. *Nat Nanotech*, 2021, 16, 748–759.

[8] E. Buzas. *Nat Rev Immunol*, 2023, 23, 236–250.

[9] P. Vader et al. *Adv Drug Delivery Rev*, 2016, 106, 148–156.

[10] R. Kalluri and V. LeBleu. *Science*, 2020, 367.

[11] J. Maia et al. *Front Cell Dev Biol*, 2018, 6.

[12] L. A. Mulcahy, R. C. Pink, and D. R. F. Carter. *J Extracellular Vesicles*, 2014, 3, 24641.

[13] F. Perissinotto et al. *Nanoscale*, 2021, 13, 5224–5233.

[14] C. Théry et al. *J Extracellular Vesicles*, 2018, 7, 1535750.

[15] J. Grouleff et al. *Biochim Biophys Acta, Biomembr*, 2015, 1848, 1783–1795.

[16] A. Luchini and G. Vitiello. *Biomimetics*, 2020, 6, 3.

[17] H.Ingolfsson et al. *J Am Chem Soc*, 2014, 136, 14554–14559.

[18] M. Markones et al. *Langmuir*, 2018, 34, 1999–2005.

[19] P. Niemelä, M. Hyvönen, and I. Vattulainen. *Biophys J*, 2006, 90, 851–863.

[20] D. Marquardt et al. *Chem Phys Lipids*, 2016, 199, 17–25.

[21] E. London and D. Brown. *Biochim Biophys Acta, Biomembr*, 2000, 1508, 182–195.

[22] J. C. Lawrence et al. *Biophys J*, 2003, 84, 1827–1832.

[23] R. M. A. Sullan et al. *Biophys J*, 2010, 99, 507–516.

[24] L. Redondo-Morata et al. *Biophys J*, 2016.

[25] Y. Ma et al. *Biophys J*, 2016, 110, 1355–1366.

[26] T. McMullen et al. *Curr Opin Colloid Interface Sci*, 2004, 8, 459–468.

[27] K.-L. Lee et al. *Cancers*, 2019, 11, 1334.

[28] B. Senigagliesi et al. *Nanomed Nanotechnol Biol Med*, 2022, 44, 102582.

[29] P. Balgavy et al. *Biochim Biophys Acta, Biomembr*, 2001, 1512, 40–52.

[30] A. Badana et al. *Journal of breast cancer*, 2016, 19, 372–384.

[31] H. A. Rinia et al. *Febs Letters*, 2001, 501, 92–96.

[32] A. Alessandrini and P. Facci. *Soft Matter*, 2014, 10, 7145–7164.

[33] L. Liu, C. Duan, and R. Wang. *J Chem Phys*, 2024, 160.

[34] R. Verta et al. *Cells*, 2022, 11, 146.

[35] N. K. Teiwes et al. *ACS Appl Mater Interfaces*, 2021, 13, 25805–25812.

[36] P. Mühlenbrock et al. *Biophys J*, 2020, 119, 151–161.

# 6. General discussion and Conclusions

## 6.1 Summary of Chapters

Plasma membranes are central to numerous processes that support cellular physiology, from enabling cell-to-cell communication to controlling cellular trafficking [1, 2]. In both eukaryotic and prokaryotic organisms, membrane functionality is crucial for survival, highlighting the need to understand their behaviour at a molecular level. However, plasma membranes are inherently heterogeneous systems operating within crowded environments [3, 4], making it challenging to fully characterise their properties and interactions. The development of model membranes has represented a significant advancement in this field, allowing researchers to simplify these complex bilayer systems while preserving their essential characteristics [5–7]. Model membranes have facilitated the study of many membrane-associated biological phenomena, from understanding membrane protein function [8, 9] to phase separation behaviour [7, 10, 11]. Despite these advances, many membrane mechanisms remain unknown, emphasising the potential of model systems for further exploration.

In my thesis, I have contributed to this field by designing and developing a model membrane system for the *E. coli*'s inner membrane, mimicking its compositional, thermodynamic, and physical properties. Using this model with DSC, AFM imaging, and force spectroscopy modes, I provided new insights into the phase separation properties of biological membranes. Additionally, I designed and developed an eukaryotic-based model membrane to investigate how membranes facilitate EV uptake and the specific role of lipid rafts in this process. My findings are summarised as follows:

- Chapter 3 details the design and development of a model system for the *E. coli*'s inner membrane. While bacterial model membranes have been studied previously, inconsistencies in composition across studies have limited their comparability and applications in complex biophysical research [12–15]. For example, models lacking CL often fall short for protein reconstitution studies, where CL plays a crucial role [16]. To address this, I identified several artificial lipid mixtures based on *E. coli* membrane composition using commercially available lipids. These mixtures are composed of PE, PG, and CL in varying molar ratios with long acyl chains (>16 carbons) to replicate the chemical composition, bilayer thickness, and surface charge distribution of the native membrane.

  I assessed the thermodynamic properties of these candidate mixtures using DSC, with results compared to two complex *E. coli* native extracts. I identified five ideal mixtures: two binary systems (lacking CL) and three complete ternary systems that closely replicate the thermodynamic behaviour of the native membrane.

  Additionally, I confirmed the stability of these mixtures for forming model membrane systems, such as large unilamellar vesicles and SLBs. The candidate mixtures have been further validated as *E. coli*-like models by probing their mechanical properties using AFM force spectroscopy. Results showed comparable resistance to compression (expressed through the Young's modulus) and stretching (indicated by the stretching modulus) between the candidate mixtures and the native lipid extracts. These similarities reinforce their potential as *E. coli* membrane models for future studies on bacterial membrane function. In particular, due to their matching physical properties and the inclusion of CL, these models present an ideal in vitro platform for studying membrane proteins involved in mechanotransduction processes.

- Chapter 4 investigates the phase transition behaviour of lipid membranes, focusing specifically on how external contacts impact the compositional, thermodynamic, topographical, and mechanical properties of these membranes. Cellular environments are densely crowded, with complex structures in constant contact with the plasma membrane [3, 4]. The influence of these interactions on membrane properties remains poorly understood. In particular, interactions with external structures are usually

absent in model membrane systems such as GUVs, which exist in solution, free from external or internal contact-induced perturbations.

To address this gap, I compared unsupported lipid vesicles to supported lipid bilayers (SLBs) to reveal how external contacts alter membrane properties. First, I assessed the thermodynamic behaviour of each system using calorimetric techniques: DSC for vesicles and temperature-controlled AFM for SLBs. The results demonstrate that interactions with the substrate significantly stabilise SLBs, increasing the $T_m$ and reducing lipid mobility, which in turn slows the phase transition process. Substrate interactions also modify the local molecular composition, topography, and mechanical characteristics of the bilayer. By observing SLBs below their $T_m$ over a 24-hour period with AFM imaging, I documented an initial nucleation-and-growth phase transition mechanism that shifted to a spinodal-like process. Notably, the mechanical properties of the SLBs also evolved, as force spectroscopy measurements showed that $S_o$ domains became progressively stiffer and more densely packed over time. This mechanical shift occurred on the same timescale (hours) as the onset of the spinodal process.

Although a precise compositional profiling of the SLBs was not feasible due to experimental limitations, these observations suggest that supported bilayers undergo compositional reorganisation during the phase transition process. I hypothesise that substrate-induced perturbations facilitate lipid flip-flop in SLBs, promoting compositional reorganisation and leaflet asymmetry over long timescales. This hypothesis has been supported by previous studies on substrate interactions that highlight their role in energetically enabling lipid flip-flop processes [17–20]. Additional experiments with single-lipid SLBs and unsupported vesicles confirm that this morphological and mechanical evolution is intrinsic to binary systems under substrate-induced perturbation. Overall, these findings point to a compositional rearrangement in supported bilayers driven by membrane-surface interactions. My results offer new insights into how contacts with external structures, such as cytoskeletal and filamentous proteins, can modulate membrane properties, highlighting the importance of these interactions in accurately modelling plasma membrane behaviour.

- Chapter 5 examines the role of lipid domains in facilitating the uptake of

tumor-derived extracellular vesicles in the context of dynamic membrane properties, using atomic force microscopy (AFM) for detailed analysis. In aggressive cancers such as triple-negative breast cancer (TNBC), sEVs are crucial in intercellular communication, transporting pro-tumoral factors that promote uncontrolled cell proliferation, inhibit repair mechanisms, and aid immune evasion [21, 22]. The study specifically investigates how lipid rafts and domain fluidity within the membrane impact sEV uptake, providing insights into the interactions between sEVs and plasma membrane lipid domains.

The first part of the chapter focuses on the development and characterisation of an eukaryotic membrane model enriched in cholesterol, given its critical role in membrane structure and function. Cholesterol, which constitutes up to 50% of the eukaryotic plasma membrane, is essential for forming and maintaining lipid rafts but presents imaging challenges at high concentrations in AFM. To balance membrane stability and imaging reproducibility, I optimised a DOPC-SM (2:1) model with 17% cholesterol, which provided a stable SLB suitable for sEV interaction studies.

Using AFM's high spatial and temporal resolution, this optimised model membrane was then used to explore its interactions with sEVs derived from the highly aggressive MDA-MB-231 breast cancer cell line. In contrast to previous studies involving non-cancerous cell-derived sEVs, tumor-derived sEVs displayed a strong preference for interacting with cholesterol-rich lipid rafts, disrupting their structure upon fusion. This disruptive effect, which leads to the fluidization of the SLB, is hypothesised to facilitate the release of sEV molecular cargo and redistribution of lipids within the bilayer. This hypothesis aligns with previous findings [23], where vesicles expressing spike proteins displayed enhanced interaction and invasiveness, underscoring the role of cargo in modulating sEV function.

Subsequent experiments have been conducted using alternative SLB compositions to distinguish whether the primary determinant for this interaction preference was the lipid raft's chemical composition or its fluidity. By removing cholesterol from the SLB and varying lipid content with DOPC and SM, I demonstrated that membrane fluidity, rather than chemical composition, is the primary factor governing sEV interaction. Tumor-derived sEVs preferentially interact with lipid phases exhibiting low

lateral mobility, such as ordered $L_o$ (in cholesterol presence) and $S_o$ domains (without cholesterol). Additionally, the degree of interaction remained consistent regardless of the chemical composition of these domains.

Interestingly, while sEVs disrupted $L_o$ domains, they did not destabilise the more tightly packed $S_o$ domains, emphasising the role of packing order and rigidity in the internalisation process of these vesicles. These findings highlight the significance of lipid rafts in the pathological internalisation of sEVs, suggesting that membrane biophysical properties—especially fluidity and packing order—are crucial for predicting and potentially regulating sEV uptake. This insight is also essential for the future development of lipid-based vesicles as targeted drug delivery systems.

## 6.2 General discussion

Overall, this thesis explores the properties and functions of the plasma membrane through the design, development, and application of model membrane systems. The common theme emerging from the thesis is a distinctive characteristic of native membranes: the presence of functional lipid nanodomains. This has been done by working with a series of model membrane systems in combination with AFM (which represented my main experimental tool), DSC and DLS.

Starting from the design and developing a model membrane system for *E. coli*'s inner membrane, the thesis uses different models to explore the formation and function of lipid domains in both prokaryotic and eukaryotic plasma membranes: first, a simplified binary bacterial model (Chapter 4), and then a series of eukaryotic-like systems with varying concentrations of cholesterol (Chapter 5). The use of fully controlled model systems makes it possible to gain new insights into the formation and function of the lipid rafts. The mechanisms driving lipid domain formation is shown to depend on external elements, reshaping the membrane's morphology, composition, and mechanical properties on both local and global scales. These rafts play a clear functional role with their activity not solely dependent on the localisation of specific proteins. Lipid rafts serve as selective platforms for the internalisation of extracellular macromolecules due to their unique mechanical properties, underscoring their importance in cellular contexts and the need for further investigation into these dynamic membrane

sub-compartments.

Here, I aim to discuss the broader significance of the main results of the thesis.

### 6.2.1 The requirement for developing appropriate membrane model systems

As highlighted in Section 1.6, model membranes are indispensable tools for advancing our understanding of plasma membrane behaviour. This section emphasised the importance of developing model systems that align with the fundamental characteristics of the reference membrane while addressing the specific application needs, such as protein reconstitution or the study of external molecule interactions. In this context, the design and characterisation of robust and versatile model membrane systems formed one of the central objectives of this thesis.

Many studies have attempted to develop *E. coli* models, yet several limitations remain, particularly in replicating the critical characteristics of the native membrane. For instance, the models proposed by Murzyn et al. [24] and Zhao et al. [25] utilised a POPE-POPG lipid mixture in a 3:1 molar ratio, neglecting the inclusion of CL. The absence of CL restricts these systems from supporting key processes like membrane protein reconstitution [26, 27] and alters bilayer fluidity, a property critical for membrane function, as shown in Chapter 5. Similarly, the computational model by Pandit and Klauda [12], whilst insightful in highlighting the role of cyclised lipids in bacterial membranes, presents a level of complexity that is impractical to replicate experimentally given the limitations of commercially available lipids.

The approach described in Chapter 3 balances biological fidelity with experimental feasibility. The lipid mixtures developed in this thesis incorporate key components such as CL, ensuring that the resulting systems replicate not only the chemical environment of the *E. coli*'s inner membrane but also its functional and mechanical properties. This carefully chosen balance between simplicity and relevance allows the model to serve as a versatile platform for bacterial membrane studies. Moreover, unlike many previous systems that focus solely on lipid composition, my approach integrates thermodynamic and mechanical characterisation to better replicate the complex and dynamic behaviour of native membranes. By combining DSC and AFM, Chapter 3 provides a comprehensive

description of the model's phase transition, fluidity, and mechanical response. These insights go beyond simply mimicking the compositional pattern, creating a model membrane that captures both the chemical and physical properties necessary for studying fundamental bacterial processes.

The final *E. coli* models present valuable tools for a range of applications, particularly in understanding the mechanical behaviour of bacterial membranes and the function of MSC. Proteins like MscL and MscS play a critical role in maintaining cellular integrity under mechanical stress [16, 28, 29]. Porcar et al. [17] proposed that the lipid environment directly influences MSC gating, a hypothesis challenging to test in complex native membranes or systems requiring fluorophores, which may interfere with observations. The developed model provides an ideal platform for isolating and investigating the fundamental aspects of MSC activity, particularly its response to external stress. Furthermore, while this thesis primarily employed SLBs combined with AFM, the lipid mixtures also form stable vesicular systems, expanding their applicability to vesicle-based assays.

Despite these advancements, the models presented here are not without limitations. The lack of cyclised lipids, known to influence the mechanical and functional behaviour of bacterial membranes, represents one such shortcoming. Additionally, the absence of membrane proteins limits the system to a purely lipidic environment, offering only a partial representation of the plasma membrane behaviour. The mechanical characterisation, while robust, is AFM-centric, suggesting the need for complementary techniques to provide a better understanding of the mixtures' properties. Addressing these limitations will be crucial for future research and is discussed further in the next sections. Nonetheless, the deliberate focus on lipid composition and physical properties sets a robust baseline for membrane behaviour, forming a strong foundation for future extensions. By combining experimental feasibility with biological relevance, this work provides a novel perspective on the design of model membrane systems and highlights their potential as powerful tools for advancing our understanding of bacterial membrane processes.

### 6.2.2 The behaviour of plasma membranes in the presence of external contacts

As shown in Chapter 3, 4, and 5, surface interactions severely influence the behaviour of the lipid bilayer. By placing the membrane in direct contact with an external surface, the bilayer is perturbed, experiencing a compositional, thermodynamic, and mechanical reorganisation. Supported bilayers always present transition temperatures that exceed those of bulk vesicles due to the stabilising effect of the underneath surface. This stabilisation effect is attributed to the restriction of lipid mobility and the reduction of configurational entropy upon surface interaction [10, 30, 31]. The gap between these two experimental $T_m$ depends on the applied surface and therefore the nature of these interactions. For example, Read et al. [32] recently showed that monolayers prepared on HOPG surfaces present significantly higher $T_m$ than the one observed on hydrophilic surfaces.

While the stabilising effect of surfaces is well-documented, this thesis introduces a novel perspective by examining the subsequent evolution of supported bilayers and the functional implications of these interactions. Chapter 4 provides experimental evidence of how substrate interactions drive mechanical and compositional changes within SLBs over time. By focusing on systems near their critical temperature, these results shed light on the relationship between external perturbations and lipid phase separation.

The results of Chapter 4 experimentally validate theoretical predictions that external contacts promote lipid flip-flop and bilayer reorganisation [17, 20, 33–35]. Using AFM to monitor the mechanical and topographical evolution of SLBs, this study revealed how surface interactions alter membrane properties. For example, strong and stable interactions, such as those with mica, slow lipid diffusion and suppress domain coarsening, consistent with theoretical and experimental studies that link reduced mobility to hindered phase evolution [36–38]. Over hours, these interactions facilitate a morphological and mechanical evolution of the membrane, with emerging evidence of lipid flip-flop driving leaflet asymmetry. Conversely, weaker interactions, such as those with PDMS or lipid-coated surfaces, accelerate this same compositional and topographical evolution of the bilayer (under 1 hour). The different timescales highlight an interplay between surface interactions, lipid

mobility, and critical temperature in regulating bilayer dynamics, suggesting that variations in local micro-environmental conditions could have significant implications on native membranes.

Although my results align with theoretical predictions, this approach lacks the ability to directly track individual lipid movements, indirectly inferring rather than explicitly demonstrating the flip-flop phenomenon. However, the multi-parametric approach employed here—combining mechanical tracking, topographical observations, and surface variability—provides a robust framework to suggest lipid rearrangements. Further refinement of experimental approaches could address these limitations. For instance, label-free techniques such as small-angle neutron scattering (SANS) [39] and neutron reflectometry (NR) [40] have shown potential for directly tracking lipid flip-flop. In a previous work by Gerelli et al. [40], NR experiments confirmed a relationship between flip-flop rates and the system's temperature with respect to the SLB's critical temperature. These observations suggested a correlation between higher lipid mobility and enhanced flip-flopping, supporting my results when using different surfaces. Other techniques, such as sum-frequency vibrational spectroscopy, have recently emerged as a powerful tool for probing lipid translocation without lipid modification, as shown by Liu and Conboy [41, 42]. Future studies could incorporate such techniques to complement the insights provided here.

The effect of these membrane-surface interactions have significant implications for studying native membranes, where cytoskeleton filaments and other macromolecular structures are invariably present. Native membranes exhibit intricate interactions between lipid domains and the cytoskeleton [43–45], which could modulate the dynamics described here. For example, ordered lipid domains are known to be formed thanks to the pulling effect of cytoskeleton filaments in cells such as neurons [46]. These results emphasise the importance of integrating surface interactions into the study of membrane processes, as they offer a predictive framework for understanding lipid raft formation and evolution in physiological settings. This work lays the groundwork for future studies that will explore the effects of varying surface properties, such as stiffness, hydrophobicity, and chemical composition, on membrane dynamics, a topic discussed further in the next sections.

### 6.2.3 The role of lipid rafts in EVs uptake: a protein-independent process

One of the most compelling areas of study in plasma membrane biology is the characterisation of lipid rafts' role in cellular processes. As discussed in Section 1.4, these nanodomains have been at the centre of extensive research, revealing their critical involvement in both physiological and pathological functions. Despite their importance, distinguishing the specific contributions of the lipid constituents from those of the membrane proteins localised within these domains remains an experimental challenge. By working with purely lipid model membranes in combination with high-resolution techniques like AFM, it becomes possible to isolate and focus on the role of these amphiphilic molecules.

The findings presented in Chapter 5 highlighted the pivotal role of lipids in cellular trafficking, particularly in regulating the uptake mechanism of external vesicles. Notably, the results demonstrated that vesicle internalisation is not exclusively mediated by membrane proteins, but is also influenced by lipid regions with distinct physical properties. Ordered lipid rafts emerge as preferential sites for external vesicle interactions, serving as platforms where membrane fusion and cargo release take place. Interestingly, for fluid SLBs enriched with cholesterol ($L_o$ phase), the adsorption process is characterised by the formation of small sEV clusters protruding from the outer leaflet. At these interaction sites pore formation is observed, leading to a progressive fluidification step and loss of lipid raft integrity. Conversely, in cholesterol-depleted SLBs, the adsorption process follows a budding-fission pathway which preferentially interacts with the $S_o$ domains. This latter mechanism is marked by complete lipid mixing between the vesicle and the SLB without the loss of the lipid domain's structure. The contrasting pathways highlight the dependence of sEV fusion mechanisms on the bilayer's fluidity and phase behaviour [47].

This observation is particularly novel as it underscores the active role of lipid domains not based on their chemical composition [48–50], but rather their biophysical characteristics, specifically fluidity. The regulation of lipid domain fluidity emerges as a key factor for maintaining efficient cellular trafficking across the membrane. Moreover, the study underscores that not only the lipid domain phase, but also its ability to dynamically adapt to external perturbations,

is central to its role in vesicular interactions. Combining the insights from Chapters 4 and 5, it is evident that external interactions induce compositional fluctuations that can alter not only the membrane's physical properties, but also its functional behaviour. For example, external contacts modulate the composition and fluidity of lipid domains, which in turn govern their role in processes like EV internalisation. The disruption of cholesterol-rich domains during sEV fusion, in particular, emphasises the vulnerability of fluid lipid rafts to pathological processes. Disruption or absence of such interactions could impair these physiological processes and alter the membrane's behaviour.

Additionally, the findings in Chapter 5 reveal that EV-lipid raft interactions are also influenced by the nature of the EVs themselves. EVs derived from different cell types exhibit varying membrane compositions (e.g. lipids and proteins) and intra-vesicular cargos. While the heterogeneity of EVs has been well-documented [51–53], the results suggest that this diversity underpins the multiple interaction mechanisms observed in earlier studies [54]. Specifically, the experiments presented here demonstrate that tumour-derived EVs uniquely disrupt lipid raft structures, a finding consistent with Badana et al. [55], who highlighted the dependence of breast cancer cell survival on lipid raft disruption. By contrast, non-pathological EVs do not exhibit the same interaction behaviour. Further studies are required to delineate these fusion mechanisms in greater detail and to clarify the role of specific EV constituents in mediating these interactions.

## 6.3 Future work

Further studies are essential to validate the general applicability of these findings and to address current limitations in model membrane technology and experimental approaches. Below, I outline several key questions and research directions that can extend the insights gained in this thesis.

- The membrane's ability to withstand stretching forces is a key property for cell survival, as it allows the plasma membrane to adapt to mechanical stresses. Techniques such as micropipette aspiration have been developed to directly assess these mechanical properties, providing insights into the elasticity and strength of both cellular membranes [56] and larger vesicular models [56–59]. To reinforce the findings obtained in this thesis, further mechanical characterisation of the model mixtures using micropipette aspiration could complement and validate current results, particularly by comparing vesicle-based systems to supported planar bilayers. Additionally, a key future direction would be to enhance the complexity and realism of these model membranes by reconstituting integral membrane proteins. Due to the presence of cardiolipin in the optimised mixtures, these models should facilitate the integration of proteins and potentially provide stable protein-lipid interactions [16, 26, 27, 60]. This platform could be especially valuable for studying membrane proteins involved in mechanotransduction, such as MscL. MscL proteins are significant due to their roles in cellular responses to mechanical stress and their widespread presence across diverse organisms such as *E. coli* and human cells [61–63]. Despite their importance, their gating mechanisms, lipid interactions, and clustering behaviour remain still partially unknown [63, 64]. Using AFM with this complex membrane system could provide high-resolution insights into processes such as MscL opening and clustering under tension. Specifically, to observe MscL opening, an important but challenging step will be to find ways to increase membrane tension within these SLB systems. This could be achieved by preparing dynamic substrates with tuneable mechanical properties or by introducing external macromolecules to induce tension. For example, cyclodextrins are a family of cyclic glucose oligomers that are known for their ability to remove lipids [65, 66]. This removal of lipids

increases the area occupied per lipid, resulting in an increase in membrane tension [67, 68], which could be employed also in biomimetical models such as the one here presented. This approach to study MSC gating has been already confirmed on small MSC (MscS) of *E. coli* [69], confirming the possible application of these macromolecules to induce membrane tension. Finally, modulating lipid composition within these SLBs could elucidate the specific lipid roles in MscL function. This could be done also after opening of MscL, as specific cyclodextrin show high lipid-specificity [70–72].

- SLBs are traditionally formed on flat, hydrophilic surfaces like mica, which provides both stability and compatibility with high-resolution techniques such as AFM [10]. While other substrates, including HOPG [32, 73] and silica [74, 75], have been explored, they remain stiffer than native biological surfaces. Future work could involve the development of biomimetic substrates that better replicate the mechanical properties of biological scaffolds [76]. These biomimetic substrates present a cushion which separates the bilayer from the underlying surface, creating more space for protein reconstitution and reducing the membrane-substrate interactions [76–78]. For instance, previous studies have reported protocols for the preparation of bio-functionalised surfaces presenting various cushions such as polymers [76, 79] or biological macromolecules [78, 80, 81] that could better mimic the cellular environment. However, further studies are needed to optimise the surface preparation's protocols, to reproducibly form a lipid bilayer on top of these cushions and to demonstrate their compatibility with experimental techniques such as AFM and fluorescence microscopy. SLB preparation on the actin-covered surface has been successful and found to decrease the diffusion coefficient of the lipids involved compared to the bare silica [80], highlighting the possible effect of these macromolecules on the membrane's phase transition properties. By manipulating the underlying cushion, the chemical nature of the SLB-surface interactions are varied, allowing to explore different scenario and profile how different perturbation effect membrane's behaviour [76]. These biomimetic approaches would allow more accurate studies on how membrane–surface interactions influence membrane stability and dynamics, offering deeper insights into cellular processes.

- To approach native-like conditions, sEV-membrane interaction studies should progress to using biomimetic models with integrated complexity, particularly by incorporating membrane proteins relevant to breast cancer and sEV uptake. For example, Her2, a member of the epidermal growth factor receptor family, is known for its role in regulating cell growth and differentiation [82]. Her2 is frequently overexpressed in aggressive breast cancers and is associated with poor prognosis [82, 83]. Beyond its prognostic value, Her2 has been shown to cluster preferentially with lipid raft domains known as caveolae [84]. Considering the significance of lipid rafts in sEV uptake, the role of caveolae in vesicular trafficking [85], and Her2's localisation within these domains [84], creating a Her2-integrated model could provide important insights. By combining this platform with AFM imaging, it would be possible to investigate whether sEV uptake is modulated by Her2 presence and the specific lipid-protein interactions within rafts.

  In addition to its value in understanding cancer pathology, this model could mimic a tumor-like membrane environment, providing a platform to study critical functions related to cancer progression. Such a system could help clarify the effects of lipid rafts on Her2 clustering and signalling, while also offering new perspectives on targeting lipid raft-associated proteins in cancer therapy. One challenging aspect of developing such a model is to mimic caveolae domains. Compared to generic lipid rafts, cavaeolae are nanometric membrane invaginations, with an average size of 60 $nm$ [86]. Preliminary tests have been performed on silica-based porous substrates where caveolin-1 protein has been reconstituted [87, 88]. However, further work is needed for the identification of the optimal material and protocols for both surface preparation and sample deposition.

## 6.4 Conclusions

In conclusion, this thesis successfully addresses key questions regarding plasma membrane and lipid raft behaviour, offering novel perspectives and advancing understanding in the field. Firstly, it establishes a robust and reproducible method for developing a novel model of *E. coli*'s inner membrane, which incorporates the compositional, thermodynamic, and mechanical characteristics of the native membrane. By utilising a simplified version of this model in combination with AFM, the study examines the significant impact of external contacts on bilayer behaviour near its critical temperature. The findings demonstrate that external perturbations (e.g. external biological surfaces) enhance lipid flip-flop dynamics, resulting in a complex phase separation profile. The latter part of this thesis focuses on the application of eukaryotic model membranes to investigate the interactions between EVs and lipid raft domains. The results underscore the crucial role of these domains as mediators of membrane trafficking. Lipid rafts act as sites for EV interaction even in the absence of membrane proteins, a behaviour attributable solely to their unique fluidity properties compared to the surrounding less-ordered membrane. Furthermore, the experiments provide valuable insights into the diverse fusion mechanisms of EVs carrying different cargos, particularly highlighting the disruptive effects of tumour-derived EVs on cholesterol-rich domains.

# References


[1] B. Alberts et al. W.W. Norton & Co., 2022.

[2] H. Lodish et al. W.H. Freeman, 2021.

[3] R. Ellis. *Curr Opin Struct Biol*, 2001, 11, 114–119.

[4] A. Duncan et al. *Sci Rep*, 2017, 7, 16647.

[5] Y.-H. M. Chan and S. G. Boxer. *Curr Opin Chem Biol*, 2007, 11, 581–587.

[6] M. Eeman and M. Deleu. *Biotechnol Agron Soc Environ*, 2010, 14, 719–736.

[7] V. Kiessling, S.-T. Yang, and L. K. Tamm. In: *Current Topics in Membranes*. Vol. 75. Elsevier Ltd, 2015, 1–23.

[8] G. R. Sanganna et al. *Nat Commun*, 2021, 12, 4363.

[9] N. Dolder, P. Müller, and C. von Ballmoos. *Soft Matter*, 2022, 18, 5877–5893.

[10] A. Alessandrini and P. Facci. *Soft Matter*, 2014, 10, 7145–7164.

[11] L. Picas, P.-E. Milhiet, and J. Hernández-Borrell. *Chem Phys Lipids*, 2012, 165, 845–860.

[12] K. R. Pandit and J. B. Klauda. *Biochim Biophys Acta, Biomembr*, 2012, 1818, 1205–1210.

[13] J. Shearer et al. *J Chem Phys*, 2020, 153.

[14] H. Hwang et al. *Biochim Biophys Acta, Biomembr*, 2018, 1860, 2566–2575.

[15] T. J. Piggot, D. A. Holdbrook, and S. Khalid. *Biochim Biophys Acta, Biomembr*, 2013, 1828, 284–293.

[16] P. Ridone et al. *Eur Biophys J*, 2015, 44, 567–576.

[17] L. Porcar and Y. Gerelli. *Soft Matter*, 2020, 16, 7696–7703.

[18] B. Wah et al. *Langmuir*, 2017, 33, 3384–3394.

[19] R. L. Schoch et al. *J Chem Phys*, 2018, 148.

[20] Y.-H. Ma et al. *J Phys Chem C*, 2019, 123, 17899–17907.

[21] B. Senigagliesi et al. *Nanomed Nanotechnol Biol Med*, 2022, 44, 102582.

[22] G. Raposo and W. Stoorvogel. *J Cell Biol*, 2013, 200, 373–383.

[23] R. Verta et al. *Cells*, 2022, 11, 146.

[24] K. Murzyn, T. Róg, and M. Pasenkiewicz-Gierula. *Biophys J*, 2005, 88, 1091–1103.

[25] W. Zhao et al. *Biochimie*, 2008, 90, 930–938.

[26] R. A. Corey et al. *Sci Adv*, 2021, 7, 1–10.

[27] S. Ryabichko et al. *Sci Rep*, 2020, 10, 6296.

[28] R. Buda et al. *PNAS*, 2016, 113, E5838–E5846.

[29] A. J. Oakley et al. *Protein Sci*, 1999, 8, 1915–1921.

[30] H. M. Seeger et al. *Biophys J*, 2009, 97, 1067–1076.

[31] A. Charrier and F. Thibaudau. *Biophys J*, 2005, 89, 1094–1101.

[32] H. Read, S. Benaglia, and L. Fumagalli. *Soft Matter*, 2024, 20, 5724–5732.

[33] S. Stanglmaier et al. *Langmuir*, 2012, 28, 10818–10821.

[34] A. Sreekumari and R. Lipowsky. *Soft Matter*, 2022, 18, 6066–6078.

[35] S. Botterbusch and T. Baumgart. *App Sci*, 2021, 11, 1288.

[36] A. J. Wagner and J. M. Yeomans. *Phys Rev Lett*, 1998, 80, 1429–1432.

[37] H. Tanaka and T. Araki. *Phys Rev Lett*, 1998, 81, 389–392.

[38] C. A. Stanich et al. *Biophys J*, 2013, 105, 444–454.

[39] M. Nakano et al. *Phys Rev Lett*, 2007, 98, 238101.

[40] Y. Gerelli et al. *Langmuir*, 2013, 29, 12762–12769.

[41] H. Liu et al. *Int J Food Microbiol*, 2004, 95, 147–155.

[42] J. S. Allhusen and J. C. Conboy. *Accounts Chem Res*, 2017, 50, 58–65.

[43] G. R. Chichili and W. Rodgers. *Cell Mol Life Sci*, 2009, 66, 2319–2328.

[44] P. Cowin and B. Burke. *Curr Opin Cell Biol*, 1996, 8, 56–65.

[45] B. P. Head, H. H. Patel, and P. A. Insel. *Biochim Biophys Acta, Biomembr*, 2014, 1838, 532–545.

[46] A. M. Sebastião et al. *Neuropharmacology*, 2013, 64, 97–107.

[47] L. Liu, C. Duan, and R. Wang. *J Chem Phys*, 2024, 160.

[48] E. Morel et al. *Biochim Biophys Acta, Mol Cell Biol Lipids*, 2018, 1863, 199–211.

[49] J. B. Helms and C. Zurzolo. *Traffic*, 2004, 5, 247–254.

[50] G. A. Kumar and A. Chattopadhyay. *Biochim Biophys Acta, Mol Cell Biiol Lipids*, 2021, 1866, 158882.

[51] S. A. Kooijmans, O. G. de Jong, and R. M. Schiffelers. *Adv Drug Delivery Rev*, 2021, 173, 252–278.

[52] E. Willms et al. *Front Immunol*, 2018, 9.

[53] D. W. Greening and R. J. Simpson. *Expert Review of Proteomics*, 2018, 15, 887–910.

[54] L. A. Mulcahy, R. C. Pink, and D. R. F. Carter. *J Extracellular Vesicles*, 2014, 3, 1–14.

[55] A. Badana et al. *Journal of breast cancer*, 2016, 19, 372–384.

[56] Y. Sun, T. L. Sun, and H. W. Huang. *Biophys J*, 2014, 107, 2082–2090.

[57] E. Evans et al. *Biophys J*, 2003, 85, 2342–2350.

[58] E. Evans and W. Rawicz. *Phys Rev Lett*, 1990, 64, 2094–2097.

[59] Y. Zhou and R. M. Raphael. *Biophys J*, 2007, 92, 2451–2462.

[60] M. Dahlberg and A. Maliniak. *J Phys Chem B*, 2008, 112, 11655–11663.

[61] I. Iscla and P. Blount. *Biophys J*, 2012, 103, 169–174.

[62] I. R. Bootha and P. Blount. *J Bacteriol*, 2012, 194, 4802–4809.

[63] S. L. Grage et al. *Biophys J*, 2011, 100, 1252–1260.

[64] C. Pliotas et al. *Nat Struct Mol Biol*, 2015, 22, 991–998.

[65] C. D. Cox et al. *PNAS*, 2021, 118, e2104820118.

[66] G. Crini. *Chem Rev J*, 2014, 114, 10940–10975.

[67] M. V. Clausen et al. *PNAS*, 2017, 114, E8343–E8351.

[68] M. Staykova et al. *PNAS*, 2011, 108, 9084–9088.

[69] Y. Zhang et al. *Nature*, 2021, 590, 509–514.

[70] Z. Huang and E. London. *Langmuir*, 2013, 29, 14631–14638.

[71] S. Mahammad and I. Parmryd. *Methods Mol Biol*, 2015, 1232, 91–102.

[72] J. C. Debouzy et al. *J Pharma Sci*, 1998, 87, 59–66.

[73] H. Bi et al. *Langmuir*, 2018, 34, 9561–9571.

[74] Y. Jing et al. *Soft Matter*, 2014, 187–195.

[75] S. D. Connell, G. R. Heath, and J. A. Goodchild. In: *Methods Mol Biol*. Vol. 1886. Humana Press, New York, NY, 2019, 29–44.

[76] J. Andersson and I. Köper. *Membranes*, 2016, 6, 30.

[77] M. Wagner and L. Tamm. *Biophys J*, 2000, 79, 1400–1414.

[78] W. Knoll et al. *Biointerphases*, 2008, 3, FA125–FA135.

[79] H. Su et al. *ACS Appl Mater Interfaces*, 2019, 11, 43799–43810.

[80] S. M. Sterling et al. *Biophys J*, 2015, 108, 1946–1953.

[81] R. Caceres, M. Abou-Ghali, and J. Plastino. *Biochim Biophys Acta, Mol Cell Res*, 2015, 1853, 3006–3014.

[82] D. Koboldt et al. *Nature*, 2012, 490, 61–70.

[83] Y. Yarden. *Oncology*, 2001, 61, 1–13.

[84] M. R. P. Pereira et al. *Nat Commun*, 2018, 9, 5137.

[85] I. S. Babina et al. Vol. 401. InTech New York, 2011, 428.

[86] M. Stoeber et al. *PNAS*, 2016, 113, E8069–E8078.

[87] N. K. Teiwes et al. *ACS Appl Mater Interfaces*, 2021, 13, 25805–25812.

[88] Y. Zhang et al. *Molecules*, 2021, 26, 6201.